Study of light nuclei by 13C beam induced reactions

Prepolec, Lovro

Doctoral thesis / Disertacija

2015

University of Zagreb

FACULTY OF SCIENCE

Lovro Prepolec

Study of light nuclei by ^{13}C beam induced reactions

DOCTORAL THESIS

Zagreb, 2015.

University of Zagreb

FACULTY OF SCIENCE

Lovro Prepolec

Study of light nuclei by ^{13}C beam induced reactions

DOCTORAL DISSERTATION

Supervisor: Dr. sc. Neven Soić

Zagreb, 2015.

Sveučilište u Zagrebu

PRIRODOSLOVNO-MATEMATIČKI FAKULTET

Lovro Prepolec

Lake atomske jezgre proučavane reakcijama izazvanim snopom ^{13}C

DOKTORSKI RAD

Mentor: Dr. sc. Neven Soić

Zagreb, 2015.

University of Zagreb
Faculty of Science
Department of Physics

Doctoral Thesis

Study of light nuclei by ^{13}C beam induced reactions

Lovro Prepolec
Ruđer Bošković Institute, Zagreb

The study of light nuclei is one of the most active areas in the nuclear physics today. Nuclei in the mass region $A < 20$ have been used as a testing sample for different theoretical models since the early days of nuclear physics. Nowadays the advent of *ab initio* calculations in various frameworks and the astrophysical interest makes the precise experimental data even more important. One of the topics of interest in the structure of light nuclei are the neutron-rich oxygen isotopes, starting already with astrophysically important ^{17}O. One of the challenging questions in this field of research is how does the well developed cluster structure in ^{16}O change with addition of neutrons in heavier oxygen isotopes. Therefore, the topic of this work is the study of the cluster-structure of the ^{17}O and ^{18}O.

In this work results of two experiments are presented: the ^{13}C+^{4}He resonant elastic scattering on a thick gas target measurement and the ^{13}C+^{9}Be resonant particle spectroscopy measurement at $E_{^{13}\mathrm{C}} = 72$ MeV. Both measurements were used due to their selectivity in populating the cluster-state candidates in ^{17}O and ^{18}O.

The known ^{13}C(^{4}He,^{4}He) elastic scattering cross-section has been extended both in angle (to the 175° in direct kinematics) and energy (up to $E_x(^{17}\mathrm{O})$=13.8 MeV). The measured cross-section can be reproduced by using published set of parameters from the comprehensive R-matrix fit. The new part of the spectrum contains several resonances of interest, for which the tentative values of spin, parity and Wigner ratio were determined using a simplified R-matrix fitting method. The resonant particle spectroscopy study of the $^{13}\mathrm{C}+^{4}\mathrm{He}\rightarrow\ ^{13}\mathrm{C} + {}^{4}\mathrm{He} + {}^{5}\mathrm{He}$ reaction has provided an improvement in statistics and the energy range covered by the previous study. Resonances decaying to the ^{13}C*+^{4}He decay channel were observed as well. The results of both measurements combined point to the pronounced α-cluster nature of the 8.9 MeV, 9.15 MeV and the 13.57 MeV ^{17}O excited states. This is in accordance with predictions of the ^{17}O rotational band based on the weakly coupled neutron to the well-known α-cluster structure in the ^{16}O. However, precise determination of exact spins and parities, as well as partial and total widths are crucial to confirm the existence of the proposed rotational band.

The results for the ^{18}O nucleus were obtained from the ^{13}C+^{9}Be reaction measurements using the resonant particle spectroscopy method. The decays of the ^{18}O* nucleus to the ^{14}C+^{4}He and ^{14}C*+^{4}He channels were studied, confirming the results and extending the excitation energy range of previous studies, as well as observing the α-decay of highly excited states for the first time. The results suggest that the ^{18}O states decaying to the ^{14}C+^{4}He channel do not decay to the ^{14}C*+^{4}He channel and vice-versa, possibly due to a different structure. The ^{6}He decay of the ^{18}O has been observed for the first time, at an excitation energy $E_x(^{18}\mathrm{O}) \approx 26.5$ MeV. Additional studies are necessary to assess the possibility of the ^{12}C+2n+^{4}He molecular structure of the ^{18}O nucleus. In the study of the $^{13}\mathrm{C}+^{9}\mathrm{Be}\rightarrow\ ^{10}\mathrm{Be}+\ ^{8}\mathrm{Be}_{\mathrm{gs}}+\ ^{4}\mathrm{He}$ reaction a few possible peaks that could indicate the ^{10}Be+^{8}Be$_{\mathrm{gs}}$ decay of the ^{18}O nucleus were observed, but statistics was too low to obtain conclusive results.

Therefore, additional measurements have to be performed. The resonant particle spectroscopy method may be used to collect the high quality data that would allow to compare the partial widths of the states, as well as to extract additional information using a DWBA calculation. The resonant elastic scattering may be used in order to clarify the spin and parity assignments of the cluster or molecular state candidates at higher ^{18}O excitation energies, but the data on all the relevant inelastic channels have to be measured as well.

(209 pages, 119 references, 149 figures, 13 tables, original in English)

Keywords: ^{17}O, ^{18}O, nuclear structure, resonant elastic scattering, resonant particle spectroscopy, cluster states, molecular states, rotational bands

Supervisor: Dr. sc. Neven Soić, Ruđer Bošković Institute, Zagreb

Reviewers:
1. Assoc. prof. dr. sc. Tamara Nikšić, University of Zagreb
2. Assoc. prof. dr. sc. Carl Wheldon, University of Birmingham, United Kingdom
3. Dr. sc. Neven Soić, Ruđer Bošković Institute, Zagreb

Thesis accepted: 2015

Sveučilište u Zagrebu
Prirodoslovno-matematički fakultet
Fizički odsjek

Doktorski rad

Lake atomske jezgre proučavane reakcijama izazvanim snopom ^{13}C

Lovro Prepolec
Institut Ruđer Bošković, Zagreb

Proučavanje lakih jezgra danas je jedno od najaktivnijih područja nuklearne fizike. Jezgre masenog područja A<20 korištene su za ispitivanje raznih modela nuklearne strukture još od ranih dana nuklearne fizike. Danas su pojavom *ab initio* računa u raznim modelima te zbog astrofizičke važnosti lakih jezgara precizni eksperimentalni podaci još potrebniji. Jedno od izazovnih pitanja u ovom području istraživanja je kako se naglašena klasterska struktura jezgre ^{16}O mijenja dodavanjem neutrona u težim izotopima kisika. Stoga je tema ovog rada proučavanje klasterske građe izotopa ^{17}O i ^{18}O.

U ovom su radu predstavljeni rezultati dvaju eksperimenata: rezonantnog elastičnog raspršenja ^{13}C+^{4}He na debeloj plinskoj meti te mjerenja reakcija ^{13}C+^{9}Be, koje su analizirane metodom rezonantne čestične spektroskopije. Oba su mjerenja odabrana zbog visoke selektivnosti za pobuđivanje stanja moguće klasterske građe u jezgrama ^{17}O i ^{18}O.

Područje poznatog udarnog presjeka elastičnog raspršenja ^{13}C(^{4}He,^{4}He) prošireno je u kutnom rasponu (ovo mjerenje odgovara kutu od 175° u direktnoj kinematici) te energiji (do $E_x(^{17}\mathrm{O}) = 13.8$ MeV). Izmjeren udarni presjek može se reproducirati korištenjem objavljenih parametara koji su rezultat opsežne prilagodbe višekanalnom R-matricom. Novoizmjereni dio spektra sadrži nekoliko zanimljivih rezonanci za koje su pojednostavljenom prilagodbom R-matrice određeni provizorni spin i paritet te Wignerov omjer. Metodom rezonantne čestične spektroskopije proučena je reakcija ^{13}C+^{4}He $\rightarrow$ ^{13}C+^{4}He+^{5}He a dobiveni rezultati imaju bolju statistiku i pokrivaju šire područje energija pobuđenja od ranije objavljenih. Također su opažene rezonance koje se raspadaju kanalom ^{13}C*+^{4}He. Rezultati oba mjerenja ukazuju na izraženu α-klastersku građu pobuđenih stanja jezgre ^{17}O na energijama 8.9 MeV, 9.15 MeV i 13.57 MeV. Taj je rezultat u skladu sa predviđanjem rotacijske vrpce ^{17}O zasnovane na poznatoj α-klasterskoj strukturi jezgre ^{16}O i slabo vezanom neutronu. Ipak, precizno određivanje spinova i pariteta stanja, kao i njihovih parcijalnih i ukupnih širina, ključno je za potvrđivanje postojanja predložene rotacijske vrpce.

Rezultati za jezgru ^{18}O dobiveni su mjerenjem reakcija ^{13}C+^{9}Be, pomoću metode rezonantne čestične spektroskopije. Raspadi jezgre ^{18}O* kanalima ^{14}C+^{4}He i ^{14}C*+^{4}He potvrdili su informacije o poznatim stanjima te proširili područje energija pobuđenja iz ranijih istraživanja. Pritom je za visokopobuđena stanja jezgre ^{18}O po prvi puta opažen α-raspad. Dobiveni rezultati pokazuju da se stanja koja se raspadaju kanalom ^{14}C+^{4}He ne raspadaju kanalom ^{14}C*+^{4}He i obrnuto, vjerojatno zbog različite strukture. Po prvi je puta opažen ^{6}He raspad jezgre ^{18}O, na energiji pobuđenja $E_x(^{18}\mathrm{O}) \approx 26.5$ MeV. Potrebna su dodatna istraživanja kako bi se donio zaključak o postojanju moguće molekularne strukture oblika ^{12}C+2n+^{4}He. Analizom reakcije $^{13}\mathrm{C}+^{9}\mathrm{Be} \to {}^{10}\mathrm{Be} + {}^{8}\mathrm{Be}_{\mathrm{gs}} + {}^{4}\mathrm{He}$ pronađeni su mogući vrhovi koji bi mogli ukazivati na ^{10}Be+^{8}Be$_{\mathrm{gs}}$ raspad pobuđenih stanja jezgre ^{18}O, no broj događaja je premalen da bi se mogao donijeti zaključak.

Dakle, potrebna su dodatna mjerenja. Tehnikom rezonantne čestične spektroskopije mogli bi se prikupiti visokokvalitetni podaci, iz kojih bi bilo moguće usporediti parcijalne širine stanja, kao i izdvojiti podatke o strukturi korištenjem DWBA računa. Rezonantno elastično raspršenje može se iskoristiti za razjašnjavanje vrijednosti spina i pariteta klasterskih ili molekulskih stanja na višim energijama pobuđenja ^{18}O, no pritom treba prikupiti i podatke o neelastičnim kanalima.

(209 stranica, 119 literaturnih navoda, 149 slika, 13 tablica, izvornik na engleskom jeziku)

Ključne riječi: ^{17}O, ^{18}O, nuklearna struktura, rezonantno elastično raspršenje, rezonantna čestična spektroskopija, klasterska stanja, molekulska stanja, rotacijske vrpce

Mentor: Dr. sc. Neven Soić, Ruđer Bošković Institute, Zagreb

Povjerenstvo za obranu:

1. Izv. prof. dr. sc. Tamara Nikšić, Sveučilište u Zagrebu
2. Izv. prof. dr. sc. Carl Wheldon, University of Birmingham, Ujedinjeno Kraljevstvo
3. Dr. sc. Neven Soić, Ruđer Bošković Institute, Zagreb

Rad prihvaćen: 2015

I would like to thank my advisor, dr. sc. Neven Soić, for giving me the opportunity to work in this field and for the guidance of this thesis. I would also like to thank prof. Martin Freer, who proposed the resonant elastic scattering experiment and guided its analysis despite his tight schedule. I am indebted to dr. sc. Matko Milin, whose help was invaluable for this thesis. My gratitude goes to Vedrana for her expertise, insight and advice. I would like to thank colleagues from the Laboratory for nuclear physics for all their help and support over these years, especially Milivoj, Deša, Tea and Mladen. I would like to thank dr. sc. Suzana Szilner her support and for providing me with the opportunity to participate in experiments of the PRISMA collaboration. I am grateful to Natko, both for the ^{13}C *beam and his help with the Orsay experiment.*

My thanks goes to our colleagues from the University of Birmingham and INFN-LNS Catania who collaborated on experiments performed for this thesis.

My immense gratitude goes to my family and friends. Mum, dad, Ivan and Jelena, thank you! Among my friends, I have to mention Marko and Marijan, as well as Mario, Andrija, Danijel, Ivan, Goran, Ángel, Toni, Kruno, Vuko, Matija, Antun, Daniel, Ivica, Milivoj, Jurica and many others. Your support made this work possible.

Finally, I would like to thank God, from whom all good things come.

Prošireni sažetak

Danas je jedno od najaktivnijih područja nuklearne fizike istraživanje lakih jezgara, jezgara koje imaju do dvadeset nukleona. Budući da imaju mali broj stanja na umjerenim pobuđenjima, u tom masenom području jezgre su pogodne za ispitivanje raznih modela nuklearne strukture još od ranih dana nuklearne fizike. Danas razvijeni moderni *ab initio* računi u raznim modelima čine precizne eksperimentalne podatke još potrebnijima. Stoga se ulažu veliki napori kako bi se došlo do onih podataka koji još uvijek nedostaju a nužni su za ocjenu ispravnosti teorijskih modela.

Do danas je postignuto gotovo potpuno poznavanje spektroskopije za jezgre sa do devet nukleona. Nekoliko važnih stanja još uvijek nije jasno identificirano (npr. prvo pobuđeno $\frac{1}{2}^+$ stanje u ^{9}B), no ključan dio eksperimentalnog istraživanja je napravljen.

Za područje nešto viših masa ($A = 10$ do 20) postoji nekoliko važnih smjerova istraživanja: izotopi sa $A = 10$ i 11 sa svojim različitim klasterskim strukturama koje su pronađene ali još nisu sistematizirane, jezgra ^{12}C i stanja koja pripadaju rotacijskoj vrpci Hoyleovog stanja te naposljetku neutronski bogati izotopi kisika, počevši sa izotopom od astrofizičkog značaja, ^{17}O. Ova radnja će se usredotočiti na posljednju od navedenih tema.

Jezgra ^{16}O je posebna po mnogočemu. Njezino osnovno stanje je gotovo savršenog sfernog oblika, što je posljedica dvostruke magičnosti te jezgre u modelu ljusaka. Iz istog razloga prvo pobuđeno stanje u ^{16}O ima vrlo visoku energiju pobuđenja, $E_x = 6.05$ MeV (samo ^{14}C ima više prvo pobuđeno stanje među jezgrama s masenim brojem većim od četiri). S druge strane, ona je klasičan primjer klasteriranja, sa ^{12}C+α konfiguracijom niskoležećih stanja [1]. Prvo pobuđeno stanje je također početno stanje rotacijske vrpce (sa stanjem spina i pariteta 2^+ na energiji $E_x = 6.92$ MeV, 4^+ na $E_x = 10.36$ MeV i 6^+ na $E_x = 16.28$ MeV). Rotacijska vrpca negativnog pariteta za istu strukturu je također dugo poznata (stanje spina i pariteta 1^-

na energiji $E_x = 9.59$ MeV, 3^- na $E_x = 11.60$ MeV, 5^- na $E_x = 14.66$ MeV i 7^- na $E_x = 20.86$ MeV), što je također klasični primjer drugog važnog fenomena koji se pojavljuje kod asimetričnih klasterskih struktura: primjer cijepanja po paritetu [2]. Istovremeno postojanje stanja modela ljusaka i klasterskih stanja kod ^{16}O danas se prilično dobro razumije iz teorijske perspektive i osigurava dobru bazu za proučavanje težih kisikovih izotopa.

Esencijalno pitanje pri proučavanju neutronski bogatih kisikovih izotopa je sljedeće: opstaje li jako izražena klasterska struktura ^{16}O pri dodavanju neutrona i kako se mijenja kada se dodaju neutroni?

Da bi se dobio sistematičan odgovor na ovo pitanje, prvo je potrebno proučiti jezgru ^{17}O, prepoznati klasterska stanja i dobiti kvantitativan opis stupnja klasteriranja za svako od njih (npr. pomoću reduciranih parcijalnih širina). Rana kvalitativna istraživanja u tom smjeru učinjena su prije otprilike trideset godina ([2], [3], [4], [5]), dok je novije istraživanje [6] potvrdilo neke od prijašnjih rezultata i sistematiziralo ih. Neka stanja ^{17}O (između $E_x = 5.9$ i 7.3 MeV) također su od velike važnosti za astrofiziku, zbog činjenice da je reakcija ^{13}C(α,n)^{16}O trenutno najbolji kandidat za izvor neutrona pri s-procesu nukleosinteze u termički pulsirajućim zvijezdama male mase na asimptotskoj grani divova ([7], [8]). Za izračun udarnih presjeka i brzina odvijanja reakcija na astrofizičkim energijama potrebni su vrlo precizni podaci o rezonancijama u ovoj reakciji. Također se poduzimaju istraživanja pomoću indirektnih metoda, npr. metodom trojanskog konja [9].

Dodavanjem sljedećeg neutrona dobivamo ^{18}O, jezgru s ukupnim brojem stanja sličnim ^{17}O (stotinjak stanja do energije ekscitacije 20 MeV). Klasteriranje u ^{18}O je također predmet proučavanja već desetljećima (npr. [10], [11]), no nedavni eksperimentalni rezultati [12], [13] i [14] ju ponovno čine zanimljivom. Još uvijek postoji niz otvorenih pitanja ([13], [15], [16]), stoga su novi eksperimentalni podaci nužni za dobivanje jasne slike konfiguracija pobuđenih stanju u ^{17}O i ^{18}O.

Glavni cilj ovog istraživanja je bolje razumijevanje strukture jezgara ^{17}O i ^{18}O. Pritom ćemo se usredotočiti na stanja klasterske i molekulske građe, no za postizanje punog razumijevanja obije jezgre nužan je i uvid u građu stanja modela ljusaka. Glavna hipoteza ovih istraživanja je da dobro poznata klasterska stanja u ^{16}O imaju odgovarajuće partnere u ^{17}O i ^{18}O te da ih se može povezati modelom slabog vezanja [17] te tako stvoriti bazu za daljnja proučavanja težih izotopa kisika, sve do linije neutronskog curenja (posljednji čestično vezan izotop kisika je ^{24}O).

Struktura lakih jezgara

Jezgra ^{4}He ili α-čestica jedna je od najbolje vezanih lakih jezgara. Njeno prvo pobuđeno stanje nalazi se na energiji nešto višoj od 20 MeV. Interakcija među α-česticama je slaba i privlačna na većim udaljenostima a na malim udaljenostima vrlo odbojna zbog Paulijevog principa. Stoga je oblik potencijala između dvije α-čestice po obliku sličan van der Waalsovom potencijalu. Zbog svih ovih karakteristika, α-čestica predstavlja idealan klaster. Osim α-čestice i ostale jezgre zatvorenih ljusaka, kao što je ^{16}O, ili zatvorenih podljusaka, kao što su ^{12}C i ^{14}C, mogu imati ulogu klastera.

Klasterske se strukture u jezgrama s podjednakim brojem protona i neutrona ($A = Z$ ili α-konjugirane jezgre) počinju opažati kada njihovo stvaranje postane energijski povoljno: za vrlo lake jezgre kao što je ^{8}Be to je moguće već u osnovnom stanju dok je za teže jezgre na energijama pobuđenja koje su bliske pragu raspada jezgre emisijom α-čestice (vidi Sliku 2.2 na str. 6).

Jedan od najljepših potpisa klasterskih struktura su rotacijske vrpce (vidi Sliku 2.3 na str. 7). One nastaju jer su klasterska stanja deformirana te stoga postaju glava vrpce pobuđenih stanja čiji su viši članovi njihova rotacijska pobuđenja. Asimetrične klasterske strukture, kod kojih su klasteri različitih veličina, tvore dvije rotacijske vrpce suprotnih pariteta koje se nazivaju kvazimolekulskim rotacijskim vrpcama, prema sličnosti sa spektrima molekula u atomskoj fizici.

Klasterske strukture u jezgrama koje nisu α-konjugirane znatno su složenije. Dodatni neutroni mogu sa klasterskim strukturama tvoriti egzotične konfiguracije, u kojima slabo vezani neutroni mogu dodatno vezati klastere, slično kao što kod kovalentne veze elektoni vežu atome u molekulu. Stoga su i primjeri takvih struktura nazvani nuklearnim molekulama. Jasni dokazi takvih struktura su pronađeni za berilijeve izotope ^{9}Be i ^{10}Be ([21], [24]), dok je potraga za molekulskim strukturama u sustavima s više centara u tijeku (ugljikovi izotopi kao primjer sustava s tri centra i kisikovi izotopi kao primjer sustava s četiri centra).

Povijesno gledano, prvi su mikroskopski opisi klasterskih struktura dobiveni pomoću modela rezonantnih grupa (*engl.* resonanting group model, RGM) [25]. Uslijedili su model generirajućih koordinata (*engl.* generator coordinate model, GCM) [26] i polumikroskopski model uvjeta ortogonalnosti (*engl.* orthogonality condition model, OCM) [27]. Model molekulskih orbitala (*engl.* molecular orbital model, MO) [31] zasniva se na postavkama iz atomske fizike, a uz odgovarajuća proširenja prostora modela i dodatak spin-orbit interakcije dobro opisuje stanja jezgara ^{9}Be i ^{10}Be. Antisimetrizirana molekulska dinamika (*engl.* antisymmetrized molecular dynamics, AMD) je teorijski model koji uspješno reproducira stanja modela ljusaka i klasterska stanja lakih jezgara ([29] i reference navedene u članku). Sam račun ne pretpostavlja strukturu jezgre, već polazeći od pojedinačnih nukleona predstavljenih Gaussovim valnim paketima gradi jezgru. Proračuni AMD modelom osim berilijevih izotopa također uspješno opisuju kisikove izotope. Postoje i nastojanja da se modelima koji se tradicionalno nisu koristili za opis klasterskih stanja lakih jezgara steknu dodatni uvidi u njihovu građu. Tako je proračunom u modelu energijskih funkcionala gustoće bez dodatnih pretpostavki dobivena klasterska građa osnovnog stanja jezgre ^{20}Ne [28].

Pri promatranju klasterske građe kisikovih izotopa najbolje je krenuti od ^{16}O, dvostruko magične jezgre. Njena je građa izvrsno poznata i s teorijske i s eksperimentalne strane, te već prvo pobuđeno stanje ima klastersku građu ^{12}C+^{4}He, što je potvrđeno brojnim mjerenjima i teorijskim modelima. Budući da se radi o asimetričnoj strukturi, javljaju se dvije rotacijske vrpce projekcije momenta impulsa $K^\pi = 0^\pm$.

Dodavanjem jednog neutrona jezgri ^{16}O dobiva se ^{17}O. Njegova je struktura bitno složenija od one koja bi se očekivala za intertnu ^{16}O sredicu i jedan neutron. Dakle, pobuđenja ^{16}O sredice doprinose spektru. Objašnjenje stanja negativnog pariteta u spektru ^{17}O dobiva se miješanjem konfiguracija 2 čestice i jedne šupljine (2p-1h) te klasterskih konfiguracija 4p-3h. Usprkos složenosti spektra neka se stanja mogu opisati modelom slabog vezanja neutrona sa klasterskim stanjima ^{16}O.

Strukture pobuđenih stanja u ^{18}O mogu se klasificirati u tri skupine: stanja ^{16}O$\otimes$2n građe, ^{14}C$\otimes\alpha$ građe te ^{12}C$\otimes 2n \otimes \alpha$ građe. Na temelju brojnih eksperimentalnih i teorijskih istraživanja, predložene su rotacijske vrpce $K^\pi = 0_1^+$, $K^\pi = 0_1^-$, $K^\pi = 0_2^\pm$ i $K^\pi = 0_4^\pm$. Pritom $K^\pi = 0_1^+$ vrpca odgovara osnovnom stanju jezgre strukture $^{16}O \otimes 2$n i završava maksimalnim spinom 4^+. Predložena vrpca $K^\pi = 0_1^-$ koja započinje stanjem $E_x = 4.457\ MeV$, $J^\pi = 1_1^-$ i odgovara pobuđenjima protona u jezgri. Vrpce $K^\pi = 0_2^\pm$ odgovaraju klasterskoj građi ^{14}C$\otimes^4$He. Dok su prva četiri člana rotacijske vrpce pozitivnog pariteta dobro poznata, rotacijska vrpca negativnog pariteta je tek predložena. Zadnje dvije predložene rotacijske vrpce, $K^\pi = 0_4^\pm$, trebale bi imati molekulsku građu ^{12}C$\otimes 2n \otimes \alpha$.

Avila *et al.* [14] nedavno su objavili rezultate višekanalne prilagodbe R-matricom, od praga α-raspada ^{18}O do energije pobuđenja od 14.9 MeV. Uočeno je da umjesto jednog jakog klasterskog stanja, kao što je bilo očekivano, postoji više susjednih stanja sa izraženom α-klasterskom građom. Teorijsko objašnjenje tih rezultata pomoću modela klaster-nukleon konfiguracijske interakcije (*engl.* cluster-nucleon configuration interaction model) [43] ukazuje na značajno miješanje konfiguracija, kakvo nije predviđeno u ranijim teorijskim radovima pomoću GCM ili AMD-RGM modela.

Mjerenje rezonantnog elastičnog raspršenja ^{13}C+α

Mjerenje rezonantnog elastičnog raspršenja ^{13}C+^{4}He izvršeno je na akcelatorskom postrojenju Instituta Ruđer Bošković u Zagrebu. Mjerenje ekscitacijske funkcije, odnosno mjerenje ovisnosti udarnog presjeka o energiji, može se vršiti na više načina: u direktnoj ili inverznoj kinematici te pomoću tanke ili debele mete. Mjerenje u inverznoj kinematici pomoću debele plinske mete omogućuje istovremeno pokrivanje širokog spektra energija, zaustavljanje snopa unutar plina uz istovremenu mogućnost mjerenja lakih čestica na 0°. Pritom se svaki dio spektra pokriva s više mjerenja, kako bi se moglo odrediti jakost doprinosa neelastičnih procesa izmjerenom udarnom presjeku.

Detektorski se postav sastojao od jednog dvostranog silicijskog detektora segmentiranog na pruge dimenzija 50×50 mm smještenog na 0°. Detektor sa prednje i sa stražnje strane ima po šesnaest pruga, a budući da su jedne pruge horizontalne a druge vertikalne to u konačnici daje 256 efektivnih piksela, pri čemu je piksel definiran kao presjecište jedne horizontalne i jedne vertikalne pruge. Pri mjerenju je korišten standardni elektronički postav koji se sastojao od pretpojačala, pojačala, diskriminatora, analogno-digitalnih pretvarača i računala za prikupljanje podataka. Komora za mjerenja bila je odvojena od eksperimentalne linije tankom metalnom membranom od slitine Havar te napunjena helijem. Mjerenje temperature i tlaka plina pomoću termočlanka i apsolutnog vakuumetra omogućilo je točno određivanje gustoće plina.

Kalibracija detektora izvršena je pomoću mjerenja elastičnog raspršenja ^{7}Li na tankoj zlatnoj meti na energijama snopa od 12 i 16 MeV te mjerenja elastičnog raspršenja ^{9}Be na tankoj meti zlata pri energiji od 17 MeV. Kod mjerenja je detektor bio pomaknut sa 0° na 44.6°. Pri kalibraciji je uočeno malo odstupanje kalibracijskih točaka od pravca. Uvođenjem efektivnog mrtvog sloja silicijskog detektora od 0.5 μm gotovo sve kalibracijske točke su padale unutar 20 keV od kalibracijskog pravca. Mjerenje elastičnog raspršenja na tankoj meti zlata sa membranom od Havara postavljenom na ulaz u komoru je iskorišteno za dobivanje njene debljine, koja iznosi 2.11 ± 0.02 μm.

Analiza podataka prikupljenih pri mjerenju na debeloj plinskoj meti vrši se pod pretpostavkom da je svaka detektirana čestica α-čestica iz elastičnog raspršenja. To naravno nije uvijek slučaj, no pri svakom mjerenju na određenom tlaku i energiji snopa najviši dio spektra je lišen doprinosa neelastičnih procesa (u slučaju neelastičnog procesa detektirana energija α-čestice je nužno niža). Stoga se usporedbom mjerenja na različitim energijama može doći do ocjene utjecaja neelastičnih procesa u određenom području spektra. Dimenzije korištenog detektora su relativno velike, stoga kutni raspon koji pokriva nije zanemariv. Kako bi se zadržala točnost proračuna, 256 piksela u detektoru je podijeljeno u 28 kategorija, ovisno o udaljenosti od središta. Tada je za svaku kategoriju piksela i za svako mjerenje izvršen proračun koji povezuje energiju detektirane α-čestice sa energijom u sustavu centra mase snopa i mete, koja se dodavanjem energije praga raspada jezgre ^{17}O u ^{13}C+^{4}He pretvara u energiju pobuđenja jezgre ^{17}O. Tako dobivene točke su interpolirane polinomom te korištene u kodu za analizu podataka. Rezultat analize za pojedino mjerenje je odgovarajuća ekscitacijska funkcija ^{17}O dobivena iz svih prikupljenih podataka. S obzirom da se efikasnost detekcije određenog pobuđenja u ^{17}O mijenja unutar pojedinog mjerenja, ovisno o točki u kojoj se događa raspresenje, potrebno je korigirati podatke s obzirom na efikasnost. Uobičajeni pristup, zasnovan na Monte Carlo simulaciji koja pretpostavlja izotropnu raspodjelu čestica u sustavu centra mase, zamijenjen je jednostavnim uvjetom na kut emisije α-čestice u sustavu centra mase $\left(\vartheta^{\mathrm{CM}}_{^4\mathrm{He}} < 5^\circ\right)$. Kako bi taj uvjet bio bolje primijenjen, pri analizi podataka je položaj detekcije unutar pojedinog piksela nasumično odabran za svaki događaj te je tako dobivena glatka raspodjela detektiranih čestica po kutu. Podaci korigirani uvjetom na kut emisije u sustavu centra mase pokazali su se međusobno konzistentnima, bez značajnih doprinosa neelastičnih procesa. Zatim se pristupilo uprosječivanju dobivenih ekscitacijskih funkcija. Prije uprosječivanja rezultati mjerenja su normalizirani prema visini vrhova iz mjerenja br. 35, na energiji snopa od 35 MeV i tlakom plina od 720 mbar. Nakon toga su sve ekscitacijske funkcije poravnate prema ekscitacijskoj funkciji mjerenja br. 25, koje je bilo izvedeno na najnižoj energiji snopa od 20 MeV, koristeći najniži tlak plina od 312 mbar. Pomaci su iznosili od -0.030 do 0.020 MeV. Zbog malih sistematskih pomaka vrhova na niskim energijama pri uprosječivanju ekscitacijskih funkcija do energije pobuđenja od 9.75 MeV korišteni su samo rezultati mjerenja br. 25 i 27 ($E_{^{13}\mathrm{C}}$=25 MeV and $\mathrm{p}_{^4\mathrm{He}}$=461 mbar). Konačna uprosječena ekscitacijska funkcija odgovara mjerenju u direktnoj kinematici na 175° u laboratorijskom sustavu. Stoga smo uprosječenu ekscitacijsku funkciju usporedili sa mjerenjima rezonantnog elastičnog raspršenja u direktnoj kinematici, na kutevima od 165.9° i 165.0°. Rezultati ovog rada dobro odgovaraju ranijima pri čemu je vidljivo sistematsko odstupanje niskoenergijskih vrhova koji ne nalaze na $E_x(^{17}\mathrm{O}) = 8.4$, 8.9 i 9.2 MeV. Ono redom iznosi 0.046, 0.035 i 0.026 MeV za tri navedena vrha. Uzrok odstupanju je debljina efektivnog mrtvog sloja utvrđena iz kalibracijskih mjerenja pomoću ^{7}Li i ^{9}Be, koja nije adekvatna za jezgru ^{4}He. Stoga je energijska rezolucija konačnog spektra nešto lošija od očekivane. Usporedbom s ranijim mjerenjima uočen je sistematski pomak cijelog uprosječenog spektra, koji je iznosio 0.038 MeV i koji je korigiran. Tom je prilikom izvršena i normalizacija podataka na ranije izmjeren udarni presjek. Normalizacijski faktor za uprosječenu ekscitacijsku funkciju ^{17}O iznosi 0.0006 te daje zadovoljavajuće preklapanje s objavljenim podacima.

Nakon što je iz izmjerenih podataka dobiven udarni presjek, moglo se pristupiti reproduciranju objavljenog proračuna R-matricom. Pritom je bilo važno uzeti u obzir sve reakcijske kanale koji se značajno pobuđuju u reakciji. Prag raspada jezgre ^{17}O neutronom nalazi se na $E_x(^{17}\mathrm{O}) = 4.144$ MeV a α-česticom na $E_x(^{17}\mathrm{O}) = 6.359$ MeV. Stoga je pri analizi udarnog presjeka bitno uzeti u obzir i neelastične neutronske reakcijske kanale. Najintenzivnije pobuđivani su $^{16}\mathrm{O}^{*}+\mathrm{n}'$ i $^{16}\mathrm{O}^{**}+\mathrm{n}''$, koji odgovaraju prvom i drugom pobuđenom stanju jezgre ^{16}O [61]. Sveobuhvatna prilagodba eksperimentalnih podataka modelom fenomenološke R-matrice objavljena je u radu Heila *et al.* [7]. Za potrebe tog rada autori su izvršili detaljna mjerenja elastičnog udarnog presjeka $^{13}\mathrm{C}(^{4}\mathrm{He},^{4}\mathrm{He})^{13}\mathrm{C}$ na velikom broju kuteva te mjerenja totalnog udarnog presjeka reakcije $^{13}\mathrm{C}(^{4}\mathrm{He},\mathrm{n})^{16}\mathrm{O}$. U prilagodbu su uključena i mjerenja $^{16}\mathrm{O}(\mathrm{n},\mathrm{n})^{16}\mathrm{O}$, $^{13}\mathrm{C}(^{4}\mathrm{He},\mathrm{n})^{16}\mathrm{O}$, $^{16}\mathrm{O}(\mathrm{n},^{4}\mathrm{He})^{13}\mathrm{C}$ te $^{16}\mathrm{O}(\mathrm{n},\mathrm{n}'')$ drugih autora. Istovremenom prilagodbom eksperimentalnih podataka za sve ranije navedene kanale metodom fenomenološke R-matrice, koristeći kod SAMMY dobivene su energije, spinovi i pariteti te parcijalne širine stanja. Prilagodba je obuhvaćala područje ekscitacije ^{17}O do približno 11.1 MeV. Polazeći od tih rezultata, u ovom smo radu krenuvši od objavljenih parametara rezonanci pomoću koda AZURE2 nastojali reproducirati objavljenu prilagodbu. Pritom su neke vrlo malene ili vrlo velike vrijednosti parametara uzrokovale numeričke probleme u programu koji smo koristili te smo ih trebali promijeniti. Slaganje između rezultata našeg proračuna i objavljene prilagodbe za elastični kanal $^{13}\mathrm{C}+^{4}\mathrm{He}$ na niskim energijama je vrlo dobro. Do razlika dolazi otvaranjem neelastičnih neutronskih reakcijskih kanala $^{16}\mathrm{O}^{*}+\mathrm{n}'$ i $^{16}\mathrm{O}^{**}+\mathrm{n}''$ na energijama pobuđenja $E_x(^{17}\mathrm{O}) = 10.193$ i 10.273 MeV. Proračun dobro reproducira glavne značajke udarnog presjeka elastičnog raspršenja neutrona na jezgri ^{16}O. Bitne razlike između objavljenih podataka i rezultata prilagodbe vidljivi su za $^{16}\mathrm{O}(\mathrm{n},\mathrm{n}'')$ reakciju, prije svega zbog nužnih promjena parcijalnih širina kako bi se programom

AZURE2 mogao izvršiti izračun udarnih presjeka. Dobiveni rezultati dobro reproduciraju totalan udarni presjek ^{16}O(n,^{4}He)^{13}C i ^{13}C(^{4}He,n)^{16}O sve do energija pobuđenja $E_x(^{17}O) \approx 9$ MeV, dok na višim energijama još uvijek slijedi trend podataka, no uz sistematsko odstupanje. Ovo odstupanje je također povezano s nužnim promjenama parametara. Nakon provjere, prilagodba R-matricom je iskorištena za izračun udarnog presjeka elastičnog raspršenja ^{13}C(α,α)^{13}C na $\approx$175° u laboratorijskom sustavu, pri direktnoj kinematici, što odgovara podacima izmjerenim u ovom radu, uz eksperimentalnu rezoluciju od 0.030 MeV. Izračunati udarni presjek dobro odgovara izmjerenim podacima, uz sistematsko odstupanje pri vrhu na $E_x(^{17}\mathrm{O}) \approx 10.0$ MeV u skladu s općim trendom povećanja odstupanja s povećanjem kuta koji je vidljiv iz ranije objavljenih podataka.

Proširenje prilagodbe R-matricom na dio spektra pobuđenja od 11.1 do 13.8 MeV nije bilo moguće zbog nepostojanja objavljenih podataka u drugim relevantnim kanalima, što onemogućuje jednoznačnu prilagodbu. Stoga je provedena pojednostavljena analiza kvaziizoliranih rezonanci u novoizmjerenom dijelu spektra kako bi se odredio približan iznos spina i utvrdio Wignerov omjer. Pojednostavljenje se sastojalo u uklanjanju svih reakcijskih kanala osim elastičnog ^{13}C+^{4}He, uklanjanju svih rezonanci osim jedne te ograničavanju područja prilagodbe na promatrani vrh kvaziizolirane rezonance. Tom metodom za svaki je vrh izvršeno više prilagodbi sa širokim spektrom različitih spinova i pariteta, te je kao najvjerojatniji odabran onaj koji je davao najmanja odstupanja od podataka. Metoda je iskušana na dvije kvaziizolirane rezonance čiji su spinovi i pariteti bili poznati iz već objavljene prilagodbe R-matricom, te se pokazalo da uspješno predviđa približan iznos spina kao i povećani Wignerov omjer što je indikacija moguće klasterske građe. Potom je ta metoda primijenjena na tri kvaziizolirana vrha koja se nalaze u području $E_x(^{17}\mathrm{O}) > 11.1$ MeV: vrh na 12.0, 12.8 i 13.6 MeV. Za vrh na 12.0 MeV pojednostavljena analiza daje dvije vrijednosti: $J^\pi = \frac{13}{2}^-$ i $J^\pi = \frac{11}{2}^+$. Pripadne vrijednosti Wignerovog omjera su redom 0.925 i 0.153. Stoga, ukoliko su spin i paritet rezonance na 12.0 MeV jednaki $\frac{13}{2}^-$ ona vjerojatno ima naglašenu α-klastersku građu. Vrhu na 12.8 MeV najbolje odgovara $J^\pi = \frac{7}{2}^-$, pri čemu je Wignerov omjer 0.107. Za vrh na 13.6 MeV kao najvjerojatniji spin i paritet dobiva se $J^\pi = \frac{11}{2}^-$ uz Wignerov omjer 0.246. Pritom je važno imati na umu da su ove vrijednosti rezultat pojednostavljene prilagodbe koja uzima u obzir samo jednu rezonancu i jedan reakcijski kanal te usko područje oko pojedinačnog vrha.

Mjerenje reakcija ^{9}Be+^{13}C pri E$_{\mathrm{lab}}$= 72 MeV

Cilj ovog mjerenja je bio proučavanje stanja ^{17}O i ^{18}O koja se raspadaju emisijom ^{4}He, te potraga za pobuđenim stanjima ^{18}O koja se raspadaju emisijom ^{6}He i ^{8}Be. Reakcije prijenosa α-čestice, ^{5}He ili n+^{4}He su vjerojatne pri energiji snopa od 72 MeV zbog strukture jezgre mete ^{9}Be, što je i uočeno u ranijem eksperimentu [6]. U istom je eksperimentu također uočeno da se jače pobuđuju stanja ^{17}O nego stanja ^{18}O. Mjerni postav korišten u ovom eksperimentu omogućio je prikupljanje dovoljnog broja događaja za obije ranije navedene jezgre.

Metoda kojom su dobiveni podaci o pobuđenim stanjima jezgara naziva se rezonantna čestična spektroskopija a zasniva se na koincidentnoj detekciji $n-1$ od n izlaznih čestica, čime je reakcija u potpunosti kinematički određena. Tada se može jednoznačno identificirati reakcijski kanal kojem pripadaju detektirane čestice kao i pobuđenja jezgara koje su nastale u prvom koraku reakcije.

Ovo je mjerenje izvedeno na akceleratorskom Tandem Van de Graaff postrojenju IPN Orsay u Francuskoj. Mjerni se postav sastojao od šest silicijskih detektorskih teleskopa. Svaki od detektorskih teleskopa sastojao se od jednog para silicijskih detektora: prednji detektor bio je jednostrani silicijski detektor segmentiran na pruge debljine 20 μm (ΔE detektor) dok je stražnji detektor bio dvostrani silicijski detektor segmentiran na pruge debljine 1000 μm (E detektor), oba proizvodi tvrtke Micron Semiconductor Ltd. Dimenzije aktivne površine prednjeg i stražnjeg detektora su 50×50 mm. Detektorski postav pokrivao je širok kutni raspon, od približno 11° pa sve do 115°. Priprema mjernog postava i samo mjerenje bili su prilično zahtjevni zbog kratkih vremenskih rokova za pripremu te neočekivanih problema s kolimiranjem snopa i akceleratorom. Stoga je količina dostupnih kalibracijskih podataka bila ograničena, što je onemogućilo kalibraciju stražnjih detektorskih teleskopa T5 i T6. Elektronički lanac korišten u eksperimentu sastojao se od standardne nuklearne elektronike (skica elektroničkog lanca prikazana je na Slici 4.5 na str. 69). Signali iz detektora obrađivali su se kao energijski signali čija se amplituda pohranjivala pomoću sustava za prikupljanje podataka i kao logički signali, pomoću kojih se vršio odabir događaja koji će se pohraniti i formirao signal za okidanje sustava. Procijenjeno mrtvo vrijeme u ovom eksperimentu bilo je nešto veće od očekivanog zbog načina na koji je vršeno okidanje te problema sa kolimiranjem snopa. Raspršenja na kolimatorima uzrokovala su povećani broj detektiranih čestica, najviše u detektorskom teleskopu T2. Istovremeno, sustav okidanja je omogućavao preklapanje koincidentnih događaja sa jednostrukim događajima koji potječu od raspršenja. Povećan multiplicitet događaja povećava vrijeme potrebno za obradu signala u analogno-digitalnim pretvaračima (*engl.* analog to digital converter, ADC). Povećan multiplicitet koincidentnih događaja (zbog preklapanja jednostrukih događaja) te povećan broj jednostrukih događaja (bilježio se svaki 555. jednostruki događaj) doveli su do povećanja mrtvog vremena.

Prvi korak u kalibraciji svih detektora bio je korištenje spektroskopskog α-izvora s tri karakteristična vrha na energijama 5.155, 5.486 and 5.805 MeV (^{239}Pu-^{241}Am-^{244}Cm izvor). U drugom koraku korišteni su podaci sa mjerenja elastičnog raspršenja ^{13}C+^{197}Au na energiji $E_{\mathrm{snop}} = 46.13$ MeV. Dodatno su korišteni i podaci dobiveni koincidentnom detekcijom ^{13}C+^{9}Be, kao i reakcije ^{9}Be(^{13}C,^{7}Li)^{15}N te ^{9}Be(^{13}C,^{6}Li)^{16}N.

Kao prvi korak u kalibraciji ovog eksperimenta izvršeno je usklađivanje pojačanja prednjih i stražnjih segmenata dvostranih detektora segmentiranih na pruge [18]. Za usklađivanje su korišteni rezultati običnih, ne kalibracijskih, mjerenja na ^{9}Be meti. Rezultat tog postupka je linearna funkcija koja omogućuje da se amplituda signala iz pojedinog prednjg ili stražnjg segmenta detektora pretvori u ekvivalentnu amplitudu referentnog segmenta (u našem slučaju odabran je prednji segment br. 8). Taj je korak značajno olakšao daljnju kalibraciju. Preliminarna kalibracija za sve detektore dobivena je pomoću mjerenja sa spektroskopskim α-izvorom i E-detektorima. Potom je mjerenje sa spektroskopskim α-izvorom i ΔE-E detektorskim teleskopom iskorišteno za dobivanje debiljne ΔE detektora za pojedine piksele u E detektoru. Nakon ovog koraka se kalibracija prednjih (T1, T2) detektorskih teleskopa i onih na srednjim kutevima (T3, T4) razlikuje. Za prednje detektore je kut fino podešen pomoću mjerenja elastičnog raspršenja, koje je kasnije iskorišteno za dobivanje punog profila ΔE detektora kao i visokoenergijskih kalibracijskih točaka za E-detektor. Fino podešavanje kuta za detektorske teleskope T3 i T4 izvršeno je pomoću koincidentne detekcije ^{13}C+^{9}He, pri čemu su korištene kombinacije detektora ^{13}C(T1)+^{9}Be(T4) te ^{13}C(T2)+^{9}Be(T3). Profil i kalibracija ΔE detektora teleskopa T3 dobiveni su isključivo pomoću podataka prikupljenih u kalibracijskom mjerenju sa α-izvorom. Kalibracijske točke na visokoj energiji za E detektor teleskopa T4 dobivene su iz izmjerenih podataka za reakcije ^{9}Be(^{13}C,^{7}Li)^{15}N te ^{9}Be(^{13}C,^{6}Li)^{16}N, koje su iskorištene i za dobivanje profila i kalibracije ΔE detektora.

Nakon kalibracije detektora provjeren je sastav mete. Utvrđeno je da osim ^{9}Be sadrži tragove ugljika, kisika te nekog teškog elementa, najvjerojatnije željeza.

Analiza svih reakcijskih kanala sastojala se od nekoliko identičnih koraka, koje ćemo ovdje ukratko opisati. Prvo bi se u podacima odabrali odgovarajući koincidentni događaji u kojima su identificirane detektirane jezgre, zatim bi ih se prikazalo u Catania grafu [81] (vidi npr. Sliku 4.15 na str. 87). Svaki od lokusa u Catania grafu odgovara određenom reakcijskom kanalu. Nakon odabira odgovarajućeg reakcijskog kanala u jednodimenzionalnom ili dvodimenzionalnom grafu Q-vrijednosti (vidi npr. Sliku 4.20 na str. 90) pristupa se izračunu relativnih energija. Relativne energije između pojedinih parova čestica omogućuju određivanje koje su od njih nastale raspadom iste jezgre majke (vidi npr. Sliku 4.21 na str. 91).

Prvo ćemo iznijeti rezultate za ^{17}O, dok će fizikalna interpretacija biti dana u zaključku. Proučavanjem reakcije ^{9}Be+^{13}C $\rightarrow$^{13}C+^{4}He+^{5}He prikupljene su informacije o stanjima ^{17}O koja se raspadaju kanalima ^{13}C+^{4}He i ^{13}C*($E_x \approx 7$ MeV)+^{4}He. U raspadu kanalom ^{13}C+^{4}He uočeno je više stanja, od kojih je najintenzivniji vrh na 13.57 MeV, koji odgovara pobuđenom stanju na 13.58 MeV spina i pariteta $J^{\pi} = \left(\frac{11}{2}, \frac{13}{2}\right)^{-}$. Ostali vrhovi nalaze se na energiji pobuđenja 9.15, 10.0, 10.75, 12.25 (širok), 14.9, 15.8 te 19.3 MeV. Najintenzivniji vrhovi za reakcijski kanal ^{13}C*+^{4}He nalaze se na 15.7 i 17.3 MeV a odgovaraju stanjima na 15.95 MeV $J^{\pi} = \left(\frac{9}{2}^{+}, \frac{11}{2}^{+}\right)$ i 17.06 MeV $J^{\pi} = \frac{11}{2}^{-}$. Osim tih vrhova, uočeni su i vrhovi na energijama 12.9, 14.8, 18.6 te 16.9 MeV.

Struktura jezgre ^{18}O proučavana je preko tri reakcijska kanala: ^{14}C+^{4}He+^{4}He, ^{12}C+^{6}He+^{4}He te ^{10}Be+^{8}Be$_{\mathrm{gs}}$+^{4}He, gdje jezgre ^{14}C, ^{12}C i ^{10}Be mogu biti u osnovnom ili pobuđenim stanjima. Od navedenih reakcijskih kanala rezultati s dovoljno velikim brojem detektiranih događaja su dobiveni proučavanjem ^{14}C+^{4}He, ^{14}C*+^{4}He te ^{12}C+^{6}He koincidentnih događaja. U ^{14}C+^{4}He koincidencijama uočen je niz vrhova, od kojih su najintenzivniji na $E_x(^{18}\mathrm{O}) = 11.63$, 12.51 i 13.75 MeV. Uz njih su također uočeni vrhovi na energijama pobuđenja od 10.30, 15.75, 16.9, 18.0, 18.8, 19.8 i 21.3 MeV.

Proučavanjem koincidentnih događaja ^{14}C($E_x \approx 7$ MeV)+^{4}He u spektru pobuđenja jezgre ^{18}O uočeni su jaki vrhovi na energijama od 16.1 i 20.5 MeV, dok su se ostali vrhovi nalazili na energijama pobuđenja od 19.3, 22.3, 23.5 i 26.3 MeV.

Koincidentnom detekcijom ^{12}C+^{6}He po prvi put je uočen raspad ^{18}O* emisijom jezgre ^{6}He. Vrh je uočen na energiji pobuđenja ^{18}O od 26.5 MeV, uz mogući vrh na 29.5 MeV te naznaku vrha na 23.5 MeV.

U reakcijskom kanalu ^{10}Be+^{8}Be$_{\mathrm{gs}}$+^{4}He bilo je moguće detektirati bilo koje dvije od tri čestice. Pritom su ^{10}Be+^{4}He koincidencije imale najveći broj detektiranih događaja, dok su ^{10}Be+^{8}Be$_{\mathrm{gs}}$ te ^{8}Be$_{\mathrm{gs}}$+^{4}He koincidentni događaji bili znatno rjeđi, jer je detekcija jezgre ^{8}Be$_{\mathrm{gs}}$ koincidentna detekcija dvije α-čestice. Budući da je osnovno stanje jezgre ^{8}Be rezonanca dvije

α-čestice a Q-vrijednost raspada osnovnog stanja jednaka 91.8 keV, postavljanjem uvjeta na relativnu energiju α-čestica možemo uspješno odabrati jezgre ^{8}Be u osnovnom stanju. Većina rekonstruiranih pobuđenih stanja jezgara je pripadala ^{12}C i ^{14}C. Ipak, pronađene su i neke indikacije vrhova koji bi mogli odgovarati pobuđenim stanjima ^{18}O: obradom ^{10}Be+^{8}Be$_{\mathrm{gs}}$ koincidentnih događaja uočen je mogući vrh na $\approx$24 MeV, dok je analizom koincidentnih događaja ^{8}Be$_{\mathrm{gs}}$+^{4}He uočen mogući vrh na energiji pobuđenja $\approx$25 MeV. Stoga, u reakcijskom kanalu sa svim česticama u osnovnom stanju postoji mogući vrh na energiji $E_x(^{18}\mathrm{O}) \approx 24-25$ MeV. Za reakcijski kanal kod kojeg je jezgra ^{10}Be u prvom pobuđenom stanju $E_x(^{10}\mathrm{Be}) = 3.37$ MeV, $J^\pi = 2^+$, mogući vrh je uočen na $E_x(^{18}\mathrm{O}) \approx 25$ MeV za ^{8}Be$_{\mathrm{gs}}$(T2)-^{4}He(T1) koincidentne događaje. Reakcijski kanal u kojem je $E_x(^{10}\mathrm{Be}) \approx 6.2$ MeV pokazuje mogući vrh na $E_x(^{18}\mathrm{O}) \approx$ 29 MeV.

Zaključak

U ovom su radu predstavljeni rezultati dva eksperimenta: rezonantnog elastičnog raspršenja ^{13}C+^{4}He i mjerenja reakcija ^{13}C+^{9}Be na energiji snopa $E_{^{13}\mathrm{C}} = 72$ MeV. Ova su dva eksperimenta odabrana zbog njihove selektivnosti u pobuđivanju stanja potencijalno klasterske građe u jezgrama ^{17}O i ^{18}O.

Mjerenjem rezonantnog elastičnog raspršenja ^{13}C+^{4}He područje izmjerenog elastičnog udarnog presjeka prošireno je na područje 11.1 MeV$<E_x(^{17}\mathrm{O})<$13.8 MeV. Dva najzanimljivija vrha u tom području su vrh na 13.6 MeV za kojeg je predložena struktura $^{16}\mathrm{O}(6^+, 16.29\,\mathrm{MeV}) \otimes p_{1/2}$, te intenzivan vrh na 12.0 MeV. Budući da na novoizmjerno područje nije bilo moguće primijeniti punu prilagodbu R-matricom, učinjena je pojednostavljena prilagodba (ograničena na usko područje oko vrha, samo jednu rezonancu i isključivo elastični kanal). Rezultati pojednostavljene prilagodbe pokazuju da su obije rezonance visokog spina ($\frac{11}{2}^+$ za vrh na 12.0 MeV te $\frac{11}{2}^-$ za vrh na 13.6 MeV). U pojednostavljenoj slici oba vrha imaju povećani Wignerov omjer, koji je indikacija klasterske građe. Koristeći metodu rezonantne čestične spektroskopije iz koincidentnih mjerenja reakcije ^{13}C+^{9}Be$\to$^{13}C+^{4}He+^{5}He vidljivo je da je upravo stanje na $E_x(^{17}\mathrm{O})$=13.58 MeV najjače pobuđeno. Usprkos činjenici da spin i paritet tog stanja još nisu utvrđeni, dosadašnji rezultati upućuju na visok spin stanja. Stoga je potrebno izvršiti daljnja mjerenja kako bi se utvrdila točna vrijednost spina i pariteta, te kako bi se utvrdilo je li ovo jedno stanje ili dublet stanja.

Vrh na 12.0 MeV odgovara stanju na $E_x(^{17}\mathrm{O}) = 12.005$ MeV iz kompilacije stanja, te je također uočeno među stanjima ^{17}O koja se raspadaju ^{13}C+^{4}He kanalom, ali kao dio širokog vrha na $E_x(^{17}\mathrm{O}) \approx 12.25$ MeV.

Osim dvije ranije navedene rezonance, niskoenergijski dio ekscitacijske funkcije sadrži i dvije rezonance za koje je predloženo da su članovi rotacijske vrpce u ^{17}O, građe ^{16}O(4$^+$, 10.35 MeV)$\otimes p_{1/2}$: stanja $E_x(^{17}\mathrm{O}) = 8.97$ MeV $J^\pi = \frac{7}{2}^-$ i $E_x(^{17}\mathrm{O}) = 9.15$ MeV $J^\pi = \frac{9}{2}^-$. Rezultati objavljene višekanalne prilagodbe R-matrice pokazuju da su obije rezonance α-klasterske građe ($\Gamma_\alpha >> \Gamma_n$), njihove energije i spinovi te pariteti su: 8.9672 MeV $\frac{9}{2}^-$ i 9.1737 MeV $\frac{7}{2}^-$. U kompilaciji stanja jezgre ^{17}O [50] spin oba stanja je $\frac{7}{2}^-$. Navedena stanja također su opažena u mjerenju rezonantnog elastičnog raspršenja ^{13}C+^{4}He. Sve ukazuje da imaju klastersku građu, no spin i paritet koji im se pridjeljuju različiti su, ovisno o izvoru, stoga ih tek treba točno utvrditi.

Mjerenje ^{13}C+^{9}Be reakcija posebno je pogodno za proučavanje neutronski bogatih kisikovih izotopa zbog velike vjerojatnosti prijenosa α-čestice ili ^{5}He, što je uzrokovano strukturom ^{9}Be. Navedena reakcija je ranije korištena za proučavanje strukture ^{17}O [6], no nije prikupljeno dovoljno podataka za proučavanje strukture ^{18}O. U ovom je eksperimentu korišten visokosegmentiran detektorski postav koji je pokrivao veći prostorni kut, što je omogućilo prikupljanje velike količine podataka.

Pobuđena stanja ^{17}O koja se raspadaju kanalom ^{13}C+^{4}He uočena u ovom mjerenju poklapaju se sa stanjima uočenim u mjerenju rezonantnog elastičnog raspršenja ^{13}C+^{4}He: vrhovi na 9.15 MeV i 13.57 MeV, oba sa izraženom α-klasterskom strukturom. Stanja jezgre ^{17}O koja se raspadaju u osnovno i pobuđeno stanje ^{13}C odgovaraju ranije objavljenim rezultatima, no s boljom statistikom i proširenim rasponom energija pobuđenja ^{17}O.

Da zaključimo, rezultati prikazani u ovom radu daju jake naznake da stanja ^{17}O na 8.9, 9.15 i 13.58 MeV imaju izraženu α-klastersku građu te bi mogla pripadati rotacijskoj vrpci zasnovanoj na klasterskom stanju ^{16}O(6.05 MeV, 0$^+$). Vrh na 12.0 MeV, istaknut u rezonantnom elastičnom raspršenju, nije jako izražen u mjerenju ^{13}C+^{9}Be, što je vjerojatno posljedica geometrije detektorskog postava. Opažena su dva stanja koja se raspadaju i u ^{13}C+^{4}He i u ^{13}C*+^{4}He kanal (stanja na energijama 15.1 MeV i 15.95 MeV). Pobuđena stanja na 17.06 i 18.72 MeV jako su izražena u ^{13}C*+^{4}He kanalu raspada, ali su u ^{13}C+^{4}He kanalu vrlo slaba, vidljiva tek kao široke strukture u spektru. Potrebna su daljnja istraživanja kako bi se utvrdili spinovi i pariteti spomenutih stanja.

Pobuđena stanja ^{18}O stvorena reakcijama ^{13}C+^{9}Be, proučavana su pomoću metode rezonantne čestične spektroskopije. Opažena su stanja koja se raspadaju poznatim kanalima raspada, kao što su ^{14}C+^{4}He te ^{14}C*+^{4}He. Po prvi put je opažen raspad pobuđenog stanja ^{18}O kanalom ^{12}C+^{6}He.

Stanja koja se raspadaju kanalom ^{14}C+^{4}He slažu se sa stanjima opaženim u ranijim eksperimentima. Područje energije pobuđenja ovim je radom znatno prošireno na više energije, stoga su po prvi puta opaženi ^{14}C+^{4}He raspadi stanja $E_x(^{18}\mathrm{O}) = 15.75$, 16.9, 18.0, 19.8 i 21.3 MeV.

Stanja koja se raspadaju ^{14}C*+^{4}He kanalom ne podudaraju se sa stanjima koja se raspadaju kanalom osnovnog stanja, vjerojatno zbog različite strukture ^{14}C i ^{14}C*. U ovom su kanalu opažena stanja na energijama pobuđenja 16.1, 19.3, 20.5, 22.3, 23.5 i 26.3 MeV. Od navedenih stanja najistaknutiji vrhovi su pripadali stanjima na energiji pobuđenja od 16.1 i 20.5 MeV.

Također je proučen reakcijski kanal ^{10}Be+^{8}Be$_{\mathrm{gs}}$+^{4}He. Malen broj prikupljenih događaja ne dopušta donošenje zaključaka, mada su uočeni neki mogući vrhovi. Važno je naglasiti da eventualna stanja ^{18}O koja bi se raspadala kanalom ^{10}Be+^{8}Be$_{\mathrm{gs}}$ najvjerojatnije nemaju molekulsku strukturu s neutronom koji povećava vezanje α-čestica. Vjerojatnije je da je neutron vezan u jezgri ^{10}Be.

Konačno, po prvi put je opažen raspad ^{18}O kanalom ^{12}C+^{6}He, na $E_x(^{18}\mathrm{O}) \approx 26.5$ MeV. Također su opaženi slabi mogući vrhovi na $\approx$23.5 MeV i $\approx$29.5 MeV. Ovo je indikacija moguće egzotične klasterske građe u ^{18}O. Potrebno je izvršiti dodatna mjerenja kako bi se potvrdilo ove rezultate te došlo do podataka o α-raspadu tih stanja. Takvi bi rezultati mogli dokazati postojanje molekulske ^{12}C+2n+^{4}He strukture jezgre ^{18}O.

Usprkos činjenici da reakcije prijenosa α-čestice ili α+n selektivno pobuđuju pobuđena stanja jezgara, jasno je da su spinovi i pariteti stanja, zajedno sa parcijalnim širinom za α-raspad te totalnom širinom stanja nužni za razjašnjenje prirode klasterskih struktura jezgara ^{17,18}O. Stoga su nužni daljnji eksperimenti, koji će proširiti područje energija pobuđenja. Kvaliteta i kvantiteta podataka prikupljenih u mjerenju rezonantnog elastičnog raspršenja ^{14}C+^{4}He može se drastično poboljšati potankom pripremom eksperimenta, koja se sastoji od optimizacije mjernog postava za koincidentnu detekciju i ^{14}C i ^{4}He jezgre u područjima pobuđenja koja su od posebnog interesa. Alat koji omogućuje detaljne proračune naziva se REX [19]. U tom bi eksperimentu izazov predstavljali neelastični reakcijski kanali, koje je nužno mjeriti kako bi se omogućila odgovarajuća interpretacija podataka korištenjem metode fenomenološke R-matrice. Mjerenje udarnog presjeka neelastičnih kanala predstavlja izazov kada uključuje mjerenje neutrona, jer ih je moguće mjeriti samo s nižom rezolucijom i efikasnošću od mjerenja nabijenih čestica, što otežava eksperiment. Drugi izazov predstavlja pronalaženje akceleratoskog postojenja koje je u mogućnosti osigurati snop ^{14}C (bilo iz izotopno obogaćene radioaktivne mete bilo kao radioaktivni snop). Metoda rezonantne čestične spektroskopije, korištena u mjerenju ^{13}C+^{4}He u ovom eksperimentu, također može osigurati vrijedne podatke. Da je pri mjerenju bilo manje teškoća, detektorski teleskopi na stražnjim kutevima (T5 i T6) omogućili bi prikupljanje dodatnih informacija o pobuđenim stanjima izotopa kisika putem koincidentnih događaja u kojima se na stražnjem kutu detektira odbijena α-čestica a u jednom od prednjih teleskopa teški fragment. Poboljšano mjerenje ^{13}C+^{9}Be uključivalo bi mjerni postav pažljivo podešen za međusobno preklapanje područja pobuđenja jezgara koja se mogu rekonstruirati iz različitih izlaznih kanala te stabilne eksperimentalne uvjete. Podaci visoke kvalitete prikupljeni u takvom eksperimentu mogu biti iskorišteni za dobivanje podataka o strukturi korištenjem DWBA proračuna.

Da zaključimo, u ovom je mjerenju energijski opseg postojećih podataka o strukturi ^{17}O i ^{18}O proširen na više energije. Više visokopobuđenih stanja ^{17}O koja se raspadaju ^{13}C+^{4}He ili koja su uočena u mjerenju rezonantnog elatičnog raspršenja ^{13}C+^{4}He su uspješno identificirana. Stanja ^{18}O koja se raspadaju ^{14}C+^{4}He te ^{14}C*+^{4}He kanalom proučavana su mjerenjem ^{13}C+^{9}Be, a mnoga od njih nisu ranije opažena u ovom kanalu raspada. Raspad visokopobuđenog stanja ^{18}O kanalom ^{12}C+^{6}He je opažen po prvi put.

Contents

Chapter 1

Introduction

One of the most active areas of nuclear physics today is research on the light nuclei, with up to twenty nucleons. Due to relatively small number of states at moderate excitations, nuclei in this mass region have been used as a testing sample for different structure models since the early days of nuclear physics. Nowadays the advent of *ab initio* calculations in various frameworks makes the precise experimental spectroscopic data even more important, so large efforts are being invested in obtaining the pieces of information that are still missing. In general, the data on the structure of light nuclei are an important input for the various nucleosynthesis models explaining the creation of heavier elements in various astrophysical environments.

So far, rather complete spectroscopy has experimentally been achieved for nuclei with up to nine nucleons (notable exceptions are ^{6}Be, ^{8}He and ^{9}C which are still being investigated). A few important states are still not yet clearly identified (e.g. the first $\frac{1}{2}^{+}$ state in the ^{9}B), but the essential part of the experimental work is mostly done.

For slightly higher mass region ($A = 10$ to 20), there are three important frontiers of research at the moment: isotopes with $A = 10$ and 11 with different cluster and molecular configurations found but not yet fully systematized, the ^{12}C nucleus and states within the rotational band of the Hoyle state and finally neutron rich oxygen isotopes, starting already with astrophysically important ^{17}O. This thesis is based on the last of these topics.

The ^{16}O nucleus is special in many respects. Its ground state has an almost perfect spherical shape due to the fact that ^{16}O is a doubly magic nucleus in a shell-model context. For the same reason, the first excited state in ^{16}O has a very high excitation energy, $E_x = 6.05$ MeV (only ^{14}C has higher first excited state among the isotopes with A>4). On the other hand it is a classic example of clustering, with underlying ^{12}C+^{4}He configuration in low-lying excited states [1].

The first excited state is a band-head of rotational band (with 2^+ at $E_x = 6.92$ MeV, 4^+ at $E_x = 10.36$ MeV and 6^+ at $E_x = 16.28$ MeV) - the negative parity rotational band based on the same intrinsic structure is also known for a long time (1^- state at $E_x = 9.59$ MeV, 3^- state at $E_x = 11.60$ MeV, 5^- state at $E_x = 14.66$ MeV and 7^- at $E_x = 20.86$ MeV), and it is again a classic example of another important phenomenon related to (asymmetric) cluster structures: parity splitting [20]. The coexistence of shell-model and cluster-model states in ^{16}O is today rather well understood from the theoretical perspective and provides basis for studies of heavier oxygen isotopes.

The essential question in the studies of neutron rich oxygen isotopes is the following: does the well developed cluster structure in ^{16}O persist with addition of neutrons and how it changes with addition of neutrons?

To get a systematic answer one should first study the ^{17}O nucleus, identify the cluster states and try to get a quantitative description of degree of clustering (through e.g. reduced partial widths) for each of them. Early qualitative studies in that direction were done some thirty years ago ([2], [3], [4], [5]), with a recent one [6] confirming some of the results and systematizing previous results. Some of the ^{17}O states (between $E_x = 5.9$ and 7.3 MeV) are also very important from the astrophysical aspect, due to the fact that the ^{13}C(^{4}He,n)^{16}O reaction is at the moment the best candidate for the source of neutrons for s-process nucleosynthesis in thermally pulsing, low-mass, asymptotic giant branch stars ([7], [8]). A very precise data on the resonances in this reaction is needed to obtain the cross-sections and reaction rates. The problem is also studied through indirect techniques, like e.g. the Trojan Horse Method [9].

Adding a subsequent neutron gives ^{18}O, nucleus with a total number of states similar to ^{17}O (around one hundred up to the 20 MeV of excitation energy). Clustering in ^{18}O is also a subject studied for decades (see e.g. [10], [11]), and the recent experimental results ([12], [13] and [14]) make it attractive again. There is still a number of open questions ([13],[15], [16]), so new experimental data are essential to establish a clear picture of configurations of excited states in both ^{17}O and ^{18}O.

The main goal of the this studies is a better understanding of structure of states in ^{17}O and ^{18}O. The focus is on the states of cluster and molecular character, but insight on shell models states is also essential for full understanding of both nuclei. The main hypotheses of this studies is the idea that the well-established cluster states in ^{16}O have their partners in ^{17}O and ^{18}O, which can be related by a weak-coupling model [17] and provide the basis for later studies of heavier oxygen isotopes, up to the neutron drip-line (the last bound isotope is the ^{24}O).

Chapter 2

Structure of light nuclei

In this chapter general remarks on the cluster and molecular states will be presented, followed by a description of theoretical models commonly used to describe them. Next, a brief summary of the ^{16,17,18}O states most important for this work is given. This chapter will end with a section on the phenomenological R-matrix theory.

2.1 Cluster and molecular states in light nuclei

The ^{4}He nucleus (the α-particle) has one of the highest binding energies per nucleon among light nuclei. Its first excited state lies close to 20 MeV in excitation. Therefore the α-particle can survive inside the nucleus for a significant time [21]. Furthermore, the interaction between two α-particles is weak and attractive at distances of several femtometers, but has a strongly repulsive core at very small distances due to the Pauli principle. Therefore, its shape has been compared to the shape of the van der Waals potential (see Fig. 2.1). These characteristics make

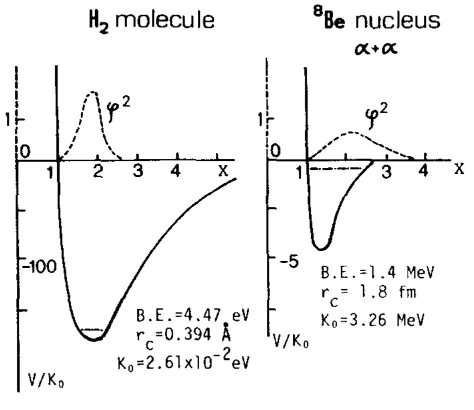

Figure 2.1: The comparison of the potential for the H_2 molecule from the atomic physics and the α-α potential from the nuclear physics. Adopted from [22].

it an ideal cluster candidate. Apart from the α-particle, the other closed-shell nuclei, such as ^{16}O, or closed sub-shell nuclei, like ^{12}C and ^{14}C, may appear as clusters.

In the spectra of the nuclei the α-cluster states usually do not appear in the ground state, except for very light systems. As Ikeda stated in Ref. [23], the clustering occurs in the vicinity of the respective decay threshold. The Ikeda diagram illustrates the process of gradually moving from configuration with one α-particle to pure α-cluster states with increasing excitation energy.

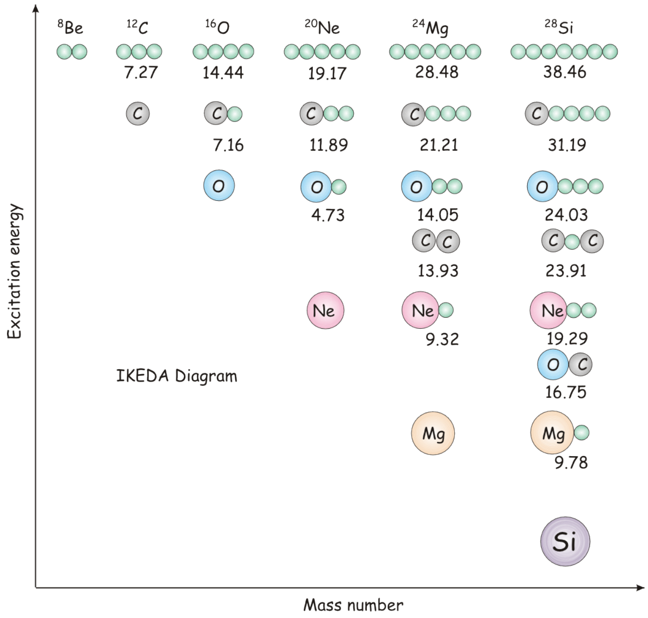

Figure 2.2: The Ikeda diagram [23], depicting the approximate energies at which the α-cluster states are expected. Adopted from [24].

One of the clear signatures of the cluster-structure are the rotational bands, formed of the rotational excitations of a particular cluster state. For symmetric cluster structures like α+α or ^{12}C+^{12}C from symmetry considerations follows that only allowed rotational excitations are 2^+, 4^+, 6^+, 8^+, etc. For asymmetric cluster structures, such as ^{12}C+^{4}He cluster structure of ^{16}O or ^{16}O+^{4}He of ^{20}Ne, the splitting of the rotational band in two is observed (see Fig. 2.3). The $K^\pi = 0^+$ rotational band for the ^{16}O has a 6.05 MeV 0^+ state as its band-head, followed by the 2^+ state at $E_x = 6.92$ MeV, 4^+ state at $E_x = 10.36$ MeV and the 6^+ state at $E_x = 16.28$ MeV. The band-head of the $K^\pi = 0^-$ rotational band is the 1^- state at $E_x = 9.59$ MeV, followed by the 3^- state at $E_x = 11.60$ MeV, the 5^- state at $E_x = 14.66$ MeV and the 7^- state at $E_x = 20.86$ MeV.

The splitting of rotational bands for the ^{16}O and the ^{20}Ne nuclei has been explained by Horiuchi and Ikeda (see Ref. [20]). Evoking the similarity with the rotational bands of the diatomic molecules in molecular physics, the authors explained the emergence of the rotational

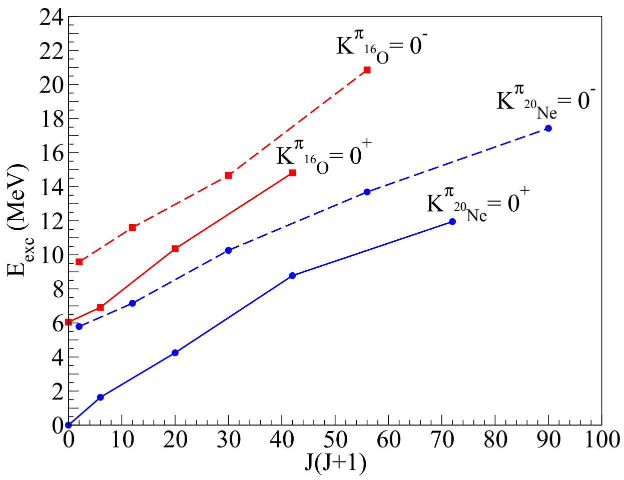

Figure 2.3: The inversion-doublet of quasi-molecular rotational bands for the ^{16}O and the ^{20}Ne nuclei (adopted from [14]).

bands in term of the two eigenstates of parity. One starts with the two possible configurations of the α-cluster and the residual nucleus, displayed in the Fig. 2.4. These two configurations are

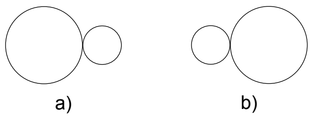

Figure 2.4: Two possible configurations of the α-cluster (small circle) and the residual nucleus (large circle). Adopted from [20].

not eigenstates of parity, but their linear combinations, displayed in the Fig. 2.5, are. The two rotational bands of positive and negative parity would be degenerate if the tunnelling probability between the configurations a) and b) in the Fig. 2.4 was equal to zero. The finite potential barrier between the two configurations gives rise to the energy splitting between the two eigenstates of parity.

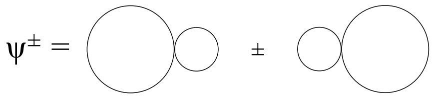

Figure 2.5: The eigenstates of parity for the asymmetric cluster strucutre. Adopted from [20].

The α-clustering of the $N = Z$ nuclei has been investigated thoroughly both in theory and experiment ([21], [24]). From experimental point of view, several indications point to possible cluster structure of a particular state:

- the state is strongly populated in the α-transfer reactions
- the excitation energy, spin and parity of the state allow for its placement in a rotational band

- the state has large Γ_α width, close to single-particle limit
- the γ-transitions between the members of rotational band are enhanced

Consequently, to establish the cluster nature for a particular state evidence from multiple experiments are needed.

The clustering of other, non-α-conjugate nuclei proved to be more challenging. The addition of neutrons to the cluster structure may give rise to more exotic configurations. The weakly bound neutrons can provide the additional binding to the deformed cluster structure, similar to the one provided by valence electrons in the atomic molecules. Because of that analogy, such states are called nuclear molecules. The extended Ikeda diagram by von Oertzen schematically shows multiple nuclear molecule configurations. Among nuclei depicted on the Fig. 2.6, clear evidence for molecular states have been found for the excited states of the ^{9}Be and ^{10}Be nuclei only ([21], [24]). One of the fronts of the research is to clearly identify molecular states in the three-centre systems (carbon isotopes) and four-centre systems (oxygen isotopes).

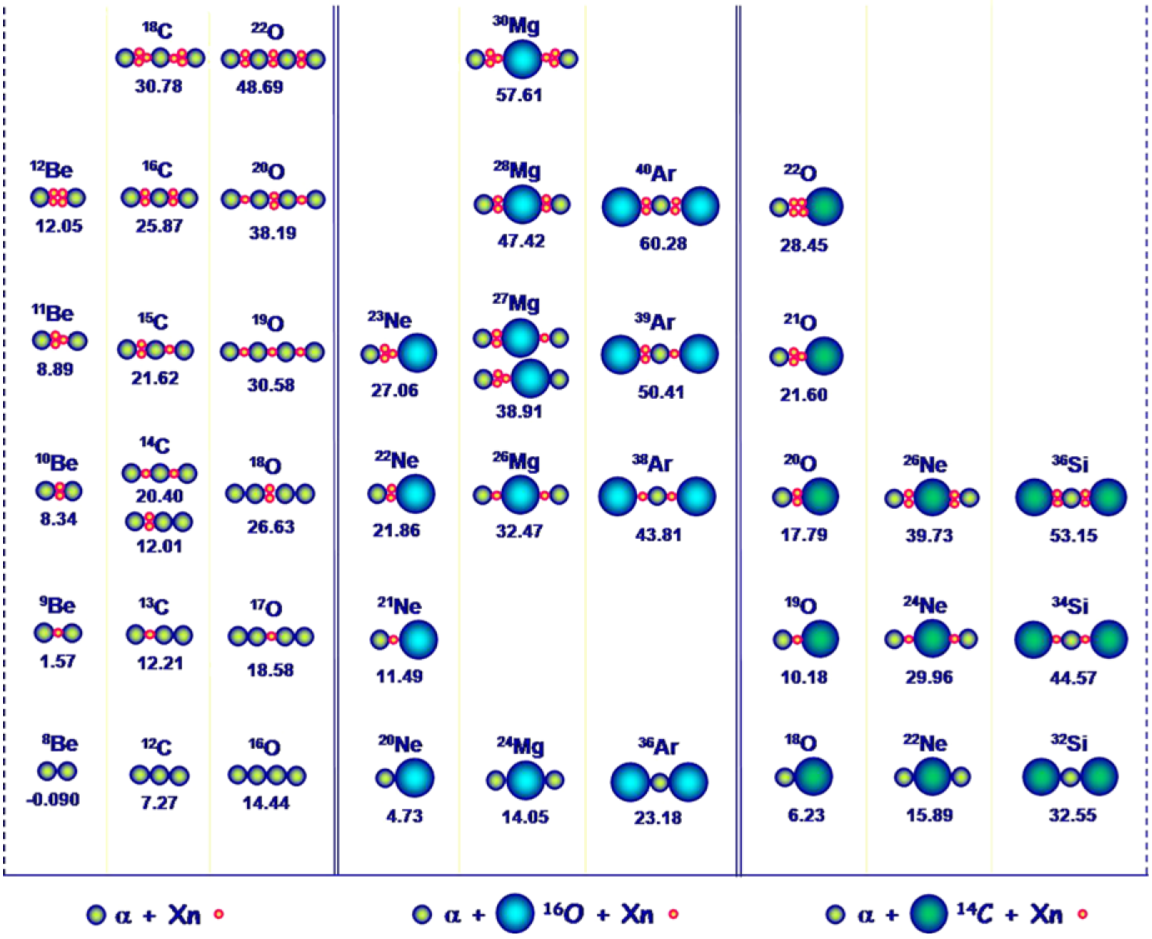

Figure 2.6: The extended Ikeda diagram, including the molecular states. Adopted from [24].

2.2 Theoretical models

Historically, the first microscopic cluster models were based on the resonating group method (RGM) [25], followed by the generator coordinate method (GCM) [26] and the orthogonality condition method (OCM) [27], which is a semi-microscopic cluster model.

Apart from cluster models, the deformed mean-field models may reproduce cluster structure as well. The deformed shell model gives rise to the Nilsson level scheme, where shell closures appear at different magic numbers due to changes in energies of orbitals with deformation. The Nilsson-Strutinsky model is a combination of a microscopic contribution (variation of shell structure due to deformation) and a macroscopic liquid-drop energy [21].

Recently an energy-density functional model had been used to reproduce clustering in the ground state of ^{20}Ne [28]. The energy density functionals (EDFs) are a fully microscopic model that can consistently describe the ground-state properties of a wide range of nuclei, spanning entire chart of nuclei. In the article a remarkable difference in the ground state nucleon density has been observed, depending on the choice of the energy-density functional. The non-relativistic Skyrme SLy4 and the relativistic DD-ME2 energy-density functional gave different results: the relativistic one predicts a clusterized ground state of the ^{20}Ne, while the non-relativistic one predicts just a prolate ground state. The difference between the two functionals lies in the depth of the potential: the relativistic potentials are deeper due to the consistent treatment of both the self-consistent single-nucleon mean-field and the effective spin-orbit potential. The authors concluded that the cluster structures in the light nuclei represent a mid-point of the phase transition from the quantum crystal structure to the quantum liquid structure, the phase being determined by the $\alpha = b/r_0$, where b is the dispersion of the nucleon wave function and $r_0 = 1.2$ fm the typical inter-nucleon distance.

Various *ab initio* models are using the two-body and three-body interactions between nucleons to reproduce the structure of light nuclei. Particularly successful in the description of states of light nuclei, both cluster-like or shell-model like, was the antisymmetrized molecular dynamics model [29].

2.2.1 Generator-coordinate method

The generator-coordinate method (GCM) [26] is a method used to describe the collective motion in nuclei. The fundamental idea of the model is to construct a trial wave function of the form

$$\Psi(\mathbf{x}_1,\ldots,\mathbf{x}_2)=\int\varphi\left(\mathbf{x}_1,\ldots,\mathbf{x}_2;\alpha\right)f(\alpha)\mathrm{d}\alpha), \tag{2.1}$$

where φ is the preliminary wave function which solves the problem in the construction potential and depends on the generator coordinate α (in case of the deformed nuclei α can be a deformation). The coordinate α bears the name generator coordinate because it does not appear in the final wave function but nevertheless generates it. The energy of the system is minimized with respect to the choice of $f(\alpha)$. The variational calculation yields the integral equation for $f(\alpha)$, called the generator wave equation.

For description of cluster states, the GCM model uses a linear combination of Bloch-Brink wave functions and the position of cluster centres as the generator coordinates. The form of Bloch-Brink wave function for the system composed of n clusters is

$$\Psi(\mathbf{S_1},\ldots,\mathbf{S_n})=n_0\mathscr{A}\left\{\psi(C_1,\mathbf{S_1}),\ldots,\psi(C_n,\mathbf{S_n}\right\}, \tag{2.2}$$

where $\psi(C_i,\mathbf{S_i})$ are the wave-functions for the i-th cluster located at the position $\mathbf{S_i}$ and $\mathscr{A}$ is the antisymmetrizaton operator. When number of clusters is increased, usually the model space has to be truncated. This model has been particularly successful in the study of cluster and molecular structure of beryllium isotopes [30].

2.2.2 Molecular orbital model

To describe the structure of molecule-like systems in nuclear physics, theoretical model used in atomic physics has been adapted for the nuclear case. The model for the description of the atomic molecules in terms of cores and valence electrons is called the linear combination of atomic orbitals (LCAO), while its nuclear counterpart bears the name of linear combination of nuclear orbitals (LCNO). The basic idea of the theory is to construct the molecular orbits from the linear combination of single-particle wave functions. The model was successfully used to calculate the orbits of valence neutron surrounding the α-clusters for the ^{9}Be and ^{13}C nuclei [31]. The ^{9}Be nucleus is an example of an improved binding provided by the addition of the weakly to the ^{8}Be nucleus that is unbound. Due to the pronounced cluster structure of the ^{8}Be, the ^{9}Be nucleus can be treated in this model as α+α+n structure. In that case the single-particle $p_{3/2}$ orbitals combine to form the π or σ molecular orbitals. The π molecular orbitals have the neutron localized above and bellow the α-particle axis, while the σ molecular orbital localizes the neutron between the two α-clusters. Itagaki *et al.* [32] extended the model space and expressed the orbits as linear combination of local Gaussians. Additionally, the improved model allows to take into account the spin-orbit interaction, its strength being determined from the α+n scattering. The improved model allowed to reproduce many details of the ^{10}Be structure [32].

2.2.3 Antisymmetrized molecular dynamics

The antisymmetrized molecular dynamics (AMD) ([29] and references therein) is a model that can simultaneously reproduce both cluster and molecular structure of nuclei, as well as their shell-model like states. This model treats each nucleon as a Gaussian wave packet, without any assumptions on cluster structure. The AMD wave function for a given nucleus is a Slater determinant of wave functions for individual nucleons:

$$\Phi_{\mathrm{AMD}} = \frac{1}{\sqrt{A!}} \mathscr{A} \left\{ \phi_1, \phi_2, \ldots, \phi_A \right\}. \tag{2.3}$$

Wave functions of the individual particles are given by:

$$\begin{aligned}
\phi_i &= \phi_{\mathbf{X}_i} \chi_i \tau_i && (2.4) \\
\phi_{\mathbf{X}_i}(\mathbf{r_j}) &\propto \exp\left\{ -\nu \left(\mathbf{r}_j - \frac{\mathbf{X}_i}{\sqrt{\nu}} \right)^2 \right\}, && (2.5) \\
\chi_i &= \left(\frac{1}{2} - \xi \right) \chi_\uparrow + \left(\frac{1}{2} - \xi_i \right) \chi_\downarrow, && (2.6)
\end{aligned}$$

where the χ_i is the intrinsic spin function parametrised by ξ_i. The τ_i is the isospin function with the value “up” for protons or “down” for neutrons. The coordinates $\mathbf{X}_i$ are complex and denote the centre of each of the nucleons. The set of complex coordinates $Z \equiv \{\mathbf{X}_{ni}, \xi_i\}$, where $i = 1, 2, 3$ (three axis in coordinate space) and $n = 1, \ldots, A$ are considered as a set of independent parameters and are subject to the minimization procedure called the “frictional cooling method” [29]. The “frictional cooling method” is a variational procedure in which the energy of the system $\mathscr{E} \equiv \langle \Phi | H | \Phi \rangle \, / \, \langle \Phi | \Phi \rangle$ is minimized. The parity projected eigenstates are superpositions with both signs

$$\Phi(\mathbf{Z}) = (1 \pm P)\Phi_{\mathrm{AMD}}(\mathbf{Z}), \tag{2.7}$$

where P is the parity projection operator. The spin-parity projection is performed by superposing rotated states:

$$\Phi(\mathbf{Z}) = P^{J}_{MK'}\Phi_{\mathrm{AMD}}(\mathbf{Z}) = \int \mathrm{d}\Omega D^{*J}_{MK'}(\Omega)R(\Omega)\Phi_{\mathrm{AMD}}(\mathbf{Z}), \tag{2.8}$$

where Ω represents the Euler angles. The total wave function can be a superposition of spin parity projected AMD wave functions:

$$\Phi(\mathbf{Z},\mathbf{Z}') = cP^{J\pm}_{MK'}\phi_{\mathrm{AMD}}(\mathbf{Z}) + c'P^{J\pm}_{MK'}\phi_{\mathrm{AMD}}(\mathbf{Z}') + \ldots. \tag{2.9}$$

The more advanced version applies the frictional cooling method to the spin-parity projected state, using the wave function $\Phi = P^{J\pm}_{MK'}\Phi_{\mathrm{AMD}}(\mathbf{Z})$. This method, called the variation after projection (VAP), is essential for successful study of the excited states of nuclei. However, variation after the parity projection but before the total spin projection can be used to describe the low-lying states [29]. While with the VAP method one can calculate the wave function for the lowest $J^{\pm}_{1}$ state, to get the higher excited states $J^{\pm}_{n}$ an additional requirement has to be fulfilled: the wave functions have to be orthogonal to the lower-energy states. The following expression is used to obtain the parameters $Z^{J\pm}_{n}$ for the n-th $J^{\pm}$ state:

$$\Phi(\mathbf{Z}) = P^{J\pm}_{MK'}\phi_{\mathrm{AMD}}(\mathbf{Z}) - \sum_{k=1}^{n-1} \frac{\langle P^{J\pm}_{MK'}\phi_{\mathrm{AMD}}(\mathbf{Z}^{J\pm}_{k})|P^{J\pm}_{MK'}\phi_{\mathrm{AMD}}(\mathbf{Z})\rangle}{\langle P^{J\pm}_{MK'}\phi_{\mathrm{AMD}}(\mathbf{Z}^{J\pm}_{k})|P^{J\pm}_{MK'}\phi_{\mathrm{AMD}}(\mathbf{Z}^{J\pm}_{k})\rangle} P^{J\pm}_{MK'}\Phi_{\mathrm{AMD}}(\mathbf{Z}^{J\pm}_{k}), \tag{2.10}$$

where the parameter $\mathbf{Z}$ is varied and the variation of this expression represents the variation of the component orthogonal to lower states. The improved wave functions for the $J^{\pm}_{n}$ states is obtained by simultaneously diagonalizing the Hamiltonian and the norm matrix. This wave function is used for the comparison with the experimental data. Apart from the level energy, the AMD model enables the calculation of radii, magnetic dipole and electric quadrupole moments, as well as transition strengths of electromagnetic and weak processes.

The single particle wave functions can be extracted from the AMD wave function $\Phi_{\mathrm{AMD}}(\mathbf{Z})$. This enables the calculation of the neutron, proton and total density, useful for the study of molecular structures containing weakly bound neutrons (see results for ^{9,10}Be in Ref. [24]). The strength of this approach is the lack of any assumption on pre-formation of clusters, they emerge in a model independent way.

2.3 The cluster structure of the ^{16}O nucleus

The ^{16}O nucleus has been studied since the beginnings of nuclear physics. Very early models by Hafstad and Teller [33] described its ground state as a tetrahedral structure of α-particles. In the Ikeda picture (see Ikeda diagram on Fig. 2.2), the ground state is compact and the cluster structure emerges in the vicinity of respective thresholds. The threshold for the emission of the α-particles is at $E_x = 7.16$ MeV, while the decay to four α-particles needs at least $E_x = 14.44$ MeV. The results on the structure of ^{16}O provided by many experiments have been classified in several rotational bands in Ref. [34]. Apart from the well established $K = 0$ parity-inversion doublet of quasi-molecular bands, the authors proposed a $K^{\pi} = 2^{-}$ band from the 12.53 MeV 2^{-} band-head state . While this proposed band has not been confirmed, the $K^{\pi} = 2^{+}$ is: the band-head is the 2^{+} state at $E_x = 9.845$ MeV and the second member of the band the 3^{+} state at $E_x = 11.080$ MeV. The theoretical description of the first excited state of

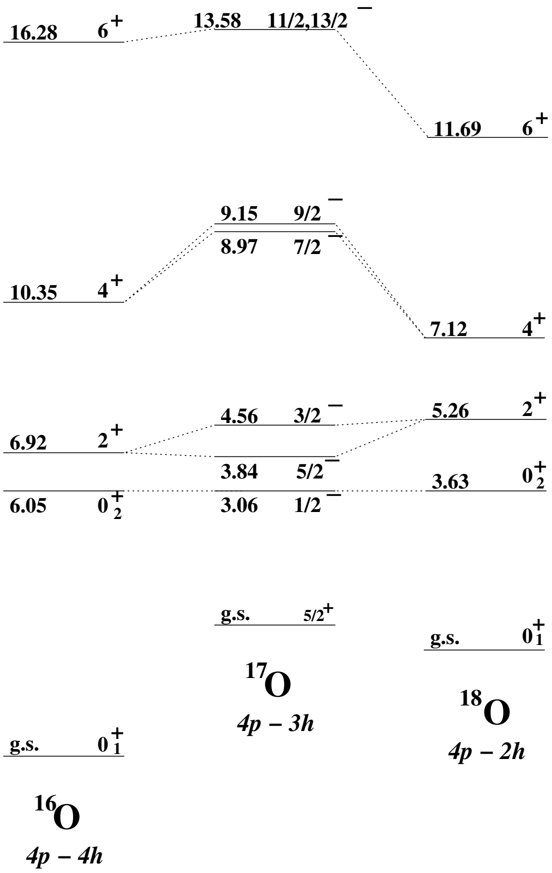

Figure 2.7: Plot of the 4p-nh states for the $^{16-18}$O, adopted from [6].

^{16}O at $E_x = 6.05$ MeV with $J^\pi = 0^+$ was provided by multiple models. In Nilsson-Skrutinsy and Hartree-Fock models this state is represented as a four-particle–four-hole (4p-4h) excitation. The physical meaning of such an excitation is the excitation of the α-particle outside the $1p_{\frac{3}{2}}$ orbitals. Other models predict similar structure: in Hartree-Fock calculation oscillator quanta lie on two axis. The Nilsson-Skrutinsky model can explain this structure with a shell-gap for oblate deformation. The gamma-width for the transition from the $E_x = 6.92$ MeV $J^\pi = 2^+$ to the band-head state is in accordance with the majority of theoretical predictions. The structure of this state, independently of model used, is the ^{12}C+α [35]. The search for a possible chain state and its rotational band has been performed in several experiments, however the most recent one found no evidence for rigid chain-like structure [36].

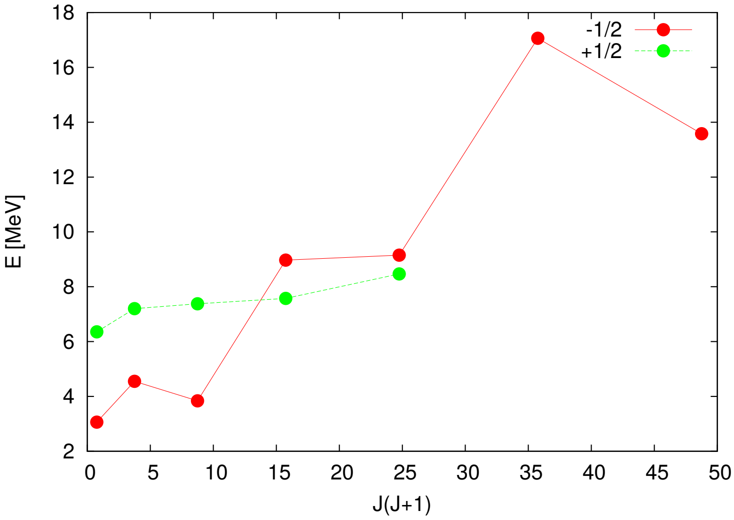

Figure 2.8: Plot of ^{17}O rotational bands proposed in Refs. [6] and [37].

2.4 The cluster structure of the ^{17}O nucleus

Adding one neutron to the doubly magic ^{16}O nucleus gives the ^{17}O. Although one would expect it to be an ideal example of single-particle shell-model structure, the excitation of the ^{16}O core has to be taken into account to explain even the low-lying excited states [38]. In the work of Furutani *et. al.* [39] the importance of configuration mixing between the 2p-1h shell model states and the 4p-3h cluster states to explain the negative-parity states has been emphasized. Nevertheless, some of the excited states of the ^{17}O may be described in terms of the weak coupling model [17], which was successfully applied on the ^{18}O [40]. That states would be related to known cluster states in the ^{16}O spectrum. Candidate states have been identified from the published results in Ref. [6], based on improvement of rotational bands proposed from Refs. [41] and [42]. The candidate states are displayed in Fig. 2.7. Apart from the $K^\pi = \frac{1}{2}^-$ rotational band proposed in [6], the $K^\pi = \frac{1}{2}^+$ rotational band has been proposed in Ref. [37]. The proposed $K^\pi = \frac{1}{2}^+$ relies on the assumption that the $E_x = 8.466$ MeV state has the $J^\pi = \frac{9}{2}^+$, however the comprehensive R-matrix fit from Heil *et al.* determined it to be $J^\pi = \frac{7}{2}^+$. Both rotational bands are displayed in the Fig. 2.8, where characteristic staggering of the $K^\pi = \frac{1}{2}^-$ rotational band due to Coriollis decoupling is pronounced.

2.5 The cluster structure of the ^{18}O nucleus

The Fig. 2.9 shows three different configurations of the ^{18}O in both shell model and cluster model. The ^{14}C+^{4}He cluster state is represented in the shell model as a four-particle two-hole excitation, lifting the two protons from the $p_{\frac{1}{2}}$ shell to the *sd* shell to form an α-particle. If additional two neutrons are lifted from the $p_{\frac{1}{2}}$ to the *sd* shell, in the cluster model picture one gets an exotic ^{12}C+2n+^{4}He configuration.

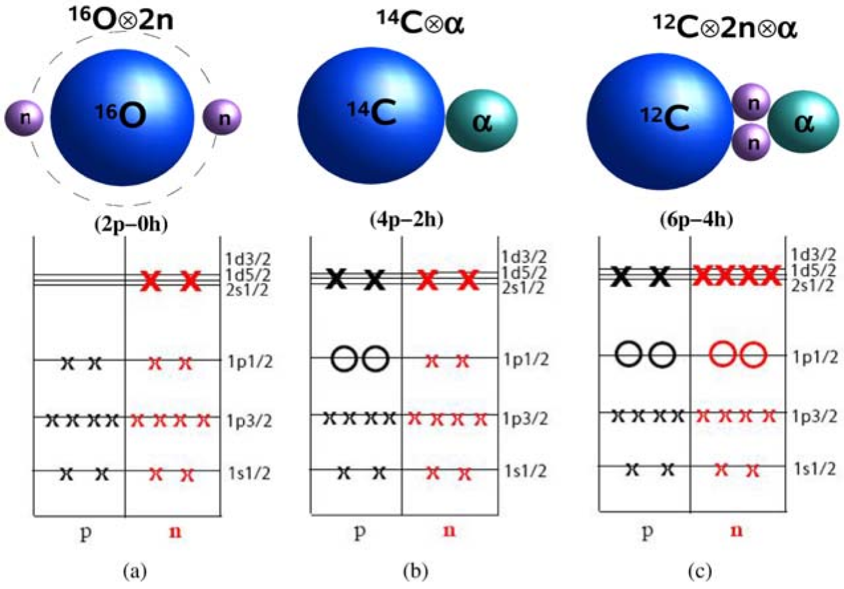

Figure 2.9: The relation between the ^{18}O excited states of different structures in the cluster and shell model picture, adopted from [13].

In the detailed study of the ^{18}O states populated in the ^{12}C(^{7}Li,p) reaction at $E_{\text{lab}} = 44$ MeV spectroscopic data on ^{18}O was improved and systematised [13]. Although the direct measurement of spins and parities was not possible, the measured cross-ssections and excitation energy systematics were used to assign tentative spins, therefore allowing classification of the excited states in tentative rotational bands, displayed in Fig. 2.10. The $K^\pi = 0^+_1$ ground-state band has the $^{16}\mathrm{O} \otimes 2\mathrm{n}$ structure and ends with expected maximum spin op $J^{\pi} = 4^{+}$. On the other hand, the $K^{\pi} = 0^{-}_{1}$ band has been proposed to be a proton excitation band with band-head $E_x = 4.457$ MeV $J^{\pi} = 1^{-}_{1}$ state. The $K^{\pi} = 0^{+}_{2}$ and $K^{\pi} = 0^{-}_{2}$ bands are proposed to have the $^{14}\mathrm{C} \otimes ^{4}\mathrm{He}$ cluster structure. The first four members of the $K^{\pi} = 0^{+}_{2}$ are well established, while the $K^{\pi} = 0^{-}_{2}$ hasn't been identified before. The $K^{\pi} = 0^{+}_{4}$ and $K^{\pi} = 0^{-}_{4}$ rotational bands in Fig. 2.10 are proposed to have the $^{12}\mathrm{C} \otimes 2\mathrm{n} \otimes \alpha$ molecular structure. The authors also suggested that the ^{14}C nucleus has the same potential to form the cluster structures as the ^{16}O nucleus.

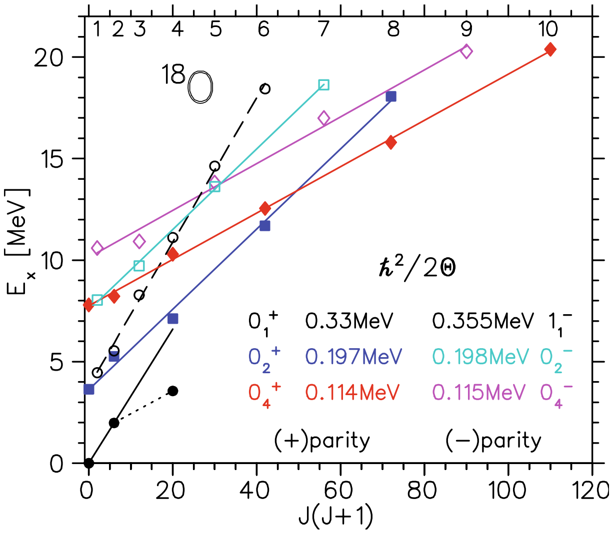

Figure 2.10: The ^{18}O rotational bands suggested in Ref. [13], adopted from [13].

The recent comprehensive multichannel R-matrix fit published in Ref. [14] determined the excitation energies, spins, parties and partial widths of many ^{18}O states in the excitation energy range from the threshold to the $E_x = 14.9$ MeV. The experimental results showed that the α-strength is typically not concentrated in one state, but spread among multiple states, making the rotational bands proposed in Ref. [13] unlikely. The results from [14] have been treated using the cluster-nucleon configuration interaction model (CNCIM) [43]. The results for the negative-parity states suffer from noticeable discrepancies, probably due to the truncation of the configuration space. The results of the theoretical calculation point to significant configuration mixing, and are in contrast with previous results obtained using the generator-coordinate method (GCM) [30] and AMD-RGM method [44]. Therefore, the nature of the ^{18}O cluster structure remains controversial.

2.6 The R-matrix theory

The R-matrix theory was initially developed for describing resonances in nuclear reactions. Nowadays it is a powerful tool of quantum mechanics that can be used either for solving the Schrödinger equation for a large variety of problems or for accurately parametrizing both resonant and non-resonant parts of the measured cross sections. The former is called the calculable R-matrix method and the latter the phenomenological R-matrix method. Both R-matrix methods share the common theoretical apparatus and differ in the way a potential is obtained. The theory was presented in a comprehensive review by Lane and Thomas [45] and more recently in a review by Descouvemont and Baye [46]. While the full derivation of the R-matrix theory is beyond the scope of this work, some important results will be presented in this section. This section will follow the main steps of the derivation of the R-matrix theory presented in the book by Thompson and Nunes [47]. Therefore, the notation is adopted from the [47] as well.

The fundamental idea of the R-matrix method is the division of space in two regions: the internal and the external, bordering at a certain radius $R = a$ called the channel radius. The value of the channel radius has to be large enough that the particles interact only via the Coulomb force (if particles are charged). While in the external region the wave function is expressed as a combination of Coulomb Hankel functions, the internal region is a confined system with a basis of discrete eigenstates.

Several important results for the single-channel single-resonance case from the [47] are discussed in the rest of this section. One can start from the internal region, $R < a$. The eigenfunctions in the internal region are solutions of the radial part of the Schrödinger equation:

$$\left(-\frac{\hbar^2}{2\mu}\left(\frac{\mathrm{d}^2}{\mathrm{d}R^2}-\frac{L(L+1)}{R^2}\right)+V(R)-\varepsilon_n\right)w_n(R)=0, \tag{2.11}$$

where $n = 1, 2, \ldots$ denotes the number of nodes of the spatial part of the wave function w_n and μ is the reduced mass.

The basis of internal eigenstates is orthogonal over a finite interval if all of them satisfy the following condition:

$$\beta = \frac{\mathrm{d}}{\mathrm{d}R}\ln w(R) \equiv \frac{w'(R)}{w(R)}, \quad R = a \tag{2.12}$$

fixing their logarithmic derivative at the channel radius R to a numeric constant β. The internal eigenfunctions satisfy $w(0) = 0$, too. At this point the channel radius a and β, the value of the logarithmic derivative at $R = a$, are free parameters and the physical results obtained should not depend on their values.

Now one can express the scattering solution $\chi(R)$ as a superposition of the wave functions w_n:

$$\chi(R) = \sum_{n=1}^{N} A_n w_n(R). \tag{2.13}$$

The value of the expansion constants A_n is

$$A_n = \frac{\hbar^2}{2\mu} \frac{w_n(a)}{\varepsilon_n - E} \left(\chi'(a) - \beta\chi(s) \right). \tag{2.14}$$

Using Eq. (2.13) and (2.14) one gets

$$\frac{\chi(a)}{\chi'(a) - \beta\chi(a)} = \sum_{n=1}^{N} \frac{\hbar^2}{2\mu} \frac{w_n(a)^2}{\varepsilon_n - E}. \tag{2.15}$$

The left side is one of the definitions of the R matrix (see Box 6.1 of [47]):

$$\mathbf{R} = \frac{1}{a} \frac{\chi(R)}{\chi'(R) - \beta\chi(R)}. \tag{2.16}$$

When the Eq. (2.16) substitutes the left-hand side of the Eq. (2.15), one gets:

$$\mathbf{R} = \sum_{n=1}^{N} \frac{\hbar^2}{2\mu a} \frac{w_n(a)^2}{\varepsilon_n - E}. \tag{2.17}$$

With the definition of the reduced width amplitude

$$\gamma_n = \sqrt{\frac{\hbar^2}{2\mu a}} w_n(a) \tag{2.18}$$

the R matrix assumes the usual form:

$$\mathbf{R} = \sum_{n=1}^{N} \frac{\gamma_n^2}{\varepsilon_n - E}. \tag{2.19}$$

If the sum is carried out for all the values of n the result should not depend on a or β. The γ^2 is called the reduced width and can have both positive and negative values, the sign reflecting the interference between levels. The width of the resonance is given by

$$\Gamma = 2\gamma^2 P_l, \tag{2.20}$$

where P_l denotes the Coulomb penetrability, which depends on the channel radius a. Now the **S** matrix can be written as:

$$\mathbf{S} = \frac{H^- - a\mathbf{R}\left(H^{-\prime} - \beta H^-\right)}{H^+ - a\mathbf{R}\left(H^{+\prime} - \beta H^+\right)}, \tag{2.21}$$

where $H^\pm$ are Coulomb Hankel functions. From now on a single-channel single-pole case will be described. The energy of the pole is ε_p. Using the properties of the Coulomb functions, it can be rewritten in the form:

$$\mathbf{S} = \frac{E - \left(\varepsilon_p - \gamma^2 S^0 + \mathrm{i}\gamma^2 P\right)}{E - \left(\varepsilon_p - \gamma^2 S^0 - \mathrm{i}\gamma^2 P\right)} \cdot e^{2\mathrm{i}\varphi}. \tag{2.22}$$

If one defines

$$\begin{aligned} E_r^f &= \varepsilon_p - \gamma^2 S^0 = \varepsilon_p - \gamma^2 \left(S - a\beta\right) && (2.23) \\ \Gamma^f &= 2\gamma^2 P, && (2.24) \end{aligned}$$

where $S(E)$ is a shift function, defined as:

$$S(E) = ka\frac{\dot{F}F + \dot{G}G}{F^2 + G^2} \tag{2.25}$$

and $P(E)$ penetrability

$$P(E) = \frac{ka}{F^2 + G^2}. \tag{2.26}$$

In the previous equations F and G are the Coulomb functions. The formal resonance energy and width E_r^f and Γ^f generally differ from the observed ones, although there exists a choice of the boundary conditions that removes the shift for particular energy. The difference between the observed parameters and the R-matrix parameters can be taken into account by using the Brune transformation [48]. That approach was adopted in the AZURE2 code [49], enabling the user to input the observed data from which the R-matrix parameters are deduced.

The physical meaning of the reduced width amplitude γ is the magnitude of an interior eigenfunction $w(R)$ at the surface $R = a$. Well localized eigenfunctions of narrow physical resonances have small values of γ because the wave function is small outside the channel radius. Therefore, narrow physical resonances will have small widths Γ. If one considers a weak potential in the inside region, the corresponding eigenstate might be estimated as a state of uniform probability density in the volume of interior. In that case a Wigner limit γ_W^2 can be derived for reduced widths:

$$\gamma_W^2 = \frac{\hbar^2}{2\mu a} |w(a)|^2 = \frac{3\hbar^2}{2\mu a^2}, \tag{2.27}$$

where $w(R) = \sqrt{\frac{3}{a^3}} R$ was used. Although the Wigner limit depends strongly on the value of the channel radius a, it is useful if no structural information is available. The dimensionless ratio between some observed reduced width γ^2 and the calculated reduced width at Wigner limit γ_W

$$\theta_W^2 = \frac{\gamma^2}{\gamma_W^2} \tag{2.28}$$

is called the Wigner or single particle ratio. While it isn't a spectroscopic factor, sometimes it can be used like one in a simple limit. However, one has to bear in mind that they depend exclusively on the properties of the surface of channel radius and not on the volume integral, which is the case for the spectroscopic factor.

Chapter 3

Resonant elastic scattering of ^{13}C on thick ^{4}He gas target

The spectroscopy of the oxygen isotopes is a challenging field of study when it comes to ^{17}O. A large level-density of approximately 90 known states in the first 15 MeV of excitation [50] makes ^{17}O rather exceptional among the light nuclei. Previous measurements of the ^{13}C+^{4}He excitation function provide insight in the structure of the ^{17}O excited states [7]. However, the previous work didn't include the excitation energy range $E_x(^{17}\text{O}) > 11.1$ MeV that contain several states of interest. The experiment presented in this chapter forms a part of an effort to shed more light on the structure of excited states of ^{17}O, especially the cluster-states candidates.

An increasingly popular method for measurement of the excitation functions is the thick-target inverse-kinematics method or resonant elastic scattering on a thick gas target method, first proposed by [51]. The fundamental idea of the method is to use the gas as both the target and the degrader, stopping heavy particles before the detectors but allowing the detection of light ones. The method allows to obtain a broad range of the excitation-energy function with a single beam-energy run as well as measurement at the 0° in the laboratory frame of reference.

In this work the resonant elastic scattering of the ^{13}C nuclei on a thick helium gas target was measured. In this section the experiment, calibration and data analysis will be presented in detail. The ^{17}O excitation function obtained is compared to previous results. The R-matrix calculation based on previously published comprehensive fit is used to assess the reliability of the data from this measurement. The previously unpublished part of the spectrum is studied using a simplified method suitable for the quasi-isolated resonances. The results are discussed in terms of tentative spin and parity assignments and Wigner ratios for the quasi-isolated resonances.

3.1 Experimental setup

3.1.1 Accelerator facility and the nuclear reactions beam-line

This experiment was performed at the accelerator facility of the Ruđer Bošković Institute in Zagreb, Croatia (see Fig. 3.3). The facility consists of two accelerators, the 1.0 MV High Voltage Engineering Tandetron accelerator and the 6.0 MV EN Tandem Van de Graaff accelerator. The latter provided the beam for the experiment. Sputter target used in the SNICS ion source for this experiment was a natural carbon target. The natural abundance of the ^{13}C is only 1%, and due to that the beam tuning and optimisation was performed using the ^{12}C. Once the beam was optimal, the fields of an analysing and switching magnet were corrected for a previously calculated amount needed to get the ^{13}C beam through the magnetic elements and to the beam-line. The ^{13}C beam intensity was estimated to be smaller then 1 pnA. Collimation apertures were 2 and 3 mm in diameter. The latter was located just before the gas target window foil at the edge of the chamber. The former collimator was placed further in the beam-lime, approximately 1 m from the edge of the chamber.

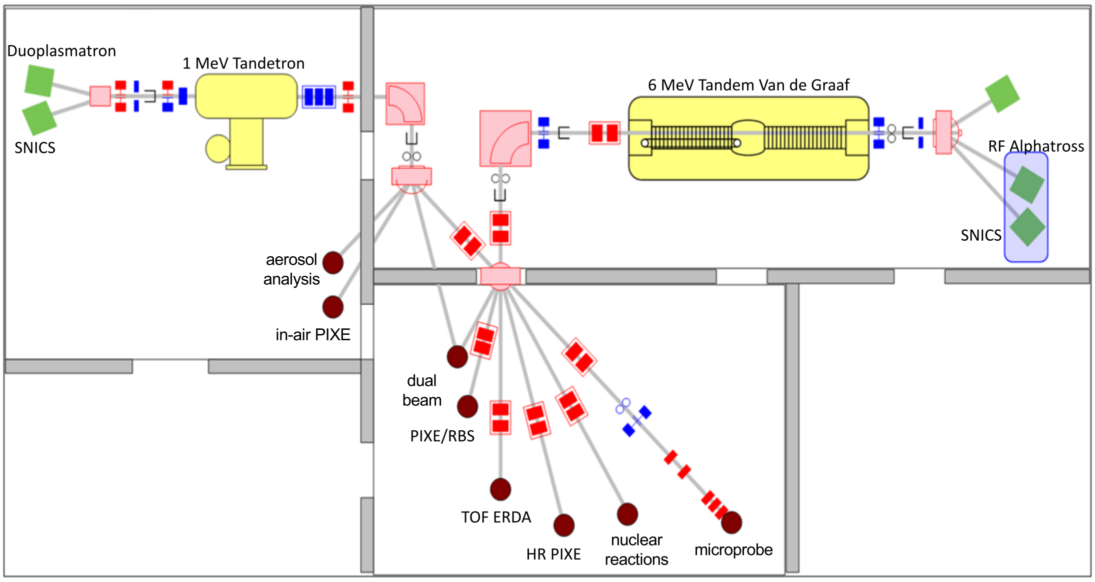

Figure 3.1: The Ruđer Bošković Institute accelerator facility.

The nuclear reactions beam-line consists of a quadrupole magnet, an electrostatic beam-deflector, a collimating system and a reaction chamber. The vacuum in the beam line and in the reaction chamber is maintained by turbomolecular pumps. Prior to experiment, the vacuum chamber was extensively tested for leaks, leaks were repaired and new elements necessary for the gas-target measurements were installed. The window-holder was designed to facilitate the mounting of the Havar foil windows mounted on a small flange between the chamber and the beam-line. An additional collimating system was designed and mounted immediately after the window, inside the vacuum chamber. That system would allow us the supression of scattering of the beam ions on the Havar foil. Furthermore, several foils were tested, filling the chamber with helium and maintaining the vacuum in the beamline. The results of these tests showed that the vacuum chamber is properly sealed, even when filled with helium at pressures of hundreds of milibars. The density of the helium gas target is determined by the temperature of the gas and its pressure. The pressure of the gas has to be measured precisely, while the temperature measurement doesn't influence the calculated density as much. The Vacuubrand DVR 3 vacuum gauge was used to measure the gas pressure, while a simple multimeter with a thermocouple monitored the temperature in the chamber.

3.1.2 Detector setup

The detector setup consisted of a single double-sided silicon strip-detector located at the 0°, behind the 2 μm-thick Havar foil. The collimating apertures were located in the beam-line, approximately 1 m from the gas-target window. Additional collimating apertures intended for use in the gas were removed to facilitate the measurement which was performed with a low beam current and to facilitate the measurement of the properties of resonances which are populated in the first few centimetres of gas. A circular base-plate with the precise angular scale allowed to move the detector to a different angle for the calibration and the beam-tuning. Detector position

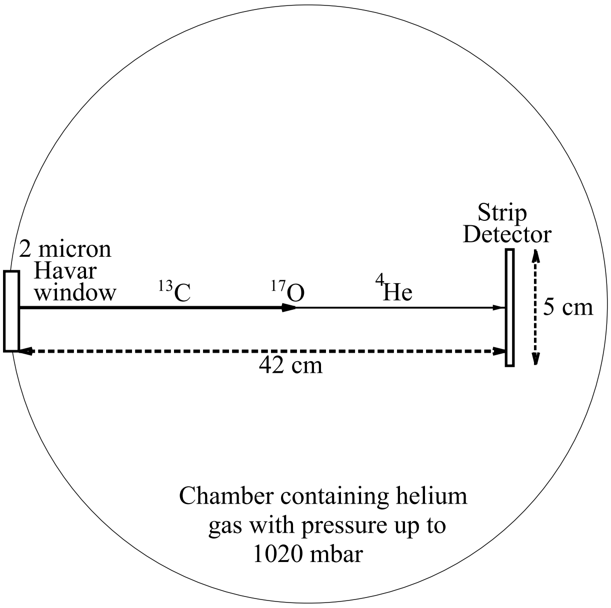

Figure 3.2: The experimental setup used for the measurement of the ^{13}C+^{4}He resonant elastic scattering.

was precisely aligned using the theodolite located approx. 4 meters behind the chamber.

This kind of setup requires careful planning of the beam energies and gas pressures because the beam has to be stopped in the gas before the detector (see Tab. 3.1). They were estimated with a safety margin not to damage the detector. Spacing of the beam-energies of different runs was adjusted to cover the full energy range with inelastic-free regions. The inelastic-free region of the excitation energy spectrum of the compound nucleus can be easily calculated as follows:

Table 3.1: Beam energies and gas pressures used in the experiment. The upper limit for the inelastic-free region doesn't take into account the energy loss in the Havar-foil window.

$E_{^{13}\mathrm{C}}$ [MeV]	$p_{^4\mathrm{He}}$ [mbar]	Inelastic-free $E_x(^{17}\mathrm{O})$ range	Run numbers
20.00	312	$7.977-11.066$	25
25.00	461	$9.154-12.243$	27
30.00	$591, 589, 587$	$10.331-13.420$	28-30, 32
33.00	699	$11.037-14.126$	33
35.00	720	$11.508-14.597$	35

$$E_{x\,min\,\mathrm{inel.free}} = E_{thr} + E_p^{cm} - E_x(^{17}\mathrm{O}^*) = E_{thr} + E_p^{lab} \cdot \frac{m_{^4\mathrm{He}}}{m_{^4\mathrm{He}} + m_{^{13}\mathrm{C}}} - E_x(^{17}\mathrm{O}^*), \tag{3.1}$$

where $E_{thr} = 6.3592\,\mathrm{MeV}$ is the decay threshold of ^{17}O to the ^{13}C+^{4}He channel, E_p is the beam energy and $E_x(^{17}\mathrm{O}^*) = 3.089\,\mathrm{MeV}$ is the energy of the first excited state in the ^{13}C. Using this kinematical the inelastic-free intervals in the Tab. 3.1 were calculated. Comparison of the overlapping parts of the ^{17}O spectrum measured at different beam energies will allow us to estimate the influence of inelastic processes on the data. The runs listed in the table provide us with overlapping inelastic-free regions covering the ^{17}O excitation energy range from 8 to 14 MeV.

3.1.3 Detector and electronics

For this measurement a double-sided silicon strip-detector (DSSSD) manufactured by Micron Semiconductors Ltd was used. The active area of the DSSSD detector is 50×50 mm^2, divided into sixteen mutually orthogonal strips on both front and back face. The detector mount was designed in such a way that the front detector strips were horizontal and the back strips vertical. Each strip provides one output signal. In this way one effectively gets 256 3 mm-wide pixels, separated by approximately 100 μm of inter-strip region. Detector bias was supplied to the detector using a custom-built printed-circuit board.

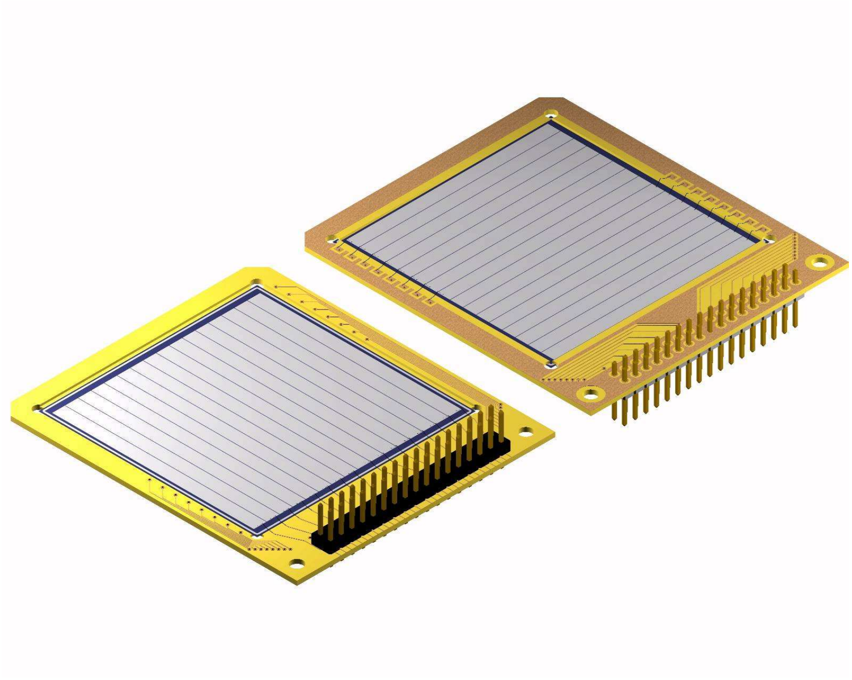

Figure 3.3: The Micron Semiconductor double-sided silicon strip-detector (DSSSD), adopted from [52].

After passing through cabling both in vaccum and in air, a signal reaches the preamplifier. The preamplifiers used were 16-channel double-width NIM modules based on the improved version of the charge-sensitive preamplifier chip developed for the CHARISSA colaboration and used for the TIARA array. The signal was amplified in the Silena 761F 16-channel shaping amplifier. The amplifier provided the linear outputs, used as an ADC inputs, and logic outputs, which were processed by the Phillips Scientific 705 8-channel discriminators and used for creating the gate signal triggering the ADCs. The Silena 9412/6V VME ADCs were used. They were controlled by the Silena 9418 Aquisiton Control (SAC) module, which was operated using the MIDAS data acquisition software running on the Motorola MVME 2434 VME CPU board. The VME CPU board was controlled by a Sun Microsystems Solaris 10 server, which was used for the on-line analysis of the data as well.

3.2 Data analysis

In this part all the steps needed to extract the excitation function of the compound nucleus from the raw data are covered. The section will follow the order in which the analysis was performed, starting with a calibration and ending with the normalised excitation function of the ^{17}O.

3.2.1 Calibration

There were four data sets for calibration at ones disposal: measurement with the three-peak ^{239}Pu-^{241}Am-^{244}Cm α-source, 17 MeV ^{9}Be elastic scattering on thin a gold target, 12 and 16 MeV ^{7}Li elastic scattering on thin gold target. The α-source calibration was used only for an online analysis. The detector calibration was performed using the three beam-runs. During the calibration runs the detector was moved from the 0° to the 44.6°. The variety of particles and energies in the calibration runs permitted us to deduce the dead layer thickness, which is important for the low-energy particles.

For the calibration the angle of the center of each pixel for the detector in the calibration position was calculated, needed to calculate the kinematics of the elastic scattering on a thin gold target. Energy losses in the target for both incident and scattered particles were taken into account, as well as energy loss in a given thickness of the dead layer.

During the course of the experiment no dedicated dead layer measurement was performed. The two ^{7}Li runs and the ^{9}Be calibration run were expected to lie on slightly different calibration lines due to the dead layer and ion A and Z dependent energy loss mechanisms in silicon (see [53] for details). An example of the influence of the effective dead layer thickness on the calibration is shown in the Fig. 3.4. While a change in an effective dead layer thickness doesn't change the residuals of the calibration points drastically, it does remove the systematic discrepancy. The slope of the calibration line changes with the dead layer thickness much less than the offset, which changes for approx. 100 keV.

By varying the effective dead layer thicknes, one can find the optimal value for which all the calibration data for both the front and the back-side strips lie on the same calibration line. It is important to bear in mind that such an effective dead layer thickness is optimal only for the ions used for the calibration measurements and that it implicitly contains corrections for the ion-type dependent energy loss processes in silicon.

That said, the effective dead layer thickness was varied until all the three data sets lay on their common calibration line for all the strips, both front and back. The thickness that gave optimal result was $d_{dl} = 0.275\,\mu\mathrm{m}\,\mathrm{Si}$ which is of the same order of magnitude as values provided by the manufacturer ($d_{dl}^{\mathrm{nominal}} = 0.5\ \mu\mathrm{m}$ [54]).

The results of the calibration are displayed in the Tab. 3.2. The front strip number 2 was dead. The discrepancy between the calibration points and the calibration line for front and back strips are displayed in the Fig. 3.5 and the Fig. 3.6, respectively. The dead layer adjustment

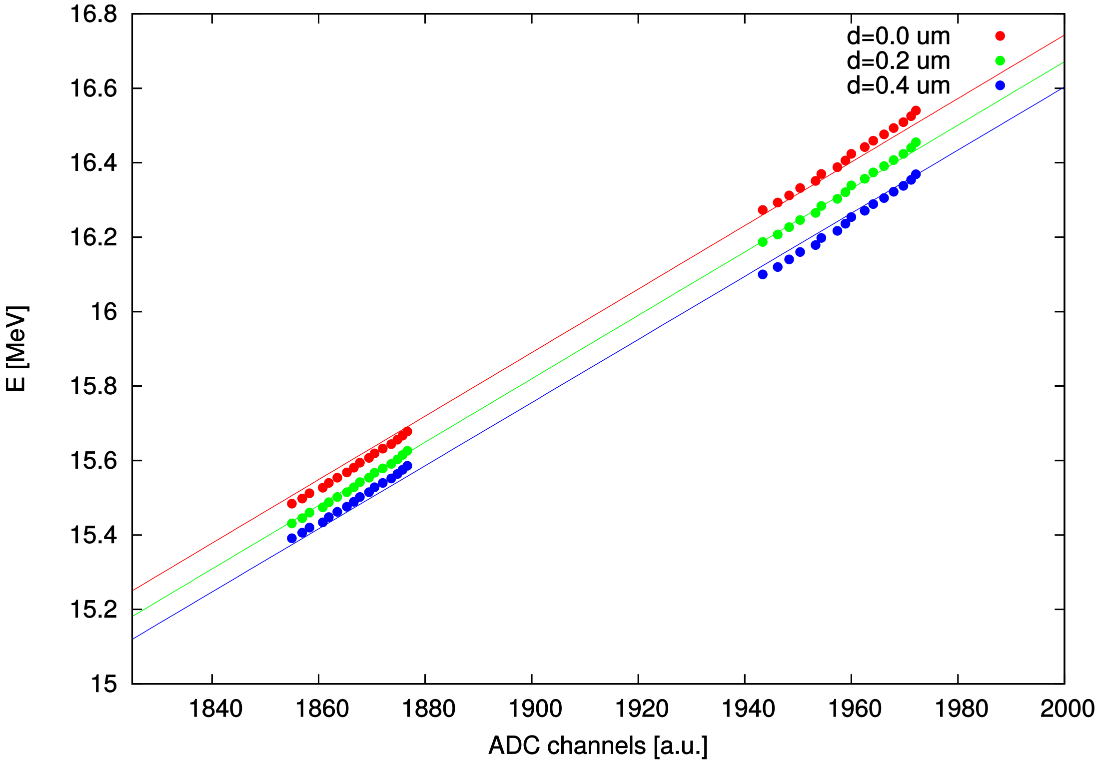

Figure 3.4: Calibration dependence on an effective dead layer thickness for the front strip no. 8. The data from left to right are for the 16 MeV ^{7}Li and for the 17 MeV ^{9}Be scattering measurement on a thin gold target, respectively. The range of this plot does not show calibration data for the 12 MeV ^{7}Li scattering on a thin gold target that was included in the calibration as well. The calibration lines are a result of a least-squares fit to all three calibration runs. The deposited energy was calculated taking into account energy losses in the target and in the dead layer. The plot demonstrates that a finite dead layer thickness significantly improves the quality of the calibration.

allowed us to make a calibration using two different types of detected ions and three beam energies which is linear within the 20 keV. The only systematic shift can be noticed for the back strip 16.

The Havar-window thickness

The Havar foils were obtained from the Goodfellow Ltd. and used as a gas-target window. They had a quoted thickness of 2 μm and the thickness uncertainty of 25%. The thickness was measured using the 12 MeV ^{9}Be beam passing through the gas-target window, entering the evacuated scattering chamber and scattering on the thin golden target. The detector was moved to the angle 22.58°. The thickness of the Havar foil was determined from the energies of the elastic scattering peaks in front and back strips by comparing them to the averaged detected energy in a strip, calculated by averaging over corresponding pixels. The Havar thickness was

Table 3.2: Calibration parameters for front and back strips.

Strip number	Front side strip		Back side strip	
	a [keV/ch]	b [keV]	a [keV/ch]	b [keV]
1	8.661	-372.6	11.223	-276.1
2			11.028	-324.6
3	8.822	-402.2	10.822	-311.3
4	8.809	-383.4	10.691	-313.6
5	8.405	-397.1	11.093	-305.2
6	8.139	-372.0	11.372	-270.1
7	8.605	-391.5	11.167	-282.2
8	8.510	-375.9	10.998	-300.4
9	8.812	-306.6	10.821	-77.5
10	8.944	-291.1	10.883	-44.0
11	8.719	-305.5	11.173	-44.8
12	8.401	-322.1	10.974	-77.2
13	8.400	-301.8	11.084	-79.0
14	8.785	-315.0	10.983	-71.5
15	8.355	-328.5	11.238	-65.0
16	8.607	-330.5	10.694	-54.8

calculated to be:

$$d_{\text{Havar}} = 2.11 \pm 0.02\,\mu\text{m}. \tag{3.2}$$

The discrepancies between the calculated scattered ^{9}Be energy averaged over the pixels in the strip and the measured energy are less than 10 keV.

3.2.2 Event selection

The good events in the detector were selected using a cut on total difference between the detected energy in the front strip and in the back strip:

$$-0.050\,\text{MeV} \leq E_b - E_f \leq 0.050\,\text{MeV}. \tag{3.3}$$

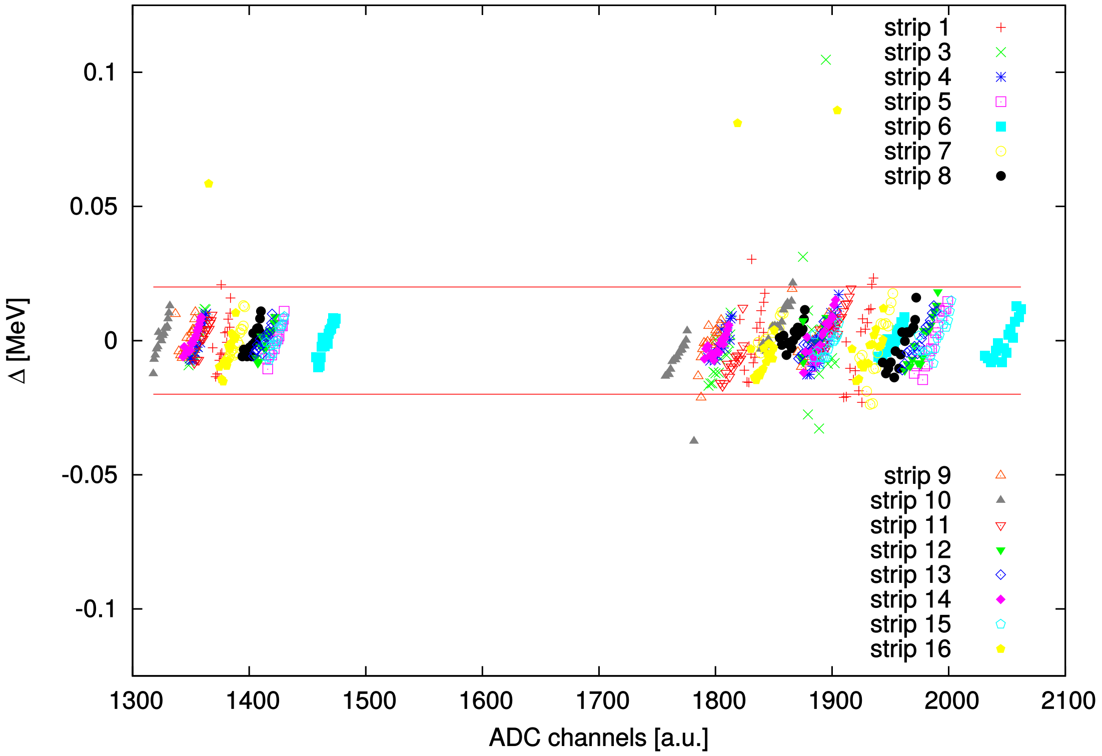

Figure 3.5: The discrepancies Δ between the calibration points for the front strips (horizontally oriented) and the calibration obtained by a linear fit. The red lines represent the 20 keV limit. The vast majority of points lie within the red lines. The strip 2 was not included because it was a dead strip.

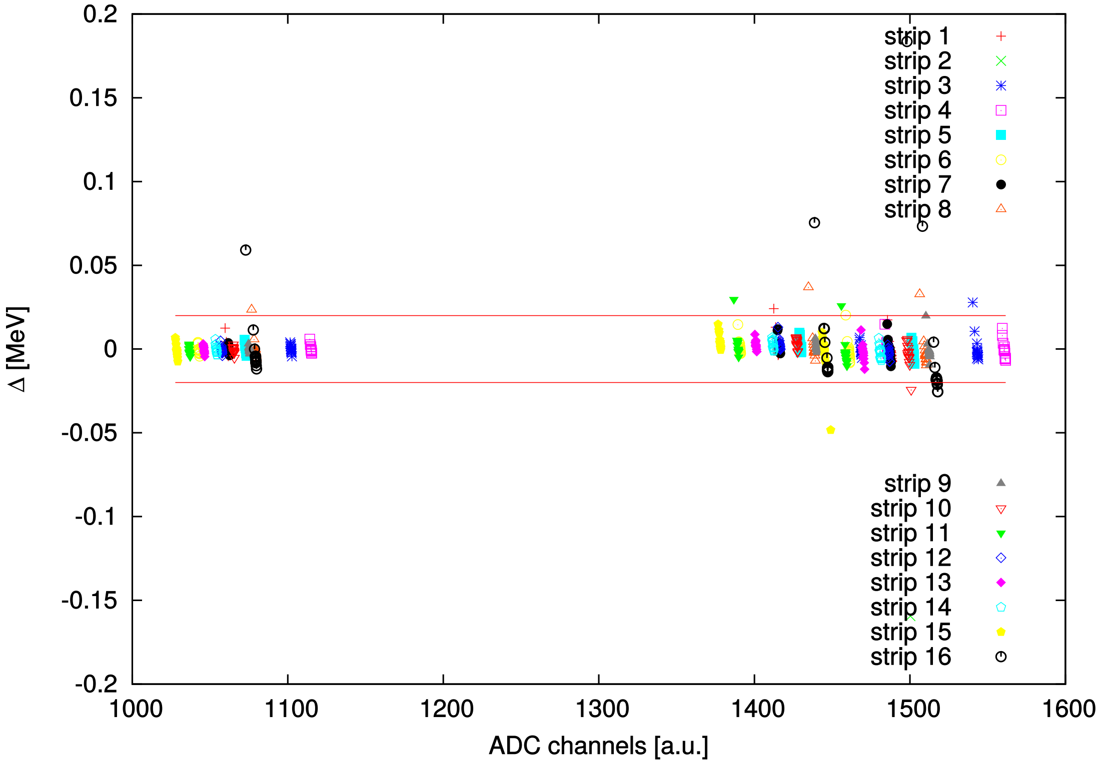

Figure 3.6: The discrepancies Δ between the calibration points for the back strips (vertically oriented) and the calibration obtained by a linear fit. The red lines represent the 20 keV limit. The majority of points lie within the red lines.

A low energy threshold of 0.5 MeV was applied on both front and back detector strips. For a good event, the front strip energy was used in the subsequent calculations due to its higher energy resolution in comparison with the back-strip.

3.2.3 Analysis procedure for scattering on gas

Having calibrated the detector, the next step was to establish a relation between the detected energy and the centre-of-mass energy of the ^{13}C+^{4}He system. The setup didn't enable particle identification, so one had to assume all the detected particles were ^{4}He ions. In case there were significant contributions of other reactions that would be seen while comparing runs at different beam energies and gas pressures.

In the analysis for the sake of simplicity it was assumed that the beam is point-like, aimed at the centre of the detector and does not spread while traversing the chamber. If necessary, these effects can be simulated using a sophisticated simulation package for resonant elastic scattering on thick gas targets [19].

The position of detector at 0° enabled us to segment it in annular-shaped regions (see Fig. 3.7). All the following calculations were performed for each region. While the detector itself was segmented, its position enabled us to divide it in 32 ($8 \times 8/2$) segments due to symmetry around the 0°. When calculating the angles of the pixels it became clear that the number of different segments can be further reduced to 28, simplifying the calculation while maintaining accuracy.

For each of the detector segment the centre-of-mass energy as a function of the detected energy was calculated ($E_{\mathrm{cm}}\left(E_{\mathrm{det}}\right)$). The calculation is performed in 1 mm steps for all depths in the gas until the incident beam stops. For each step a calculation takes into account:

1. energy loss of the incident ^{13}C beam
   (a) in the Havar-foil gas-target window $E_{\mathrm{loss}}^{^{13}\mathrm{C,Havar}}$
   (b) in the x mm of the ^{4}He gas at p mbar $E_{\mathrm{loss}}^{^{13}\mathrm{C},^{4}\mathrm{He}}$
2. kinematics of the ^{13}C+^{4}He elastic scattering where the outgoing ^{4}He ion scatters to the centre of the pixel (representative of the detector segment) $E_{^{4}\mathrm{He}}^{\mathrm{lab}}$
3. energy loss of the scattered ^{4}He ion
   (a) in the length of the ^{4}He gas from the interaction point to the detector segment $E_{\mathrm{loss}}^{^{4}\mathrm{He},^{4}\mathrm{He}}$
   (b) in the dead layer of the DSSSD detector $E_{\mathrm{loss}}^{^{4}\mathrm{He,dl}}$

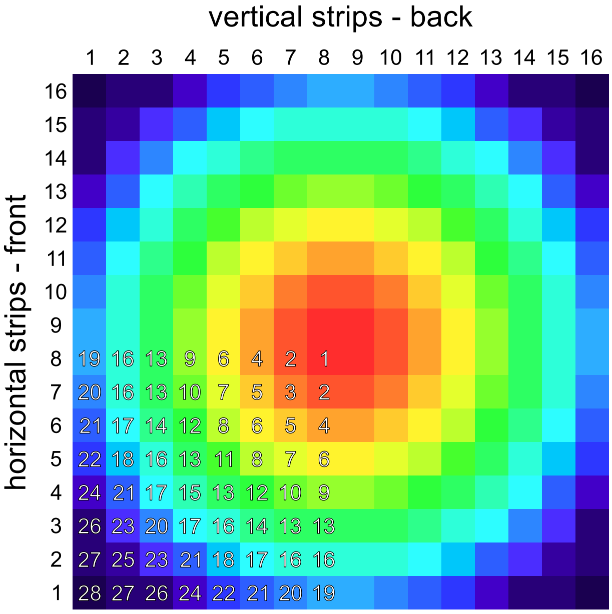

Figure 3.7: Segments of the DSSSD which are treated together for the E_{det}-E_{cm} calculation. Numerical labels are used in the first 64 pixels only and apply symmetrically to the rest of the detector. The total number of detector segments is 28.

From the energy of the incident ion at depth of the scattering x one can easily get the centre-of-mass energy and the ^{17}O excitation energy:

$$E_{\text{cm}}^{\text{tot}} = (E_p - E_{\text{loss}}^{^{13}\text{C,Havar}} - E_{\text{loss}}^{^{13}\text{C},^{4}\text{He}}) \cdot \frac{m_{^4\text{He}}}{m_{^{13}\text{C}} + m_{^4\text{He}}} \tag{3.4}$$

$$E_x(^{17}\text{O}) = E_{\text{cm}}^{\text{tot}} + E_{\text{threshold}} = E_{\text{cm}}^{\text{tot}} + 6.3592\,\text{MeV} \tag{3.5}$$

The calculation is repeated for each beam energy and gas pressure setting. The stopping powers used were Ziegler data available from the LISE++ software, version 9.8.18. The excitation energy of the $E_x(^{17}\text{O})$ is plotted against detected energy E_{det} (see Fig. 3.8) and fitted using a polynomial ansatz:

$$E_x^{^{17}\text{O}}(E_{\text{det}}) = a_1 + a_2 \cdot E_{\text{det}} + a_3 \cdot E_{\text{det}}^2 + a_4 \cdot E_{\text{det}}^3 + \frac{a_5}{E_{\text{det}}} + \frac{a_6}{E_{\text{det}}^2} + \frac{a_7}{E_{\text{det}}^3}, \tag{3.6}$$

where E_{det} is the detected energy and $a_1 \ldots a_7$ constants determined by the fitting procedure. The discrepancy between the function and the calculated points Δ is generally smaller than 2.5 keV and only gets a bit larger at very low energies for runs with high beam energy and gas pressure.

At this point one can make a few remarks. From the Fig. 3.8 it is clear that even for the high energy and high gas pressure runs the differences between the central and border pixels

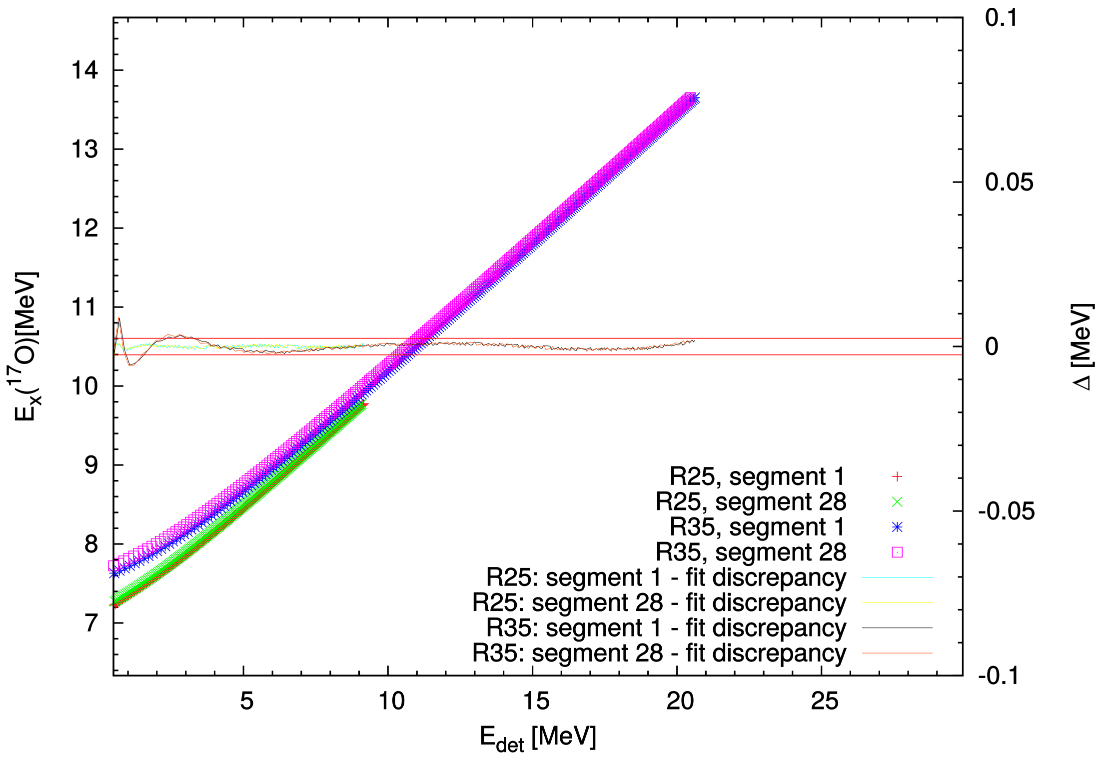

Figure 3.8: Calculated $E_x(^{17}\mathrm{O})$ as a function of the detected energy. Two runs, the run 25 and the run 35, are the lowest beam energy and gas pressure and the highest energy and gas pressure runs, respectively. For each run the relation for the innermost and the outermost segment was plotted, respectively. The calculated points were fitted with a polynomial function (see text for details) and the Δ is discrepancy between the fit and the data points. Two horizontal red lines illustrate the $\Delta < 2.5\,\mathrm{keV}$ discrepancy region.

start to be important only for the detected ^{4}He energies smaller than 10 MeV, amounting to a 0.100 MeV shift in the reconstructed excitation energy of the ^{17}O. For the low energy and gas pressure run the difference at the $E_{\mathrm{det}} = 0.5\,\mathrm{MeV}$ is approximately 0.050 MeV. While it is clear that the division of pixels to segments increased accuracy of the data analysis, one might question its importance. The small differences seen in the Fig. 3.8 when accumulated over all events spanning the entire detector, as illustrated in the Fig. 3.9, shift the peaks and change their shape. Once the $E_x^{^{17}\mathrm{O}}(E_{\mathrm{det}})$ is determined and parametrized for all the segments of the detector and all the experimental runs with different beam energies and gas pressures, the yield of the resonant elastic scattering from the data for each run can be extracted.

3.2.4 Efficiency correction

Because of a different detector acceptance for scattering events occurring at different depths in the gas due to geometry, energy loss and detection thresholds, different runs at different beam energies and pressures have to be efficiency-corrected.

During the course of this analysis, two methods were tried. The first method was a Monte

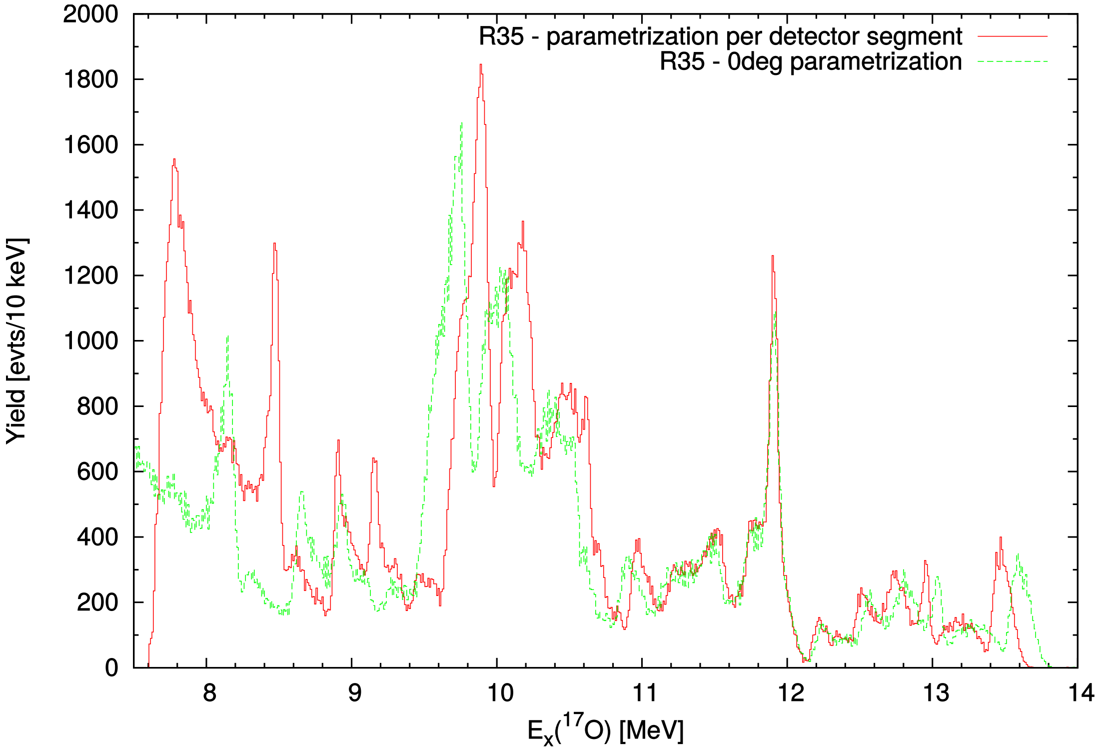

Figure 3.9: $E_x(^{17}\mathrm{O})$ reconstructed from the detected energy. In the first case (the red line) events from different detector segments were treated differently, while in the second case events originating from the entire detector were treated as if they were detected at the 0° in the laboratory frame of reference. Significant excitation-energy dependent shift as well as changed features of the spectra can be observed.

Carlo calculation of efficiency and the second a modified analysis method which allowed a cut to be placed on the $\vartheta^{\mathrm{CM}}_{^4\mathrm{He}}$. In this section only the latter method will be discussed, first used in the [55], which proved to be more reliable and assumption-free.

For each good event in the detector the $\vartheta^{\mathrm{CM}}_{^4\mathrm{He}}$ was calculated using the following kinematical equations:

$$\cos\vartheta_i^{\mathrm{CM}} = \frac{\sqrt{E_i^{\mathrm{L}}}\cdot\cos\vartheta_i^{\mathrm{L}} - a_i}{\sqrt{E_i^{\mathrm{L}} - 2a_i\sqrt{E_i^{L}}\cos\vartheta_i^{\mathrm{L}} + a_i^2}} \tag{3.7}$$

$$\varphi_i^{\mathrm{CM}} = \varphi_i^{\mathrm{L}} \tag{3.8}$$

where all variables with the index i apply to the outgoing ^{4}He nucleus. The angles ϑ_i and φ_i are the polar and the azimuthal angle, respectively. The E_i^{L} is the energy of the outgoing ^{4}He after the reaction in the laboratory frame of reference. The variable a_i is defined as:

$$a_i = \frac{\sqrt{m_i m_p E_p^{\mathrm{L}}}}{m_p + m_t}, \tag{3.9}$$

where $m_i = m_t = m_{^4\mathrm{He}}$, $m_p = m_{^{13}C}$ and E_p^{L} is the incident ^{13}C beam energy at the point of the scattering process. The results of the calculation used in previous section were not only the ^{17}O excitation energies $E_x^{^{17}\mathrm{O}}$ and the detected ^{4}He energies E_{det}, but the intermediate energies as well. Using that data it was possible to fit the dependencies of the scattering depth in the chamber x, the outgoing ^{4}He energy E_i^{L} and the incoming ^{13}C energy E_p^{L} on the calculated excitation energy of the ^{17}O, $E_x^{^{17}\mathrm{O}}$. The fit was performed for the 28 detector segments for each beam-energy and gas-pressure combination. Additionally, for each event the direct-kinematics scattering angle $\vartheta_{^4\mathrm{He}}^{\mathrm{L,DK}}$ was calculated, that is the equivalent ^{13}C(^{4}He,^{4}He)^{13}C scattering angle. That angle is necessary for the data input to the AZURE2 R-matrix calculation programme.

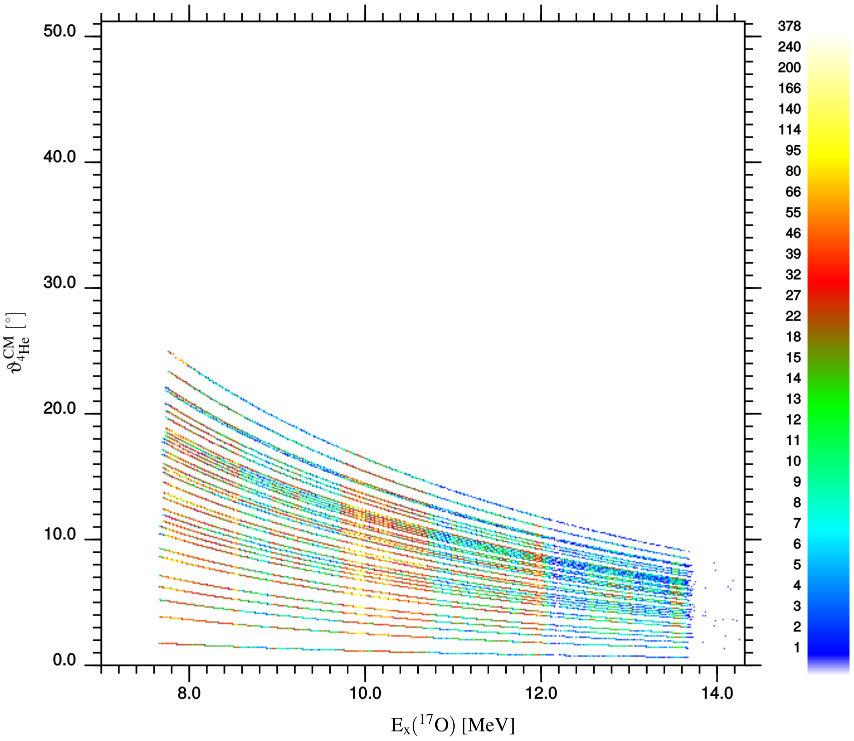

Figure 3.10: Centre-of-mass angle of the scattered ^{4}He nucleus plotted versus excitation energy in the ^{17}O. The analysis was performed using separate sets of parameters for each of the 28 pixels. It's clear that the plot shows 32, not 28 loci, which is due to the symmetry (see text for details). The vertical loci are the resonances, spanning all the segments of detector pixels.

The Fig. 3.10 shows the dependence of the $\vartheta_{^4\mathrm{He}}^{\mathrm{CM}}$ on the $E_x(^{17}\mathrm{O})$. One can notice that there are 32 loci, not 28, although pixels were divided in 28 segments. The number of loci on the figure is due to symmetry: each pixel on a diagonal shares it's angle with three other pixels (e.g. 8-8, 8-9, 9-8 and 9-9) while off-diagonal pixels can be grouped in the groups of eight (e.g. 1-2, 2-1, 1-15, 2-16, 15-16, 16-15, 16-2 and 15-1). Finally one has 256 pixels grouped in 24 groups of out-of-diagonal pixels and 8 groups on on-diagonal pixels, giving the 32 observed loci. Vertical loci may be observed in the Fig. 3.10 as well, showing the resonances in the yield of the elastic scattering. The angular independence of resonant peaks shows that the method of reconstructing the ^{17}O from the ^{4}He detected energy works well.

In order to apply the cut on the centre-of-mass polar angle of the outgoing ^{4}He, one has to modify the way in which angles are treated in this analysis. While in the previous version only the angle for the centre of each pixel was computed, now each event will be assigned a randomized position within a pixel, for which an angle will be calculated. Such a procedure will allow us to smooth out the effects of detector granularity. The typical plot is shown in Fig. 3.11, and will allow us to use a cut on the $\vartheta^{\mathrm{CM}}_{^4\mathrm{He}}$ to get a more reliable normalization. However, if the distance from the interaction point to the pixel gets small and the angular coverage of the pixel gets large, some undesired events will pass the cut as well, a feature described in detail in Ref. [55]. Typically, this contribution is small and can be neglected in this case, except for the highest beam-energy and gas-pressure runs where the data for low ^{17}O excitation energies have to be excluded.

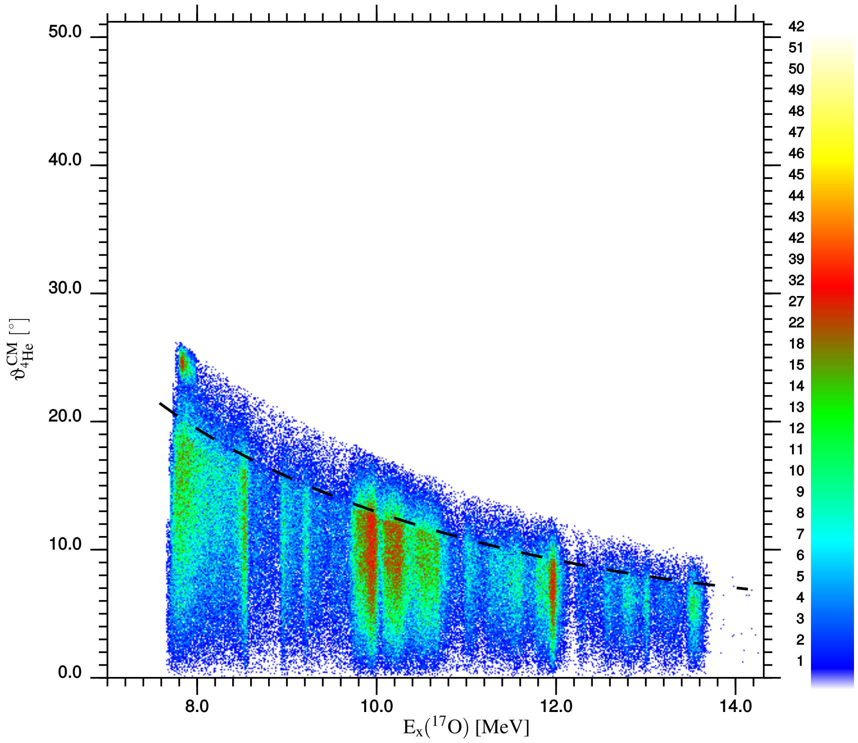

Figure 3.11: Centre-of-mass angle of the scattered ^{4}He nucleus plotted versus excitation energy in the ^{17}O. The analysis was performed using separate sets of parameters for each of the 28 pixels and the position of the incident ion inside a pixel was randomized, allowing a smooth distibution. The dashed line labels the locus of the missing data from the dead front strip number 2.

Before discussing an appropriate centre-of-mass angular cut for scattered ^{4}He ions, one can comment on a few features of the spectrum shown on the Fig 3.11. One of the features of this plot is the missing strength of resonances in the area of highest centre-of-mass angles for a particular ^{17}O excitation energy. This is due to a dead front strip number 2. The second feature is a decent resolution of the peaks, especially ones between 8 and 10 MeV, which are influenced the most by energy loss and energy and angular straggling.

The goal of the efficiency correction is to account for the geometrical, energy loss and detection threshold effects. While this can be done performing Monte Carlo simulation of the $^{17}\mathrm{O}^*$ decay to the elastic channel, the results are always biased by the assumed spin and parity of the decaying state (in the calculation assumed to be 0^+ for the sake of simplicity). A very nice way of correcting for efficiency while not using any assumption or running Monte Carlo simulation was published by [55]. It was shown that a simple cut on the centre-of-mass angle of the outgoing particle, in this case $\vartheta^{\mathrm{CM}}_{^4\mathrm{He}}$, provides the desired efficiency correction. This can be seen from the Fig. 3.11 itself: if one selects a strip of the plotted data comprising e.g. from 0 to 5°, it can be seen that it has a uniform efficiency, independently of the $E_x(^{17}\mathrm{O})$.

The efficiency correction on the data was performed using the criterion $\vartheta^{\mathrm{CM}}_{^4\mathrm{He}} \leq 5^\circ$. Other cut-off angles have been tried on the data as well, but this value is the best compromise between the angular resolution and the statistics. The yield of elastic scattering for the efficiency-corrected data is displayed in the Fig. 3.12. When comparing it to the uncorrected data, it can be seen that the cut on the centre-of-mass angle had the desired effect: the low-energy part of the spectrum is weakened while the high-energy part is strengthened.

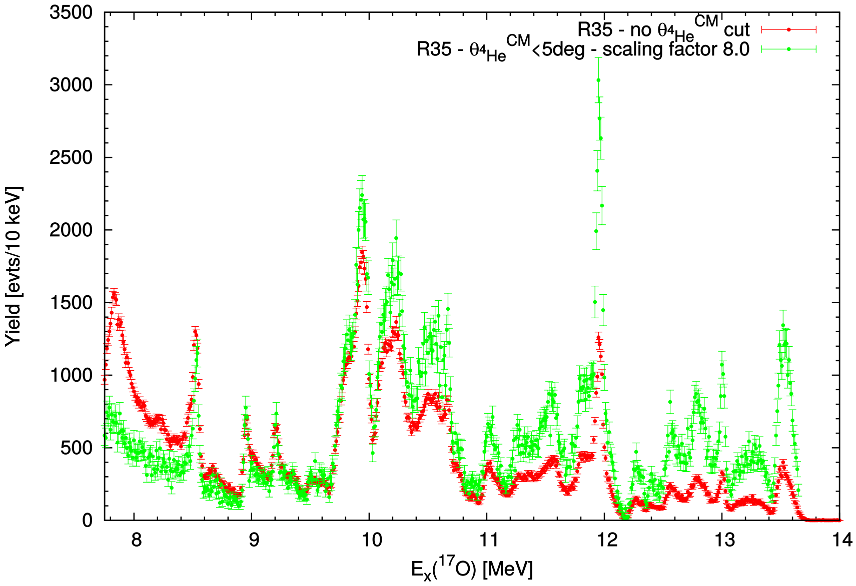

Figure 3.12: Comparison of the yield of elastic scattering for the run 35 without (red) and with the efficiency correction. Efficiency correction was performed requiring $\vartheta^{\mathrm{CM}}_{^4\mathrm{He}} \leq 5^\circ$. Please note that the efficiency corrected data was scaled by the factor of 8.0 to facilitate comparison.

This efficiency-correcting procedure was performed on all the runs, the cut-off centre-of-mass angle was kept at the same 5° value.

3.2.5 Data averaging and normalization

In order to get a single spectrum from a number of runs, one has first to normalize the data and then to average it. This might seem as a trivial process, nevertheless it gives us some insight as to the purity of the data and the magnitude of systematic errors.

Before normalizing the data, one has to make sure all the resonances from all the runs overlap and lie at the same excitation energies. However, one has to choose which run should be the most reliable in terms of the peak positions. The lowest-energy run, run 25, which has the lowest gas pressure was chosen. This run enables us to measure the low-energy part of the elastic-scattering yield with highest precision. The yields from the other runs had to be shifted from -0.030 MeV to 0.020 MeV in the ^{17}O excitation energy relative to the run 25. At the later point the position of the peaks from the run 25 was compared to the previous measurements (see 3.2.7) and the systematic shift was found to be -0.038 MeV.

It has been chosen to normalize the data to the highest-energy run, run 35. That means all the other runs will be scaled by a constant factor to overlap the best with the yield from the run 35. The scaling factor was determined by integrating an area of three prominent peaks starting at approx. 9.6 MeV and ending around 10.7 MeV of ^{17}O excitation energy. The ratio between the sum of all events in the aforementioned region of the yield from the run in question to that of the run 35 was adopted as the scaling factor.

The resulting plot is displayed in the Fig. 3.13. Several remarks can be made about the figure. First, scaled elastic-scattering yields from different runs are mutually consistent. Bearing in mind the inelastic-free regions listed in the Tab. 3.1., the consistency of runs show that inelastic contributions to the yield are negligible. Another important feature of this figure is a small but consistent systematic shift of the 8.5 MeV peak. The systematic shift of that peak indicates that the effective dead layer thickness deduced from the calibration measurements doesn't correspond to an effective dead layer thickness appropriate for the ^{4}He nuclei. This has the effect of slightly degrading the overall energy resolution of the final spectrum.

3.2.6 Averaged excitation function

The averaged yield of the excitation function was obtained from the efficiency-corrected scaled yields of all runs, slightly shifted to overlap. The low-energy part of the spectrum was most

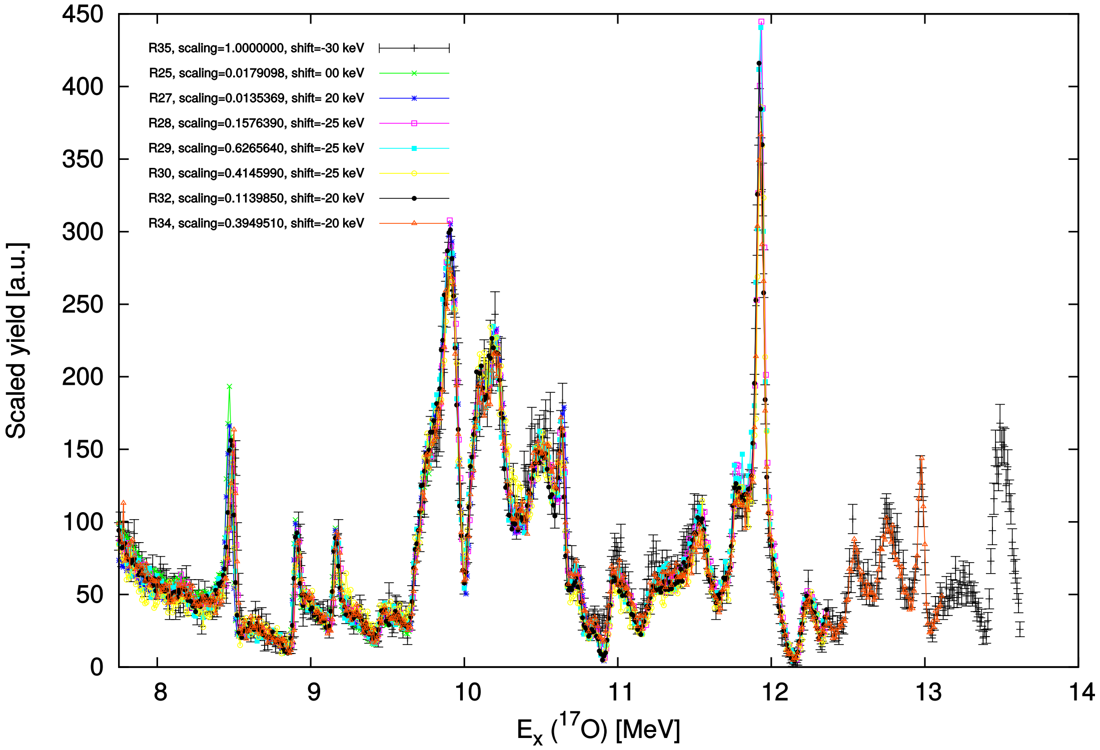

Figure 3.13: All experimental runs shifted to overlap with the lowest-energy run and scaled to the highest-energy run. The shifts are small in magnitude, they range from -0.030 MeV to 0.020 MeV in the $E_x(^{17}\mathrm{O})$. The runs are consistent among themselves, indicating negligible contribution of inelastic processes.

reliably measured in runs 25 and 27, hence only these two runs were used for the averaged yield up to the $E_x(^{17}\mathrm{O}) = 9.75$ MeV. All the other runs were used from the 9.75 MeV up. The error was computed as a standard deviation from the mean of available runs for a given bin (in the case there was only one measurement available for a given excitation energy, a corresponding statistical error of that bin was used). The averaged yield of elastic scattering is shown in the Fig. 3.14. It should be noted that the excitation energy range from the 11.1 to 13.8 MeV hasn't been measured before in this reaction channel.

3.2.7 Normalization to a known cross-section

A comparison of the averaged yield with the data by [7] measured at high angles in the direct kinematics is shown in the Fig. 3.15. The agreement between the high-energy part and the previous measurements is fair. A systematic shift of the low-energy peaks at $E_x(^{17}\mathrm{O})$ of a 8.4, 8.9 and 9.2 MeV can be observed, amounting to 0.046, 0.035 and 0.026 MeV, respectively. The source of that shift is the effective dead layer thickness and the data it was deduced from, which was discussed in the section on the data averaging.

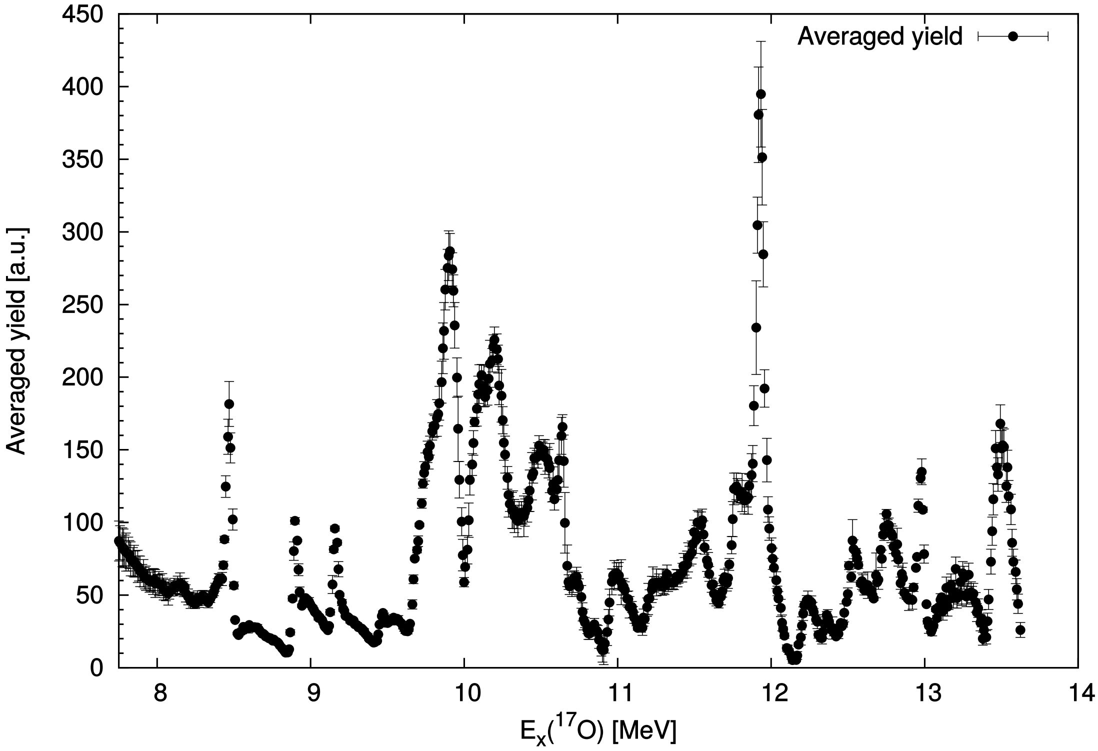

Figure 3.14: The averaged efficiency-corrected yield of the elastic scattering. The low part of the spectrum is an average of two lowest-energy runs (run 25 and 27). When more than one run covers a given excitation energy, the error was calculated as a standard deviation of available yields. For a region covered only by the data of the run 35 a statistical error is used.

In order for the data to fit the previously published data, one had to shift the entire excitation function by 0.038 MeV. This was also an opportunity to try to estimate the cross section. An empirical factor equalling 0.0006 gave satisfactory result.

3.3 Cross-section analysis

The cross section of the $^{13}C+^{4}He$ elastic scattering was previously studied for $E_x(^{17}O) \leq 11.1$ MeV [7]. The interest was due to importance of the $^{13}C(^{4}He,n)^{16}O$ cross section at astrophysical energies as a possible source of neutrons for the s-process [8]. In order to obtain the reaction S-factor the authors performed a demanding R-matrix fit to an extensive collection of experimental data for all the relevant reaction channels, spanning many detection angles. Section 2.6 is dedicated to a brief introduction to the R-matrix formalism. The AZURE2[49] code was used in this work. All the input parameters of the code are in the laboratory frame of reference, while the output cross-sections are in the centre-of-mass frame of reference.

Starting from the published resonance parameters and the data sets used in the aforementioned article, it was attempted to reproduce the previous results. The prediction of the R-matrix

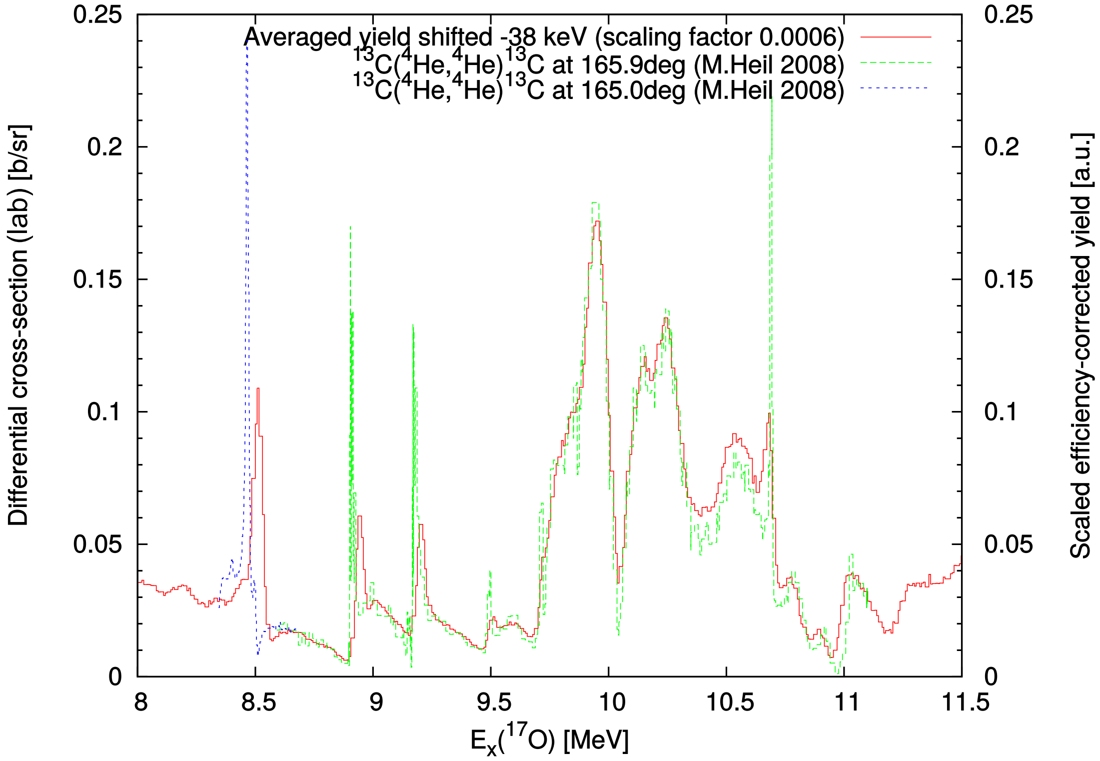

Figure 3.15: The averaged efficiency-corrected yield was compared to the existing measurements from [7]. The measurements were performed in the direct kinematics, at high angles in direct kinematics (165.9° and 165.0° for the high-energy and low-energy measurement, respectively). The effective angle in the direct kinematics of the data is approx. 175°.

calculation based on those parameters was compared to this measurement at approx. 175° for direct reaction in the laboratory frame of reference.

While helping us to confirm the normalization of the averaged yield, the results of the R-matrix calculation for this and previous measurements have shown some limitations of the published fit, as well. Possibilities for the improvement of the existing fit using the newly obtained data were discussed. A simplified method for estimating spins, parities and Wigner ratio of quasi-isolated resonances was proposed and used on a several peaks of interest.

3.3.1 Relevant reaction channels

The level-scheme of the ^{17}O nucleus shows us two thresholds important for study of the measured cross-section: the neutron-decay threshold at the excitation energy of 4.1436 MeV and the α-decay threshold at 6.3592 MeV. Other thresholds for the inelastic channels open at higher excitation energies. A simple sketch in the Fig. 3.16 can be used to illustrate all the available channels.

Let us consider the ^{13}C+^{4}He→^{17}O* reaction. An excited ^{17}O can decay through any of

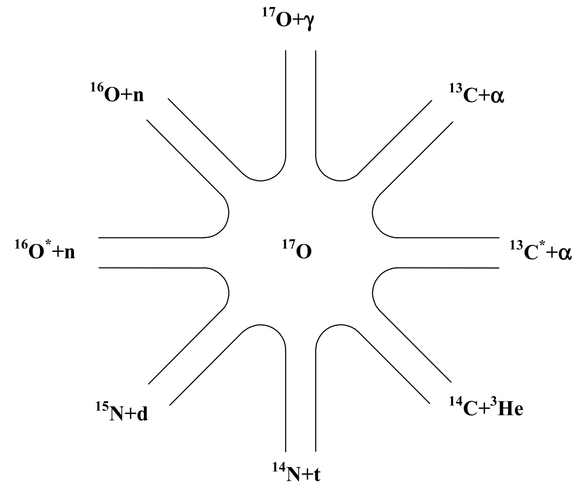

Figure 3.16: An illustration of possible channels for creation or decay of the ^{17}O nucleus. The figure was adopted from the [56].

the open channels: the neutron channel, the alpha channel and for higher excitation energies through the neutron channels with excited ^{16}O nucleus. It may decay via gamma-decay to lower excited states or the ground state, as well. The nitrogen channels are suppressed because of the large and negative Q-value for the decay, making them irrelevant at this range of excitation energies.

The relevant reaction channels are:

$$^{13}\mathrm{C}+^{4}\mathrm{He} \tag{3.10}$$

$$^{16}\mathrm{O}+\mathrm{n} \tag{3.11}$$

$$^{16}\mathrm{O}^{*}+\mathrm{n}' \tag{3.12}$$

$$^{16}\mathrm{O}^{**}+\mathrm{n}'' \tag{3.13}$$

where n$'$ and n$''$ label the neutron from the channel in which the oxygen nucleus is in the first or the second excited state, respectively. Some of these channels are always an exit channels, like the ones with an excited ^{16}O nucleus, while the other two can be both entrance and exit channels. That means that one ideally needs a set of data for any possible combination of channels (and preferably measured at many angles as well).

3.3.2 Published results

The work of M.Heil *et al.* [7] remains the most comprehensive study of the ^{17}O nucleus using the multichannel R-matrix formalism. The motivation behind their work was to constrain and extrapolate to the astrophysical energies the *S*-factor of the ^{13}C(^{4}He,n) reaction. To achieve the goal, the authors identified relevant reactions, gathered experimental data available at the time, identified the deficient reaction datasets and performed two measurements to tackle it. The two measurements were the ^{13}C+^{4}He elastic scattering measured in the direct kinematics using the silicon surface barrier detectors at a range of angles and energies and the measurement of the ^{13}C+^{4}He→n+^{16}O reaction using the 4π BaF$_2$ neutron detector. These additional data and a large measured range of angles proved to be a decisive factor for a successful fit of the cross-sections using the R-matrix formalism. Nevertheless, some of the resonances (or their characteristics) resulting from the fit seem to lack firm support from other types of measurements in which they should have been observed as well.

However, at $E_x(^{17}\mathrm{O}) > 11.1\,\mathrm{MeV}$ there are no data for the elastic channel, and a very limited data for other channels. Furthermore, that range of the spectra is influenced by the background resonances needed to reproduce the cross-sections at lower excitation energies, limiting even more the possibility of extending the range of the existing fit.

3.3.3 Reproducing the published results

When reproducing the R-matrix fit published in the [7], one has to bear in mind that the authors of the article used the R-matrix code SAMMY [57], while in this work the AZURE2 code is used. There are some differences in the available features, e.g. with AZURE2 one cannot perform the calculation of the total neutron cross-section. That, together with some details explained later, doesn't allow one to get exactly the same results as in the previous study. However, all the essential features of the published R-matrix fit were reproduced.

Experimental data

This section is dedicated to the datasets for which the cross-section was computed using the R-matrix parameters of [7]. One could start with the double differential cross-section of the ^{13}C+^{4}He elastic scattering. The data from [7] was used. It consists of two separate measurements in direct kinematics (on thin, ^{13}C enriched targets), the first one spanning the ^{4}He

Table 3.3: The R-matrix parameters

No.	J^π	$E_x(^{17}\mathrm{O})$ [MeV]	Heil *et al.* [7]				This work			
			Γ_n [keV]	Γ_α [keV]	$\Gamma_{n'}$ [keV]	$\Gamma_{n''}$ [keV]	Γ_n [keV]	Γ_α [keV]	$\Gamma_{n'}$ [keV]	$\Gamma_{n''}$ [keV]
1	3/2-	4.551	-43.4	$9.9 \cdot 10^{-7}$	0	0	-43.4	0	0	0
2	3/2+	5.084	-100.4	0.2	0	0	-100.4	0	0	0
3	9/2-	5.0701	$6.8 \cdot 10^{-7}$	$1.8 \cdot 10^{-5}$	0	0	$6.8 \cdot 10^{-7}$	0	0	0
4	3/2-	5.3752	-42.1	$4.3 \cdot 10^{-7}$	0	0	-42.1	0	0	0
5	7/2-	5.6967	3.28	$2.4 \cdot 10^{-11}$	0	0	3.28	0	0	0
6	5/2-	5.7335	0.09	$4.1 \cdot 10^{-9}$	0	0	0.09	0	0	0
7	3/2+	5.8684	8	$-4.1 \cdot 10^{-4}$	0	0	8	0	0	0
8	1/2-	5.9232	-48.1	$5.5 \cdot 10^{-9}$	0	0	-48.1	0	0	0
9	1/2+	6.3795	158.1	$1.7 \cdot 10^{-54}$	0	0	158.1	0	0	0
10	5/2+	6.8298	0.32	0.0000011	0	0	0.320	0.0000011	0	0
11	7/2-	6.9362	0.0087	0.0000033	0	0	0.0087	0.0000033	0	0
12	5/2-	7.1646	1.88	0.0043	0	0	1.88	0.0043	0	0
13	3/2+	7.2477	340.1	0.14	0	0	340.1	0.14	0	0
14	5/2+	7.3779	0.41	0.011	0	0	0.41	0.011	0	0
15	5/2-	7.3807	1.77	0.0029	0	0	1.77	0.0029	0	0
16	3/2-	7.4752	678.3	0.027	0	0	678.3	0.027	0	0
17	7/2-	7.686	-14.5	0.011	0	0	-14.5	0.011	0	0
18	1/2+	7.9669	-94	2.64	0	0	-94	2.64	0	0
19	1/2-	7.9128	234.5	10.5	0	0	234.5	10.5	0	0
20	3/2+	8.0751	87.3	7.1	0	0	87.3	7.1	0	0
21	1/2-	8.195	49.5	0.0033	0	0	49.5	0.0033	0	0
22	3/2-	8.1906	-57.9	2	0	0	-57.9	2	0	0
23	1/2+	8.3438	8.6	1.5	0	0	8.6	1.5	0	0
24	5/2+	8.4021	4.8	0.51	0	0	4.8	0.51	0	0
25	7/2+	8.4668	-0.42	7.1	0	0	-0.420	7.1	0	0
26	9/2+	8.4656	-0.89	0.0000068	0	0	-0.89	0.0000068	0	0
27	5/2-	8.5016	2.23	3.12	0	0	2.23	3.12	0	0
28	3/2-	8.6809	65.2	2.92	0	0	65.2	2.92	0	0
29	9/2-	8.9029	-0.000023	-0.45	0	0	-0.000023	-0.45	0	0
30	3/2+	8.9117	-101.8	25.3	0	0	-101.8	25.3	0	0
31	9/2-	8.9124	-0.000033	-1.08	0	0	-0.000033	-1.08	0	0
32	7/2-	8.9643	20.4	0.91	0	0	20.4	0.91	0	0
33	1/2-	9.1479	0.23	7.33	0	0	0.23	7.33	0	0
34	9/2-	9.2183	0.036	-0.044	0	0	0.036	-0.044	0	0
35	7/2-	9.1737	0.038	3.26	0	0	0.038	3.26	0	0
36	5/2+	9.194	2.29	0.24	0	0	2.29	0.240	0	0
37	3/2-	9.396	-200.5	0.3	0	0	-200.5	0.3	0	0
38	5/2-	9.4912	0.28	13	0	0	0.28	13	0	0
39	1/2+	9.518	-0.0000067	127.8	0	0	-0.0000067	127.8	0	0
40	7/2+	9.7109	17.5	1.36	0	0	17.5	1.36	0	0

beam-energy range from 2.6 to 3.1 MeV and covering 7 different angles. The second one spans the beam-energy range from 2.9 to 6.2 MeV and covers 28 different angles.

The next data set is the double differential cross-section for the ^{16}O+n elastic scattering. The data of Shouky *et al.* [58] was adopted. It covers the neutron energy-range from 0.52 to 6.17 MeV, covering 10 different angles. A low-energy dataset from Lane *et al.* [59] lies in the neutron-energy range from 0.12 to 1.68 MeV, covering 8 different angles. The excitation energy region of ^{17}O of this measurements is below the α threshold. A small shift exists between the Lane data and the Shouky data. A transformation for the Lane dataset suggested in [60] resolves that issue:

$$E = 1.0012 E_0 - 8617.7\ \mathrm{keV} \tag{3.14}$$

Table 3.4: The R-matrix parameters (continued). The last ten resonances are background resonances.

No.	J^π	$E_x(^{17}O)$ [MeV]	Heil *et al.* [7]				This work			
			Γ_n [keV]	Γ_α [keV]	$\Gamma_{n'}$ [keV]	$\Gamma_{n''}$ [keV]	Γ_n [keV]	Γ_α [keV]	$\Gamma_{n'}$ [keV]	$\Gamma_{n''}$ [keV]
41	7/2+	9.7188	-2.45	4.81	0	0	-2.45	4.81	0	0
42	3/2+	9.7289	1.92	70	0	0	1.92	70	0	0
43	3/2-	9.7817	16.5	0.0000034	0	0	16.5	0.0000034	0	0
44	9/2+	9.859	-2.44	0.47	0	0	-2.44	0.47	0	0
45	1/2-	9.8658	-29	1.72	0	0	-29	1.72	0	0
46	7/2+	9.9612	-1.81	-95.4	3.26	1.2	-1.81	-95.4	0	0
47	1/2+	10.042	-0.000072	-48.9	0.019	0.00041	-0.000072	-48.9	0	0
48	5/2-	10.165	24.5	4.92	71.8	0.0000023	24.5	4.92	0	0
49	5/2+	10.204	-0.0000097	303.3	0.027	0.0034	-0.0000097	303.3	0	0
50	1/2-	10.168	26	245	0.00041	0.12	26	245	0	0
51	3/2+	10.355	55.9	86.5	0.00000071	0.00034	55.9	86.5	0.000071	0
52	3/2-	10.378	0.0098	1.65	1.14	0.0000013	0.0098	1.65	1.14	0.000004
53	5/2-	10.512	-0.000091	-54.2	24.8	2.36	-0.000091	-54.2	0	2.36
54	7/2+	10.534	-3.05	74.8	22	0.1	-3.05	74.8	0	0.001
55	5/2-	10.553	-18.6	-4.39	18.6	0.0000074	-18.6	-4.39	0	0.0000074
56	9/2+	10.69	0.12	-6.94	0.000024	1.63	0.12	-6.94	0.000048	1.63
57	3/2-	10.782	150	-82.1	0.079	192.4	150	-82.1	0.079	0
58	1/2+	10.831	0.000014	107	5.47	43.5	0.000014	107	5.74	0
59	5/2-	10.924	-32.3	10.6	1.35	20.9	-32.3	10.6	1.35	20.9
60	1/2-	11.137	-154	-618.1	-0.89	0.0026	-154	-618.1	0.89	0.0026
61	9/2+	11.078	23.3	71.9	650.6	0.06	23.3	71.9	0.065	0.06
62	1/2-	10.836	29.4	890.4	126.2	10.9	29.4	890.4	126.2	10.9
63	5/2+	11.031	-2.05	33.6	0.00043	13.8	-2.05	33.6	0.00043	13.8
64	9/2-	11.19	56.8	-0.014	0.00076	1133	56.8	-0.014	0.00076	11.33
65	7/2+	11.534	83.9	-0.00000075	144.4	67.4	83.9	-0.00000075	0	67.4
66	7/2+	12.133	384.1	-9.68	275.5	99270	384.1	-9.68	0	992.7
67	5/2+	13.193	191.3	1199	74146	3477	191.3	1199	0	3477
68	3/2+	12.328	461.5	1.24	1.8	39.5	461.5	1.24	1.8	39.5
69	7/2-	15.359	-7980	258.7	809.7	227.7	-7980	258.7	809.7	227.7
70	9/2-	15.437	158.6	-153.9	0.31	7.93	158.6	-153.9	0.31	7.93
71	1/2+	17.209	868.8	1285	23911	823.1	868.8	1285	23911	832.1
72	1/2-	13.686	8166	0	0	2056	8166	0	2056	0
73	3/2-	14.643	18070	605.4	68.7	427.6	18070	605.4	68.7	427.6
74	3/2+	15.691	19.3	24506	2.47	60980	19.3	24506	2.47	60980
75	5/2+	19.359	-65.6	0.12	34.8	12780	-65.6	0.12	34.8	12780
76	5/2-	16.192	-2.1	13748	0	3.31	-2.1	13748	0	3.312
77	7/2-	15.747	97.8	34437	55995	0	97.8	3443.7	559.95	0
78	7/2+	16.442	-836.7	7888	4160	6.45	-836.7	-7888	0	6.45
79	9/2+	20.9	-24220	0	104.2	2714	-2422	0	104.2	2714
80	9/2-	19.068	43242	7.37	2619	6.05	432.42	7.37	26.19	6.05

where E is an incident neutron energy after and E_0 before the correction.

The inelastic neutron scattering data, $^{16}O(n,n'\gamma)^{16}O$, have been included as well. The measurements of Nelson *et al.* [61] cover the energy range from 5.03 to 19.98 MeV at 6 different angles. In this process the second excited state 3^- 6.1299 MeV of the ^{16}O dominates [61]. However, in the R-matrix calculation in [7] the reaction channel populated the first excited state was included, too.

The next channels under consideration are the $^{13}C(^4He,n)^{16}O$ and its inverse reaction $^{16}O(n,$-$^4He)^{13}C$. The datasets for the latter reaction come from three measurements: [62], [63] and [64]. The data published by Seitz *et al.* [62] covers the neutron energy range from 3.6 to 4.2 MeV, while the measurement of Walton *et al.* [63] covers the range from 3.5 to 4.4 MeV. The highest-energy data series for that channel is the one from Davis [64], spanning neutron energies from 5.0 to 8.8 MeV. Of many existing measurement of the ^{13}C(^{4}He,n)^{16}O cross-section the one from Drotleff *et al.* [65] and Harissopulos *et al.* [66] have been chosen. The energies in the data set of Drotleff had to be corrected by a factor of 0.922 in order to be consistant with the data of Shouky *et al.*, as advised in Ref. [7].

Resonance parameters

This section will focus on the published resonance parameters, which may be found in the Table X of Ref. [7]. The table contains the resonance energies, equivalent excitation energies of the ^{17}O, as well as partial widths for the relevant channels.

Now an overview of the parameters used in the *R*-matrix calculation follows. One can start with channel radii: the values of 4.0 fm for the ^{16}O+n channel and 5.2 fm for the ^{13}C+^{4}He channel were used, equivalent to those of Ref. [7]. The decay threshold of the ^{17}O to the ^{4}He channel was 6.3589 MeV and to the n-channel 4.1433 MeV. The reaction channels included are listed in the Eqs. 3.10-3.13. The R-matrix parameters from [7] and the values used for this calculation are listed in the Tabs. 3.3 and 3.4. The changes in the parameter set used in this work were due to the numerical problem the AZURE2 code had with handling some unusually large or small widths. The results of this calculation based on the results published in [7] are displayed on the Figs. 3.18, 3.19, 3.20, 3.21, 3.22, 3.23, 3.24 and 3.25.

The Figures 3.18, 3.19 and 3.20 display the ^{13}C(^{4}He,^{4}He) elastic scattering data measured at multiple angles and energy ranges. The result of the R-matrix calculation fit the data fairly, with discrepancy growing larger once the ^{16}O(n,n$'$) and ^{16}O(n,n$''$) channels open at $E_x(^{17}\mathrm{O}) = 10.193$ MeV and 10.273 MeV, respectively. The elastic-scattering data constrains the cross section up to the $E_x = 11.2$ MeV.

The ^{16}O(n,n) elastic scattering data of Shouky *et al.* is displayed in the Fig. 3.21, while the data-set of Lane *et al.* is displayed in the Fig. 3.22. While the former data-set covers excitation energies up to the $E_x(^{17}\mathrm{O}) = 10$ MeV, the latter covers only the low energy region 4.2 MeV $< E_x(^{17}\mathrm{O}) <$ 5.7 MeV. For some measurements at particular angles and energies the discrepancies between the R-matrix calculation and the measured data is large, but in general one can say that the calculation reproduces the main features of the data.

The ^{16}O(n,n$''$) inelastic scattering data of Nelson *et al.* displayed in the Fig. 3.23 shows significant discrepancies at excitation energies around $E_x(^{17}\mathrm{O}) = 10.5$ MeV. This is due to the changes in the partial widths of the states in this excitation-energy region. The original widths didn't permit the code to run, therefore they were changed. The features at higher energies are not well reproduced by the calculation, but it follows the global trends of the cross-section.

Finally, a few brief remarks on the ^{13}C(^{4}He,n) and ^{16}O(n,^{4}He) total cross section displayed in the Figs. 3.24 and 3.25, respectively. The data are well-reproduced by the R-matrix calculation up to the $E_x(^{17}\mathrm{O}) \approx 9$ MeV. The cross-section at higher energy starts to have a systematic offset in comparison to the data, although it follows a general trend of the cross-section. The source of the offset is most likely the change in parameter values one was forced to make, as was noted earlier.

In conclusion, the R-matrix parameters published by Heil *et al.* [7] had to be slightly modified in order for the AZURE2 code to run. Despite the complexity of the ^{17}O spectra and the number of resonances involved, the result of the calculation presented here still describes the available data reasonably well at excitation energies typically lower than $E_x(^{17}\mathrm{O}) = 10$ MeV.

That said, the aforesaid R-matrix calculation can be compared to the data from this work. The result of the calculation is convoluted with the experimental resolution that is due to the energy-loss and angular straggling in the gas-target window foil and the gas target.

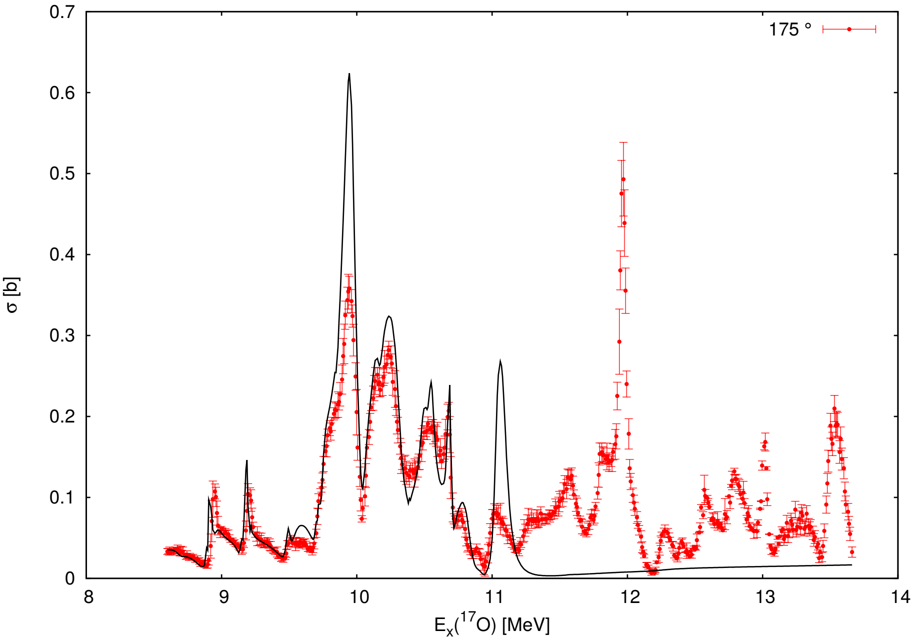

Figure 3.17: The cross section of the ^{4}He(^{13}C,^{4}He) elastic scattering data from this work (red points) together with the result of the previous R-matrix calculation (black line). See text for details.

The data from this experiment and the R-matrix calculation for the corresponding angle are displayed in the Fig. 3.17. The most striking feature is the overshoot of the $E_x(^{17}\mathrm{O})$ =9.95 MeV peak, which is getting larger with angle (see Fig. 3.19). A similar observation can be made for the $E_x(^{17}\mathrm{O}) = 11$ MeV peak: the calculated cross-section is larger than the measured one for other, smaller angles as well. The results of the calculation correspond to rest of the peaks. The lowest two peaks have a systematic shift in their position, as was noted earlier. If it wasn't for the shift, the calculation and the measured points would fit nicely. The R-matrix calculation follows the trend of the measured cross-section for the peaks in the energy region $10 < E_x(^{17}\mathrm{O}) < 11$ MeV. However, a small peak at $E_x(^{17}\mathrm{O}) \approx 10.9$ MeV is not reproduced by the calculation. Above the $E_x(^{17}\mathrm{O}) = 11$ MeV the shape of the calculated cross-section is due to the background resonances present at higher excitation energies.

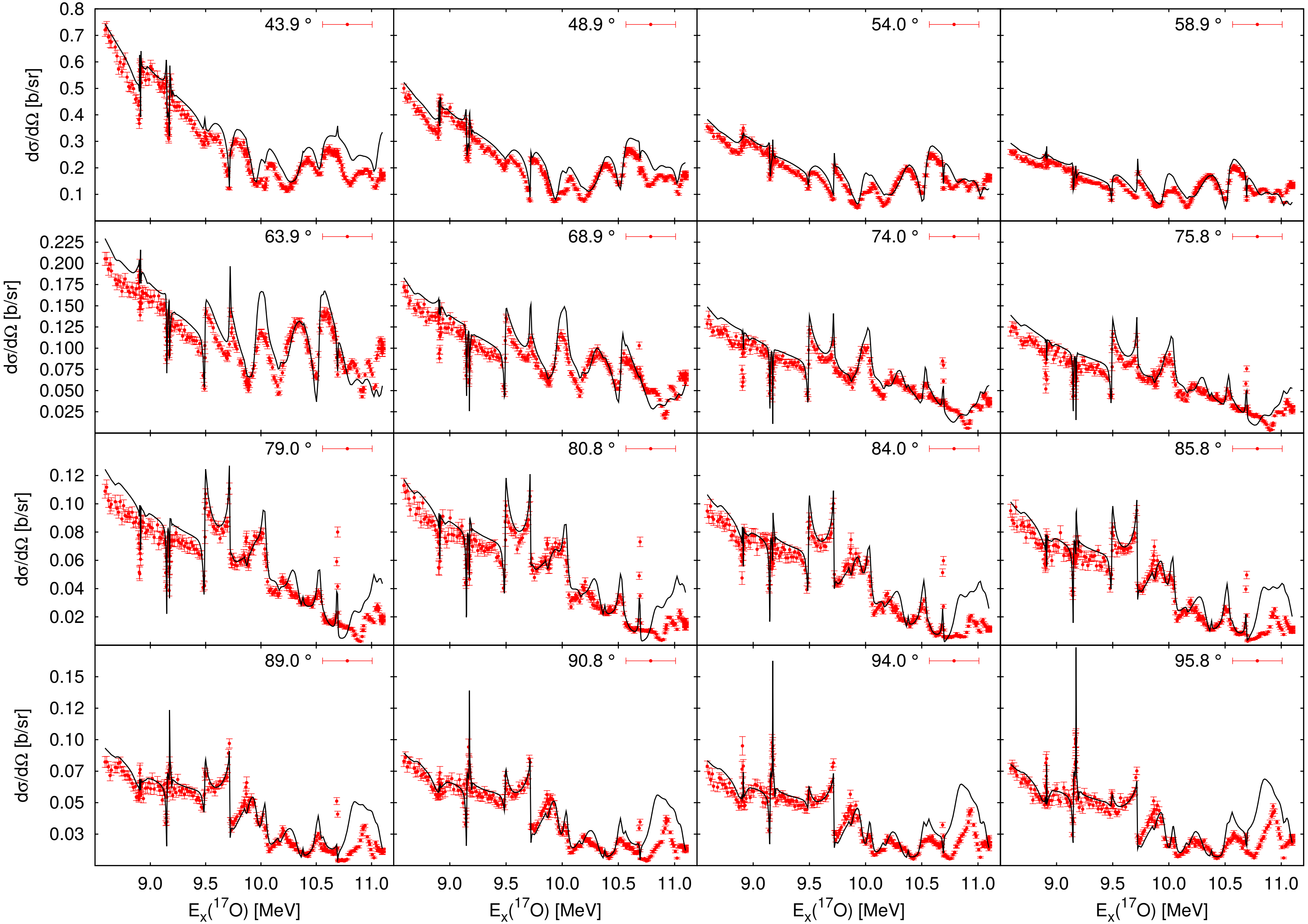

Figure 3.18: The ^{13}C(^{4}He,^{4}He) elastic scattering data of M. Heil *et al.* [7] for angles between 44.9° and 95.8° (red dots) and the result of a R-matrix calculation (black line). The scale on the leftmost plot is valid for an entire row. See text for details.

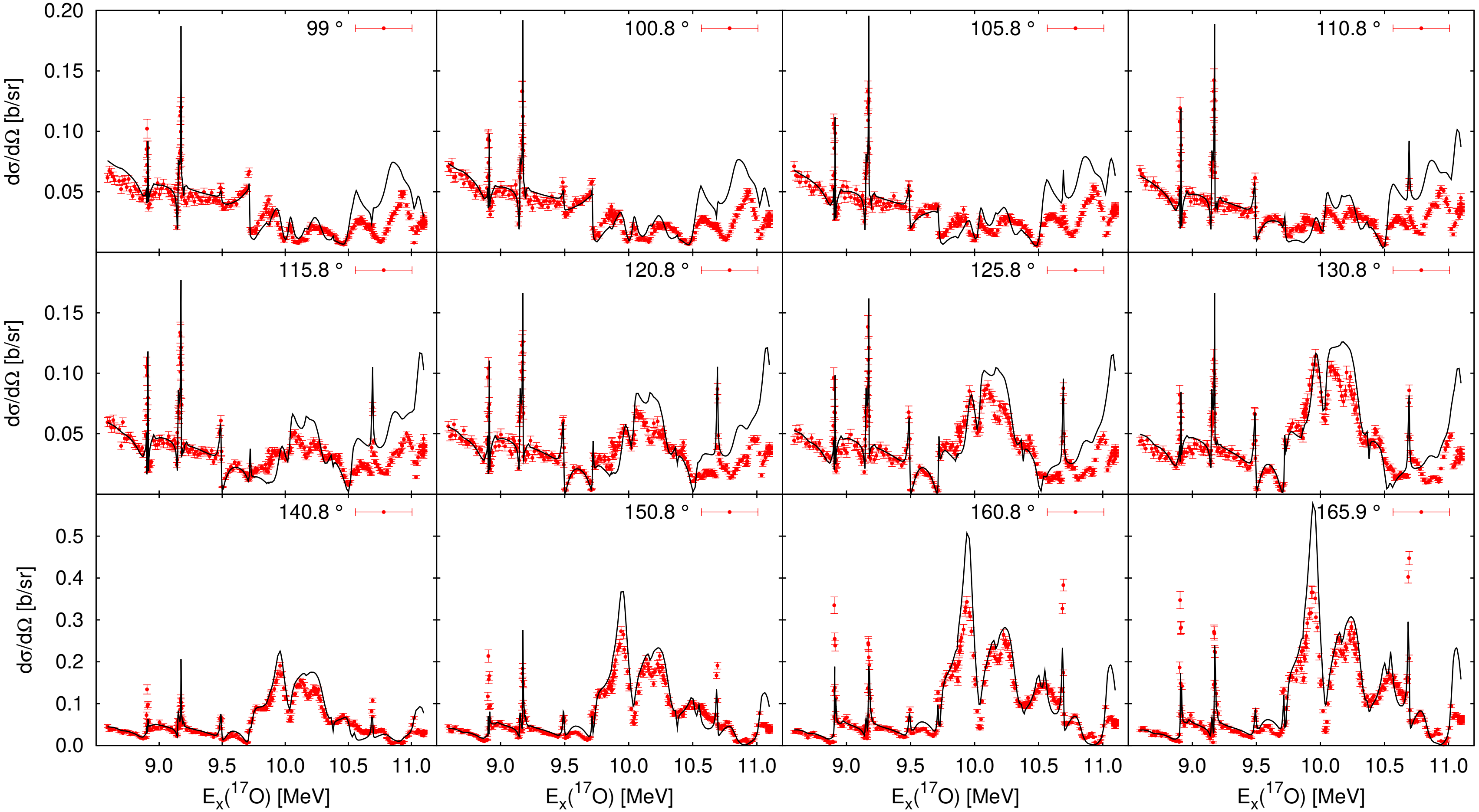

Figure 3.19: The ^{13}C(^{4}He,^{4}He) elastic scattering data of M. Heil *et al.* [7] for angles between 99° and 165.9° (red dots) and the result of a R-matrix calculation (black line). The scale on the leftmost plot is valid for an entire row. See text for details.

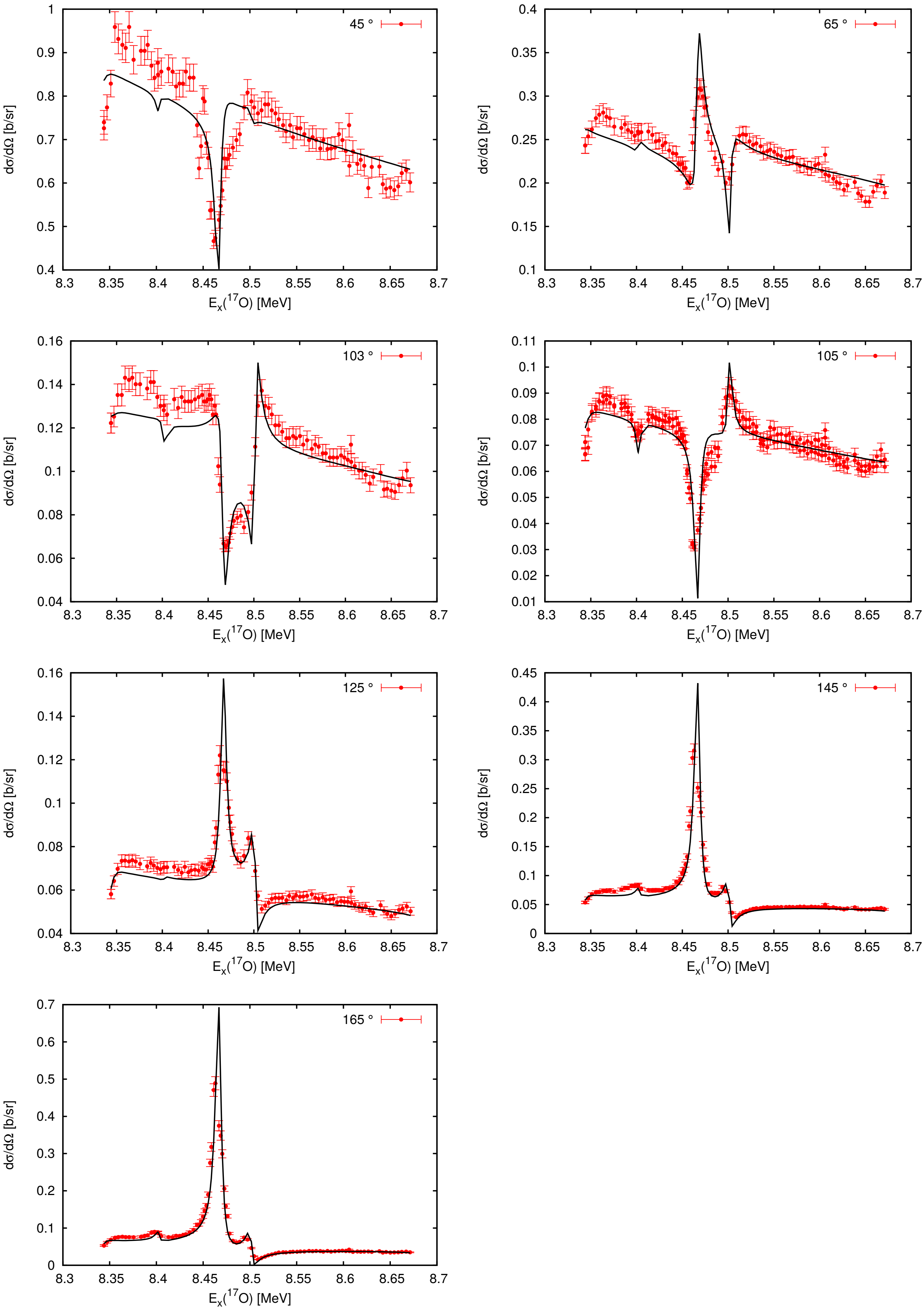

Figure 3.20: The ^{13}C(^{4}He,^{4}He) low–energy elastic scattering data of M. Heil *et al.* [7] for various angles (red dots) and the result of a R-matrix calculation (black line). See text for details.

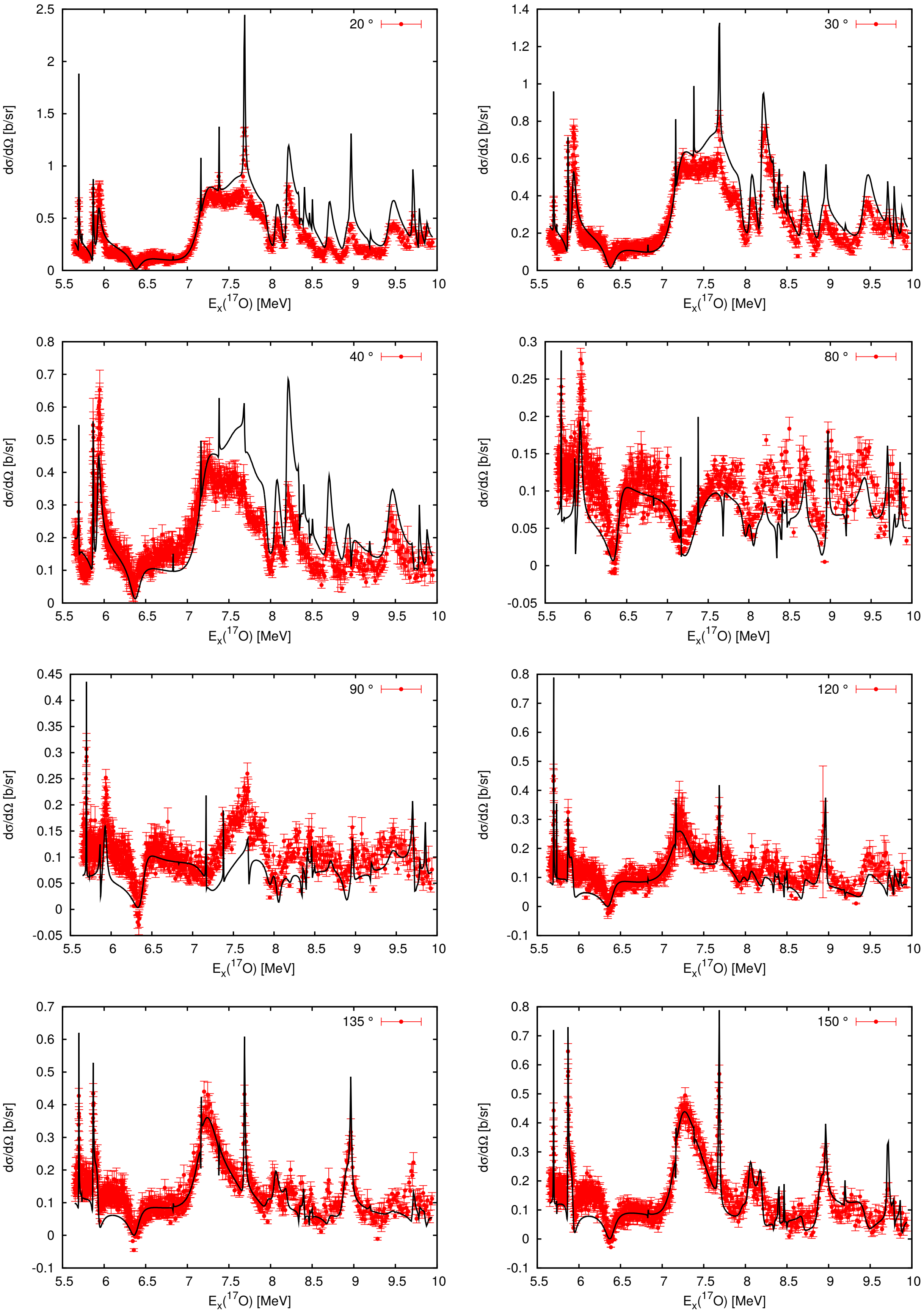

Figure 3.21: The ^{16}O(n,n) elastic scattering data of Shouky *et al.* [58] for various angles (red dots) and the result of a R-matrix calculation (black line). See text for details.

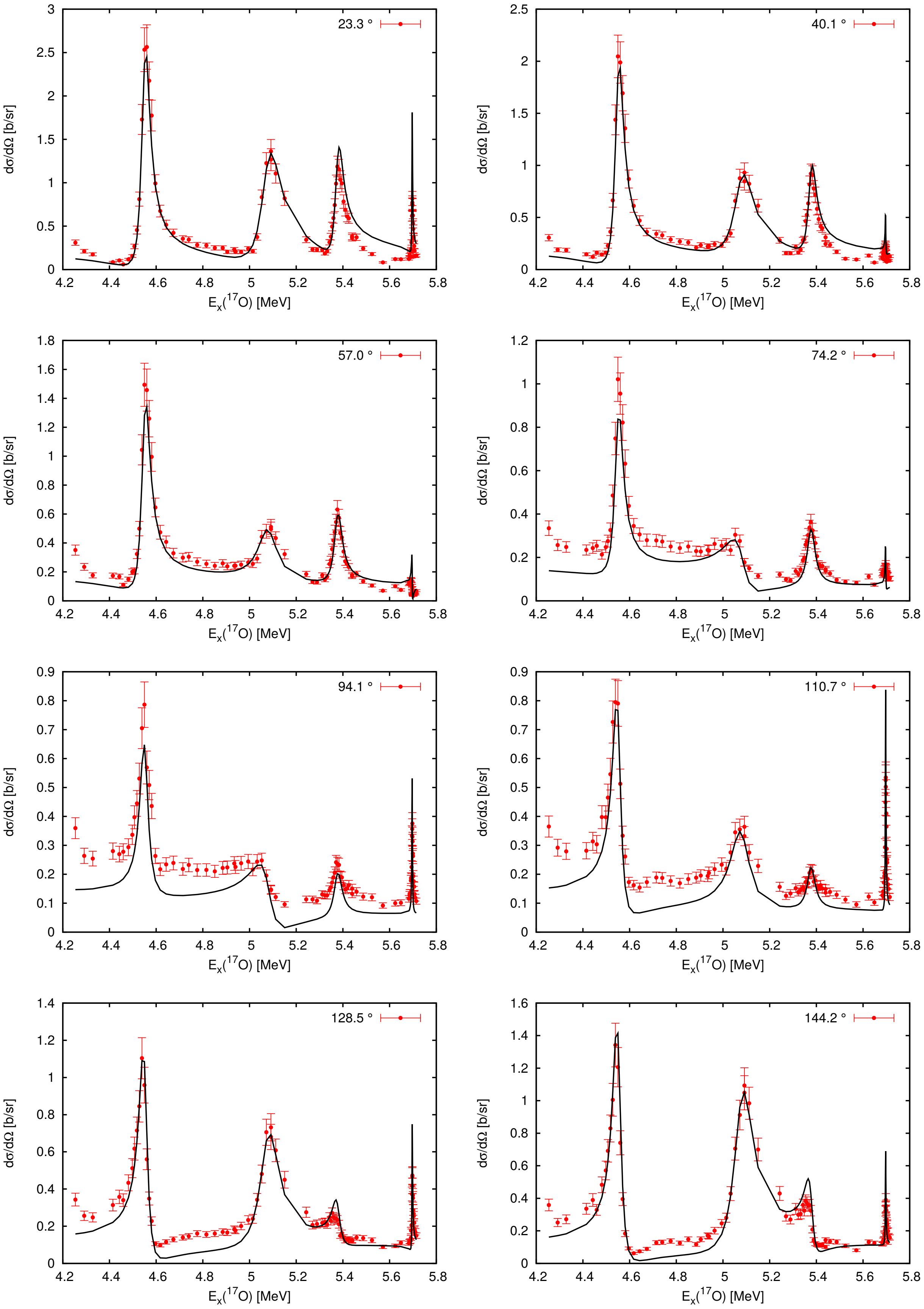

Figure 3.22: The ^{16}O(n,n) elastic scattering data of Lane *et al.* [59] for various angles (red dots) and the result of a R-matrix calculation (black line). See text for details.

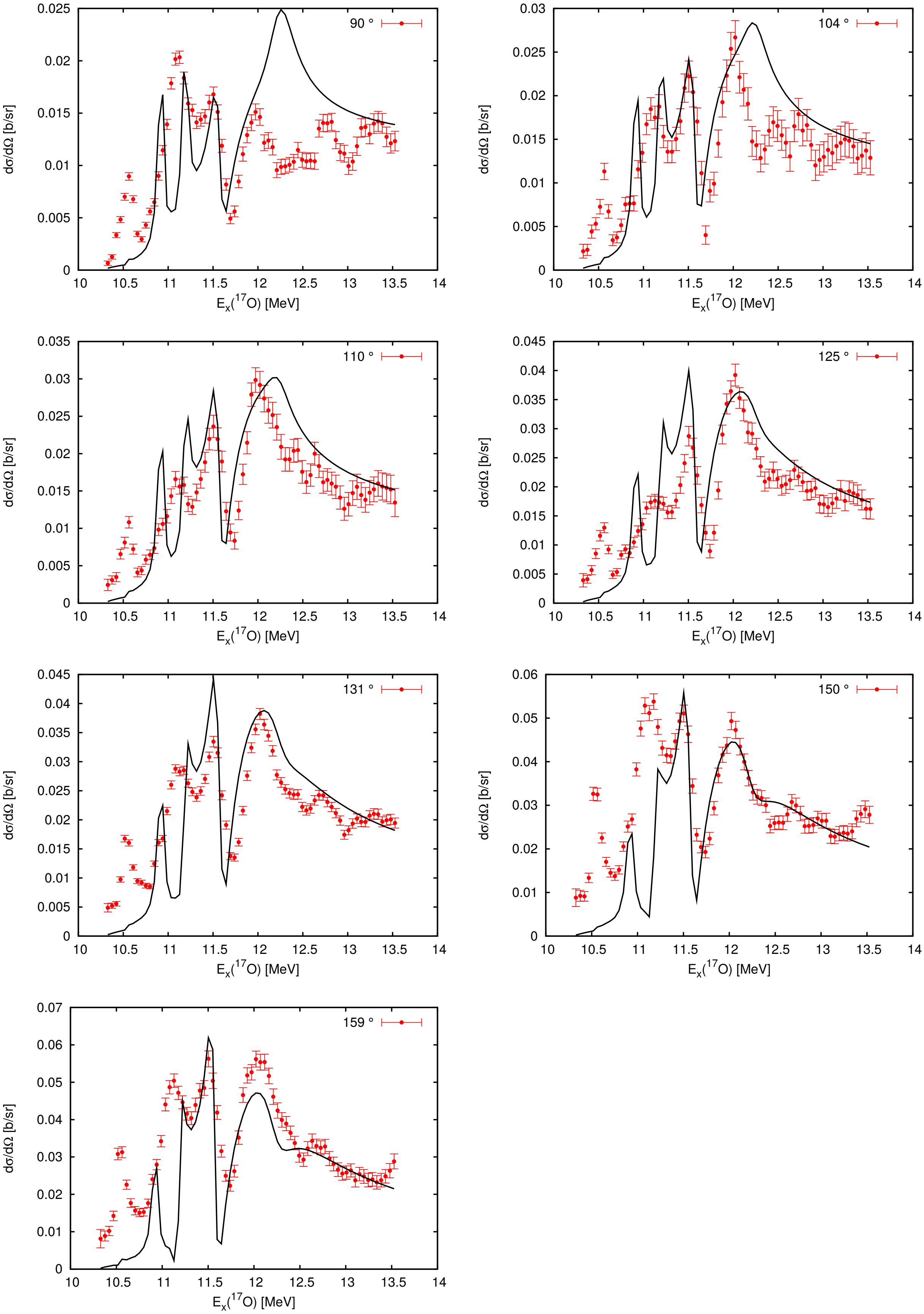

Figure 3.23: The cross section of the ^{16}O(n,n$''$) reaction from Nelson *et al.* [61] (red points) together with the result of a R-matrix calculation (black line). See text for details.

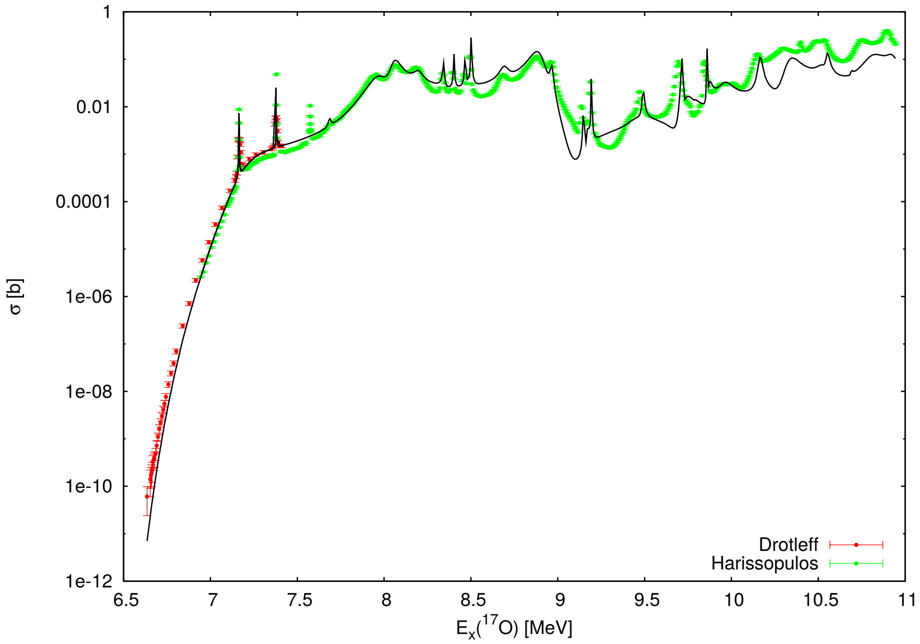

Figure 3.24: The cross section of the ^{13}C(^{4}He,n) reaction from Drotleff *et al.* [65] (red points) and Harissopulos *et al.* [66] (green points), together with the result of a R-matrix calculation (black line). See text for details.

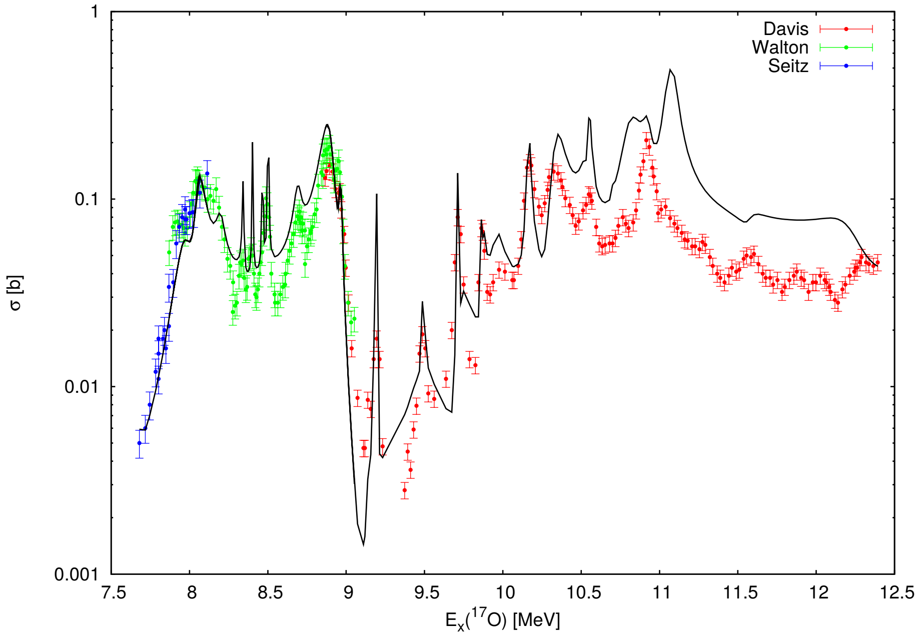

Figure 3.25: The cross section of the ^{16}O(n,^{4}He) reaction from Davis *et al.* [64] (red points), Walton *et al.* [63] (green points) and Setiz *et al.* [62] (blue points) together with the result of a R-matrix calculation (black line). See text for details.

3.3.4 Qualitative description of quasi-isolated resonances

While full multi-channel R-matrix fit to an abundant set of experimental data for all the relevant channels provides the best tool for unambiguous assignment of resonance properties, the scarcity of the data currently available doesn't allow us to perform it for $E_x(^{17}\mathrm{O}) \geq 11.1$ MeV. The fit of the full multi-channel R-matrix to the elastic scattering cross-section measured at only one angle, constrained only by some data for the ^{16}O+n$''$ reaction channel would be highly ambiguous.

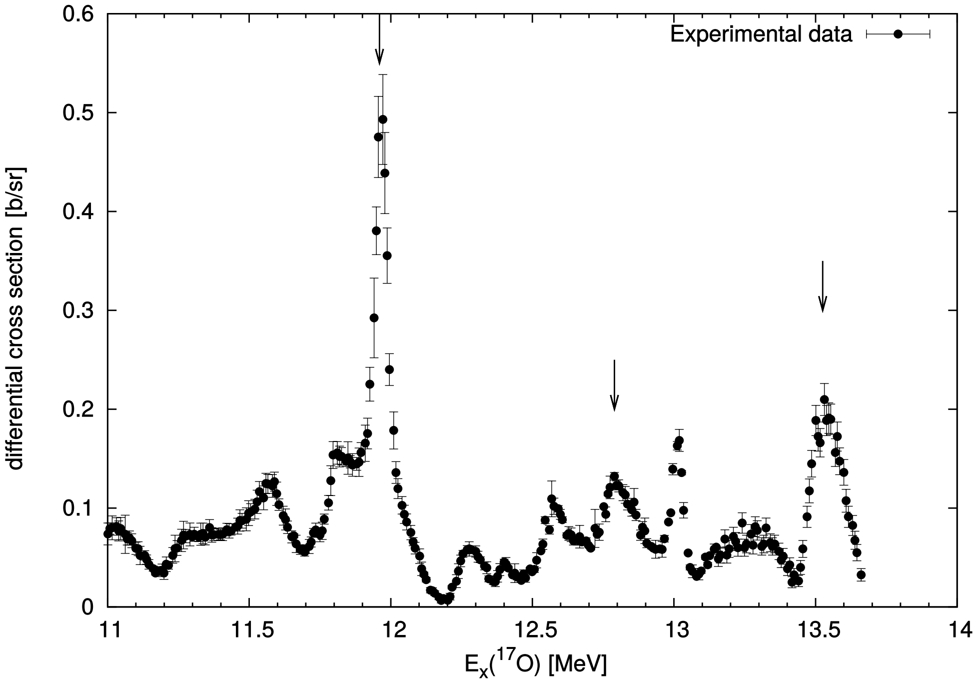

Figure 3.26: Resonant elastic cross-section for ^{17}O excitation energies higher than 11.0 MeV. Peaks of interest are labelled with an arrow.

However, the upper part of the spectrum has several resonances resembling the usual Breit-Wigner shape of a quasi-isolated resonance (see Fig. 3.26). Therefore, it was decided to use a simplified approach which should give us an estimate of spin and width necessary to reproduce the shape of the resonance in question.

Simplified method for reproducing the cross-section and the shape of a quasi-isolated resonance

The simplified method used is based on a calculation performed using the R-matrix code AZURE2 [49]. The simplification is due to removal of all but a single channel (elastic ^{13}C+^{4}He), a single resonance and a single data segment (our measurement of an excitation function). The calculation is a fit of this simplified model to a very narrow area comprising the peak of interest, aiming to reproduce the amplitude and the width of the peak. No background resonances nor hard-sphere scattering are included. The experimental resolution of 0.030 MeV is taken into account. The calculation is performed for all spin and parity combinations typically up to $\frac{13}{2}^{\pm}$.

The best fit is a particular spin and parity combination with the lowest $\chi^2/_N$, where N is the number of experimental points in the data range of the fit. For the best fit reduced width of the state γ^2 were compared to the Wigner limit [46], defined as:

$$\gamma_W^2 = \frac{3\hbar^2}{2\mu a^2}, \tag{3.15}$$

where μ is a reduced mass of the reaction channel and a is the channel radius. The Wigner limit for elastic ^{13}C+^{4}He channel, given the channel radius $a = 5.2\,\text{fm}$, is:

$$\gamma_W^2 = 0.75773\,\text{MeV}. \tag{3.16}$$

A reduced width γ^2 can be compared to the reduced width at Wigner limit γ_W^2. Such a ratio is analogous to a spectroscopic factor, although a spectroscopic factor contains a volume integral, contrary to the reduced width which depends only on surface properties of the resonance [46]. The Wigner ratio for a given channel, defined as:

$$\theta_W^2 = \frac{\gamma^2}{\gamma_W^2}, \tag{3.17}$$

can be used to gain some insight in the structure of particular resonance. For a Wigner ratio of the order of magnitude of unity, one may conclude that the structure of the resonance is predominantly the structure of the reaction channel in question. Therefore, in this case a value of Wigner ratio of the order of magnitude of unity can indicate α-cluster structure.

Testing the simplified method: known resonances at 8.9 and 9.2 MeV

Having described the method, next it will be shown how it performs on two resonances properties of which are already known. The two resonances in question are the $E_x(^{17}\text{O}) = 8.9$ MeV and the 9.2 MeV resonances (see Fig. 3.27), which are quite narrow and pronounced at high angles[*] (that features are more obvious in the M. Heil's dataset due to higher resolution [7]).

---

[*] If not stated otherwise, angles and cross-section of an experimental data are in the laboratory frame of reference, always in the direct kinematics. This is the convention for the AZURE2 data input.

These two states were identified as candidates for a parity-split rotational band in the ^{17}O analogous to the rotational band in the ^{16}O with band-head 6.05 MeV 0^+ state [6]. The pair of resonances would correspond to a structure analogous to the third member of the rotational band in the ^{16}O.

Spins, parities and partial widths of those two resonances were determined by a multi-channel R-matrix fit to an extensive set of data points in all the relevant channels [7] and are given in the Table 3.5. The two resonances in the data have a slight systematic shift of several tens of keV to higher energies in comparison to the published data. However, that does not influence the principal results of the simplified analysis.

Table 3.5: Parameters of the 8.9 and 9.2 MeV resonances, adopted from [7].

J^π	$E_x(^{17}\mathrm{O})$ [MeV]	Γ_n [keV]	Γ_α [keV]
$\frac{9}{2}^-$	8.9029	$-2.3 \cdot 10^{-5}$	-0.45
$\frac{7}{2}^-$	9.1737	0.038	3.26

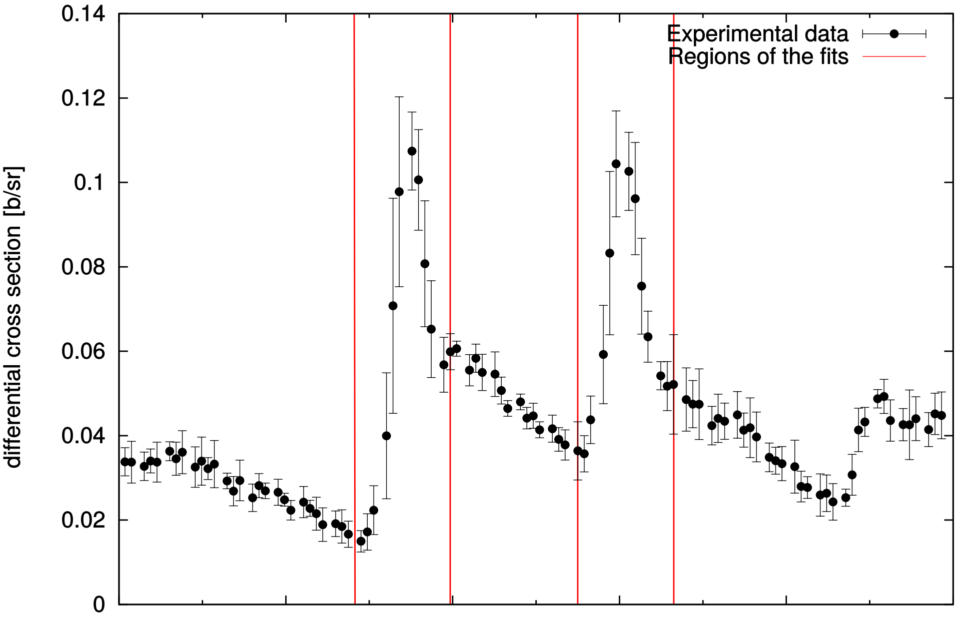

Figure 3.27: A range of the experimental data with the two peaks of interest.

The results for different spins and parities can be seen in Fig. 3.28 and 3.29 for the 8.9 MeV and 9.2 MeV resonance, respectively.

It is clear that both $\frac{9}{2}^-$ and $\frac{7}{2}^-$ assignment reproduce the shape and the height of the peak for both resonances (see Table 3.6). For those spins and parities the Wigner ratios were calculated.

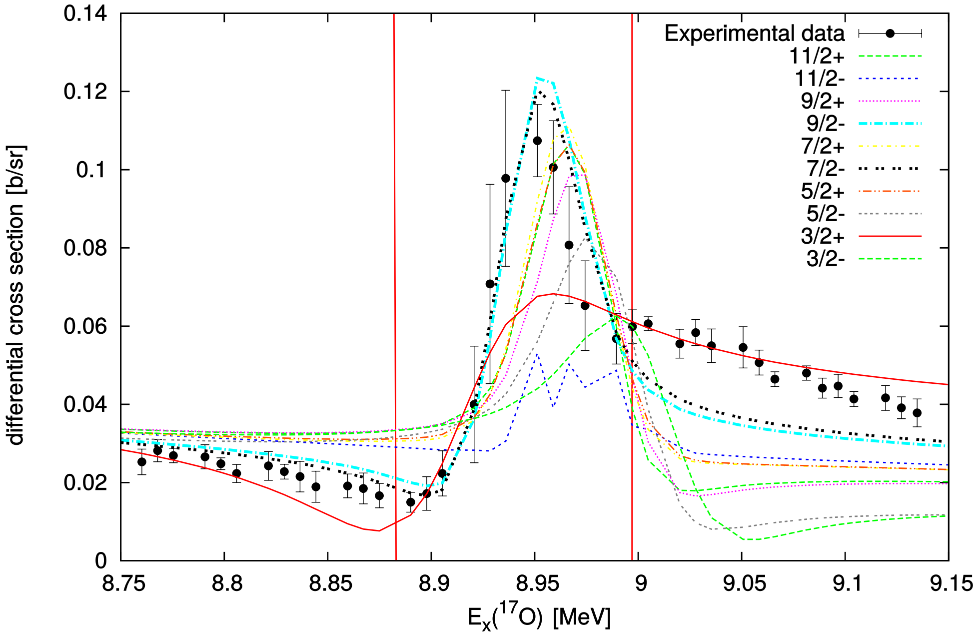

Figure 3.28: Different spin and parity combinations for the peak at 8.9 MeV using the simple method. The best results are obtained for $\frac{9}{2}^{-}$ and $\frac{7}{2}^{-}$. See text for details.

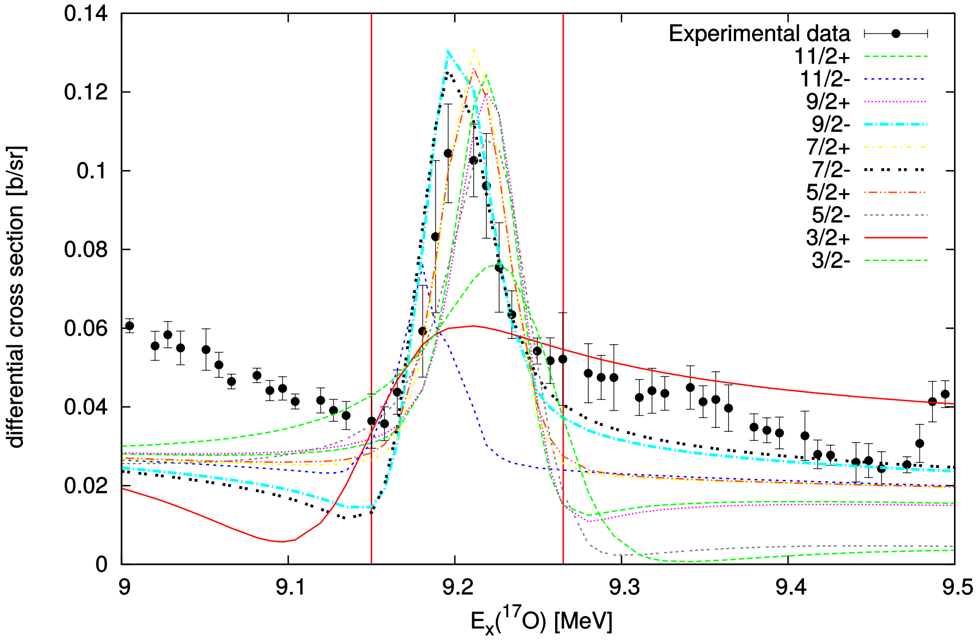

Figure 3.29: Different spin and parity combinations for the peak at 9.2 MeV using a single resonance without a background. The best results are obtained for $\frac{9}{2}^{-}$ and $\frac{7}{2}^{-}$. See text for details.

Values are presented in the Table 3.7. Wigner ratios have elevated values and that would indicate the presence of the α-cluster structure in both resonances.

In conclusion, for the two resonances of known spins and parities it has been shown that the simplified approach can yield meaningful, although not unambiguous, spins, parities and Wigner ratios. Therefore, this method was applied to other resonances for which no previously published spin and parity assignments were available.

Table 3.6: Parameters of the different spin and parity assignments for the peaks at 8.9 and 9.2 MeV, using the simplified approach (see text for details).

	Peak			
	8.9 MeV $[\frac{9}{2}^-]$		9.2 MeV $[\frac{7}{2}^-]$	
J^π	χ^2/N	γ [MeV$^{1/2}$]	χ^2/N	γ [MeV$^{1/2}$]
$\frac{11}{2}^+$	8.65641	-1.404870	2.95058	0.964883
$\frac{11}{2}^-$	13.0693	-212.654605	18.6507	162.350195
$\frac{9}{2}^+$	9.11249	-1.935581	2.91617	1.272125
$\frac{9}{2}^-$	1.55404	-0.482501	1.28492	0.408232
$\frac{7}{2}^+$	6.16731	-0.168826	1.93572	0.157728
$\frac{7}{2}^-$	1.04387	-0.632510	0.990402	0.538238
$\frac{5}{2}^+$	6.71016	-0.212625	1.50089	0.204560
$\frac{5}{2}^-$	9.47957	-0.160051	2.25899	0.181818
$\frac{3}{2}^+$	3.12034	-0.247186	3.82303	0.263506
$\frac{3}{2}^-$	12.9061	-0.215961	2.98269	0.286342
$\frac{1}{2}^+$	12.6808	-0.253529		
$\frac{1}{2}^-$	3.90002	-0.202500		

Table 3.7: Wigner ratios for the most probable spin/parity assignments for 8.9 and 9.2 MeV peaks, using the simplified approach (see text for details).

	Peak			
	8.9 MeV		9.2 MeV	
J^π	γ [MeV$^{1/2}$]	θ_W^2	γ [MeV$^{1/2}$]	θ_W^2
$\frac{9}{2}^-$	-0.482501	0.307	0.408232	0.220
$\frac{7}{2}^-$	-0.632510	0.528	0.538238	0.382

Quasi-isolated peaks in the resonant elastic excitation function at ^{17}O excitation energies higher than 11.0 MeV

Our excitation function measurement provides the differential cross-section for the ^{13}C+^{4}He elastic scattering at ^{17}O excitation energies higher than 11.1 MeV for the first time. The peaks which could be studied using the simplified method are shown in the Fig. 3.26. They were selected by shape, choosing those which most closely resemble the Breit-Wigner shape, characteristic for a quasi-isolated resonance. In this part the estimates of spins and parities for selected peaks will be presented, as well as Wigner ratios, in this case indicative of α-clustering.

Let us start with the strongest of the peaks, at $E_x(^{17}\mathrm{O}) \approxeq 12.0\,\mathrm{MeV}$ (Fig. 3.30). Red vertical lines represent the range on which the simplified method was used. It is clear that a resonance in question lies on broad background, which one cannot account for in this simplified model. However, one can still show that the best shape and amplitude of the peak are given by assuming spin and parity equal to $\frac{13}{2}^-$ or $\frac{11}{2}^+$. For a complete list, consult Tab. 3.8. If the Wigner ratio is computed for the $\frac{13}{2}^-$ and $\frac{11}{2}^+$ fits, one gets the values of 0.925 and 0.153, respectively (as listed in Tab. 3.9). One may conclude that if $\frac{13}{2}^-$ is the real spin and parity of this resonance, there is a high probability that it has an α-cluster structure.

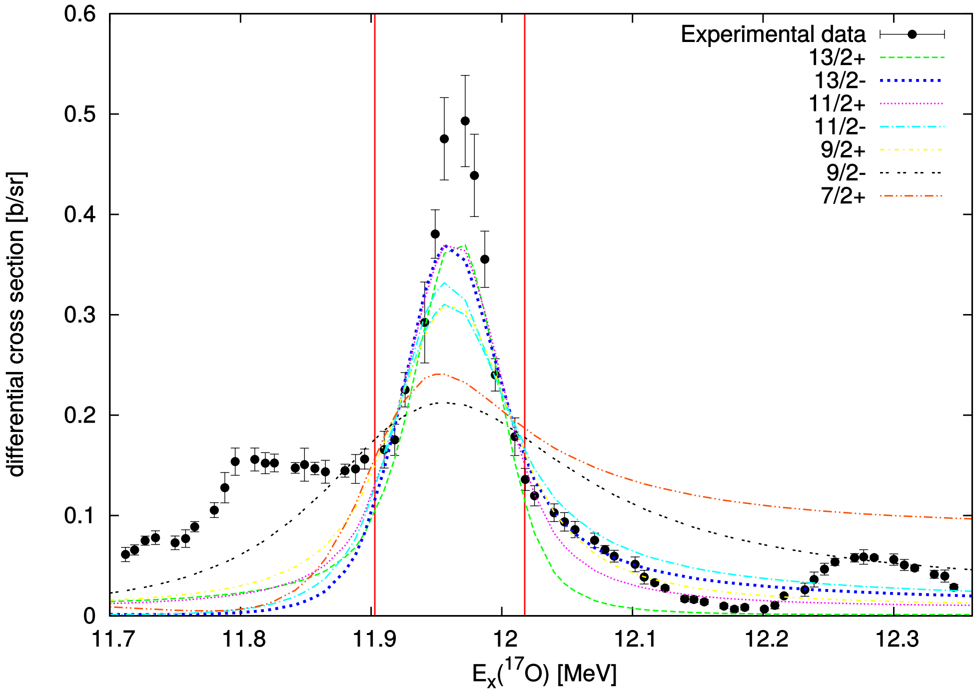

Figure 3.30: Different spin and parity combinations for the peak at 12.0 MeV using a single resonance without a background. The calculation reproduces measured results for $\frac{13}{2}^-$ and $\frac{11}{2}^+$. See text for details.

The next resonance of interest is located at the excitation energy of 12.8 MeV (Fig. 3.31). The simplified procedure suggests that the most adequate spin and parity for this resonance is $\frac{7}{2}^-$. Both the Fig. 3.31 and the Table 3.8 confirm that within the simplified model other spins and parities cannot reproduce the cross-section at the peak energy. The Wigner ratio for the $\frac{7}{2}^-$ resonance is 0.107 (see Tab. 3.9), not suggesting a significant α-cluster structure.

Finally the simplified method is used on a peak of interest at the excitation energy of 13.6 MeV (Fig. 3.32). The spin and parity which gives the best agreement is $\frac{11}{2}^-$, as can be verified in the Tab. 3.8. The Wigner ratio for the $\frac{11}{2}^-$ equals 0.246. The α-clustering might contribute to structure of this resonance.

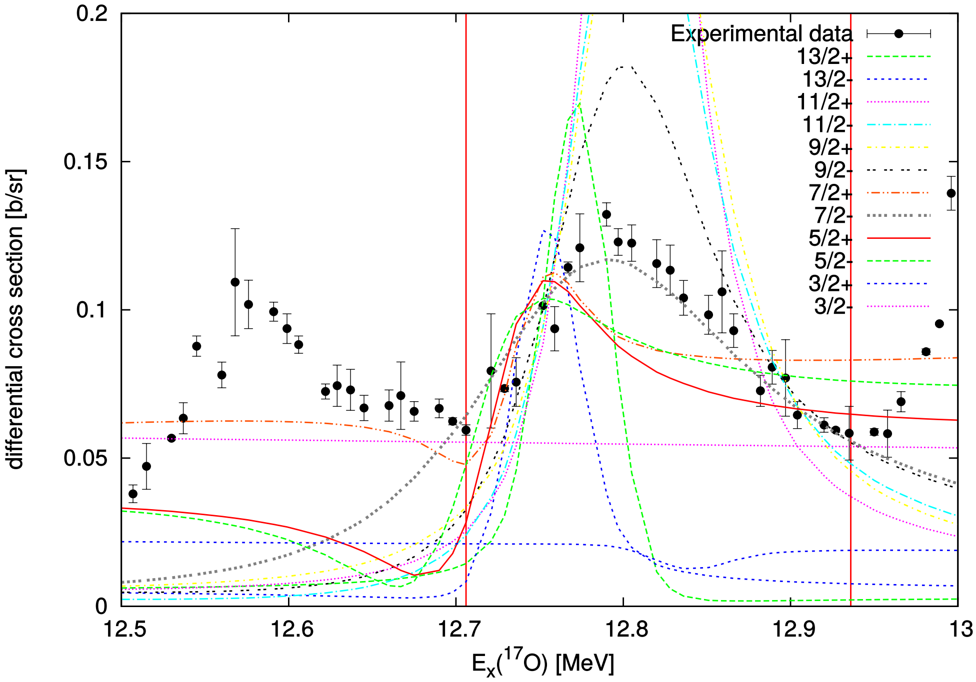

Figure 3.31: Different spin and parity combinations for the peak at 12.8 MeV using a single resonance without a background. The best correspondence is given by the spin and parity $\frac{7}{2}^{-}$. See text for details.

In conclusion, in several of these cases the interference of the resonance in question with the rest of the resonances is clear and for a more accurate description should be taken into account.

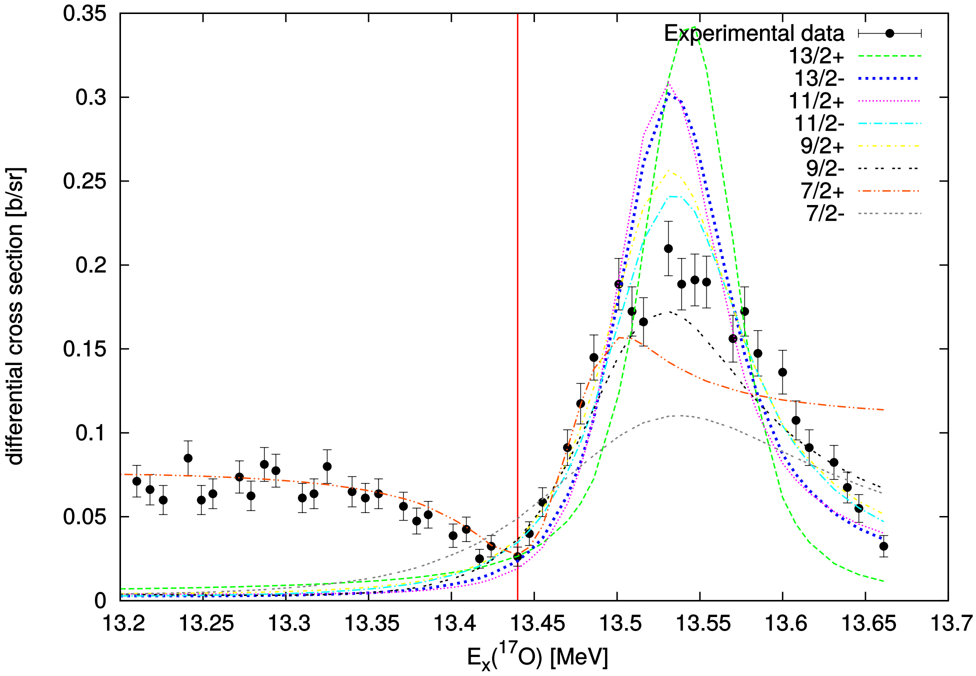

Figure 3.32: Different spin and parity combinations for the peak at 13.6 MeV using a single resonance without a background. The best shape and height of the peak is obtained for $\frac{11}{2}^{-}$. See text for details.

Table 3.8: Parameters of the best spin and parity for 12.0, 12.8 and 13.6 MeV peaks, using a simplified approach (see text for details).

	Peak					
	12.0 MeV		12.8 MeV		13.6 MeV	
J^π	${}^{\chi^2}/_{N}$	γ [MeV$^{1/2}$]	${}^{\chi^2}/_{N}$	γ [MeV$^{1/2}$]	${}^{\chi^2}/_{N}$	γ [MeV$^{1/2}$]
$\frac{13}{2}^+$			428.617	0.517172	17.9721	0.667088
$\frac{13}{2}^-$	3.12968	0.837051	372.585	0.199723	7.36744	0.350776
$\frac{11}{2}^+$	2.59072	0.339962	328.839	0.230919	8.26138	0.178544
$\frac{11}{2}^-$	6.81245	1.109264	162.386	0.574408	2.21011	0.431423
$\frac{9}{2}^+$	6.36477	0.421823	164.390	0.275639	3.00843	0.226650
$\frac{9}{2}^-$	18.4310	0.392261	37.3537	0.204215	4.55181	0.184001
$\frac{7}{2}^+$	15.6882	0.202575	56.7758	0.045765	15.3131	0.081095
$\frac{7}{2}^-$			6.68953	0.284347	15.5934	0.243196
$\frac{5}{2}^+$			25.802	0.102604		
$\frac{5}{2}^-$			42.851	0.105805		
$\frac{3}{2}^+$			5844.3	0.053220		
$\frac{3}{2}^-$			1889.45	0.674754		

Table 3.9: Wigner ratios for the most probable spin/parity assignments for 12.0, 12.8 and 13.6 MeV peaks, using a simplified approach (see text for details).

Peak								
12.0 MeV			12.8 MeV			13.6 MeV		
J^π	γ [MeV$^{1/2}$]	θ_W^2	J^π	γ [MeV$^{1/2}$]	θ_W^2	J^π	γ [MeV$^{1/2}$]	θ_W^2
$\frac{11}{2}^+$	0.339962	0.153	$\frac{7}{2}^-$	0.284347	0.107	$\frac{11}{2}^-$	0.431423	0.246
$\frac{13}{2}^-$	0.837051	0.925						

Chapter 4

Reactions of the ^{13}C beam on the ^{9}Be target

The goal of this measurement was to study excited states of the ^{17}O and the ^{18}O decaying to the ^{4}He channel, and search for excited states of the ^{18}O decaying to the ^{6}He and ^{8}Be channels.

Due to the structure of the ^{9}Be target nucleus, an α-particle, ^{5}He or n+^{4}He pick-up reactions are likely to occur at 72 MeV beam-energy. This particular choice of beam and target was proved to be a sound choice for study of α-clustering states in the ^{17}O [6]. The excited states of the ^{18}O nucleus were not populated so strongly as for the ^{17}O case [67], but nevertheless strongly enough that a decent level of statistic for the reactions could be obtained with the setup.

The data on the excited states of ^{17,18}O are obtained using the resonant particle spectroscopy method. The method relies on a coincident detection of $n-1$ reaction products for exit channel with n particles (their energy, angle, mass number A and atomic number Z), identifying particular reaction channel and the details of the intermediate states of the ^{17,18}O as well as other nuclei through which reactions can proceed (e.g. ^{12,14}C). The excitation energy spectra of oxygen isotopes obtained from the different reaction channels are compared.

Although the majority of the data presented in this chapter could be corrected for efficiency, the channels for which peculiar event-selection criteria were used are an exception: the ^{12}C+^{6}He+^{4}He and the ^{10}Be+^{8}Be$_{gs}$+^{4}He reaction channels presented in Sections 4.3.3 and 4.3.4.

The setup of this experiment and the measurement itself were quite demanding because of a short time available to prepare for the measurement and the unexpected problems with collimation and accelerator. The scattering chamber used was shipped to the laboratory shortly before the measurement and had to be complemented with custom-made mounting elements to accommodate the detector mounts. Even so, only coarse angular calibration could be performed. The beam-collimation issues influenced the particle-identification spectra of the detector telescope T2 the most. At the end of the experiment the necessary beam-time has not been delivered, therefore a continuation of measurement has been performed after a one-week brake. Overall, the aforementioned challenges made the calibration data available at the end of the experiment limited, especially for the back-angle detector telescopes T5 and T6. However, with the generous help of the Tandem staff at IPN Orsay and colleagues and collaborators, this experiment gathered fair amount of interesting data that is presented in this chapter.

4.1 Experimental setup

4.1.1 Accelerator facility

The experiment was performed at the IPN Orsay Tandem accelerator facility in October 2012, using a large-area segmented silicon detector array. The accelerator facility at the Institut de Physique Nucléaire d'Orsay, France, consists of a 15 MV MP Tandem accelerator providing stable beams and a 50 MeV linear electron accelerator, used for production of exotic species by photo-fission [68] (see Fig. 4.1). The beam for this experiment was provided by the Tandem accelerator. The beam was produced from the isotopically enriched ^{13}C target. Negative ^{13}C^{-} ions were accelerated to the accelerator terminal charged to positive potential up to 15 MV. Inside the terminal electrons were stripped and the ^{13}C^{4+} ion was accelerated from the accelerator terminal to the analysing magnet. The analysing magnet is a dipole magnet that bends the beam 90°. The set of slits on the entrance and the exit from the magnet provide efficient means to select only ions with the desired energy. Further on the beam is fed to the particular beam-line using the switching magnet. The quadrupole magnets were used to focus the beam, while the fine adjustments of the beam were performed using the steering magnets. Typical beam intensities delivered on target were 1-4 enA, corresponding to 0.25-1.0 pnA.

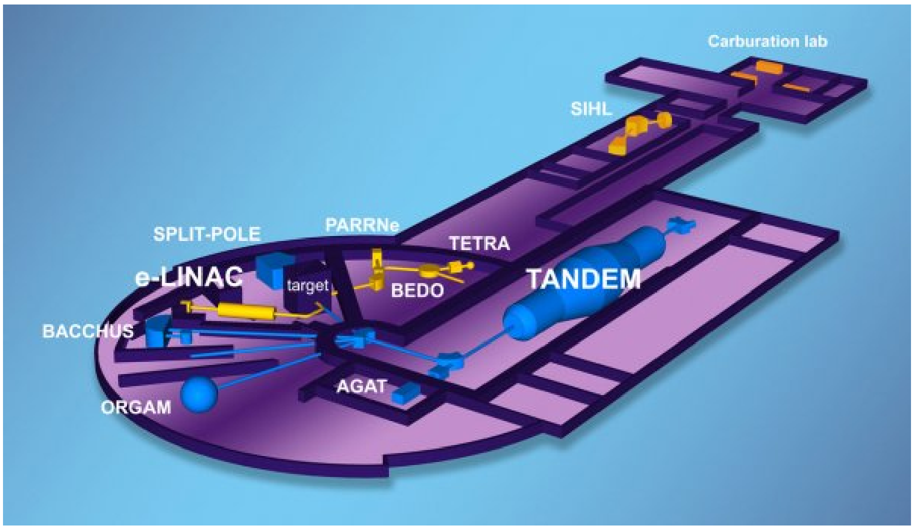

Figure 4.1: The schematics of the IPN-Orsay accelerator facility in Orsay, France.

4.1.2 Scattering chamber and detector setup

For the needs of this experiment a scattering chamber previously used with the DEMON detector setup was shipped from the GANIL in Caen to the IPN-Orsay and mounted at the 410 beam line. The detector setup consisted of six silicon detector telescopes (see Figs. 4.2 and 4.3).

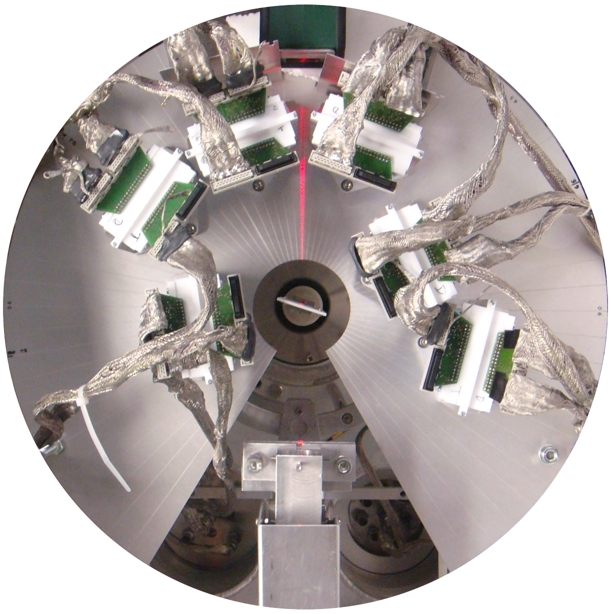

Figure 4.2: The detector setup, bird's-eye view. The $\vartheta = 0^\circ$ angle is located at the top of the figure. The beam direction is from the bottom to the top. Consult the Fig. 4.3 for the naming convention and the detector angles.

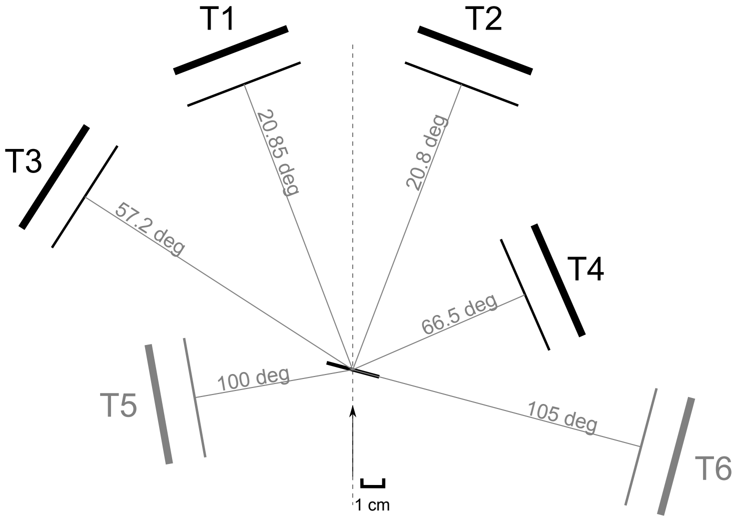

Figure 4.3: The sketch of the detector setup. Thick black line denotes the 1000 μm-thick E detectors and the thin line 20μm-thick ΔE detectors. The target was tilted by 15°. Angles correspond to the centres of the detectors. The detectors which could not be used in the data analysis are presented in grey. See text for details.

Each detector telescope consisted of a 20 μm thick single-sided silicon strip detector (SSSD) and a 1000 μm thick double-sided silicon strip detector (DSSSD), both measuring 50×50 mm^2 and manufactured by Micron Semiconductor Ltd. The choice of the 20 μm thin detectors was crucial for the identification of a broad range of isotopes (from helium to carbon) while at the same time posing a challenge for the calibration due to the prominent non-uniformity of the detector thickness. Each pair of thick and thin detectors was mounted on the common plastic frame, removable from the detector mount, forming one particle detector telescope (Fig. 4.4). Both front and back detectors were subtended only by the Mesytec type W detector adapter. Detector mounts were fixed to the base-plate, which was in turn mounted on the three arms inside the chamber. The mounting holes of the base-plate were placed at 120°, guaranteeing the proper centring of the base-plate. Its hight was adjusted at the 0° using the detector mount and the theodolite mounted at the end of the beam-line, while maintaining the plate in the horizontal position. The angular scale carved in the base-plate helped to mount the detector telescopes at the proper positions.

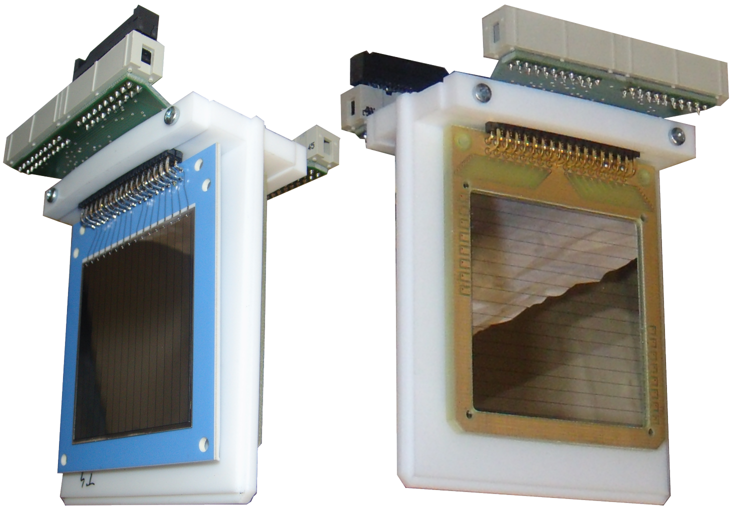

Figure 4.4: The detector telescope mounted on the plastic frame. The frame is inserted in the detector mount which is fixed on the base-plate. **Left:** The front side with the 20 μm thick SSSSD on a ceramic frame, 16 vertical strips clearly visible. **Right:** The back side of the 1000 μm thick DSSSD, showing 16 horizontal strips.

Detector telescopes were arranged to cover a wide angular range, from approx. 10° to 115°. The sketch of the detector setup is displayed in the Fig. 4.3. Angular coverages of the detectors is given in the Tab. 4.1.

The beam was collimated using the two collimating slits. The third slit was used as an anti-scattering element. The first collimator (looking from the beam-side) had the 2 mm square-shaped opening. It was located at the distance of 130 mm from the second collimator. The second collimator had a circular opening with the diameter of 2 mm. The third, anti-scattering slit, was located at 35 mm from the second slit and had a diameter of 3 mm. The entire collimator setup was located approx. 15 cm from the target.

Table 4.1: Angular coverage of the detector telescopes. Angles of T1-T4 were adjusted during calibration. See text for details.

Detector telescope	$\vartheta_{\mathrm{min}}^{\mathrm{in\,plane}}$ [°]	$\vartheta_{\mathrm{max}}^{\mathrm{in\,plane}}$ [°]	$\Delta\vartheta$ [°]
T1	11.43	30.30	18.9
T2	11.38	30.24	18.9
T3	48.10	66.31	18.2
T4	52.48	80.53	28.1
T5	83.90	116.10	32.2
T6	95.49	114.76	18.8

4.1.3 Electronics and trigger

Large-area segmented silicon detector telescopes used in this experiments provided 48 electronic channels of outputs each (16 channels for the ΔE-strips, 16+16 channels for the E-detector front and back strips). The total number of electronic channels needed was 288.

The electronics used in this experiment consisted of the Mesytec MPR-16 and MPR-32 multichannel charge-integrating preamplifiers [69]. The preamplifier output was used as an input for the Caen N568B 16-channel low-noise programmable spectroscopy amplifier [70]. The shaping times of the spectroscopy amplifiers were set to 1 μs. The amplified signal was sent to the Silena 9418 32-channel peak-sensing 12-bit analog-to-digital converter [71] (ADC). The ADC modules were controlled by the Silena acquisition control [72] (SAC) module and the Motorola MVME 2434 VME computer [73] running the MIDAS acquisition software [74]. The Motorola VME computer was connected to the data acquisition server for data storage and on-line analysis.

The fixed-amplification N568B amplifier outputs (OUTX) were used as the inputs for the custom-made Caen V895 16-channel leading-edge discriminators [75], made to work with the positive polarity input signals. Only the signals from front and back faces of the E-detectors were used to build a trigger signal. The trigger consisted of two branches: one for the single events (at least two hits in the E-detectors) and the other for coincident events (at least four hits in the E-detectors). The single-hit trigger consisted of the total sum of all discriminator outputs (-50 mV/channel above the threshold) led to the discriminator which was set to -80 mV. The discriminator output was fed to the rate divider which allowed to use only every $N-$th single-event trigger (the usual value was $^1/_{555}$). The idea was to collect only a small fraction of single events in case they would be useful for the calibration, normalization or diagnostics. The coincident trigger was built in the same manner, only the threshold of the last discriminator was changed to the -180 mV, requiring the multiplicity four or more. The logical OR of both rate-divided single trigger and coincidence trigger was used to generate the gate signal which was used to trigger the SAC unit that controlled the ADCs.

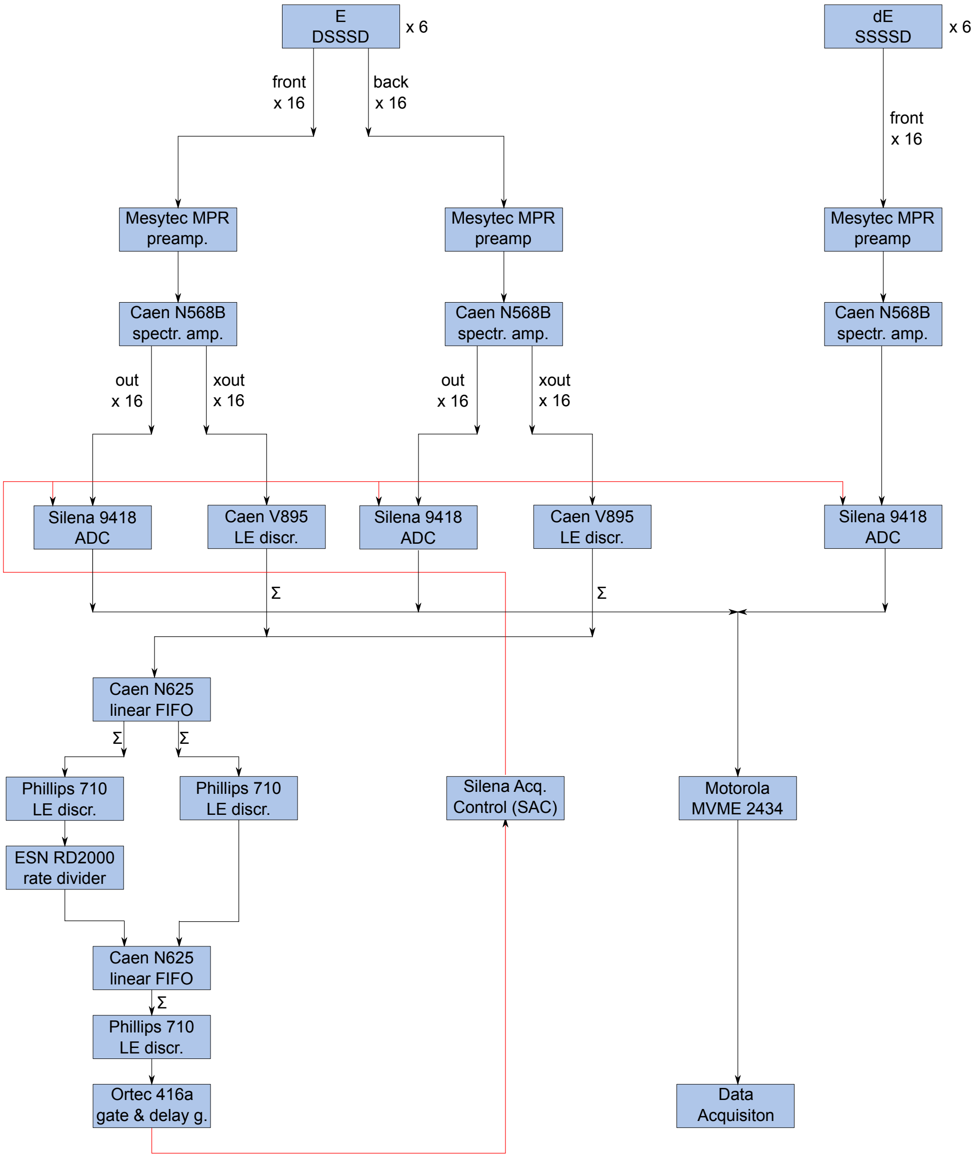

Figure 4.5: The schematics of the electronic chain for one particle detector telescope. The red line denotes the trigger signal.

The custom-made Caen V985 VME discriminators using the positive input signals proved to be a challenge in the cases where the OUTX signal amplification was very high.

This implementation of triggering logic has a weak point: it is prone to pile-up of signals from single events on top of the signals from coincident events. The experience has shown that the SAC module paired with the Silena ADCs produces bad event either when there is no signal above the threshold in any of the ADCs or when the trigger signal arrived during the conversion and read-out of the event. Therefore, if ADCs contain the data from two events and the trigger signal starts the ADC conversion and read-out, it will be counted as a single good event from the viewpoint of the acquisition.

However, if a pile-up event causes an additional trigger during the ADC conversion or read-out the acquisition system will discard both events and count them as a single bad event. In conclusion, a single-event trigger could have been passed on to the REJECT input of the Silena Acqusition Control (SAC) module to reject all of the single events overlapping with the good coincident events. That way one would still be able to collect every N-th single event but no coincident events overlapping with the single event would be accepted.

During the course of this experiment the number of bad events for beam-runs was usually around 1%. The scaler was used to count the number of triggers coming from the different parts of the setup, as well as the number of accepted events. These rates were monitored to ensure the dead time was in acceptable limits. However, it is not easy to determine the exact dead time. There is a simple model of non-extendible dead time [76] relies on a simple assumption that an arrival of additional event will not make dead time longer. In other words, each event takes the time τ, independently on number of events which arrive simultaneously. If one takes this oversimplified non-extendible dead time model,

$$\tau = \frac{m - \frac{k}{T}}{m\frac{k}{T}}, \tag{4.1}$$

where T denotes the duration of the measurement, the m the real event rate, k number of detected events and τ the dead time. The dead time was calculated using the number of input trigger signals (counted by the scaler) and divided by the duration of the measurement as the real event rate. Using the results for the run 14 (coincident events with single events scaled down 1/555) the dead time estimate was obtained:

$$\tau_{\mathrm{run14}} \approx 147\ \mu\mathrm{s}. \tag{4.2}$$

Although this value is only a very rough estimate, it has the expected order of magnitude. The meaning of the dead time in this model would be: the dead time that is needed to reduce the real number of events to the number of measured events in case of non-overlapping events, uniformly spaced in time. The real dead time can be assessed only in a dedicated measurement

[76].

Estimated dead time is larger then anticipated due to the triggering logic and collimation problems. Scattering of the collimators increased the number of events detected, in particular in detector telescope T2. The triggering logic permitted overlapping simple scattering events over coincident events. Increased multiplicity of events causes the increase of the ADC processing time. Increased multiplicity of coincident events due to the overlap of the single events with the coincident events and the increased number of single events (every 555th single event has been recorded) led to the increased value of the dead time.

4.2 Data analysis

This part will cover all the relevant steps of the data analysis. The calibration of the detector array, which was performed using a novel calibration method proposed in Ref. [18], will be described in detail. Event selection criteria will be discussed. Selected results of two-body reactions are used to identify the components in the target. An analysis of coincident events and kinematics involved is described in general terms, while results for particular reaction channels will be presented in the next part.

4.2.1 Calibration

The detector array was calibrated using a ^{239}Pu-^{241}Am-^{244}Cm calibriation α-source (providing three peaks at 5.155, 5.486 and 5.805 MeV, respectively) and an elastic scattering ^{13}C+^{197}Au run at the $E_{\text{beam}} = 46.13$ MeV. When possible, the ^{13}C+^{9}Be data collected were used as well as an additional source of useful calibration points (apart from the elastic scattering, the ^{9}Be(^{13}C,^{7}Li)^{15}N and the ^{9}Be(^{13}C,^{6}Li)^{16}N reactions were used).

The front and back faces of DSSSD detectors are divided in 16 mutually orthogonal strips. The active area of the detector is a square measuring 50×50 mm. A coincidence between a front and a back strip provides us with the location of the hit (the intersection of two orthogonal strips will be called a pixel), and two energy signals of the event, from both strips. The coordinates of the pixel are the coordinates of its centre. The two signals from front and back strips after calibration allow to distinguish good events, for which energy recorded in both strips is approximately equal, from inter-strip events and some other types of events for which the two energies differ.

An innovative approach by [18] exploits following fact: if one doesn't have a calibration, the signal from a good hit in one front strip will have corresponding signal in back strip and the two will have a simple linear interdependence:

$$s_i^{\text{back}} = a_{ri} \cdot s_r^{\text{front}} + b_{ri}, \qquad r \equiv \text{index of the reference strip} \tag{4.3}$$

where s_i is the raw signal amplitude of i-th strip, a_{ri} is the slope of the linear function and b_{ri} is its offset.

While at the first glance it might seem that fitting the data for the s_i^{back}-s_r^{front} coincidences might be a trivial task, it certainly isn't. The low-energy noise in many cases forces one to discard the data lower than e.g. channel 500 (see Fig. 4.6). Even if the low-energy noise is discarded, the quality of fit is difficult to achieve due to many points scattered outside the principal locus, and the standard χ^2 minimizations give a line off the main locus. Different approaches were tried to tackle it, including the use of the estimators more robust to noise (e.g. Theil-Sen [77]). Finally, results were obtained by using only points on the two-dimensional plot with a number of events bigger than a certain threshold (e.g. points on the plot with two or more events). An example of this procedure is displayed in the Fig. 4.6.

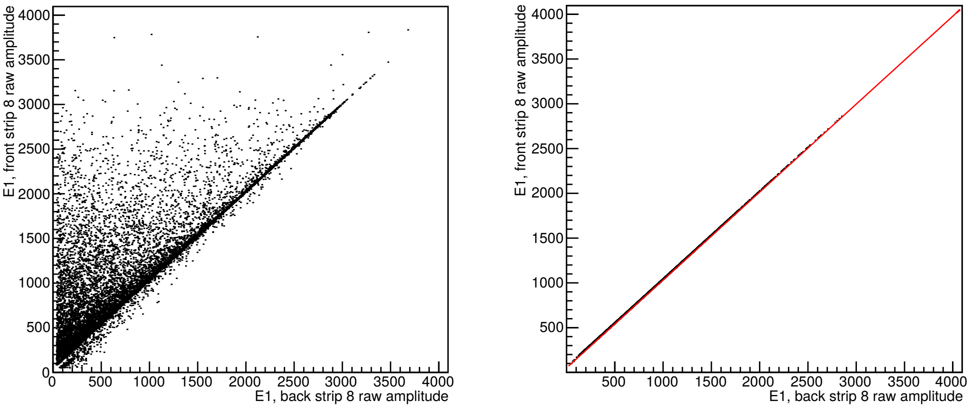

Figure 4.6: Illustration of the first step of the gain-matching procedure. **Left:** The E_8^{front}-E_8^{back} raw amplitudes plot, all points included. **Right:** The E_8^{front}-E_8^{back} raw amplitudes plot, only the points with two or more events included. The red line denotes the best fit.

It is meaningful to apply this procedure to all the back strips with respect to a single reference front strip that can be chosen arbitrarily. The procedure is repeated for the front strips as well, although in that case the calculation has to be performed through an arbitrarily chosen back-strip:

$$s_{r'}^{\text{back}} = a_{rr'} \cdot s_r^{\text{front}} + b_{rr'} \tag{4.4}$$

$$s_{r'}^{\text{back}} = a_{ir'} \cdot s_i^{\text{front}} + b_{ir'} \tag{4.5}$$

$$s_i^{\text{front}} = \frac{a_{rr'}}{a_{ir'}} \cdot s_r^{\text{front}} + \frac{b_{rr'} - b_{ir'}}{a_{ir'}}, \tag{4.6}$$

where the index i denotes the front strip, the r' the intermediate back strip and the r the reference (front) strip. Once one has a set of linear dependencies of all front strips versus all back strips one can calculate the linear factors converting the raw signal amplitude observed in any strip to the equivalent reference-strip amplitude. This amplitude will be called the gain-matched amplitude further on. The quality of the final result for the front-side strips depends on the choice of the intermediate back-side strip, so the selection of the intermediate back strip was performed by a Python code developed by Deša Jelavić Malenica and Mislav Malenica. The code uses the Dijkstra's algorithm [77] to find the optimal intermediate strip or strips for the final step of the gain-matching procedure. Finally, one arrives to the set of 32 linear equations, one for each front and back strip. The equation for the reference strip is the trivial one.

The gain-matching parameters are necessary to select good events in the thick detector, essentially using only events with the same gain-matched amplitude in both front and back strip. The gain-matching amplitude can be converted to the preliminary calibration by using the three-peak calibration α-source (^{239}Pu^{241}Am^{244}Cm) run with the thick E-detector only. After obtaining the preliminary calibration, the α-source run with the thin ΔE-detector mounted was analysed. Due to geometrical consideration, each (vertical) strip in the ΔE-detector had only two corresponding vertical strips in the E-detector (see Fig. 4.7).

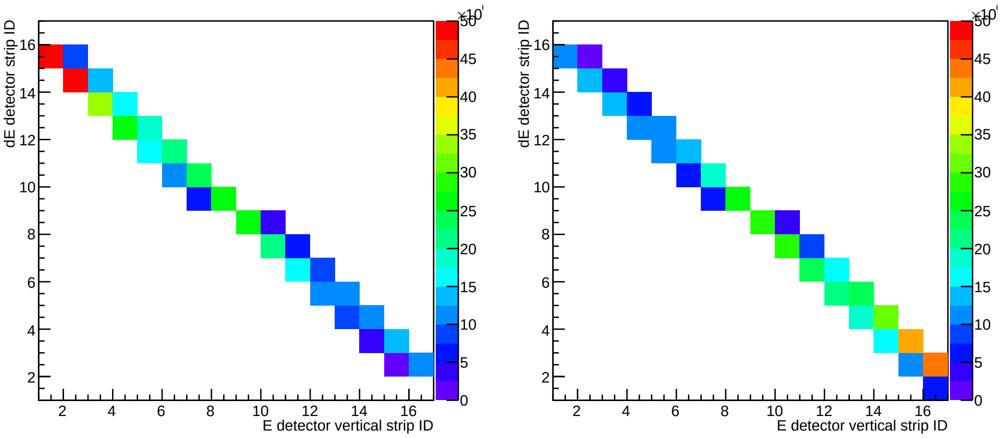

Figure 4.7: The matching of the ΔE (vertical) strips to the E-detector vertical (front) strips. The plots present the permitted combinations. **Left:** The dE_{id}-$E_{\mathrm{id}}^{\mathrm{front}}$ plot for the T1. **Right:** The dE_{id}-$E_{\mathrm{id}}^{\mathrm{front}}$ plot for the T2.

Good hits with a signal in both ΔE and E strips were used to calculate the preliminary thickness of the ΔE detector pixels. The plots were always made for the ΔE-E_{back}, the ΔE-strip with the back E-detector strip, defining the ΔE-detector pixel. This data could be obtained only for a portion of ΔE detector due to significant thickness non-uniformity. The energy difference between the detected energy of the α-source peaks in the thick detector with and without the ΔE-detector mounted was also used as one of the points for the ΔE detector calibration.

Once the preliminary ΔE detector thickness was obtained, the beam-runs were used to obtain the final calibration. The following steps for the front-angle detector telescopes T1 and T2 differ from the procedure which was used for the T3 and T4. The detector telescopes T1 and T2 had

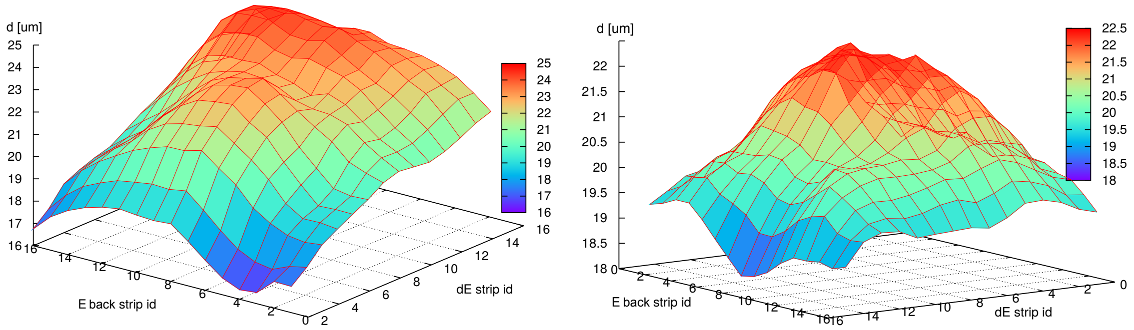

Figure 4.8: The ΔE-detector profiles for the detector telescope T1 (left) and T2 (right).

the ΔE-detector gains adjusted for the detection of a wide range of isotopes (from helium to carbon). Therefore, the calibration run ^{13}C+^{197}Au at beam energy of 46.13 MeV could be used to obtain both the high-laying calibration point for the E-detector and the full profile of the ΔE-detector. Of course, the preliminary thicknesses from the previous step were used. The final thickness profiles of the T1 and T2 ΔE-detectors are displayed in the Fig. 4.8. Simultaneously with the ΔE-thickness profile the calibration points were obtained for the ΔE-detector. The calibration points and lines can be seen in the Fig. 4.9.

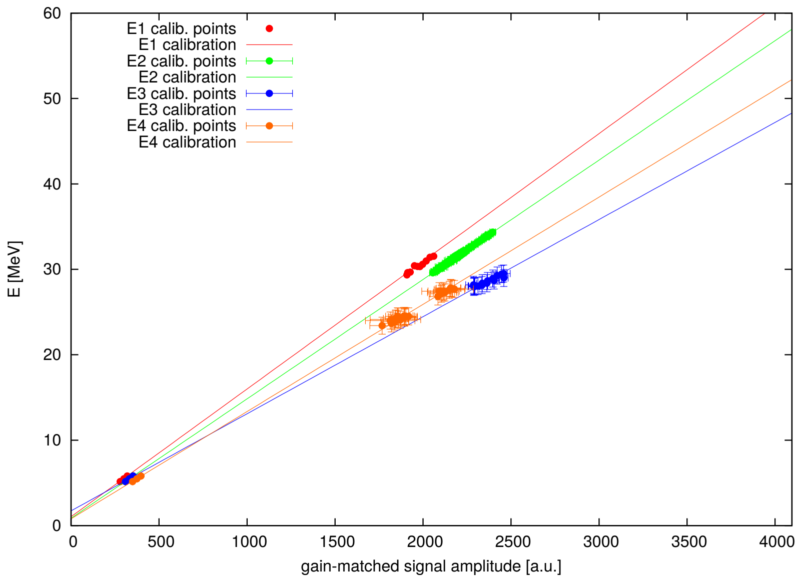

Figure 4.9: The calibration points and lines of the four E detectors.

A brief digression on the determination of the angles. The precise knowledge of angles is necessary for a sound calibration using the data points from the beam-runs. The detector angles were first determined while designing the detector mount and positioning them on it. That angles were double-checked using the photography of the setup. A further check was performed by making a simple Monte Carlo simulation to determine the relative number of events per pixel in the E-detector. All the said results confirmed that the front-angle detector-telescopes were located at approximately the same angle as planned. After the calibration was performed, the calibration was checked using the two-particle reactions available that provided results consistent with the calibration.

The calibration for the ΔE detectors of the front-angle telescopes was performed using both the α-source runs and the beam-runs. An example of the ΔE-calibration is displayed in the Fig. 4.11.

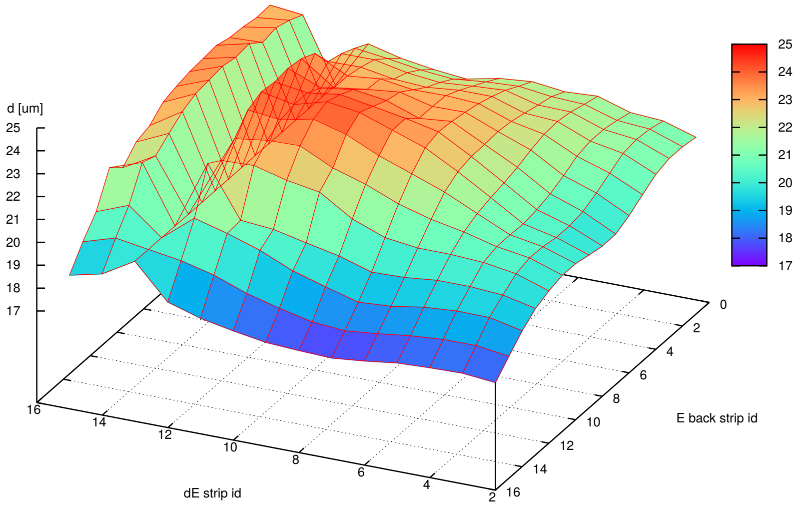

Figure 4.10: The profile of the ΔE-detector for the detector telescope T4. The missing data for a single strip is due to a dead strip in the E-detector.

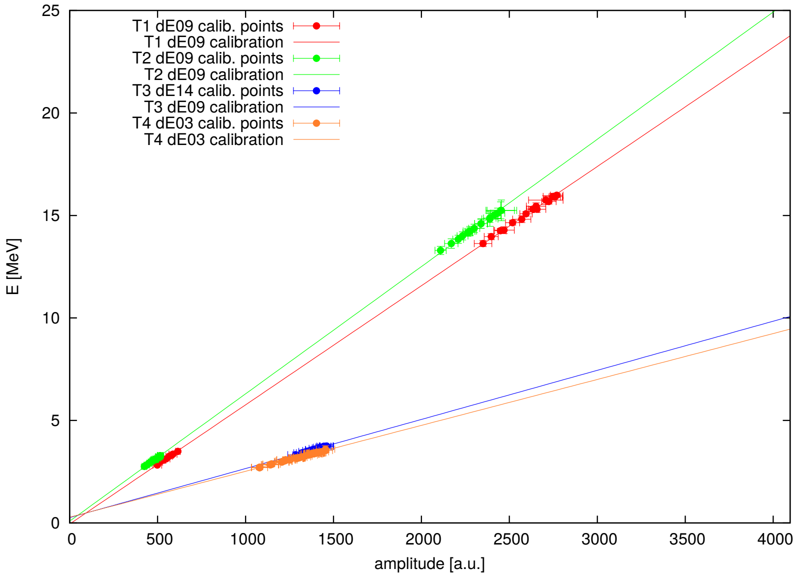

Figure 4.11: The examples of the calibration points and lines for the four ΔE detectors.

The calibration of the detector telescopes T3 and T4 was more demanding. After the gain matching procedure, the α-source runs were analysed. At this point a serious problem was encountered with the E-detector of the detector telescope T4: the fine gains were changed *after* the α-source calibration runs were taken. The α-source calibration runs with E detectors only were not repeated at the end of the experiment due to the lack of time. Therefore, the available pulser runs were studied and the channels for which a fine gain was not changed were identified (that finding was confirmed by the experiment run book). That way only the strips with reliable data were used to calibrate the gain-matched amplitude. The α-source runs provided preliminary calibration of the gain-matched amplitude together with a profile of one portion of ΔE detector (due to variation in thickness no data was available for one portion of detector, because the α-particles in the E detector were bellow the detection threshold). After the analysis of the α-source runs coincident elastic scattering ^{13}C+^{9}Be events with the corresponding front-angle detector (T1 for the T4 and T2 for the T3) were analysed. The front-angle detectors T1 and T2 were already calibrated. In the T3 and T4 detector telescopes the ^{9}Be could not be identified because of the ΔE detector signals were ot of the ADC range. Therefore, one had to find the elastic scattering events with no signal in the ΔE detector and a good signal in the E-detector. The energy loss was calculated from the thickness of the pixel obtained from the α-source run. Once both the energy and the angles of detected ^{13}C and ^{9}Be were known, the angle of the T4 and T3 were adjusted accordingly. Once an angle was known, two-particle reactions could have been used to calibrate the detector. For the T3 detector telescope an elastic scattering ^{13}C+^{197}Au data was used to obtain the high-energy calibration points for the gain-matched amplitude. The ΔE-detector calibration was carried out using the α-source data only, which was not sufficient to obtain a full profile of the ΔE detector. The high-lying points for the calibration of the detector telescope T4 came from the ^{9}Be(^{13}C,^{7}Li)^{15}N and the ^{9}Be(^{13}C,^{6}Li)^{16}N reactions. They were used for the calibration of the corresponding ΔE-detector strips as well. The profile of the ΔE-detector of the T4 was obtained from the reaction data, too (see Fig. 4.10).

The detector telescope T5 had only the α-source run data available. The gain-matching was obtained from the beam-runs. The α-calibrated gain-matched amplitude provided a good basis for the search for adequate coincident detection events of the two-particle reaction products that could provide us with means to fine-tune the angle of the detector and more importantly to obtain a high-lying calibration point for the gain-matched amplitude. None was found. The study of coincidences between the front-angle detectors and the T5 have shown that both its angle and calibration are not robust enough and it had to be discarded from the analysis.

The T6 detector telescope was located at backward angles, as well (see Fig. 4.3). The detector setup was optimized to cover as completely as possible all the angles from approx. 10° to 120°. Therefore, some gaps between the detectors were made as small as possible, as far as the detector mounts allowed it. That restricted the range of possible target angles a lot. Forced to choose between a large target angle, which would make its thickness very large, and a small angle which would cast a shadow on the T6, the latter was chosen. The size of the shadow was underestimated in setting the setup and the obtained data from the detector was not complete enough to carry out the gain-matching procedure.

4.2.2 Target composition

The calibration obtained made it possible to verify the composition of the target using the elastic scattering data. The events of the ^{13}C detected in the detector telescope T1 were used. The two-particle reaction was assumed, the undetected particle being the ^{9}Be, ^{12}C, ^{16}O or ^{56}Fe. An excitation energy of the undetected particle was computed using the formula [78]:

$$E_x = Q_0 + \frac{M_B - M_a}{M_B} E_a - \frac{M_B + M_b}{M_B} E_b + \frac{2}{M_B} \sqrt{M_a M_b} \sqrt{E_a E_b} \cos \vartheta_b, \tag{4.7}$$

where the reaction is $A(a,b)B$. The indexes of variables label the particle to which the variables corresponds. The Q_0 is the Q-value of the reaction, in this cases equal to zero. The M denotes mass, E energy and ϑ polar angle, both in the laboratory frame of reference. The vertical loci in Fig. 4.12 at $E_x = 0$ correspond to the identified target nucleus. In the case of ^{56}Fe, one can not identify the particular element or isotope, as several different elements produce the perpendicular locus. The ^{56}Fe is a likely contaminant because it is listed as a common contaminant of the bulk beryllium material, and present in higher concentration than the other contaminants of similar mass [79]. These spectra confirm the high purity of the ^{9}Be target.

4.2.3 Event selection

A good event consists of one or multiple hits, each hit is a group of signals from a single pixel of E and the corresponding strip in ΔE detector. For a series of raw ADC signals to be reconstructed as a good hit several conditions have to be fulfilled.

First the two signals from the font and the back strip of the E-detector have to fulfil this condition:

$$\Delta = \text{abs}\left(\frac{E_{\text{front}} - E_{\text{back}}}{(E_{\text{front}} + E_{\text{back}})/2} \right) < 1.0\%, \tag{4.8}$$

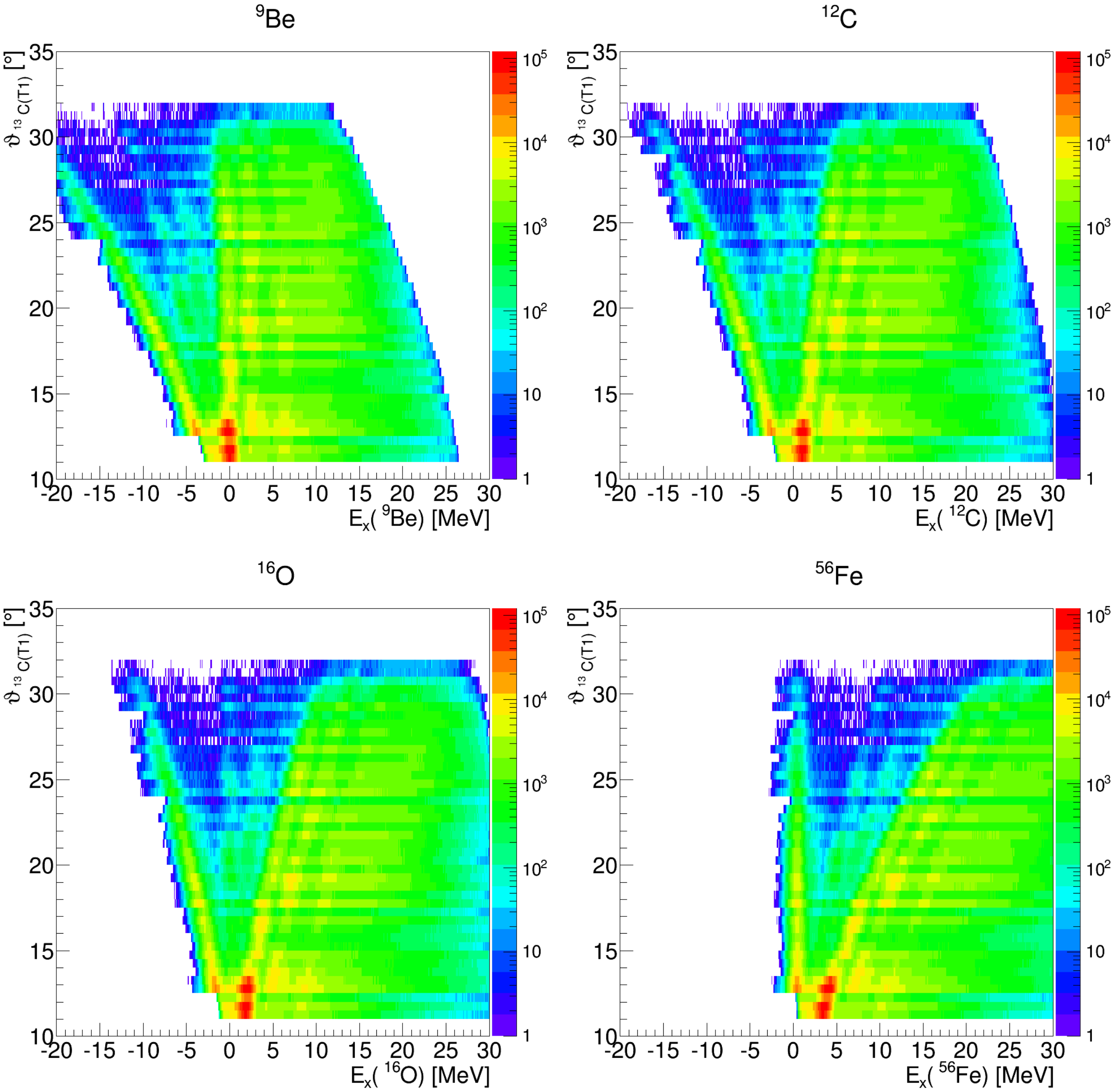

Figure 4.12: The analysis of target composition using the elastically scattered ^{13}C ions detected in the T1 detector telescope.

where E is the calibrated energy. The plot of the Δ for all the pairs of front-back strips of the E-detectors is displayed in the Fig. 4.13.

If a pair of one front and one back strip fulfil the aforementioned condition, the E-detector energy of the hit is set to be the front strip energy E_{front}. The polar angle ϑ and the azimuthal angle φ of the E-detector pixel are used further on as angular coordinates of the hit. Secondly the ΔE-detector strips corresponding to the front strip of the E-detector are checked for a signal (see Fig. 4.7). If signal is found in both of the corresponding strips, the one with the higher amplitude is assigned. This procedure is repeated for all four detector telescopes, T1-T4. A series of good hits are obtained, forming an event.

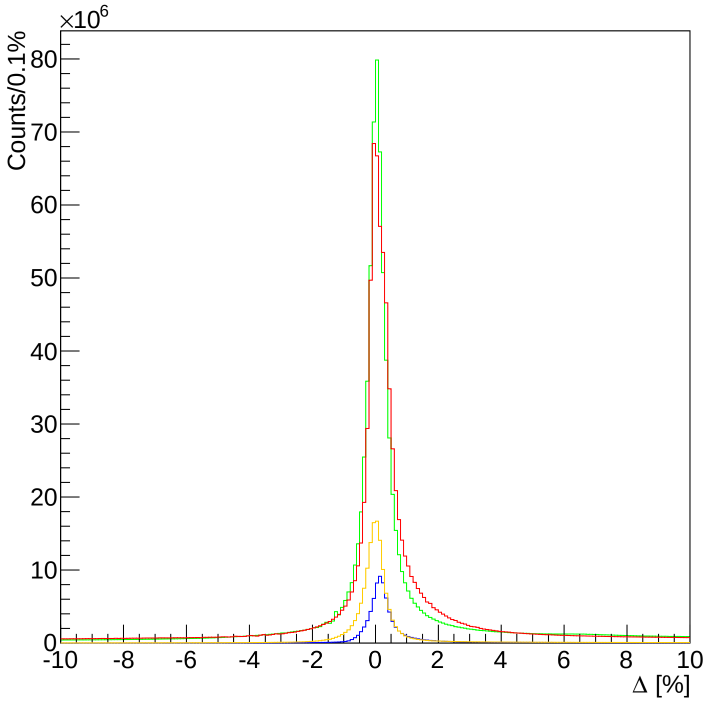

Figure 4.13: The spectra of Δ, the front-strip and back-strip energy difference relative to the average of the two. The red line denotes the detector telescope T1, the green line the T2, the blue line the T3 and the orange line T4. The cut was placed at $\mathrm{abs}\,(\Delta) < 1.0\%$.

In the next step the graphical cuts are used to identify the isotopes and assign a proper mass number A, atomic number Z and the relative atomic mass m to each hit. Both plots and graphical cuts were made one for each ΔE-strips. The exception was the T3, for which one had to make one cut per pixel because the detector profile was not available. The ΔE-E plots for a single strip were compensated for the thickness variation by introducing a new variable:

$$dE_{20\mu\mathrm{m},i,j} = \frac{dE}{d_{i,j}} \cdot 20\,\mu\mathrm{m}, \tag{4.9}$$

where ΔE is the energy detected in the thin detector, $d_{i,j}$ is the thickness of the intersection of the i-th ΔE-detector strip and the j-th E-detector back strip. For an example of the ΔE-E plot see Fig. 4.14. The three topmost strong loci are the ^{12,13,14}C, while the lowest strong locus belongs to the ^{4}He. In between one can see the ^{6,7}Li, ^{9,10}Be and $^{10-12}$B. Spurious loci are visible, as well. The vertical loci correspond to the high-energy events in the E-detector with wrong ΔE-value assigned. The loci between the helium and the lithium loci correspond to the pile-up of noise, hydrogen or helium nuclei with the α-particles. At the very top of the plot a part of ^{14}N and ^{15}N loci can be seen as well. The identification of the isotopes for all good hits

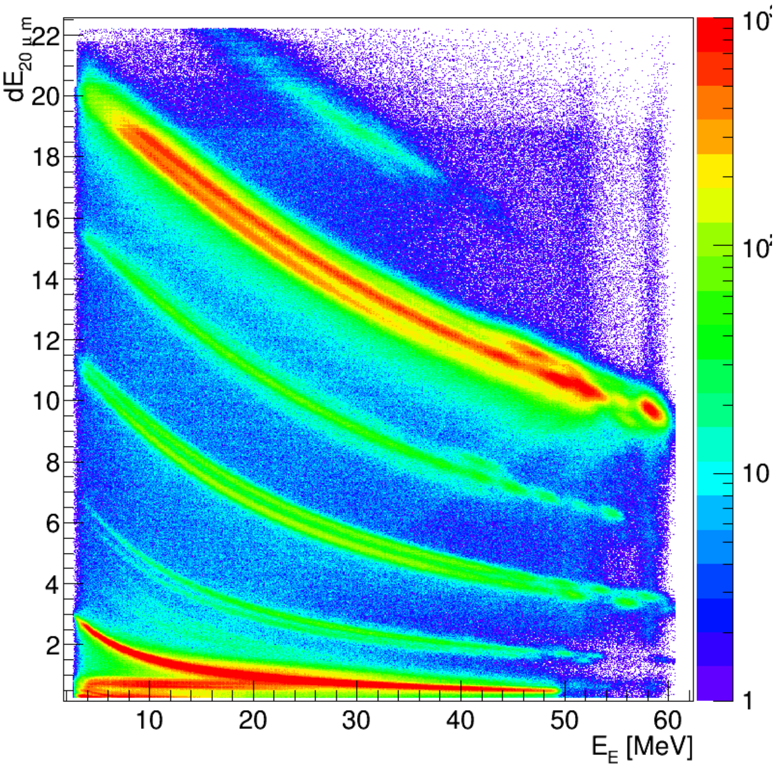

Figure 4.14: An example of the ΔE-E spectrum for the detector telescope T1, ΔE-strip 13. The plot contains all the good hits from the entire experiment.

in the event is an opportunity to calculate some simple spectra from a single detected particle (e.g. the plots in the Fig. 4.12 are filled for each identified ^{13}C nucleus).

Once all nuclei of interest have been identified in the hits, the $^{8}\text{Be}_{\text{gs}}$ reconstruction takes place. It is described in detail in the Sec. 4.3.4 and it will be skipped here.

After the ^{8}Be reconstruction the two and three-particle coincident events are studied. When a coincident event between a pair of nuclei is found, the energy losses of the nuclei in question in the target are computed and kinematic calculations are performed. The final results are saved in the plots.

4.2.4 Analysis of three-particle reactions

In this section a summary of kinematics needed for the reaction data analysis will be presented, based on Ref. [78]. The three-particle reaction used as an example will be $p+t \rightarrow 1+2+3$. All the relevant variables will be labelled using the appropriate index: p for the projectile (beam), t for the target species and 1, 2 and 3 for the outgoing particle. Particles 1 and 2 are detected while the particle number 3 remains undetected. Detection of two particles allows us to reconstruct all relevant details [80].

One can begin with the Catania plot [81]. The Catania plot is a two-dimensional plot derived from the two-particle coincidence data that enables one to determine both the mass of the undetected particle and the Q-value of the reaction. The abscissa of the Catania plot is the $\tilde{P} = \frac{p_3^2}{2m_n}$ (the m_n is the nucleon mass), while the ordinate is the $\tilde{E} = \frac{1}{A_3}\tilde{P} - Q$ (the A_3 is the mass number of the third particle). The impulse of the third particle, and consequently $\tilde{P}$, follows from the law of conservation of the momentum:

$$\vec{p}_3 = \vec{p}_p - \vec{p}_1 - \vec{p}_2, \tag{4.10}$$

while the $\tilde{E}$ is obtained using the conservation of energy:

$$\tilde{E} = E_p - E_1 - E_2. \tag{4.11}$$

Therefore, each coincident detection event (a pair of specific isotopes) can be plotted in the $(\tilde{E}, \tilde{P})$ plane. The loci corresponding to the specific reaction will be concentrated on the line with slope proportional to ${}^1/_{A_3}$. The Q-value of the locus can be found as an intersection of the line with the ordinate. The Catania plot is invaluable tool for unambiguous identification of reaction channel, which is a crucial step to discard possible target contaminants or misidentified particles.

Next, the relative energies of the outgoing particles will be discussed. Resonances in relative energies between a pair of outgoing particles indicates that they originate from the same decay process. In the expression which follow all the variables are in the laboratory frame of reference, if not stated otherwise. The relative energy between the two outgoing particles is, independently of the frame of reference:

$$\begin{aligned} E_{\mathrm{r}12} &= \frac{\mu_{12}}{2}\left(\vec{v}_1 - \vec{v}_2\right)^2 && (4.12)\\ &= \frac{\mu_{12}}{2}\left(v_1^2 + v_2^2 - 2v_1 v_2 \cos\vartheta_{12}\right) && (4.13)\\ &= \mu_{12}\left(\frac{E_1}{m_1} + \frac{E_2}{m_2} - 2\sqrt{\frac{E_1 E_2}{m_1 m_2}}\cos\vartheta_{12}\right), && (4.14) \end{aligned}$$

where $\mu_{12} = \frac{m_1 m_2}{m_1 + m_2}$ is the reduced mass of the system of particles 1 and 2, and the angle between the particles is $\cos\vartheta_{12} = \cos\vartheta_1 \cos\vartheta_2 + \sin\vartheta_1 \sin\vartheta_2 \cos\Delta\varphi$. The $\Delta\varphi = \varphi_1 - \varphi_2$ equals 0° when particles are detected on the same side or 180° if they are detected on the opposite sides of the beam.

Apart from the relative energies between the two detected particles, one needs the relative energy between one of the detected (1 or 2) and the undetected particle (3). Two different approaches can be used: the relative energy can be computed using the expression of the form (4.12) or it may be calculated from the total energy in the centre-of-mass system. Here the latter approach is used. The total energy in the centre of mass system can be expressed as a sum of the relative energy between the particle 1 and the system of the two remaining particles 2 and 3 (E_{1-23}) and the relative energy between the particles 2 and 3 (E_{23}):

$$E_{\text{tot}}^{\text{CM}} = E_{1-23} + E_{23} = E_{2-13} + E_{13}. \tag{4.15}$$

On the other hand, it is known

$$E_{\text{tot}}^{\text{CM}} = Q + \frac{m_t E_p}{m_p + m_t} \tag{4.16}$$

and in the centre-of-mass system

$$\left|\vec{p}_1^{\,\text{CM}}\right| = \left|\vec{p}_{1-23}\right|. \tag{4.17}$$

Consequently, one can calculate the relative energy of the particles 2 and 3 from the energy and angle of particle 1. From the Eq. (4.17) and the definition

$$\mu_{1-23} = \frac{m_1(m_2+m_3)}{m_1+m_2+m_3} \tag{4.18}$$

it follows

$$E_{1-23} = \frac{m1+m2+m3}{m2+m3} E_1^{\text{CM}}. \tag{4.19}$$

Using the last equation, the Eq. 4.15 can be rewritten:

$$\begin{aligned}
E_{r23} &= E_{\text{tot}}^{\text{CM}} - \frac{m_1+m_2+m_3}{m_2+m_3} E_1^{\text{CM}} && (4.20)\\
&= Q + \frac{m_t E_p}{m_p+m_t} - \frac{m_1+m_2+m_3}{m_2+m_3} E_1^{\text{CM}} && (4.21)\\
&= E_1 + E_2 + E_3 - E_p + \frac{m_t E_p}{m_p+m_t} - \frac{m_1+m_2+m_3}{m_2+m_3} E_1^{\text{CM}}, && (4.22)
\end{aligned}$$

where in the second step the Eq. 4.16 was used and in the last step the Q-value was expressed using the particle energies: $Q = E_1 + E_2 + E_3 - E_p$. In the final step one can use the expression for the centre-of-mass energy from [78]:

$$E_i^{\mathrm{CM}} = E_i^{\mathrm{L}} - 2\frac{\sqrt{m_i m_p E_p^{\mathrm{L}}}}{m_p + m_t}\sqrt{E_i^{\mathrm{L}}}\cos\vartheta_i^{\mathrm{L}} + \frac{m_i m_p E_p^{\mathrm{L}}}{(m_p+m_t)^2} \tag{4.23}$$

where the values from the centre-of-mass and the laboratory frame of reference are explicit. That way one obtains the final expression, containing only the measured energies and angles:

$$\begin{aligned} E_{r23} &= Q + \frac{m_t E_p}{m_p + m_t} && (4.24)\\ &\quad -\frac{m_1+m_2+m_3}{m_2+m_3}\left(E_1 - 2\frac{\sqrt{m_1 m_p E_p}}{m_p+m_t}\sqrt{E_1}\cos\vartheta_1 + \frac{m_1 m_p E_p}{(m_p+m_t)^2}\right), && (4.25)\end{aligned}$$

where labels for the laboratory frame of reference were omitted. Note that apart from the beam energy and the masses, the E_{r23} in this expression depends exclusively on the energy and angle of the particle 1.

Following a similar procedure, one can obtain the expression for the E_{r13} as a function of the energy and angle of the particle 2:

$$\begin{aligned} E_{r13} &= Q + \frac{m_t E_p}{m_p + m_t} && (4.26)\\ &\quad -\frac{m_1+m_2+m_3}{m_1+m_3}\left(E_2 - 2\frac{\sqrt{m_2 m_p E_p}}{m_p+m_t}\sqrt{E_2}\cos\vartheta_2 + \frac{m_2 m_p E_p}{(m_p+m_t)^2}\right), && (4.27)\end{aligned}$$

For each coincident event all three relative energies were calculated: E_{r12}, E_{r13} and E_{r23}. The three were plotted against each other on three plots: E_{r13}-E_{r12}, E_{r23}-E_{r12} and the E_{r23}-E_{r13} plot. The excited states of intermediate nuclei B decaying to the pair of nuclei b_1 and b_2 are visible as loci in the corresponding relative energy perpendicular to the axis (i.e. independent on the other two relative energies). Excitation energy of the nucleus B decaying to the pair of daughter nuclei b_1 and b_2 is calculated by adding the corresponding decay threshold energy $E^{\mathrm{thr.}}_{B\to b_1+b_2}$:

$$E_x(B) = E_{rb_1b_2} + E^{\mathrm{thr.}}_{B\to b_1+b_2} \tag{4.28}$$

The Q-value of the three-particle processes can be calculated in two different ways. One can obtain it from the measured energies of the outgoing particles:

$$Q = E_1 + E_2 + E_3 - E_p, \tag{4.29}$$

where the energy of the third, undetected particle has to be deduced from the momenta of the two detected particles. The second way is using the Catania plot, where $\tilde{E}(\tilde{P}=0)=-Q$ can be used. For a point with coordinates $(\tilde{P},\tilde{E})$, where $\tilde{P}\neq 0$ the Q-value is:

$$Q=\frac{1}{A_3}\tilde{P}-\tilde{E}, \tag{4.30}$$

where A_3 is the mass number of the third, undetected particle.

4.3 Results

The results obtained from the coincident events of different isotope pairs are presented in this section. Different reaction exit channels will be discussed one by one. Comparison of the results from this section with previously published results is given in the Chapter 5.

4.3.1 The ^{9}Be+^{13}C $\to$^{13}C+^{4}He+^{5}He reaction

The ^{9}Be+^{13}C $\to$^{13}C+^{4}He+^{5}He reaction was used to examine the populated excited states of the ^{17}O. A similar experiment has been performed before and results are published in [6]. First, Catania plots for the ^{13}C+^{4}He coincident events between different detectors will be examined in order to determine the exit channels populated by this reaction. The Catania plots for the ^{13}C(T1)-^{4}He(T2), ^{13}C(T2)-^{4}He(T1), ^{13}C(T1)-^{4}He(T4) and ^{13}C(T2)-^{4}He(T3) coincident events are displayed on the Figs. 4.15, 4.16,4.17 and 4.18, respectively.

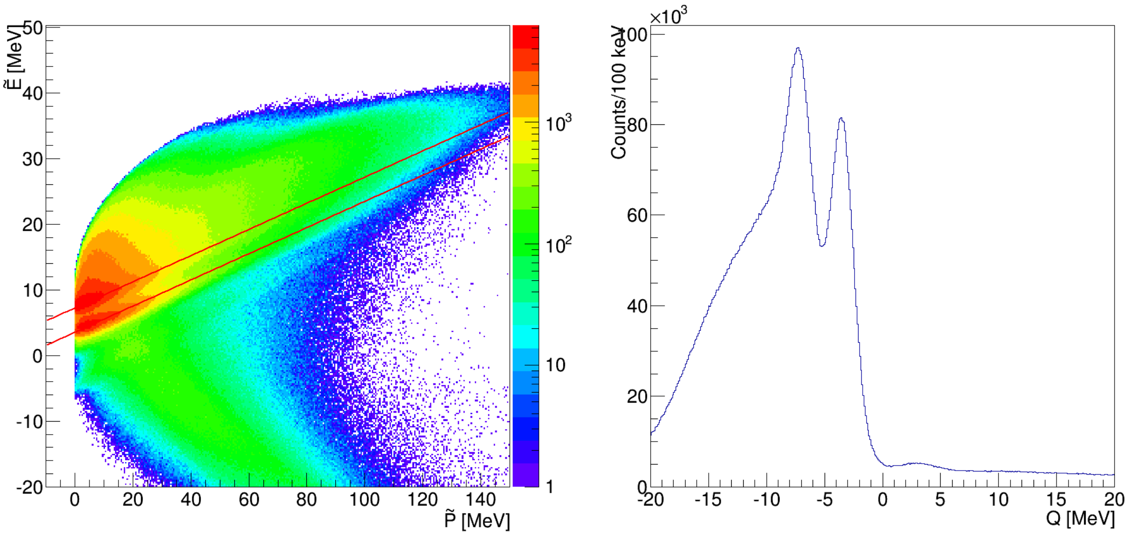

Figure 4.15: Left: The Catania plot for the ^{9}Be(^{13}C,^{13}C ^{4}He) reaction, ^{13}C detected in the T1 and ^{4}He in the T2. The two red lines are denoting the position of reaction loci for the undetected ^{5}He: the lowest for all nuclei in the ground state and the second one for the reaction channel with the ^{13}C($E_x = 3.7$ MeV). The lines were shifted by +1.0 MeV to reproduce the data. **Right:** The corresponding Q-value spectrum.

All the aforementioned Catania plots share a few common features:

1. two strong loci are visible, corresponding to the ^{13}C+^{4}He and the ^{13}C($E_x = 3.7$ MeV)+^{4}He reaction channels,
2. an additional weak locus is observed bellow the strong loci, corresponding to the ^{14}C misidentified as ^{13}C (belonging to the ^{14}C+^{4}He reaction channel) and

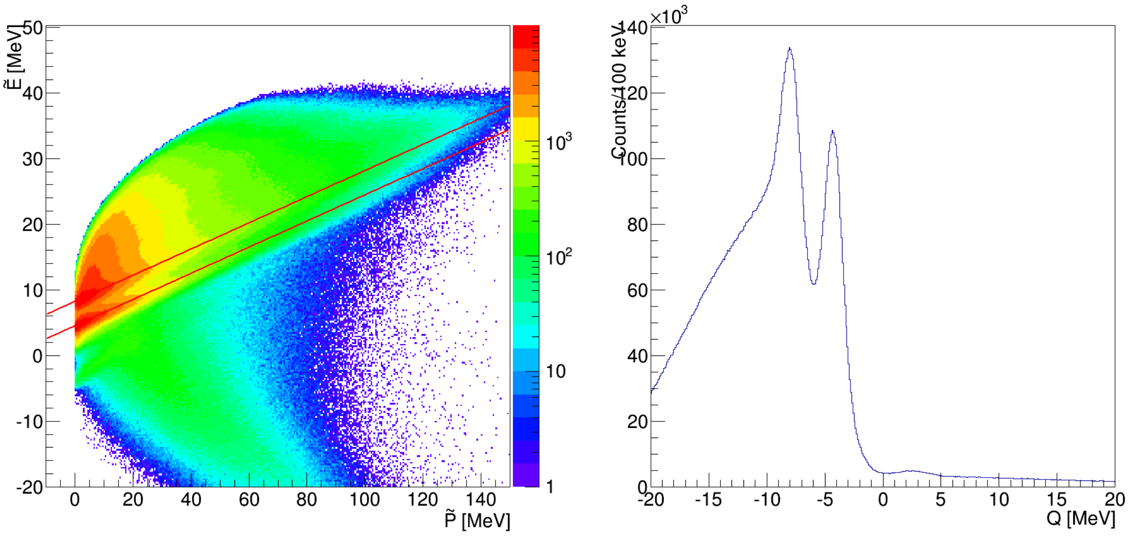

Figure 4.16: Left: The Catania plot for the ^{9}Be(^{13}C,^{13}C ^{4}He) reaction, ^{13}C detected in the T2 and ^{4}He in the T1. The two red lines are denoting the position of reaction loci for the undetected ^{5}He: the lowest for all nuclei in the ground state and the second one for the reaction channel with the ^{13}C($E_x = 3.7$ MeV). The lines were shifted by +2.0 MeV to reproduce the data. **Right:** The corresponding Q-value spectrum.

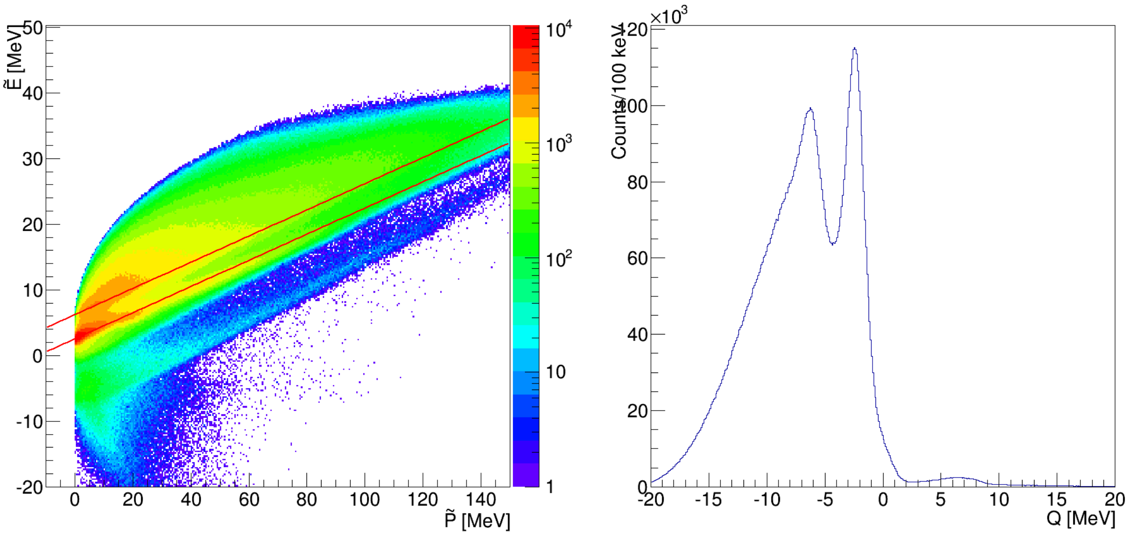

Figure 4.17: Left: The Catania plot for the ^{9}Be(^{13}C,^{13}C ^{4}He) reaction, ^{13}C detected in the T1 and ^{4}He in the T4. The two red lines are denoting the position of reaction loci for the undetected ^{5}He: the lowest for all nuclei in the ground state and the second one for the reaction channel with the ^{13}C($E_x = 3.7$ MeV). The lines were not shifted to reproduce the data. **Right:** The corresponding Q-value spectrum.

3. the ground-state exit channel forms a well-defined peaks in the Q-value spectrum, while the Q-value peak for the ^{13}C($E_x = 3.7$ MeV)+^{4}He channel for the T1-T4 and the T2-T3 coincidences contains a significant portion of background events

Let us first address the issue of the ^{14}C misidentified as the ^{13}C. The Catania plot for the T1-T4 detector coincidences will be used as an example. If Catania plot is made for the

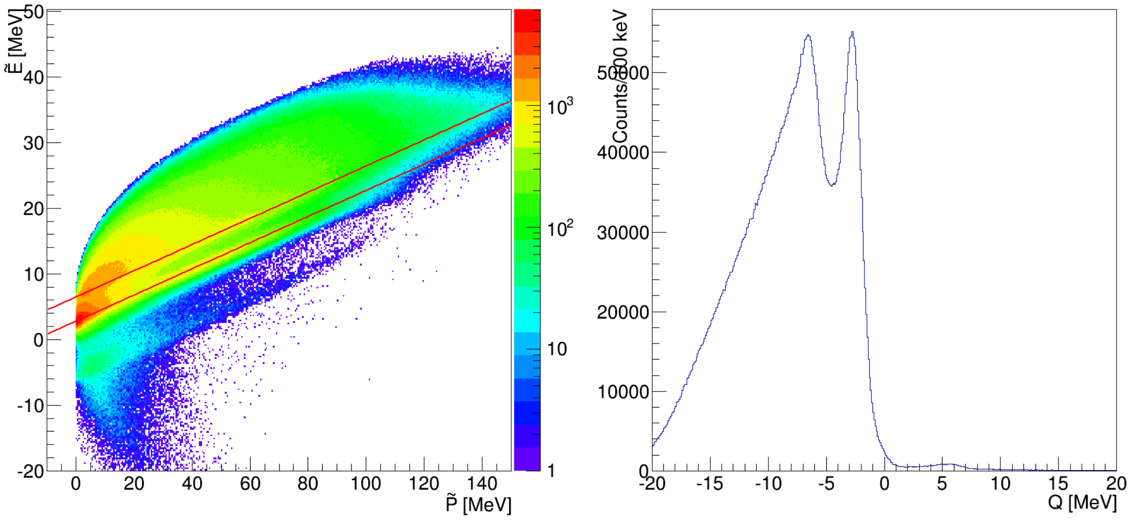

Figure 4.18: Left: The Catania plot for the ^{9}Be(^{13}C,^{13}C ^{4}He) reaction, ^{13}C detected in the T2 and ^{4}He in the T3. The two red lines are denoting the position of reaction loci for the undetected ^{5}He: the lowest for all nuclei in the ground state and the second one for the reaction channel with the ^{13}C($E_x = 3.7$ MeV). The lines were shifted by +0.25 MeV to reproduce the data. **Right:** The corresponding Q-value spectrum.

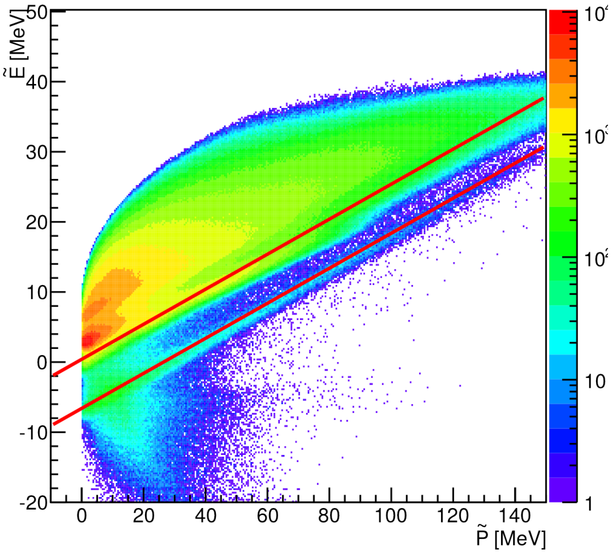

Figure 4.19: The Catania plot for the ^{13}C(T1)-^{4}He(T4) coincident events, but the $\tilde{E}$ and $\tilde{P}$ calculations were performed as if the detected nuclei were ^{14}C+^{4}He. The lines denote the ^{14}C+^{4}He loci for the ^{14}C in its ground state and a group of excited states at $E_x \approx$7 MeV, respectively. The position of the lines was not adjusted to match the data.

^{13}C+^{4}He events but $\tilde{E}$ and $\tilde{P}$ are calculated as if they were ^{14}C+^{4}He coincident events, the plot in the Fig. 4.19 is obtained. A weak locus seen in the Fig. 4.17 matches the ground-state channel of the ^{14}C+^{4}He+^{4}He reaction in the Fig. 4.19. The locus which corresponds to the ^{14}C($E_x \approx 7$ MeV)+^{4}He+^{4}He reaction lies very close to the ground-state locus of the ^{13}C+^{4}He+^{5}He reaction, partially overlapping with it. As it will be seen in the Section 4.3.2, the

$^{14}C^{*}+^{4}He+^{4}He$ is more strongly populated than the ground state channel. Consequently, the possible overlap with the ground-state $^{13}C+^{4}He+^{5}He$ channel might be problematic.

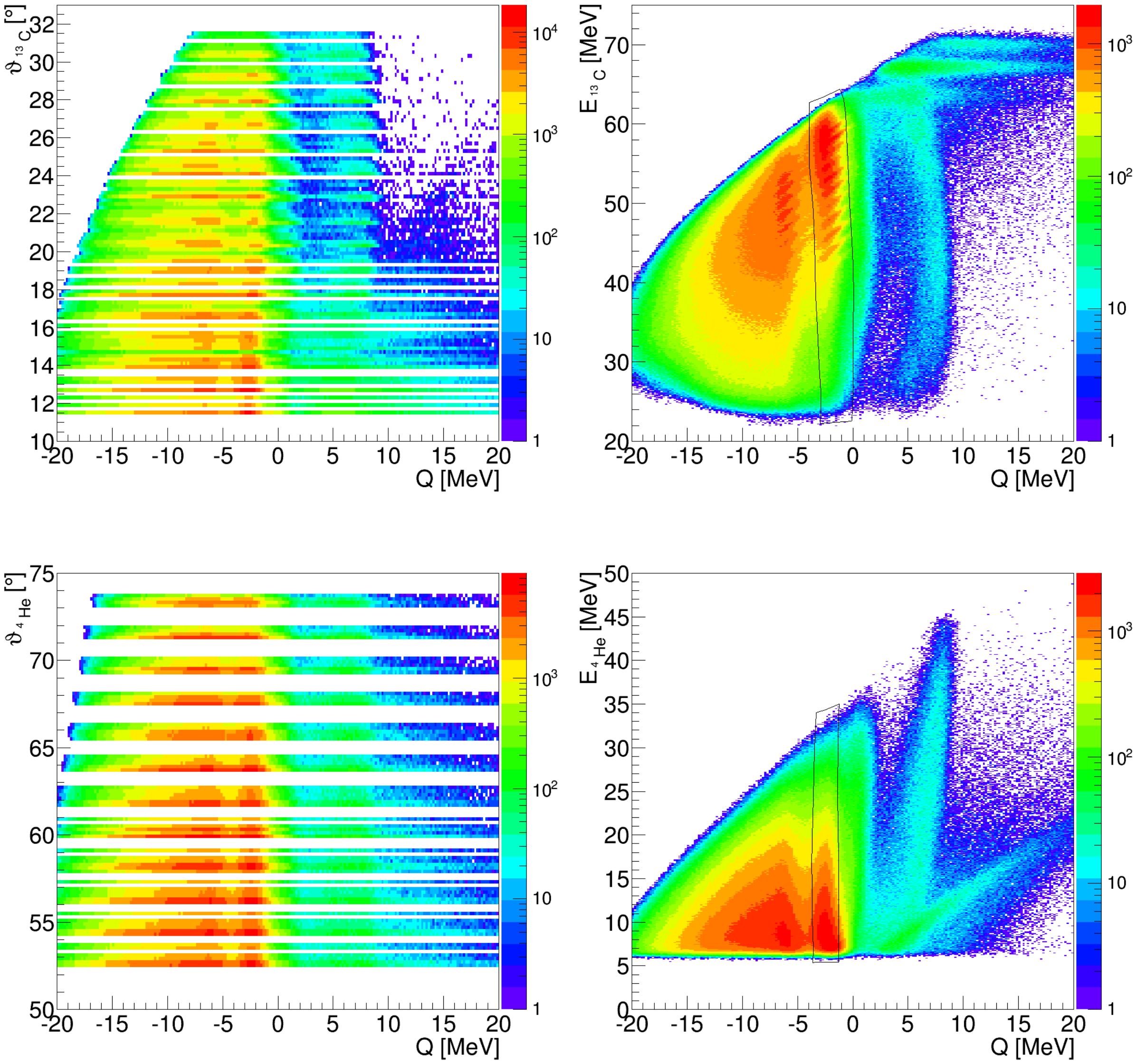

Figure 4.20: The ϑ_{det}-Q and the E_{det}-Q spectra for the ^{13}C(T1)-^{4}He(T4) coincident events. The black line denotes the graphical cuts used to select the ground state reaction channel.

One of the possible solutions to this problem of ^{14}C contamination are the E_{det}-Q plots. As one can see in the Fig. 4.20, the spurious events mainly separate out in the E_{det}-Q plots, more so for the $E_{\text{det}}^{4\text{He}}$-$Q$ plot. The $E_{\text{det}}^{13\text{C}}$-$Q$ plot shows three horizontal loci corresponding to the single-events pile up. The rightmost curved locus on the same plot corresponds to the ^{14}C nucleus misidentified as the ^{13}C. The curved locus next to the strongest $^{13}C+^{4}He+^{5}He$ locus corresponds to the misidentified $^{14}C^{*}$ nucleus and it partially overlaps with the strongest locus. In the $E_{\text{det}}^{4\text{He}}$-$Q$ plot pile-up events form the rightmost locus, tilted to the right edge of the plot.

Two loci corresponding to the misidentified ^{14}C and ^{14}C* are present as well, forming two parallel loci inclined to the right at a small angle. It is interesting to note that the ϑ_{det} plots can help to reject the spurious events only for the ^{13}C nucleus. The good events were selected by placing a graphical cut on both $E_{\text{det}}^{^{13}\text{C}}$-$Q$ and $E_{\text{det}}^{^{4}\text{He}}$-$Q$ plots for coincident events in all detector pairs. The rest of the ϑ_{det}-Q and E_{det}-Q can be found in the Appendix A, displayed on the Figs. A.1, A.2 and A.3.

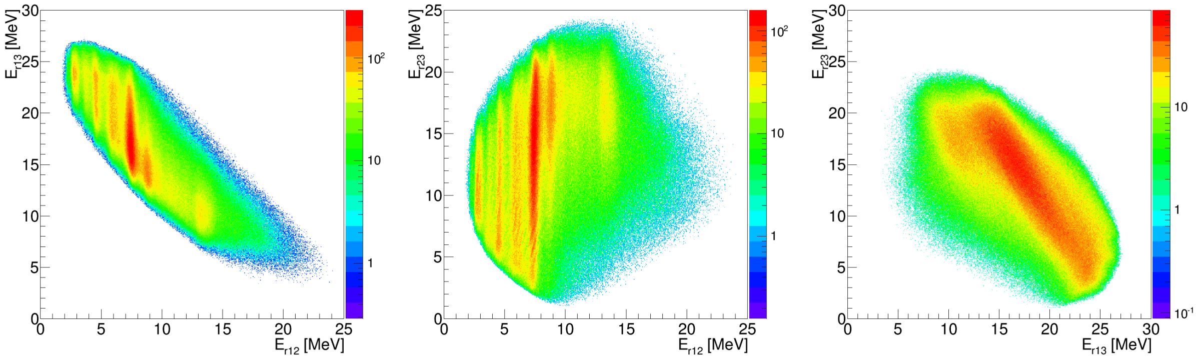

Figure 4.21: Relative-energy plots for the ^{9}Be(^{13}C,^{13}C^{4}He)^{5}He reaction. The ^{13}C(T1), ^{4}He(T2) and ^{5}He (undetected) are designated by numbers 1, 2 and 3, respectively.

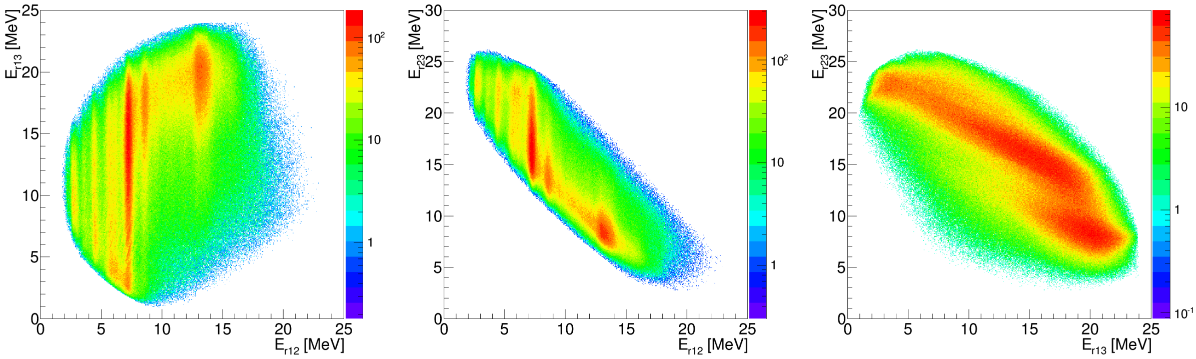

Figure 4.22: Relative-energy plots for the ^{9}Be(^{13}C,^{13}C^{4}He)^{5}He reaction. The ^{4}He(T1), ^{13}C(T2) and ^{5}He (undetected) are designated by numbers 1, 2 and 3, respectively.

The E_r-E_r plots for the T1-T2, T2-T1, T1-T4 and T2-T3 coincidences are displayed on the Figs. 4.21, 4.22, 4.23 and 4.24, respectively. Plots of the T1-T2 and the T2-T1 ^{13}C+^{4}He show a number of well-defined loci corresponding to the excited stated of the ^{17}O. No other strong loci are visible on the plots. The only visible loci on the E_r-E_r plots for the T1-T4 and T2-T3 coincidences are the $E_{\text{r}23}$ loci corresponding to the excited states of the ^{9}Be.

The excitation energy spectra were obtained by adding the relevant excitation energy thresh-

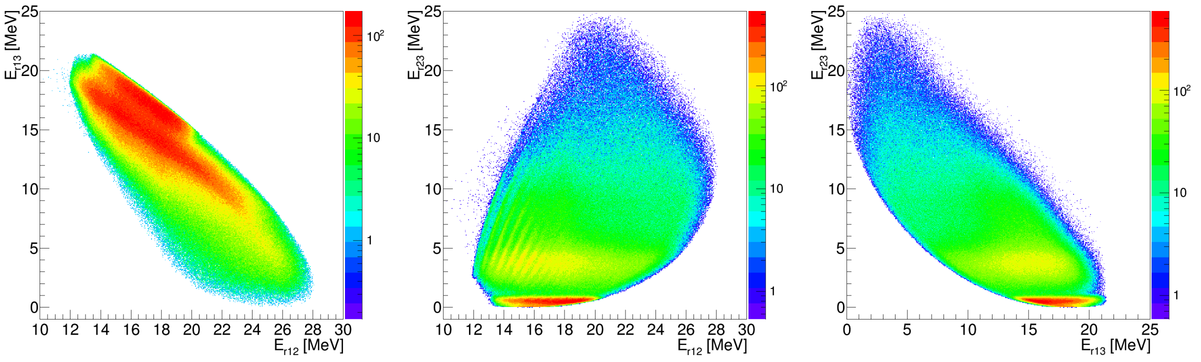

Figure 4.23: Relative-energy plots for the ^{9}Be(^{13}C,^{13}C^{4}He)^{5}He reaction. The ^{13}C(T1), ^{4}He(T4) and ^{5}He (undetected) are designated by numbers 1, 2 and 3, respectively.

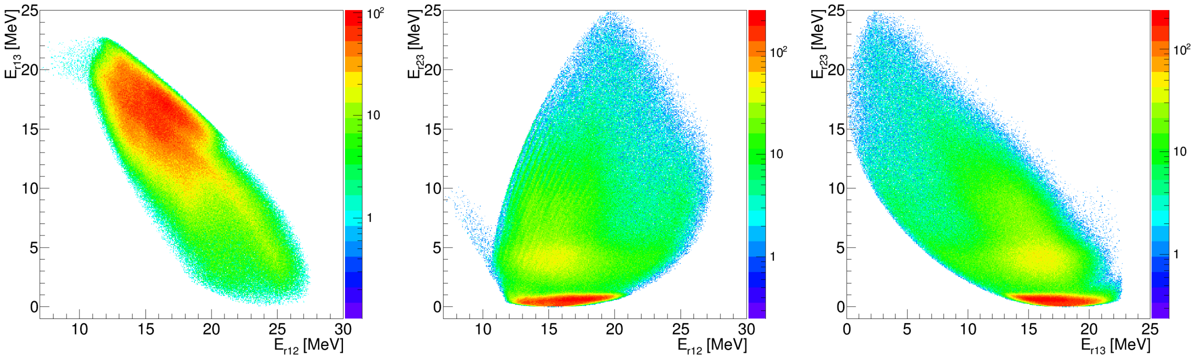

Figure 4.24: Relative-energy plots for the ^{9}Be(^{13}C,^{13}C^{4}He)^{5}He reaction. The ^{13}C(T2), ^{4}He(T3) and ^{5}He (undetected) are designated by numbers 1, 2 and 3, respectively.

old to the relative energy:

$$E_x = E_r + E_{\text{thr.}}, \tag{4.31}$$

where $E_{\text{thr.}} = 6.359$ MeV. The excitation energy spectrum of the ^{17}O is displayed in the Fig. 4.25. The green spectrum is not altered, while the excitation energy of the red one had to be adjusted by -0.150 MeV for two plots to overlap.

The Fig. 4.25 shares the principal features with the Fig. 4 of the [6], but spans a slightly larger excitation energy range and has an improved statistics.

The strongest peak at 13.58 MeV matches the one previously published. The other peaks observed in Ref. [6] are the 10.8 MeV and the 14.9 MeV peak, together with two groups of unresolved group of peaks at $E_x \approx$12 and 19 MeV. Two additional peaks, not visible in Ref. [6] are located at $E_x \approx 9.15$ and 10.0 MeV.

One can proceed to the ^{9}Be(^{13}C,^{13}C($E_x = 3.7$ MeV)^{4}He)^{5}He reaction. That reaction channel has been selected by setting a graphical cut on appropriate locus on the $E_{\text{det}}^{^{13}\text{C}}$-$Q$ plots.

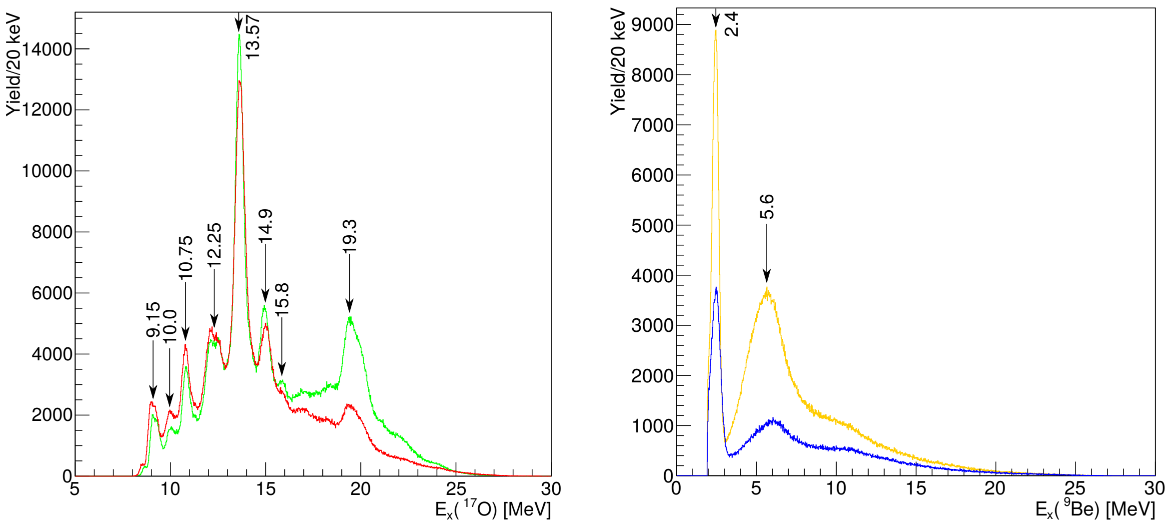

Figure 4.25: **Left:** The excitation energy spectrum of the ^{17}O reconstructed from the ^{13}C+^{4}He coincident events in detector telescopes T1-T2 (red) and T2-T1 (green). The position of T1-T2 spectrum was adjusted by -0.150 MeV to match the T2-T1 one. **Right:** The ^{9}Be excitation energy spectrum reconstructed from T1-T4 (orange) and T2-T3 (blue) coincident events, both adjusted by -0.4 MeV for peaks to match the known states.

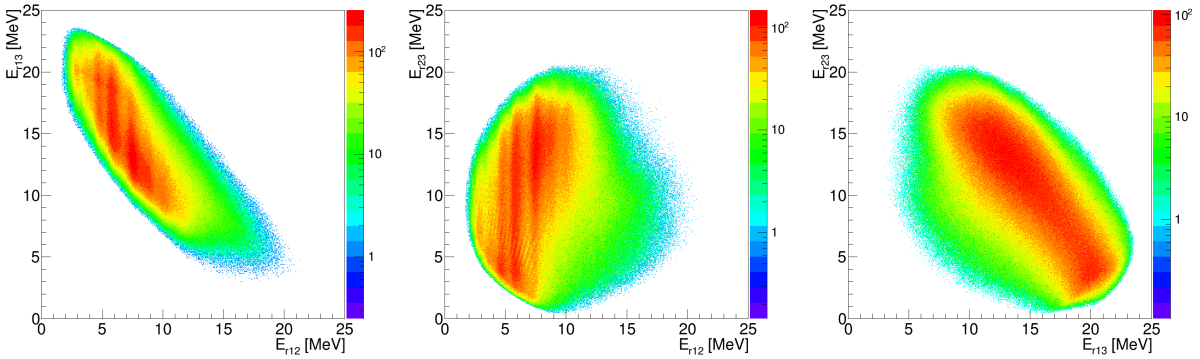

Figure 4.26: Relative-energy plots for the ^{9}Be(^{13}C,^{13}C($E_x = 3.7$ MeV)^{4}He)^{5}He reaction. The ^{13}C(T1), ^{4}He(T2) and ^{5}He (undetected) are designated by numbers 1, 2 and 3, respectively.

The E_r-E_r plots for the ^{13}C*(T1)-^{4}He(T2), ^{4}He(T1)-^{13}C*(T2), ^{13}C*(T1)-^{4}He(T4) and ^{13}C*(T2)-^{4}He(T3) are displayed on the Figs. 4.26, 4.27, 4.28 and 4.29, respectively.

The coincident events between the two front-angle detector telescopes have strong loci in the $E_{\mathrm{r}12}$, corresponding to the ^{17}O excited states. No other loci are visible. The Figs. 4.28 and 4.29 contain only the $E_{\mathrm{r}23}$ loci, corresponding to the ^{9}Be excited states.

The excitation energy spectra for the ^{13}C*(T1)-^{4}He(T2) and the ^{4}He(T1)-^{13}C*(T2) coincident events are displayed in the Fig. 4.30, in red and green, respectively. This spectra in principle could be compared to the Fig. 4.b) in Ref. [6]. However, the ^{17}O spectrum in [6] is mistaken: the spectrum begins at $E_x \approx$10 MeV and so does the spectrum for the ground-state

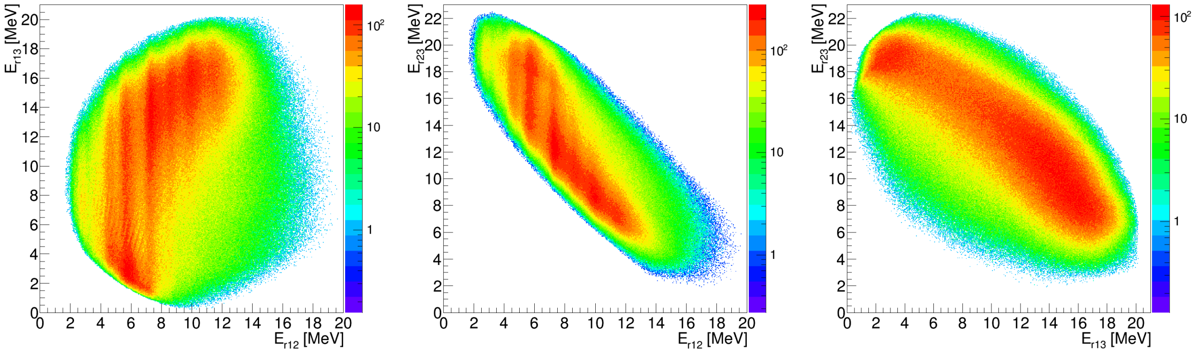

Figure 4.27: Relative-energy plots for the ^{9}Be(^{13}C,^{13}C($E_x = 3.7$ MeV)^{4}He)^{5}He reaction. The ^{4}He(T1), ^{13}C(T2) and ^{5}He (undetected) are designated by numbers 1, 2 and 3, respectively.

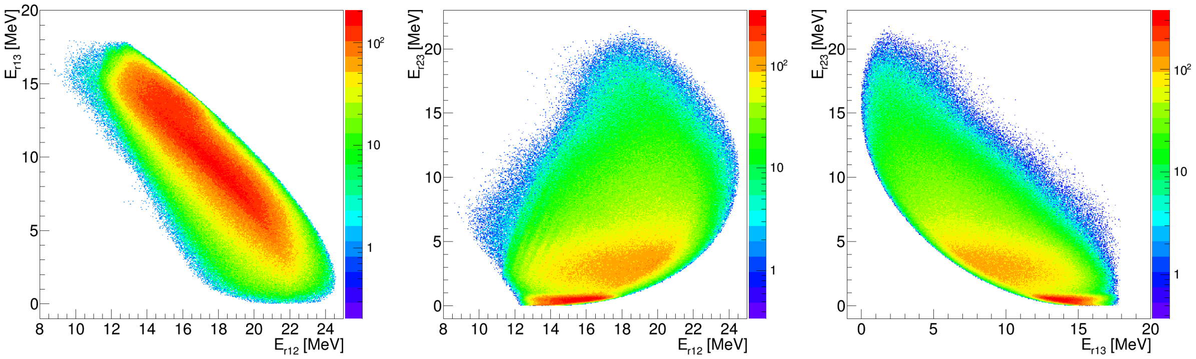

Figure 4.28: Relative-energy plots for the ^{9}Be(^{13}C,^{13}C($E_x = 3.7$ MeV)^{4}He)^{5}He reaction. The ^{13}C(T1), ^{4}He(T4) and ^{5}He (undetected) are designated by numbers 1, 2 and 3, respectively.

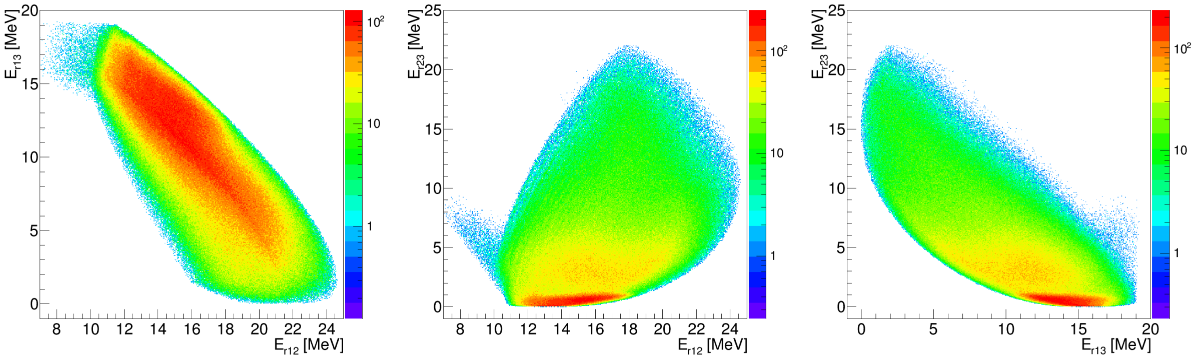

Figure 4.29: Relative-energy plots for the ^{9}Be(^{13}C,^{13}C($E_x = 3.7$ MeV)^{4}He)^{5}He reaction. The ^{13}C(T2), ^{4}He(T3) and ^{5}He (undetected) are designated by numbers 1, 2 and 3, respectively.

channel coincidences. This is not possible due to the ^{13}C excitation energy which had to be added to the sum of the relative energy E_r and the decay threshold E_{decay} in the calculation of the excitation energy E_x. Therefore when commenting on that spectrum each excitation energy will be shifted by $+3.7$ MeV. To make comparison easier, the corrected version of the plot 4.b) is displayed in the Fig. 4.31 (the labels of the peaks for the panel b) have been modified, too).

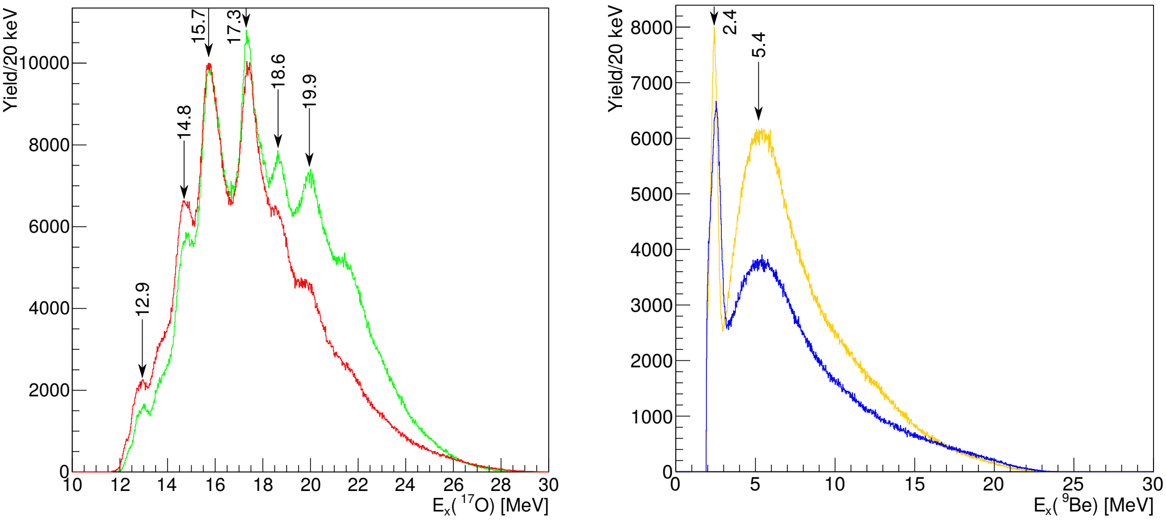

Figure 4.30: Left: The excitation energy spectrum of the ^{17}O reconstructed from the $^{13}C^*(E_x \approx 3.7\text{ MeV}) + {}^4$He coincident events in detector telescopes T1-T2 (red) and T2-T1 (green). The position of T1-T2 spectrum was adjusted by -0.150 MeV to match the T2-T1 one. **Right:** The ^{9}Be excitation energy spectrum reconstructed from T1-T4 (orange) and T2-T3 (blue) coincident events, both adjusted by -0.4 MeV.

The excitation energy spectra of ^{9}Be reconstructed from the $^{13}C^*$+^{4}He coincident events are displayed in the Fig. 4.30 right. The 2.4 MeV peak corresponding to the 2.4294 MeV $\frac{5}{2}^-$ state is still visible. The centre of the broad peak is located at $E_x = 5.4$ MeV, its shape changed in comparison to the shape of the peak obtained from the ground state reaction channel. Multiple states between $E_x = 3$ and 7.5 MeV can contribute to this peak [82].

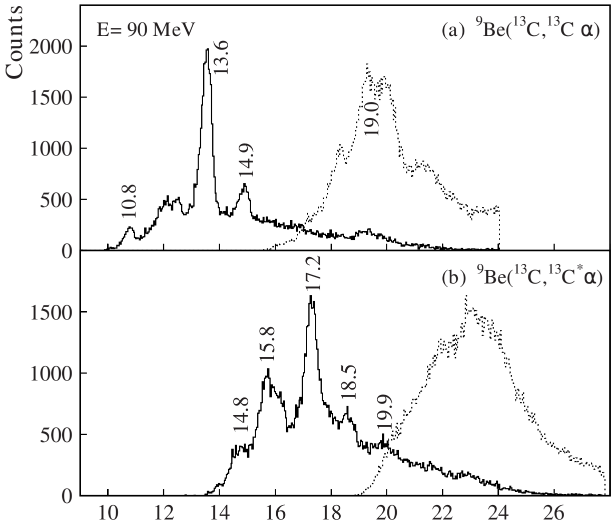

Figure 4.31: The corrected version of the ^{17}O excitation energy spectrum reconstructed from the $^{13}C + {}^4$He and the $^{13}C^*(E_x \approx 3.7\text{ MeV}) + {}^4$He coincident events, published in [6]. The position of the plots on the b) panel were adjusted by +3.7 MeV. See text for details.

4.3.2 The ^{9}Be+^{13}C→^{14}C+^{4}He+^{4}He reaction

The ^{9}Be+^{13}C→^{14}C+^{4}He+^{4}He reaction, $Q = 6.604$ MeV, was studied to obtain the data on the excited states of the ^{18}O nucleus decaying to the ^{14}C+^{4}He reaction channel. The ^{14}C nuclei were identified using the ΔE-E technique in the front-angle detector telescopes T1 and T2, while ^{4}He nuclei were identified in all of the detector telescopes.

The Catania plot for the T1-T2 coincidences is displayed in the Fig. 4.32. Three loci are visible: one corresponding to the ground state of all particles in the exit channel, the second one corresponding to the reaction channel with the ^{14}C($E_x \approx 7.0$ MeV), $Q \approx -0.4$ MeV (6.0 MeV $<$ E_x(^{14}C) $<$ 8.0 MeV) and the last one, with slightly different slope, that doesn't correspond to any particle bound ^{14}C excited state. The slope of the first two loci is in accordance with the prediction (red line). As in for the other cases, the lines denoting the reaction loci were adjusted by +1.0 MeV in $\tilde{E}$ to overlap with the data. The corresponding Q-value spectrum is displayed on the right side of the same figure and shows two prominent peaks.

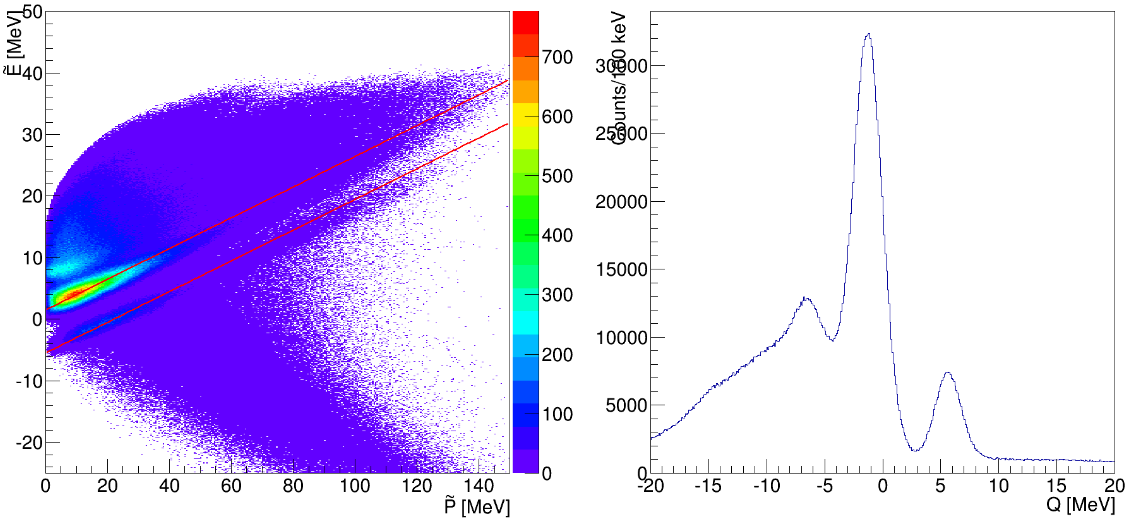

Figure 4.32: Left: The Catania plot for the ^{9}Be(^{13}C,^{14}C ^{4}He) reaction, ^{14}C detected in the T1 and ^{4}He in the T2. The two red lines are denoting the position of reaction loci for the undetected ^{4}He: the lowest for all nuclei in the ground state and the second one for the reaction channel with the ^{14}C($E_x \approx 7$ MeV). The lines were shifted by +1.0 MeV to reproduce the data. **Right:** The corresponding Q-value spectrum.

Now the issue of the third locus will be addressed. The strongest carbon locus in the ΔE-E plot is the ^{13}C locus. The energy-loss straggling contributes to the finite width of the particle-identification locus, thus mixing the carbon loci at their respective borders. Therefore, despite the narrow cuts which were employed to select the ^{14}C, some ^{13}C contamination was inevitable. To check for the contamination, ^{14}C+^{4}He coincidences were processed as if they

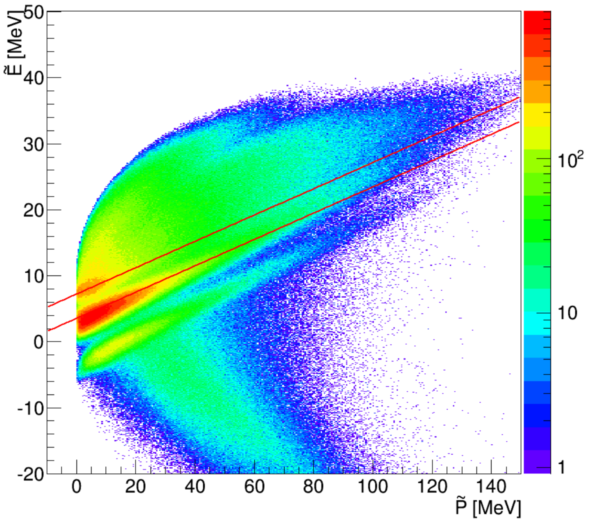

Figure 4.33: Catania plot for the ^{9}Be(^{13}C,^{14}C ^{4}He) reaction, ^{14}C detected in the T1 and ^{4}He in the T2, where the calculation was performed as if the detected particles were the ^{13}C and the ^{4}He. The two red lines are denoting the position of reaction loci for the undetected ^{5}He: the lowest for all nuclei in the ground state and the second one for the reaction channel with the ^{13}C($E_x = 3.7$ MeV). The lines were shifted by +1.0 MeV, as for the Fig. 4.32.

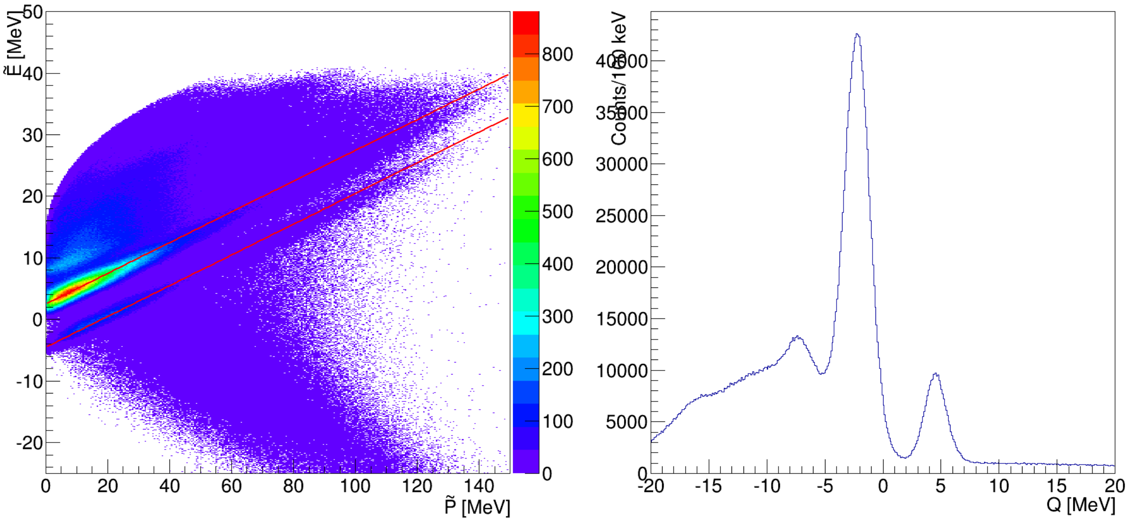

Figure 4.34: Left: The Catania plot for the ^{9}Be(^{13}C,^{14}C ^{4}He) reaction, ^{4}He detected in the T1 and ^{14}C in the T2. The two red lines are denoting the position of reaction loci for the undetected ^{4}He: the lowest for all nuclei in the ground state and the second one for the reaction channel with the ^{14}C($E_x = 7$ MeV). The lines were shifted by +2.0 MeV to reproduce the data. **Right:** The corresponding Q-value spectrum.

were ^{13}C+^{4}He coincidences and the position of the loci corresponding to the undetected ^{5}He was calculated (see Fig. 4.33). The red lines denoting loci were shifted by the same amount as for the previous plot. Two red lines depict the predicted loci for the ground state reaction channel ^{13}C+^{4}He+^{5}He and the ^{13}C($E_x = 3.7$ MeV)+^{5}He+^{4}He reaction channel. It is clear that the unknown locus fits the latter channel very well. Next a brief comment on the intesity of the locus in question. As seen in the previous section on the ^{9}Be+^{13}C→^{13}C+^{4}He+^{5}He reaction, the ^{13}C($E_x = 3.7$ MeV)+^{5}He+^{4}He reaction channel is stronger for the forward-angle coincident events (T1-T2 and T2-T1) than the ground-state channel. Thus the locus for the ground-state channel is not clearly visible, although it is overlapping with the strongest locus, while the locus for the reaction channel with ^{13}C($E_x = 3.7$ MeV) excited state is well defined on the plot. Further means of separating the spurious locus could be the E_{det}-Q and the ϑ_{det}-Q plots.

The ^{14}C(T2)-^{4}He(T1) coincident events give Catania plot with higher statistics than the one for the T1-T2 coincident events. Two well-shaped loci are visible, matching the slope of the calculated lines. The lines were shifted by +2.0 MeV in order to reproduce the data. The Q-value spectrum shows two prominent peaks, slightly narrower than the ones for the T1-T2 coincidences.

The Catania plot of the T1-T4 coincident events shows two narrow loci perfectly matching the slope of the calculated lines. The lines had to be shifted by +0.25 MeV in order to overlap with the data. The corresponding Q-value plot shows two prominent peaks very close to the actual Q-values. The T2-T3 coincident events give the Catania plot with the same features as for the T1-T4 coincidences, only with lower statistics, which can be understood in terms of smaller angular coverage, and slightly higher offset of the loci (+0.5 MeV).

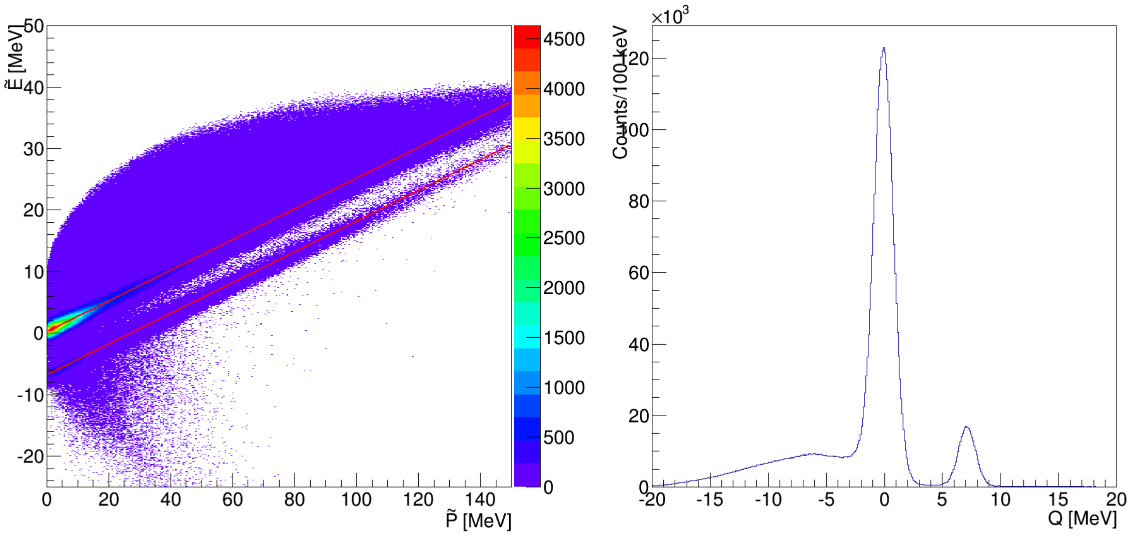

Figure 4.35: Left: The Catania plot for the ^{9}Be(^{13}C,^{14}C ^{4}He) reaction, ^{14}C detected in the T1 and ^{4}He in the T4. The two red lines are denoting the position of reaction loci for the undetected ^{4}He: the lowest for all nuclei in the ground state and the second one for the reaction channel with the ^{14}C($E_x = 7$ MeV). The lines were shifted by -0.25 MeV to reproduce the data. **Right:** The corresponding Q-value spectrum.

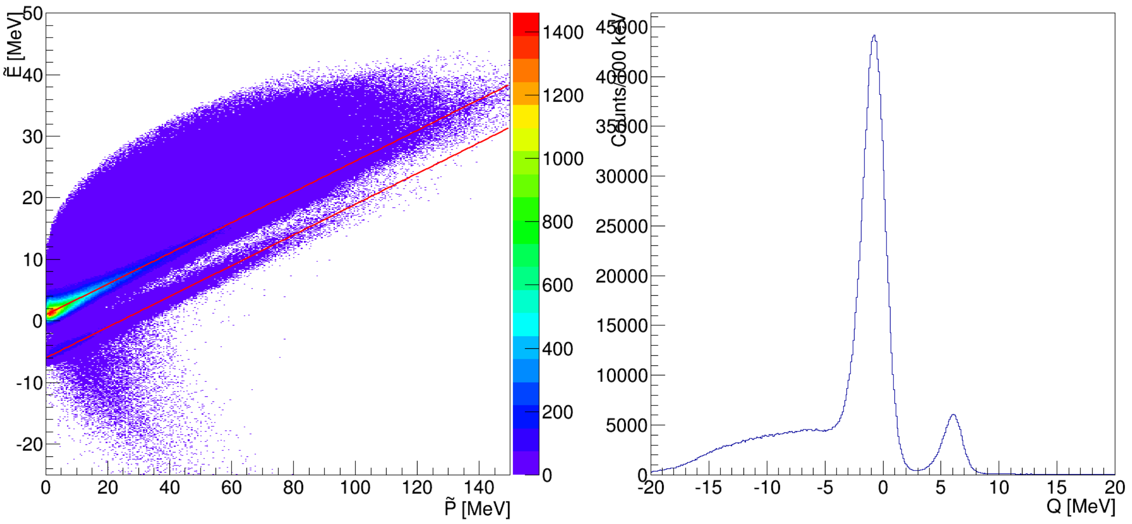

Figure 4.36: Left: The Catania plot for the ^{9}Be(^{13}C,^{14}C ^{4}He) reaction, ^{14}C detected in the T2 and ^{4}He in the T3. The two red lines are denoting the position of reaction loci for the undetected ^{4}He: the lowest for all nuclei in the ground state and the second one for the reaction channel with the ^{14}C($E_x = 7$ MeV). The lines were shifted by +0.5 MeV to reproduce the data. **Right:** The corresponding Q-value spectrum.

The E_{det}-Q and the ϑ_{det}-Q plots for all the aforementioned detector-telescope combinations can be found in the Appendix B. The energy and angle versus Q-value spectra of the ^{14}C(T1)-^{4}He(T2), ^{14}C(T2)-^{4}He(T1), ^{14}C(T1)-^{4}He(T4) and ^{14}C(T2)-^{4}He(T3) coincident events are displayed on the Figs. B.1, B.2, B.3 and B.4, respectively. The general features of all the aforementioned plots are the Q-value loci independent on the detection angle and the detected energy. The Q-value locus of the ^{13}C($E_x = 3.7$ MeV)+^{5}He+^{4}He reaction is strong only for the E_{det} region $E_{\text{det}}^{^{13}\text{C}} < 40$ MeV. In that detected-energy region a broadening of the the^{14}C($E_x = 7$ MeV)+^{4}He+^{4}He locus is observed, which is absent for the ground-state locus. The most probable reason for it is the contribution of the ^{13}C$_{\text{gs}}$+^{5}He+^{4}He events to the locus in the question. Hence a narrow cut is used on the $E_{\text{det}}^{^{14}\text{C}}$-$Q$ plot, to rule out the contribution of possible undesired events. An example of the cuts is displayed in the Fig. 4.37. The weak horizontal loci at the top of the figure correspond to the pile-up events.

The ^{14}C+^{4}He+^{4}He reaction channel can be populated via intermediate excited states of the ^{8}Be and the ^{18}O. All the daughter nuclei that are decay products of the mother nucleus decaying from its particular excited state form a locus in their relative energy. Therefore, by examining the relative-energy plots one can deduce which excited state of particular nuclei are populated in the first step of the reaction. The E_r-E_r plots for the ^{14}C(T1)-^{4}He(T2) coincident events are displayed in the Fig. 4.38. All the loci on the three E_r-E_r plots are the lines of the constant E_{r12},

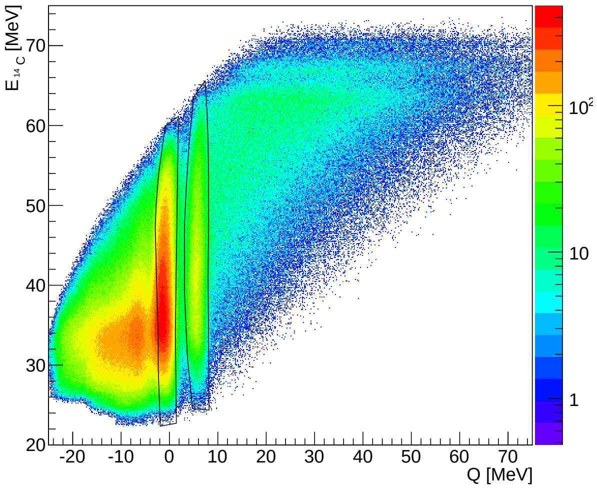

Figure 4.37: The $E_{\mathrm{det}}^{^{14}\mathrm{C}}$-$Q$ spectrum for the ^{14}C(T1)-^{4}He(T2) coincident events. Graphical cuts used to select the ground state and the ^{14}C(E_x =7 MeV) channel are displayed. See text for details.

corresponding to the excited states of the ^{18}O. No loci in $E_{\mathrm{r}13}$ or $E_{\mathrm{r}23}$ are visible.

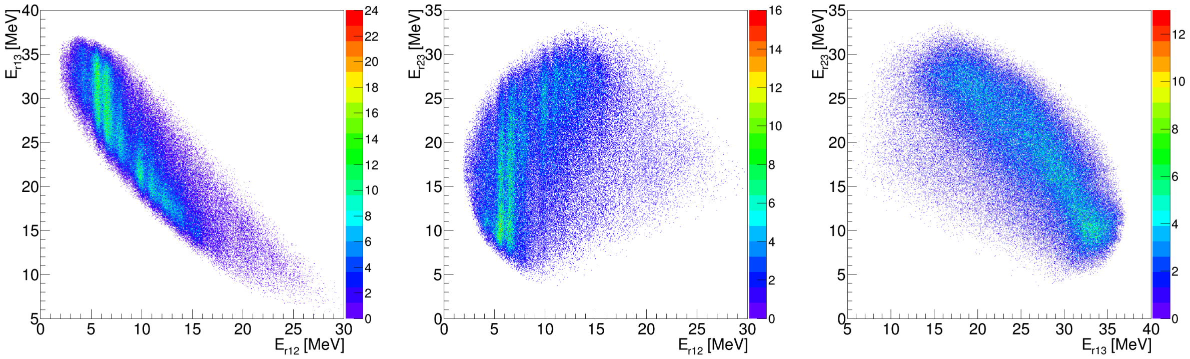

Figure 4.38: Relative-energy plots for the ^{9}Be(^{13}C,^{14}C^{4}He)^{4}He reaction. The ^{14}C(T1), ^{4}He(T2) and ^{4}He (undetected) are designated by numbers 1, 2 and 3, respectively.

The E_r-E_r spectra for the ^{4}He(T1)+^{14}C(T2) coincidences are displayed in the Fig. 4.39. Due to a different ordering of outgoing particles (particle 1 is the detected ^{4}He and particle 2 the detected ^{14}C) the axis of the plots are changed. However, plots show the same features as the previous one. The statistics and the resolution are a bit better than for the previous detector combination.

The ^{14}C(T1)-^{4}He(T4) and the ^{14}C(T2)-^{4}He(T3) coincident events show new features. Due to the difference in the detection angle now loci of the $E_{\mathrm{r}13}$ and $E_{\mathrm{r}23}$ are visible. The $E_{\mathrm{r}13}$ loci are corresponding to the excited states of the ^{18}O decaying to the ^{14}C and the undetected ^{4}He, while $E_{\mathrm{r}23}$ loci correspond to the ^{8}Be decaying to a pair of α-particles, one of which is detected. Three prominent loci are visible for both ^{18}O and ^{8}Be, most clearly seen in the $E_{\mathrm{r}23}$-$E_{\mathrm{r}13}$ of the

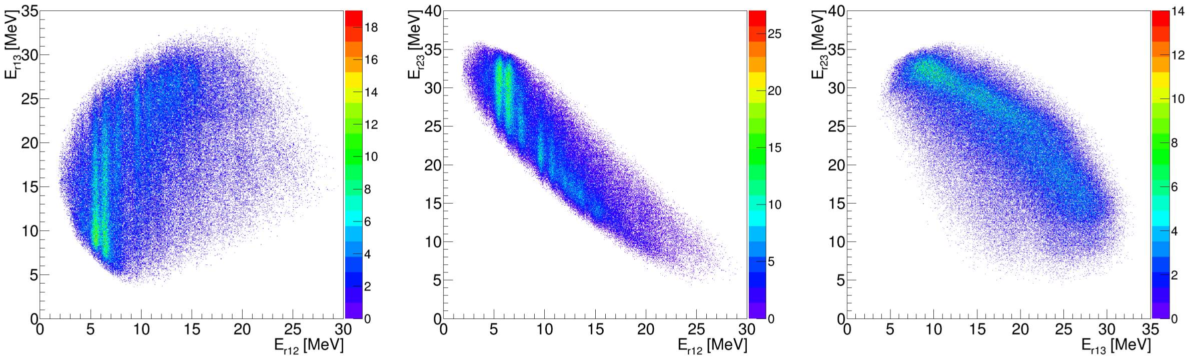

Figure 4.39: Relative-energy plots for the ^{9}Be(^{13}C,^{14}C^{4}He)^{4}He reaction. The ^{4}He(T1), ^{14}C(T2) and ^{4}He (undetected) are designated by numbers 1, 2 and 3, respectively.

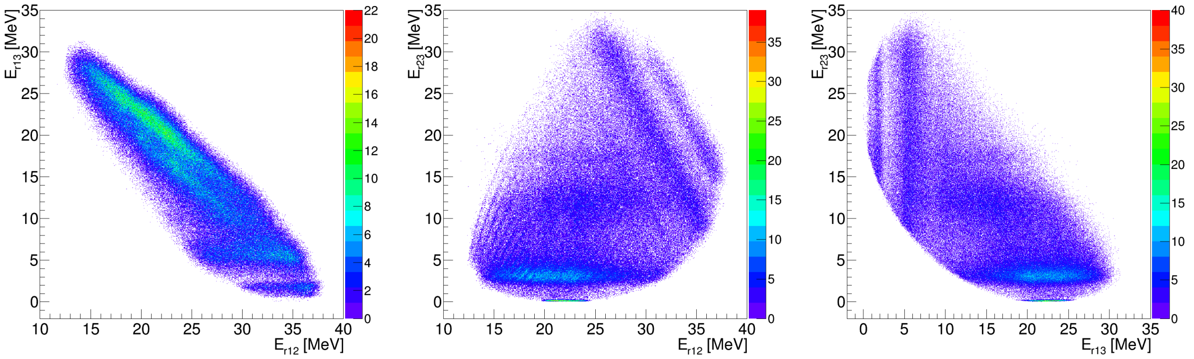

Figure 4.40: Relative-energy plots for the ^{9}Be(^{13}C,^{14}C^{4}He)^{4}He reaction. The ^{14}C(T1), ^{4}He(T4) and ^{4}He (undetected) are designated by numbers 1, 2 and 3, respectively.

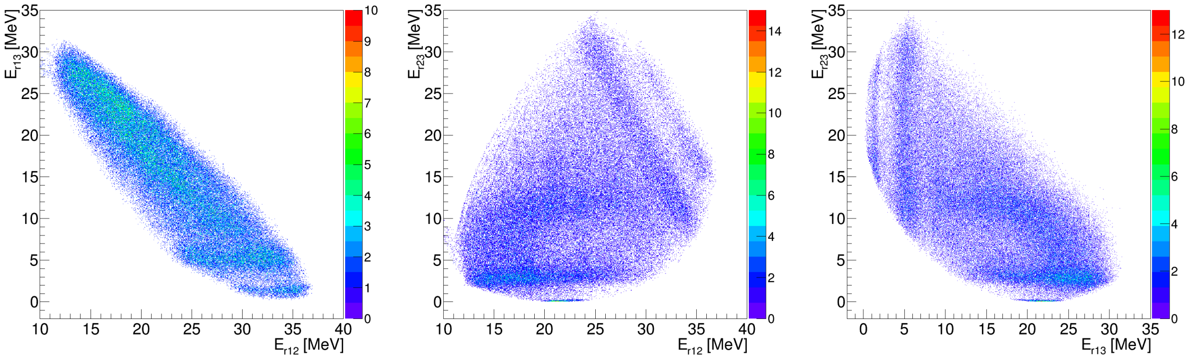

Figure 4.41: Relative-energy plots for the ^{9}Be(^{13}C,^{14}C^{4}He)^{4}He reaction. The ^{14}C(T2), ^{4}He(T3) and ^{4}He (undetected) are designated by numbers 1, 2 and 3, respectively.

Figs. 4.40 and 4.41.

Now one can use the relative energies to calculate the excitation energy of the mother nu-

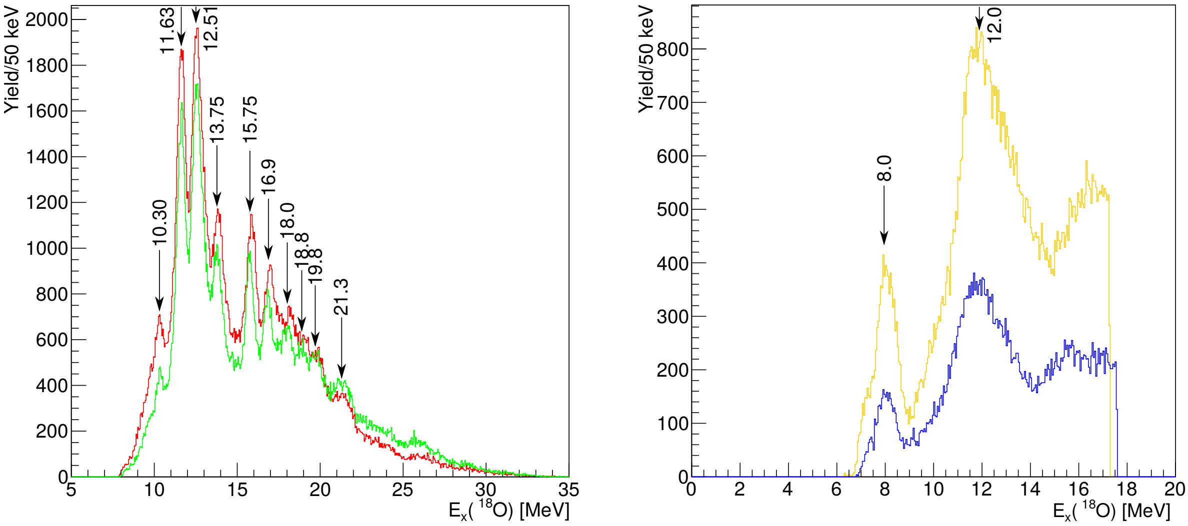

Figure 4.42: Left: The ^{18}O excitation energy spectra. The red line denotes the spectrum from the ^{14}C(T1)+^{4}He(T2) coincident events and the green line the spectrum from the ^{14}C(T2)+^{4}He(T1) coincident events. Spectra were adjusted by -0.300 MeV and -0.170 MeV to overlap and match the published α-decaying ^{18}O excited states for the T1-T2 and the T2-T1 coincident events, respectively. **Right:** The ^{18}O excitation energy spectra for the ^{14}C(T1)+^{4}He(T4) (orange line) and the ^{14}C(T2)+^{4}He(T3) (blue line) coincident events. The ^{14}C(T2)+^{4}He(T3) spectrum was adjusted by $+0.300$ MeV.

cleus. The relevant decay thresholds are:

$$E^{\text{threshold}}_{^{8}\text{Be}\to{}^{4}\text{He}^{4}\text{He}} = -0.092 \text{ MeV} \tag{4.32}$$

$$E^{\text{threshold}}_{^{18}\text{O}\to{}^{14}\text{C}^{4}\text{He}} = 6.228 \text{ MeV}. \tag{4.33}$$

In order to separate the E_{r13} from the E_{r23} loci in the Figs. 4.40 and 4.41 the following conditions were set:

$$E_x^{^{18}\text{O}} = E_{\text{r13}} + E^{\text{threshold}}_{^{18}\text{O}\to{}^{14}\text{C}^{4}\text{He}}, \quad E_{\text{r13}} < 11.0 \text{ MeV} \tag{4.34}$$

$$E_x^{^{8}\text{Be}} = E_{\text{r23}} + E^{\text{threshold}}_{^{8}\text{Be}\to{}^{4}\text{He}^{4}\text{He}}, \quad E_{\text{r13}} \geq 11.0 \text{ MeV}. \tag{4.35}$$

For the Figs. 4.38 and 4.39 the entire E_{r12} range could be used for the $E_x^{^{18}\text{O}}$ calculation without any restrictions.

The excitation energy spectra for the ^{18}O obtained from the ^{14}C(T1)+^{4}He(T2) and the ^{14}C(T2)+^{4}He(T1) were shifted in the excitation energy to overlap: ^{14}C(T1)+^{4}He(T2) was moved by -0.130 MeV. The two aforementioned spectra show good consistency up to the $E_x \approx$16 MeV. For excitation energies higher than 16 MeV there is a systematic shift of approx. 0.120 MeV between these two spectra. The peaks were identified by comparing the spectra with the data published in Ref. [14] and in Ref. [12]. A systematic shift of the spectra amounting to 0.170 MeV was observed and corrected for.

The final spectra are displayed on the left part of the Fig. 4.42. Ten peaks are visible in both spectra.

The excitation energy spectra of the ^{8}Be are displayed in the Fig. 4.43. The plot shows the ground-state and the first excited state (3.03 MeV 2^{+}) of the ^{8}Be. The third excited state at the 11.35 MeV is also present and possible doublet at the higher excitations. The ground state of the ^{8}Be can serve as a check of resolution and systematic errors. The ground state should be positioned at 0 MeV. For the ^{14}C(T1)+^{4}He(T4) and the ^{14}C(T2)+^{4}He(T3) coincident events the peak is located at 0.018 MeV and -0.030 MeV, respectively. The full width at half maximum of the two peaks is 0.12 MeV for the ^{14}C(T1)+^{4}He(T4) and the 0.14 MeV for the ^{14}C(T2)+^{4}He(T3) coincident events.

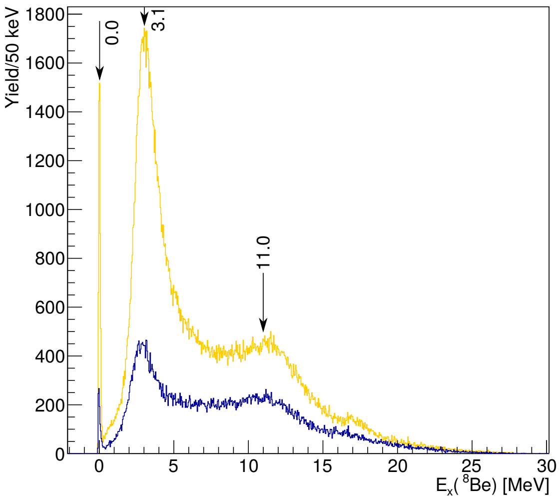

Figure 4.43: The ^{8}Be excitation energy spectra. The orange line denotes the spectrum from the ^{14}C(T1)+^{4}He(T4) coincident events and the blue line the spectrum from the ^{14}C(T2)+^{4}He(T3) coincident events.

Finally the excitation energy spectra for the ^{14}C($E_x \approx 7$ MeV)+^{4}He coincident events are presented. Let us start with the E_r-E_r spectra. The E_r-E_r plots for the ^{14}C*(T1)+^{4}He(T2) and the the ^{14}C(T2)*+^{4}He(T1) coincident events are displayed on the Figs. 4.44 and 4.45, respectively. The only strong loci are corresponding to the states of the ^{18}O. There is a hint of a weak ^{8}Be locus at $E_{\mathrm{r}13} \approx 11.5$ MeV, corresponding to its third excited state. The part of the spectrum contaminated by that locus wasn't removed because it was estimated that the influence of the

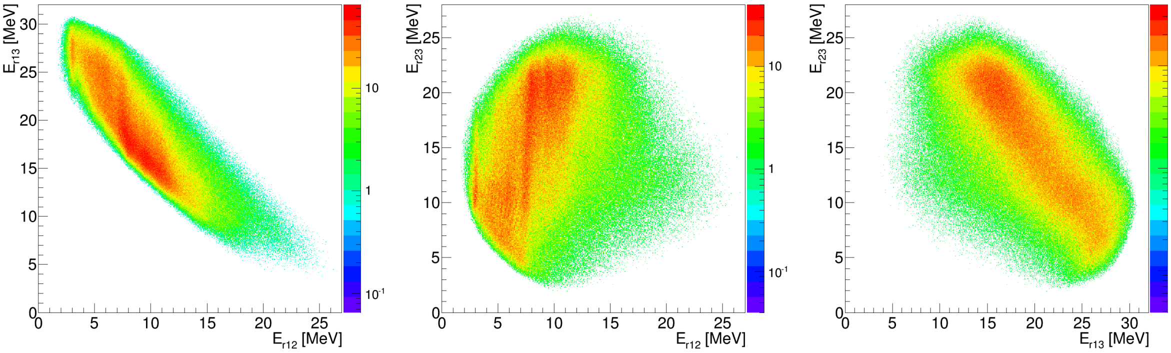

Figure 4.44: Relative-energy plots for the ^{9}Be(^{13}C,^{14}C($E_x \approx 7$ MeV)^{4}He)^{4}He reaction. The ^{14}C(T1), ^{4}He(T2) and ^{4}He (undetected) are designated by numbers 1, 2 and 3, respectively.

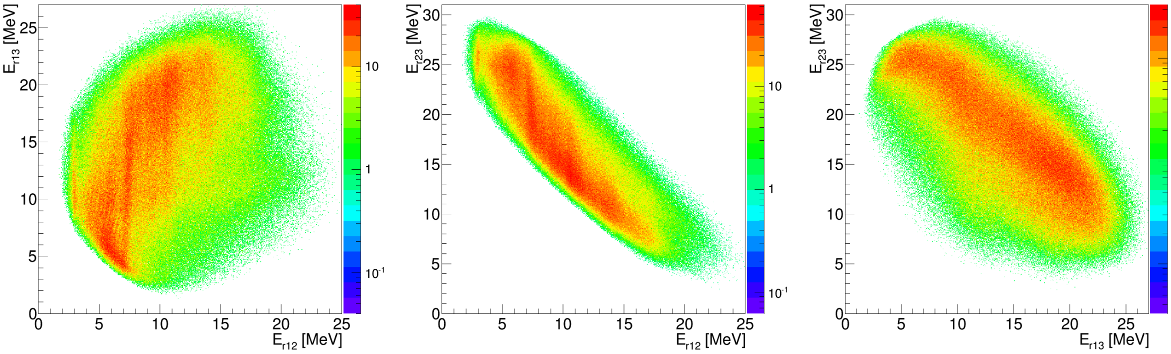

Figure 4.45: Relative-energy plots for the ^{9}Be(^{13}C,^{14}C($E_x \approx 7$ MeV)^{4}He)^{4}He reaction. The ^{4}He(T1), the ^{14}C(T2), and ^{4}He (undetected) are designated by numbers 1, 2 and 3, respectively.

^{8}Be locus is much weaker than the ^{18}O loci. The ^{18}O loci are slightly angled, instead of being vertical, which would cause undesirable broadening of peaks when projected.

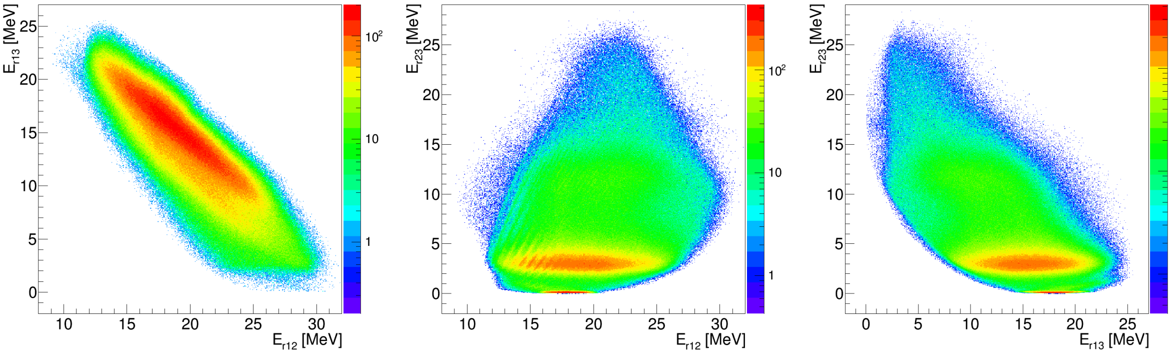

Figure 4.46: Relative-energy plots for the ^{9}Be(^{13}C,^{14}C($E_x \approx 7$ MeV)^{4}He)^{4}He reaction. The ^{14}C(T1), ^{4}He(T4) and ^{4}He (undetected) are designated by numbers 1, 2 and 3, respectively.

On the other hand, on the Figs. 4.46 and 4.47, displaying the E_r-E_r plots for the ^{14}C*(T1)+^{4}He(T4) and ^{14}C*(T2)+^{4}He(T3) coincident events respectively, the only strong loci are corresponding to

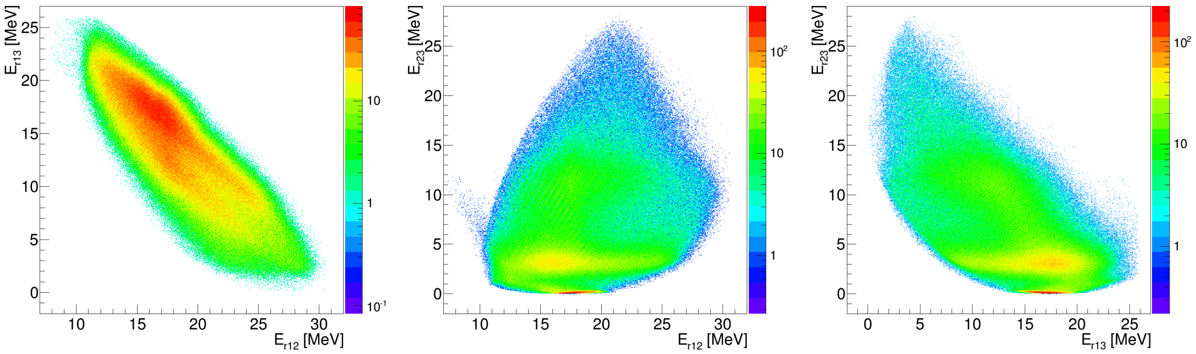

Figure 4.47: Relative-energy plots for the ^{9}Be(^{13}C,^{14}C($E_x \approx 7$ MeV)^{4}He)^{4}He reaction. The ^{14}C(T2), ^{4}He(T3) and ^{4}He (undetected) are designated by numbers 1, 2 and 3, respectively.

the excited states of the ^{8}Be. On the latter plot a hint of ^{18}O locus at $E_{\mathrm{r}12} \approx 17$ MeV is present.

After reviewing the E_r-E_r plots, the excitation energy spectra follow. As it was mentioned before, the ^{18}O loci are not exactly perpendicular to the $E_{\mathrm{r}12}$ axis. Therefore, the loci will be projected at an angle determined from the angle of the strongest locus. The lines traversing the strongest loci were defined as:

$$\text{T1-T2} \qquad E_{\mathrm{r}23} = 20.0 \cdot E_{\mathrm{r}12} - 140.0\,\mathrm{MeV} \tag{4.36}$$

$$\text{T2-T1} \qquad E_{\mathrm{r}13} = 30.0 \cdot E_{\mathrm{r}12} - 210.0\,\mathrm{MeV} \tag{4.37}$$

The projection along the slope of the strongest locus was performed using the formulae:

$$\text{T1-T2} \qquad E'_{\mathrm{r}12} = E_{\mathrm{r}12} - \frac{E_{\mathrm{r}23}}{20.0} \tag{4.38}$$

$$\text{T2-T1} \qquad E'_{\mathrm{r}12} = E_{\mathrm{r}12} - \frac{E_{\mathrm{r}13}}{30.0}, \tag{4.39}$$

where the $E'_{\mathrm{r}12}$ is a projected relative energy used to calculate the $E_x(^{18}\mathrm{O})$. The influence of this correction on the projected excitation energy spectrum is small. The excitation energy plot for the T1-T2 coincident events was adjusted to overlap the low-excitation-energy region of the T2-T1 plot. The final plot is displayed in the Fig. 4.48. The peaks which are visible are designated with their excitation energies (or average of excitation energies if they differ in two spectra).

Finally, the ^{8}Be excitation energy plot for the ^{14}C*(T1)-^{4}He(T4) and ^{14}C*(T2)-^{4}He(T3) are displayed in the Fig. 4.48, denoted by orange and blue lines, respectively. Three prominent peaks are visible: the ground-state peak, the first excited state peak ($E_x = 3.03$ MeV 2^+) and

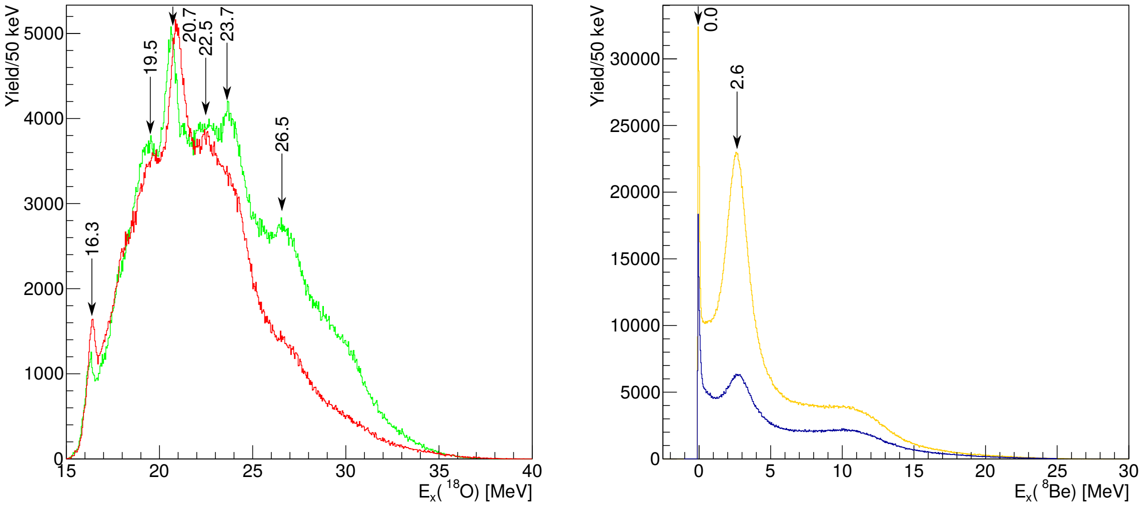

Figure 4.48: Left: The ^{18}O excitation energy spectrum reconstructed from the ^{14}C*+^{4}He coincidences (T1-T2 in red and T2-T1 in green). The slope of the loci was taken into account by projecting the $E_{\mathrm{r}12}$ along the direction of the strongest locus. See text for details. **Right:** The ^{8}Be excitation energy spectrum reconstructed from the ^{14}C*+^{4}He coincidences (T1-T4 in orange and T2-T3 in blue).

the 11.35 MeV excited state. A systematic shift between the spectra and the published data amounts to approx. 0.3 MeV.

4.3.3 The ^{9}Be+^{13}C$\rightarrow$^{12}C+^{6}He+^{4}He reaction

The study of the ^{9}Be(^{13}C,^{6}He^{12}C)^{4}He coincident events provides insight into the states of the ^{10}Be, ^{16}O and ^{18}O which might be populated in this reaction. The corresponding decay threshold is $E_{\text{thr}} = 18.38\,\text{MeV}$.

Of the three aforementioned nuclei, states of the ^{18}O decaying to this channel were of particular interest as such decay of the ^{18}O states has not been observed yet. The coincident events between the front-angle detector telescopes T1 and T2 allow for coincident detection of both ^{18}O* decay products. The ^{6}He+^{12}C coincident events between the front-angle (^{12}C detected) and mid-angle (T3, T4) detector telescopes (^{6}He detected) contain data on the ^{10}Be states. The same was observed for the ^{12}C(T1,T2)+^{4}He(T3,T4) coincidences: although a range of excitation energies in the ^{18}O is covered, no corresponding loci are observed. In these spectra only the known ^{10}Be ([83], [84], [85], [86]) states have been observed. Only the results for the front-angle coincidences are presented.

Due to the fact that this reaction channel is very weakly populated in the reaction, several steps were taken to achieve acceptable quality of the data. Let us start with the particle identification.

The carbon isotopes could be identified only in detector telescopes T1 and T2, both covering forward angles from approx. 10° to 30°. Helium isotopes can be identified in all of the detectors, however in the detector telescopes T1 and T2 the helium loci are subject to an intense pile-up. Due to the pile-up, no clear locus pertaining to the ^{6}He was visible. The pile-up was rejected by requiring an event in the telescope:

1. the multiplicity of good hits in the E-detector has to be equal to unity, and
2. the number of the ΔE-detector strips above the threshold has to be equal to unity.

The matrix of corresponding ΔE-strip - E_{front}-strip, mentioned before, was used as well. As one might observe, in that case the method for treating multiple hits in the neighbouring ΔE-detector strips becomes superfluous. The influence of the aforementioned conditions on the ΔE-E spectra is demonstrated in the Fig. 4.49. The left side plot shows a ΔE-E particle identification plot for the eighth ΔE strip of the T1 with the usual basic conditions for identifying good events. The plot on the right side shows an improved ΔE-E plot for the same strip and telescope, with new conditions applied. In order to show that the weak locus above the strong α-particle locus belongs to the ^{6}He, energy loss of the ^{4,6}He in the 20 μm of silicon was calculated and overlaid on the ΔE-E plot. A slight shift in the ΔE energy of -200 keV was applied to obtain an overlap with the data. The ^{12}C locus in the detector telescope T2 is well separated from the strongest

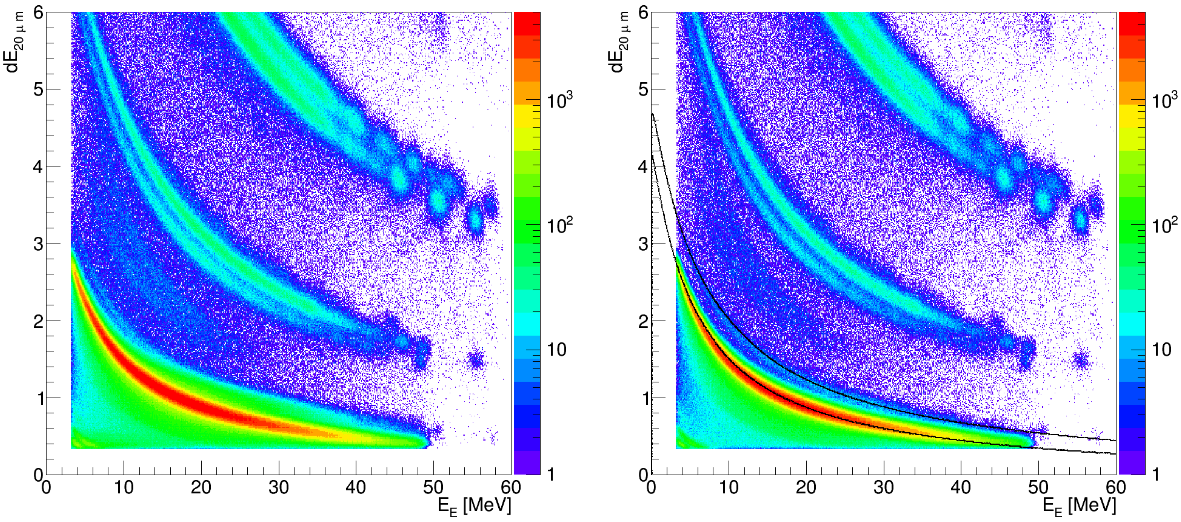

Figure 4.49: The ΔE-E plot for the T1 dE strip no. 8 without the strict requirements on multiplicity in both ΔE and E detector (left) and with them (right). A ^{6}He locus is visible after the multiplicity cuts were applied. The right-hand plot contains the energy loss calculation for the ^{4}He and ^{6}He in 20 μm thick silicon detector (black line). The resulting energy loss was shifted by -0.2 MeV for better agreement with the data.

^{13}C locus. However, a graphical cut was made narrow as much as possible in order to avoid the misidentification.

The other case, in which the ^{6}He is detected in the T2 and ^{12}C in the detector telescope T1, obtained under the same conditions, had much lower quality of data that did not allow for extracting clean spectra. A number of cuts were tried in order to resolve the problem, but to no avail. A source of the problem is probably the high rate suffered by the detector telescope T2 during the experiment. Once aforementioned conditions were applied, one could notice the ^{12}C locus was depleted of significant portion of events. At any rate, in the rest of this section only the results for the ^{6}He(T1)+^{12}C(T2) coincidences will be discussed.

The Catania plot of the ^{6}He(T1)-^{12}C(T2) coincidences is presented in the Fig. 4.50. The quality of the data can be also seen in the plot of the Q-value of reactions versus energies and angles of detected particles (Fig. 4.51). The loci are well separated, the background is low and most importantly, there is no significant Q-value dependence on neither the energy nor the angle of detected particles. Now the reaction channel with all the outgoing nuclei in the ground state can be selected from the Q-value plot. The relative-energy spectra for all the combinations of the outgoing particles is displayed in the Fig. 4.52. The pronounced feature of the plots is a strong, approx. 1 MeV wide locus in E_{r12}, located between 8 and 9 MeV. The locus is

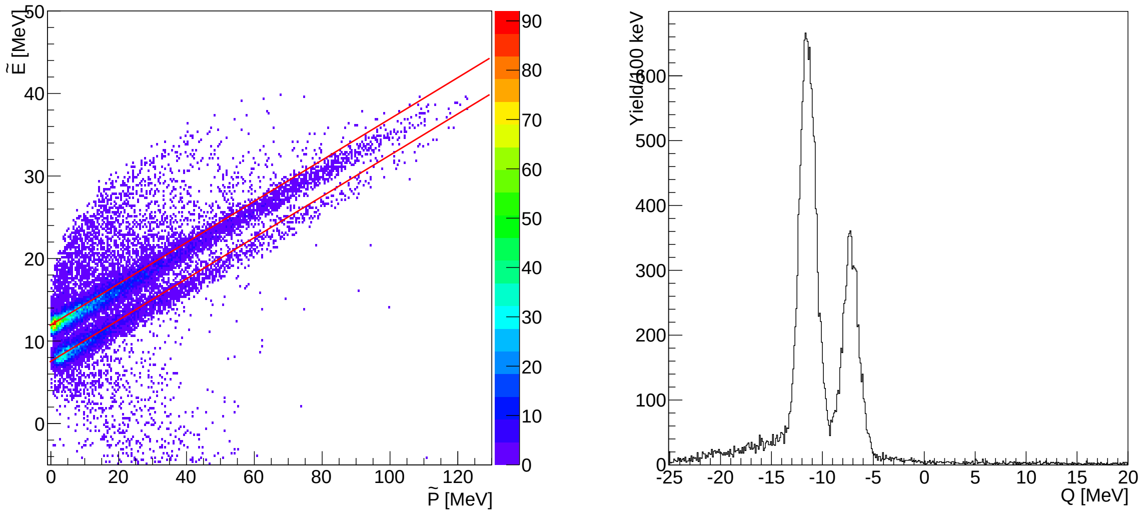

Figure 4.50: Left: The Catania plot for the ^{9}Be(^{13}C,^{6}He^{12}C) reaction. The ^{6}He and ^{12}C nuclei were detected in detector telescopes T1 and T2, respectively. The loci designated by the red lines are the predicted loci for the ^{9}Be(^{13}C,^{6}He^{12}C$_{gs}$)^{4}He (the lower one) and the ^{9}Be(^{13}C,^{6}He^{12}C$_{E_x=4.4\,\mathrm{MeV}}$)^{4}He, both shifted by $+2.0$MeV to match the data. **Right:** corresponding Q-value spectrum.

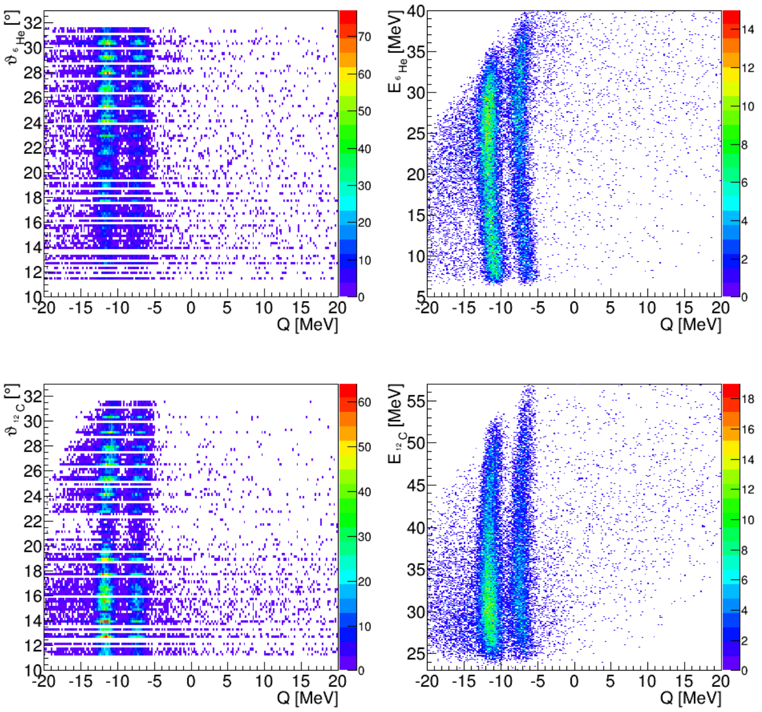

Figure 4.51: Q-value dependence on energy and angle of detected particles for the ^{9}Be(^{13}C,^{6}He^{12}C) reaction. The ^{6}He and ^{12}C nuclei were detected in detector telescopes T1 and T2, respectively.

perpendicular to its axis when plotted against other two relative energies, and forms a diagonal locus in the E_{r23}-E_{r13} plot. However, there is a strong bump, most likely corresponding to the ^{10}Be states, at the very border of the E_{r13}-E_{r12} plot. On the figure the points belonging to the

^{10}Be locus are displayed in grey, and were excluded from the analysis using a graphical cut in the E_{r13}-E_{r12} plot. The removed points and their influence on the final spectrum are shown on the rest of the figures in grey color as well. The excluded points do not form any pronounced peak in the ^{18}O excitation energy spectrum. The final ^{18}O excitation energy spectrum shows

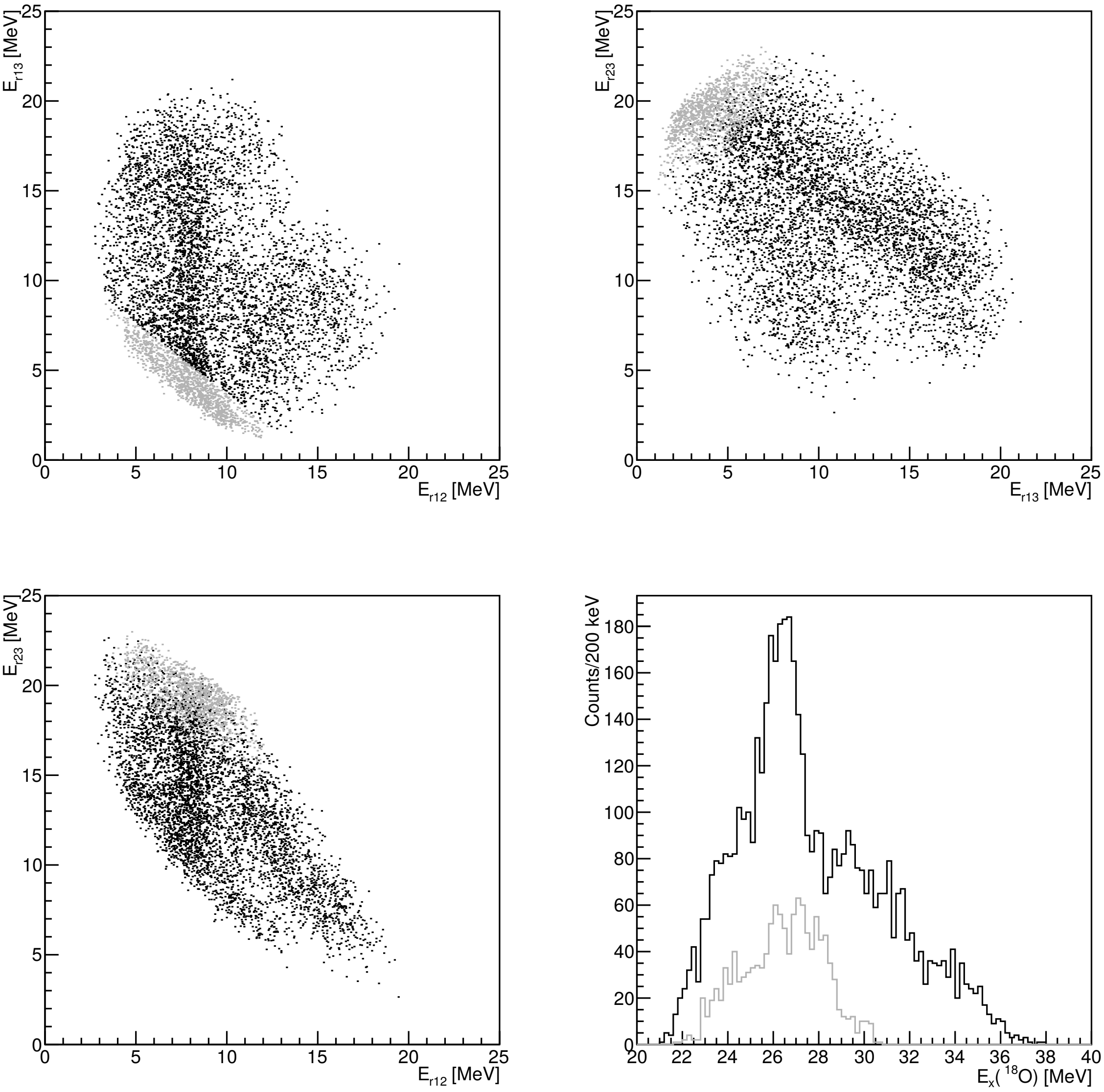

Figure 4.52: E_r-E_r plots for the ^{9}Be(^{13}C,^{6}He^{12}C)^{4}He reaction. The ^{6}He and ^{12}C nuclei were detected in detector telescopes T1 and T2, and are denoted particles 1 and 2, respectively. The last plot is an excitation energy spectrum of the ^{18}O nucleus decaying to the detected particles. The grey points denote a likely ^{10}Be locus at the border of the E_{r13}-E_{r12} plot that was removed from the analysis via graphical cut.

a wide peak at approx. 26.5 MeV, indication of a peak at 29.5 MeV and possible weak peak around 23.5 MeV. The states at such high excitation energies were previously seen only in the ^{18}O+γ experiments [87] that are not likely to populate states with the ^{6}He+^{12}C structure. This result is the first evidence for this decay mode of the ^{18}O excited states.

The relative-energy plots for the reaction channel ^{9}Be(^{13}C,^{6}He^{12}C$_{E_x=4.4\,\mathrm{MeV}}$)^{4}He are displayed in the Fig. 4.53. No clear locus of the E_r12 is visible. A strong locus (likely originating from the excited states of the ^{10}Be) was removed from analysis. However, in contrast to the ground-state exit channel, removal of the locus in question not only did not enhance the quality of the ^{18}O excitation energy spectrum, but also proved that the shape of both excluded data and the rest of the data is consistent with the usual shape of detection efficiency distribution. Consequently, no ^{18}O excited states decaying to this channel were observed.

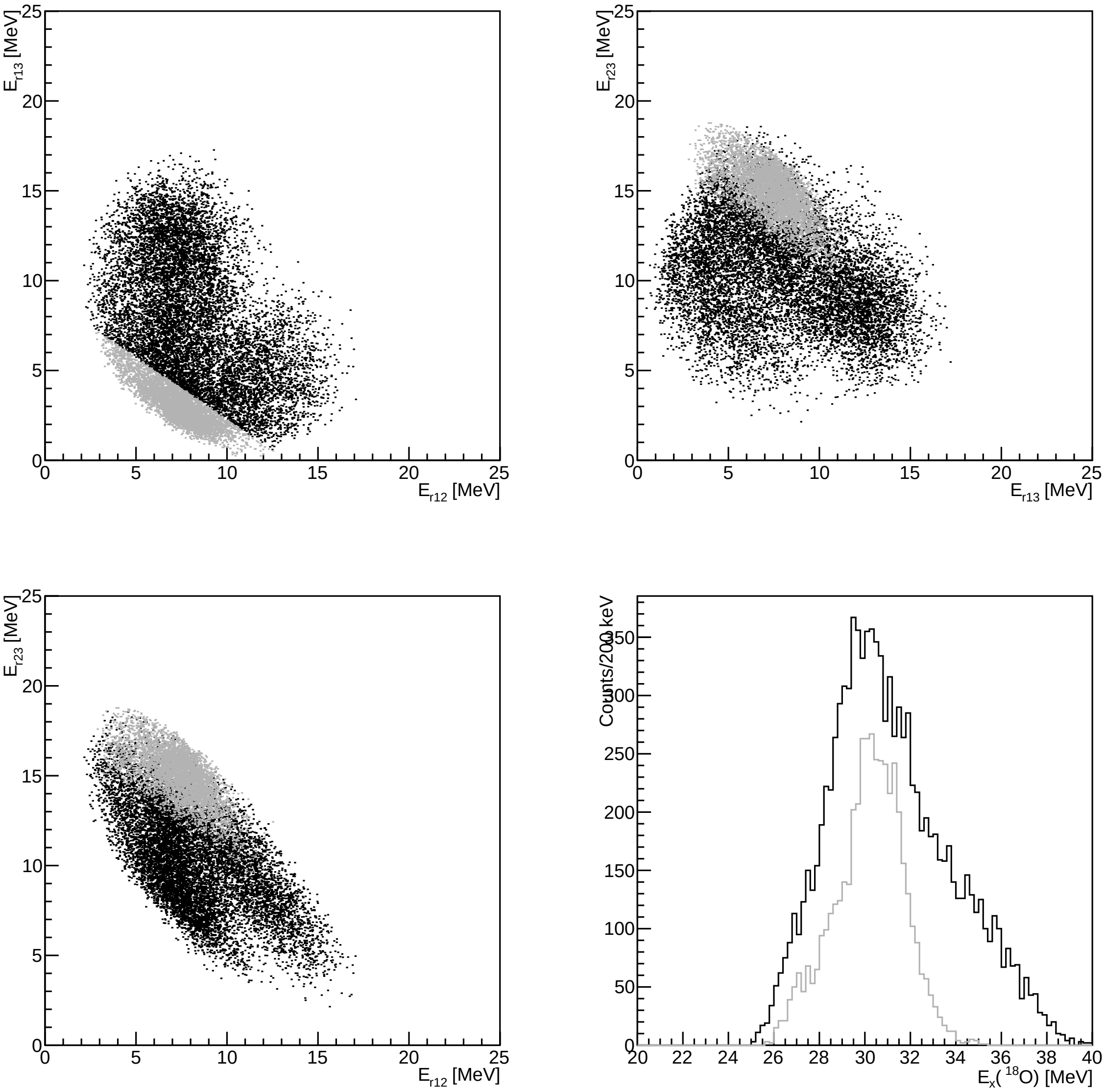

Figure 4.53: E_r-E_r plots for the ^{9}Be(^{13}C,^{6}He^{12}C*(4.4 MeV)) reaction. ^{6}He and ^{12}C*(4.4 MeV) were detected in detector telescopes T1 and T2, and are denoted particles 1 and 2, respectively. The grey points denote a likely ^{10}Be locus at the border of the E_{r13}-E_{r12} plot that was removed from the analysis via graphical cut. The last plot is an excitation energy spectrum of the ^{18}O nucleus decaying to the detected particles.

4.3.4 The ^{9}Be+^{13}C $\rightarrow$^{10}Be+^{8}Be+^{4}He reaction

The ^{9}Be+^{13}C $\rightarrow$^{10}Be+^{8}Be+^{4}He reaction has a Q-value of -5.500 MeV. It provides an opportunity to study ^{12}C, ^{14}C and ^{18}O states decaying to the ^{8}Be+^{4}He, ^{10}Be+^{4}He and ^{10}Be+^{8}Be, respectively. Results obtained from the ^{10}Be+^{4}He coincident events will be presented first. These results have the highest statistics for this reaction and excited states of the ^{12}C and ^{14}C can be unambiguously identified.

Next, a brief section on the reconstruction of the ^{8}Be from the ^{4}He+^{4}He coincidences is presented. Two sections on the coincident events involving ^{8}Be follow. Due to the fact that these coincidences are in fact three-particle coincidences, the efficiency for their detection is much lower than for the ^{10}Be+^{4}He coincidences. Therefore the statistics is lower and the excited states of nuclei are less evident.

The ^{10}Be+^{4}He coincidences

The ^{10}Be+^{4}He coincident events are reconstructed using the procedure described in the section on the data analysis, without any additional requirements. The ^{10}Be can be identified only in the front-angle detector telescopes T1 and T2, while the ^{4}He can be identified in all of the detector telescopes. Hence coincident events between T1 or T2 with any other detector telescope (including itself) are available.

Next the Catania plots and the corresponding Q-value plots for different detector combinations will be presented. On the Figs. 4.54 and 4.55 the Catania and Q-value plots are displayed for the ^{10}Be(T1)-^{4}He(T2) and the ^{10}Be(T2)-^{4}He(T1) coincident events, respectively. Three prominent loci are visible, which form three well-separated peaks in the Q-value spectra. The peaks correspond to the ground-state reaction channel ($Q = -5.50$ MeV), the ^{10}Be($E_x =$ 3.37 MeV), $Q = -8.87$ MeV, and the ^{10}Be($E_x \approx 6.2$ MeV), $Q = -11.68$ MeV, reaction channels. The latter reaction channel involves four ^{10}Be states between 5.9 and 6.3 MeV.

The coincident events between the front-angle and the mid-angle detector telescopes are displayed on the Figs. 4.56 and 4.57 for the ^{10}Be(T1)-^{4}He(T4) and the ^{10}Be(T2)-^{4}He(T3) coincident events, respectively. In these plots the Q-value peaks are less pronounced (especially for the T2-T3 coincidences), but nevertheless allow to select a particular reaction channel.

An additional confirmation of identified reaction channels are the plots of the Q-value versus angles and energies of the detected particles. Those spectra are displayed in the Appendix C, as well. All the spectra apart from the C.4 show clear vertical loci, independent both on the angle

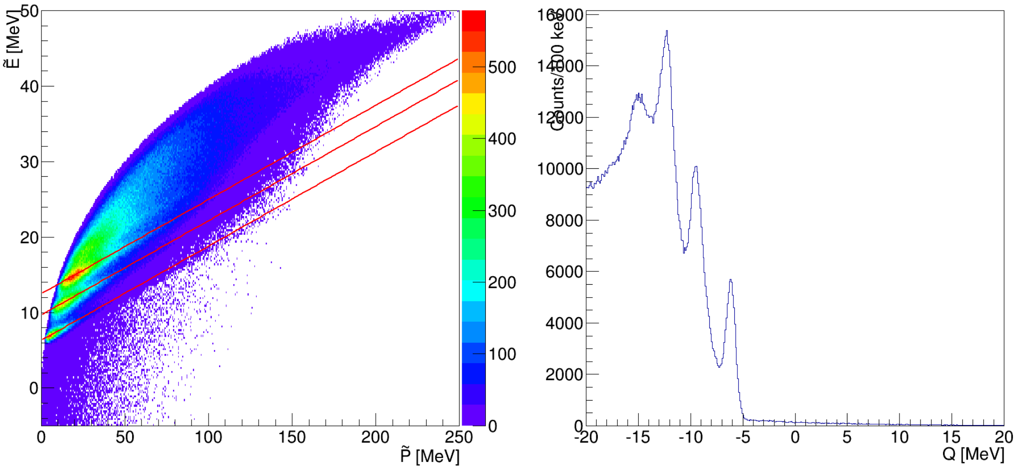

Figure 4.54: Left: The Catania plot for the ^{9}Be(^{13}C,^{10}Be ^{4}He) reaction, ^{10}Be detected in the T1 and ^{4}He in the T2. The three red lines are denoting the position of reaction loci for the undetected ^{8}Be: the lowest for all nuclei in the ground state, while the other two lines for the reaction channels in which the detected ^{10}Be nucleus is in the $E_x = 3.37$ excited state and $E_x \approx 6.2$ MeV group of excited states. All three lines were shifted by +0.75 MeV to reproduce the data. **Right:** The corresponding Q-value spectrum.

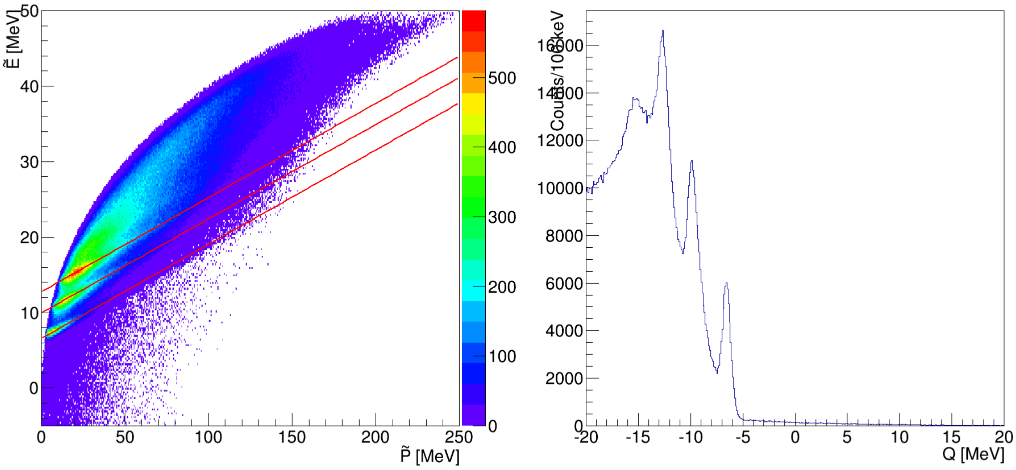

Figure 4.55: Left: The Catania plot for the ^{9}Be(^{13}C,^{10}Be ^{4}He) reaction, ^{10}Be detected in the T2 and ^{4}He in the T1. The three red lines are denoting the position of reaction loci for the undetected ^{8}Be: the lowest for all nuclei in the ground state, while the other two lines for the reaction channels in which the detected ^{10}Be nucleus is in the $E_x = 3.37$ MeV excited state and $E_x \approx 6.2$ MeV group of excited states. All three lines were shifted by +1.0 MeV to reproduce the data. **Right:** The corresponding Q-value spectrum.

and the energy of the detected particles.

The next step in the data analysis is an identification of the intermediate ^{12,14}C or ^{18}O states decaying to a particular reaction channel. First the results for the ground-state channel will be discussed. E_r-E_r plots for the T1-T2, T2-T1, T1-T4 and the T2-T3 coincident events are displayed on the Figs. 4.58 and 4.59, respectively. For each detector combination the three

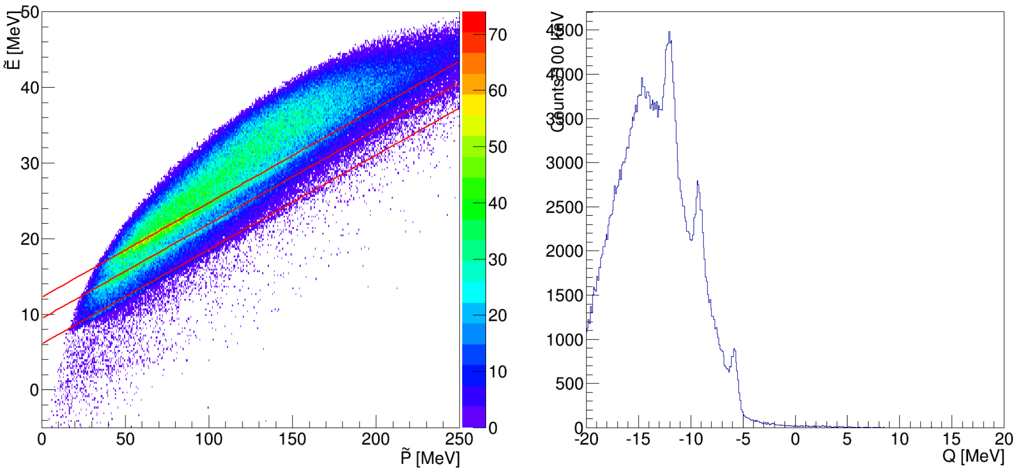

Figure 4.56: Left: The Catania plot for the ^{9}Be(^{13}C,^{10}Be ^{4}He) reaction, ^{10}Be detected in the T1 and ^{4}He in the T4. The three red lines are denoting the position of reaction loci for the undetected ^{8}Be: the lowest for all nuclei in the ground state, while the other two lines for the reaction channels in which the detected ^{10}Be nucleus is in the $E_x = 3.37$ MeV excited state and $E_x \approx 6.2$ MeV group of excited states. All three lines were shifted by +0.5 MeV to reproduce the data. **Right:** The corresponding Q-value spectrum.

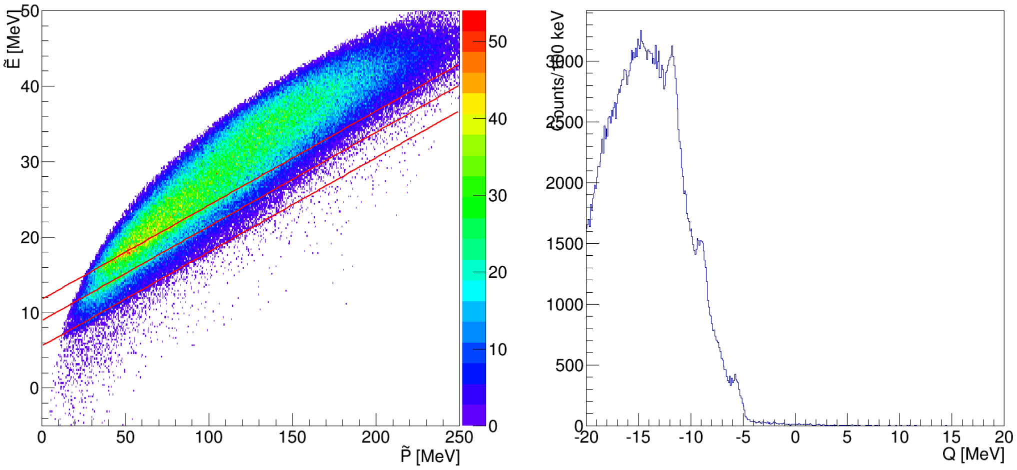

Figure 4.57: Left: The Catania plot for the ^{9}Be(^{13}C,^{10}Be ^{4}He) reaction, ^{10}Be detected in the T2 and ^{4}He in the T3. The three red lines are denoting the position of reaction loci for the undetected ^{8}Be: the lowest for all nuclei in the ground state, while the other two lines for the reaction channels in which the detected ^{10}Be nucleus is in the $E_x = 3.37$ MeV excited state and $E_x \approx 6.2$ MeV group of excited states. All three lines reproduce the data without any energy-shift applied. **Right:** The corresponding Q-value spectrum.

E_r-E_r plots are given. In this case the most interesting one is the E_{r23}-E_{r12} plot. The E_{r23} corresponds to the relative energy between the detected ^{4}He and the undetected ^{8}Be. A locus in the E_{r23} independent of other relative energies (i.e. vertical to the E_{r23} axis) proves that the two outgoing particles came from the decay of the ^{12}C. In other words, the reaction occured in two steps: ^{9}Be+^{13}C $\rightarrow$^{12}C*+^{10}Be$\rightarrow$^{8}Be+^{4}He+^{10}Be. Likewise, the loci of the E_{r12} correspond to the excited states of the ^{14}C nucleus. The loci of the third relative energy E_{r13}, if found, would correspond to the excited states of the ^{18}O. In the E_{r23}-E_{r12} plots for the T1-T2 coincidences two states of the ^{12}C are visible, at $E_{r23} \approx 1$ and 2.5 MeV. Loci corresponding to the excited states of the ^{14}C are found at the $E_{r12} \approx 3$, 4.5 MeV. There are some faint possible loci at $E_{r12} \approx 7$ and 8.5 MeV as well. In the E_{r13} no loci are visible. The E_r-E_r plots for the T2-T1 coincidences have the same features as for the former detector combination. The T1-T4 and the T2-T3 coincidences share similar features as well. The main difference between them is lower resolution and statistics for the T2-T3 combination. For these coincidences only the two loci of the E_{r23} at approx. 2 and 3.3 MeV are visible, corresponding to excited states of the ^{12}C.

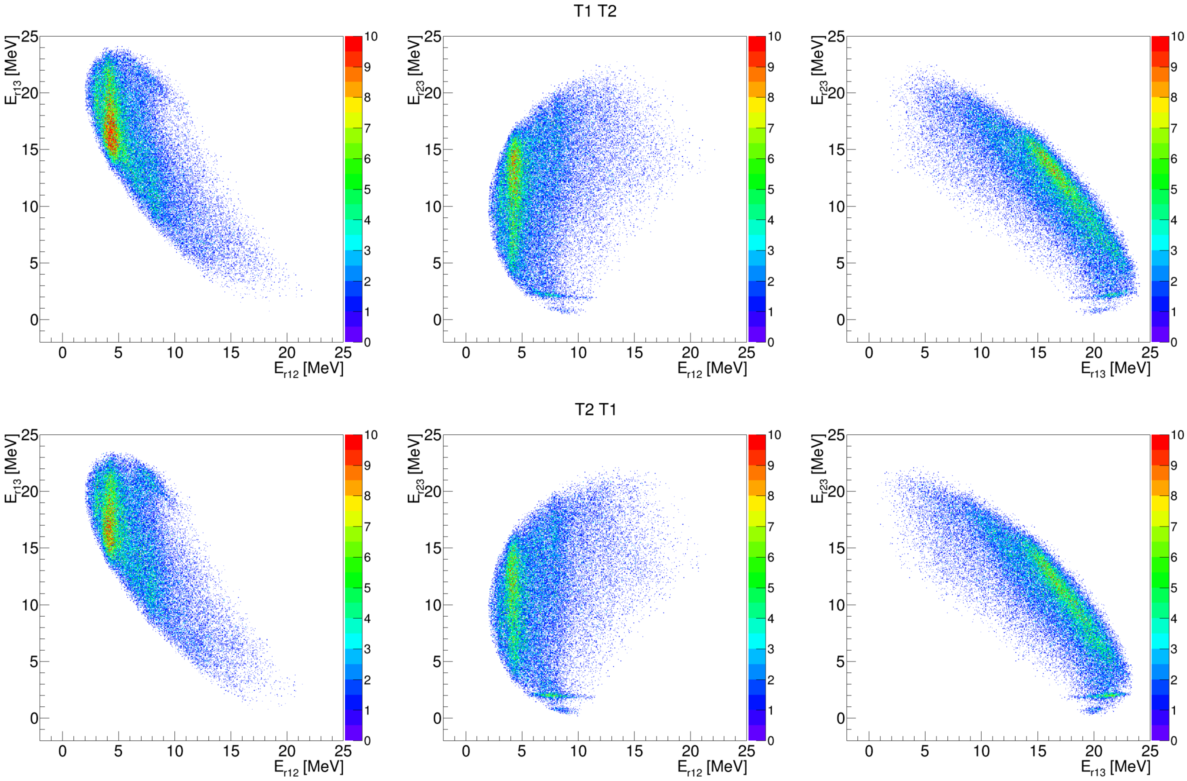

Figure 4.58: Relative-energy plots for the ^{9}Be(^{13}C,^{10}Be^{4}He)^{8}Be reaction. Different detector combinations are displayed one per row. ^{10}Be, ^{4}He and ^{8}Be are designated by numbers 1, 2 and 3, respectively.

The next reaction channel is the ^{10}Be($E_x = 3.37$ MeV)+^{4}He+^{8}Be. The E_r-E_r spectra are displayed on the Figs. 4.60 and 4.61. This reaction channel has better statistics than the ground-state channel. The front-angle detector coincidence events (T1-T2 and T2-T1) show the ^{12}C loci at the same positions as for the ground-state channel. The loci of the E_{r12} (due to the excited states of the ^{14}C) are located at $E_{r12} \approx 3$, 4.5 and 7 MeV. No E_{r13} loci are observed. For the T1-T4 and the T2-T3 coincident events the only locus visible is the $E_{r23} \approx 2.5$ MeV, corresponding to a ^{12}C excited state.

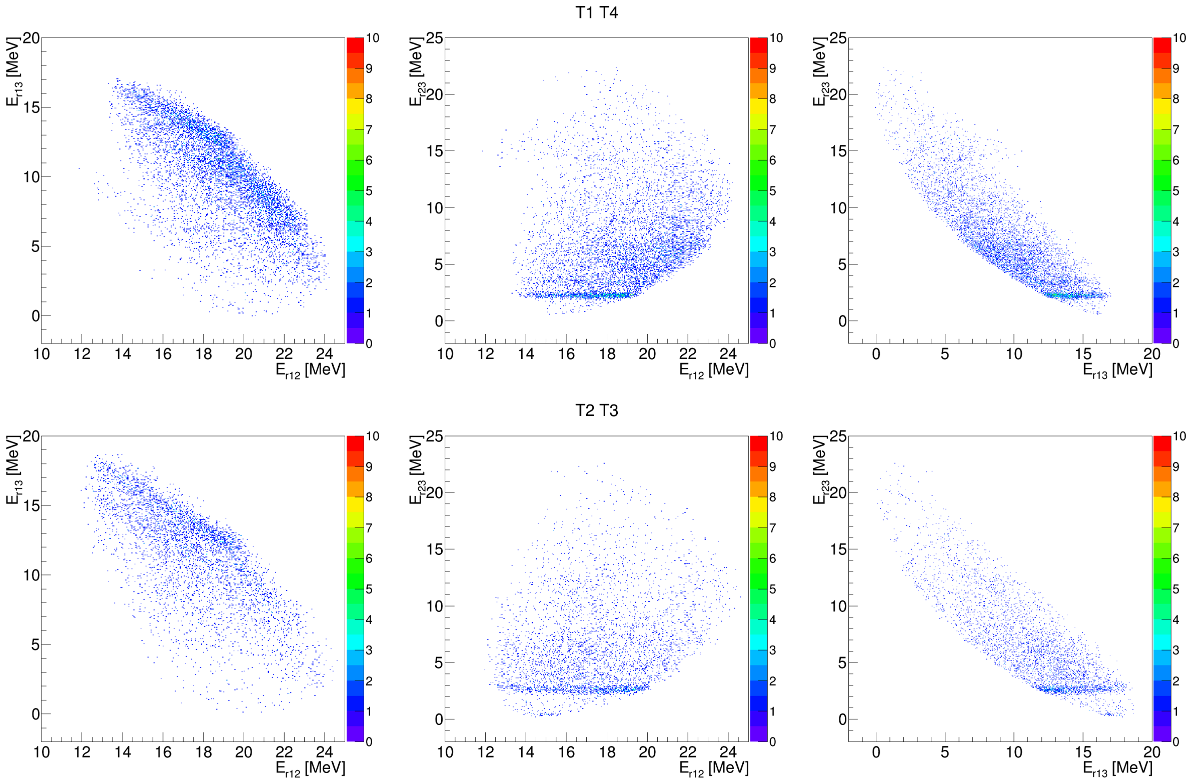

Figure 4.59: Relative-energy plots for the ^{9}Be(^{13}C,^{10}Be^{4}He)^{8}Be reaction. Different detector combinations are displayed one per row. ^{10}Be, ^{4}He and ^{8}Be are designated by numbers 1, 2 and 3, respectively.

The E_r-E_r plots for the last channel with the ^{10}Be nucleus in a group of excited states between 5.9 and 6.3 MeV are displayed on the Figs. 4.62 and 4.63. The general feature of all plots is that the ^{12}C locus at $E_{r23} \approx 1$ MeV is much weaker, while the $E_{r23} \approx 2.5$ MeV locus grows stronger. The T1-T2 and the T2-T1 coincidences show ^{14}C loci at approx. $E_{r12} \approx 3$, 4.5 and 8.5 MeV. No E_{r13} loci are visible.

For all the detector combinations and reaction channels the same cut was used to separate the ^{12}C from the ^{14}C loci: 0 MeV $< E_{r23} <$ 4.0 MeV. The events inside the cut correspond mostly to the ^{12}C loci, while those outside the cut originated mainly from the ^{14}C decays. In the cases in which no ^{14}C loci were observed, the all data were projected as the ^{12}C excited states.

Now excitation energy spectra for the ^{12}C and ^{14}C can be obtained. Excitation energy of the mother nucleus decaying to a pair of daughter nuclei equals to:

$$E_x^A = E_{rab} + E_{A\to ab}^{\text{threshold}} + E_x^a + E_x^b \tag{4.40}$$

where E_x^A is the excitation energy of the mother nucleus A, E_{rab} is the relative energy between the daughter nuclei a and b, $E_{A\to ab}^{\text{threshold}}$ is the decay threshold of the nucleus A to the nuclei a+b

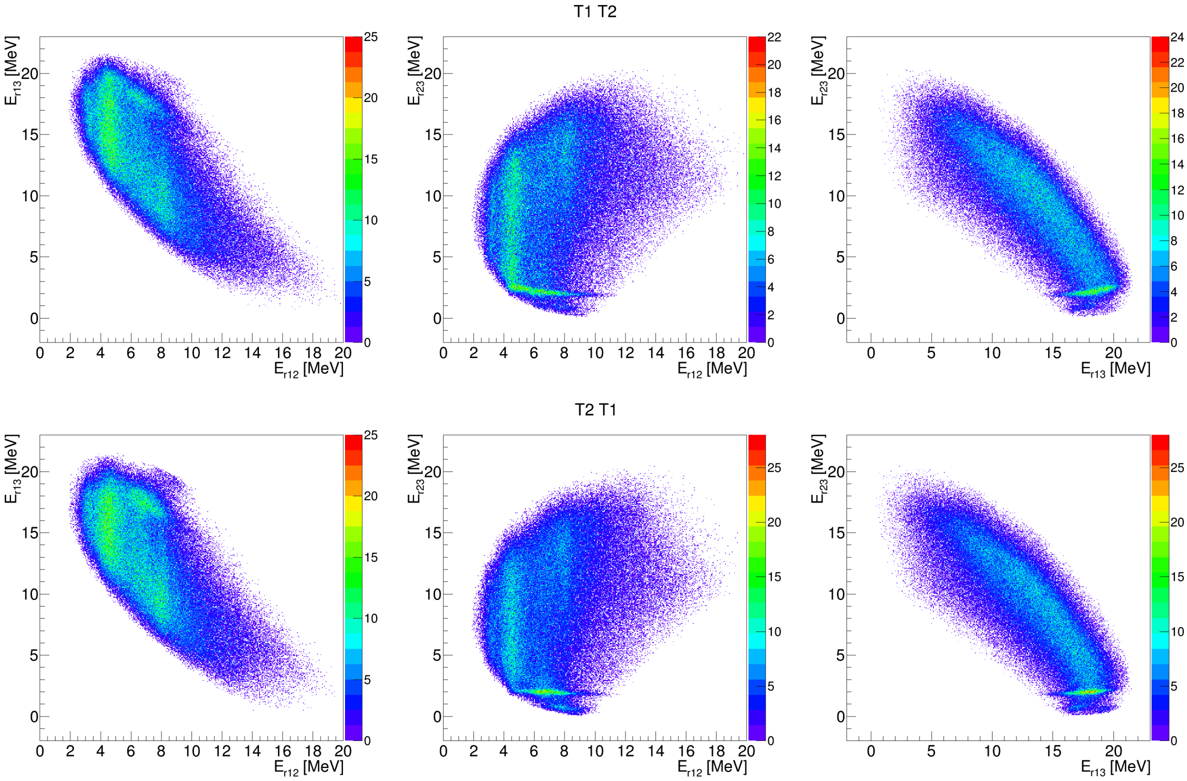

Figure 4.60: Relative-energy plots for the ^{9}Be(^{13}C,^{10}Be($E_x = 3.37$ MeV)^{4}He)^{8}Be reaction. Different detector combinations are displayed one per row. ^{10}Be, ^{4}He and ^{8}Be are designated by numbers 1, 2 and 3, respectively.

and $E_x^{a,b}$ are the excitation energies of the daughter nuclei a and b. For reaction channels in this subsection, the values of the decay thresholds are:

$$E^{\text{threshold}}_{^{12}\text{C}\rightarrow{}^{8}\text{Be}^{4}\text{He}} = 7.367\ \text{MeV} \qquad (4.41)$$

$$E^{\text{threshold}}_{^{14}\text{C}\rightarrow{}^{10}\text{Be}^{4}\text{He}} = 12.012\ \text{MeV} \qquad (4.42)$$

For relative energies between a particle in the ground state and a particle in an excited state, its excitation energy has to be taken into account. For the first excited state of the ^{10}Be the excitation energy amounts to 3.37 MeV, while for a group of excited states around 6.2 MeV the excitation energy of 6.18 MeV was used in calculations.

The excitation energy spectra of the ^{12,14}C obtained for the ground-state channel are displayed in the Fig. 4.64. The left plot shows the excitation energy spectrum of the ^{12}C. The lowest peak appears at approx. 8.0 MeV. However, the E_r-E_r plots show that the corresponding locus is not horizontal, as it should be, and that it's located at the very edge of the plot, therefore its position reflecting more the shape of the edge of the graph than its real location. The

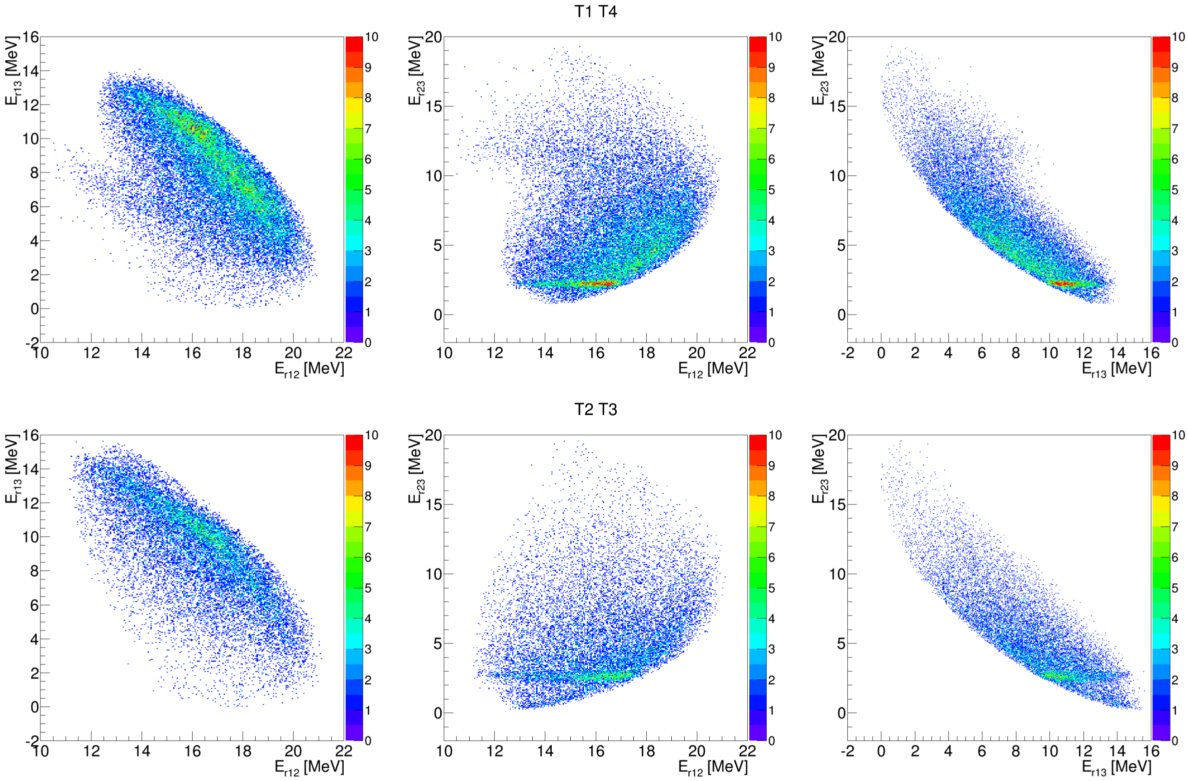

Figure 4.61: Relative-energy plots for the ^{9}Be(^{13}C,^{10}Be(E_x = 3.37 MeV)^{4}He)^{8}Be reaction. Different detector combinations are displayed one per row. ^{10}Be, ^{4}He and ^{8}Be are designated by numbers 1, 2 and 3, respectively.

events in that locus probably originate from the tail of the Hoyle state peak that could be decaying intensely to this reaction channel. The most prominent peak is located between $E_x \approx 9$ and 10 MeV and it corresponds to the ^{12}C in the 9.641 MeV 3^- excited state. An additional peak is visible for the T1-T4 coincident events (the orange line), the peak in the spectra is located at approx. $E_x = 10.7$ MeV and could correspond to the 10.844 MeV 1^- state. That peak is not visible for the T2-T3 coincident events.

The ^{14}C spectra for the ground-state channel are available only for the T1-T2 and the T2-T1 detector coincidences. Both spectra show a small peak at approx. $E_x = 15.2$ MeV, the most prominent peak at the excitation energy of approx. 16.2 MeV and another small peak at $E_x \approx 20$ MeV. An additional weak peak can be seen at approx. $E_x = 19$ MeV. The shape of the most prominent peak indicates an overlap with a weaker peak at its high-energy side. The lowest peak probably corresponds to the 15.44 MeV 3^- excited state, observed in [88], [89] and [90]. The strongest peak corresponds 16.43 MeV 6^+ excited state [91]. The highest peak probably corresponds to the peak observed in Ref. [92] at 20.02 MeV and in Ref. [90] at a 20.3(1) MeV.

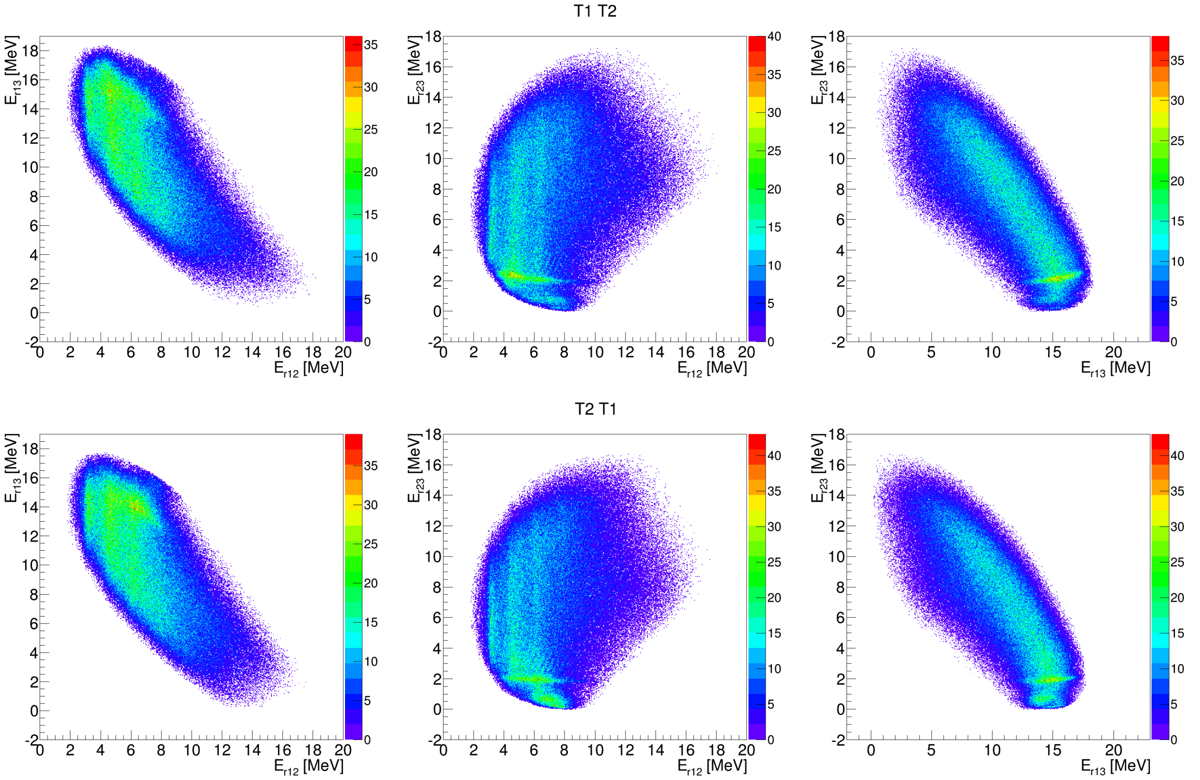

Figure 4.62: Relative-energy plots for the ^{9}Be(^{13}C,^{10}Be($E_x \approx 6.2$ MeV)^{4}He)^{8}Be reaction. Different detector combinations are displayed one per row. ^{10}Be, ^{4}He and ^{8}Be are designated by numbers 1, 2 and 3, respectively.

Excitation energy spectra of the ^{12,14}C from the ^{10}Be(E_x =3.37 MeV)+^{4}He+^{8}Be reaction channel are displayed in the Fig. 4.65. The ^{12}C excitation energy plot shows the same features as before, the two differences are that the peak at $E_x \approx 10.8$ is not so pronounced as for the ground-state channel and the decreasing strength of the 9.2 MeV peak.

The ^{14}C excitation energy plot shows the prominent peak at $E_x \approx$20 MeV, with a small peak at $E_x \approx$19 MeV. The second strongest peak is located at the $E_x \approx$23.5 MeV. Another peak is found at $E_x \approx$22.25 MeV. The 20 MeV peak has been seen in the ground-state reaction channel as well, and most likely corresponds to peaks observed in Ref. [92] at 20.02 MeV and [90] at 20.3(1) MeV. The position of the lowest-energy peak cannot be determined precisely, making the attribution harder. However, it might correspond to the same ^{14}C state as the weak $E_x \approx$19 MeV peak observed in the ground state channel. The two peaks may correspond to the 19.14 MeV state observed in Ref. [92] and the 19.07(1) MeV state observed in Ref. [88], [89] and [90]. The 22.25 MeV peak probably corresponds to the 22.45 MeV peak observed in Ref. [88] and [90], tabulated in Ref. [93] as the 22.1 MeV state of an unknown spin and parity. The 23.5 MeV peak was observed in Ref. [94] and [90] as well.

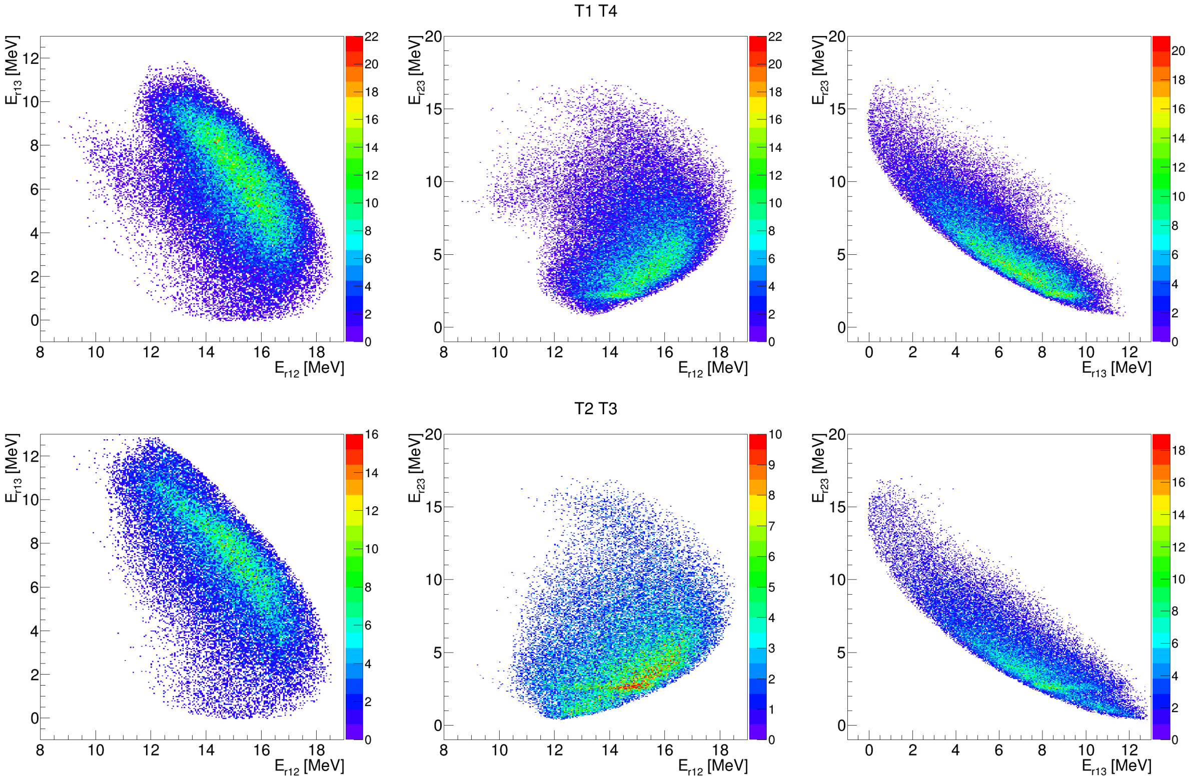

Figure 4.63: Relative-energy plots for the ^{9}Be(^{13}C,^{10}Be($E_x \approx 6.2$ MeV)^{4}He)^{8}Be reaction. Different detector combinations are displayed one per row. ^{10}Be, ^{4}He and ^{8}Be are designated by numbers 1, 2 and 3, respectively.

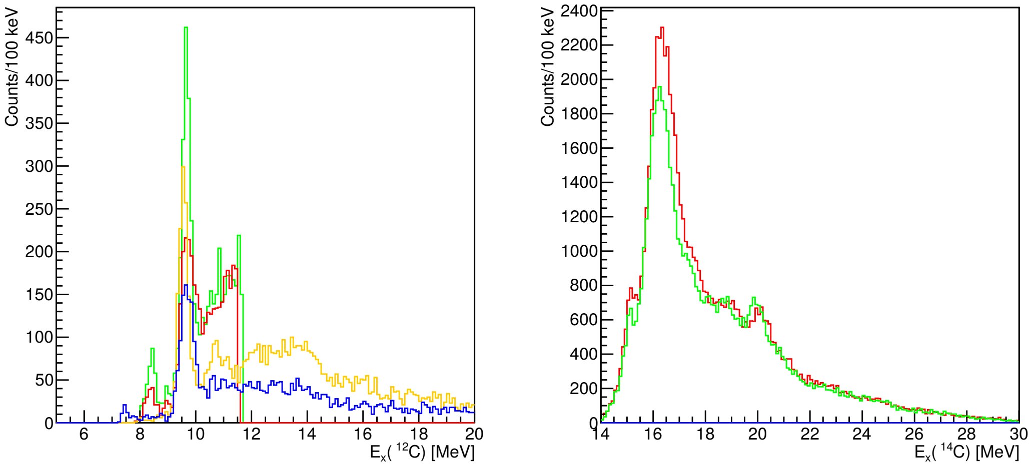

Figure 4.64: The excitation energy spectra of the ^{12}C (left) and ^{14}C (right) for the ^{10}Be+^{4}He coincident events. The red line denotes the T1-T2, the green the T2-T1, the orange the T1-T4 and the blue the T2-T3 coincident events. The spectra on the left plot were adjusted to the 9.641 MeV 3^{-} state of the ^{12}C. The spectra on the right plot were not adjusted.

Finally, results for the reaction channel with the ^{10}Be excited to a group of states around the $E_x \approx 6.2$ MeV are discussed. The plots of the excitation energy spectra of ^{12,14}C are displayed in the Fig. 4.66. In the ^{12}C excitation energy plot the lowest peak, located at $E_x \approx 8$ MeV,

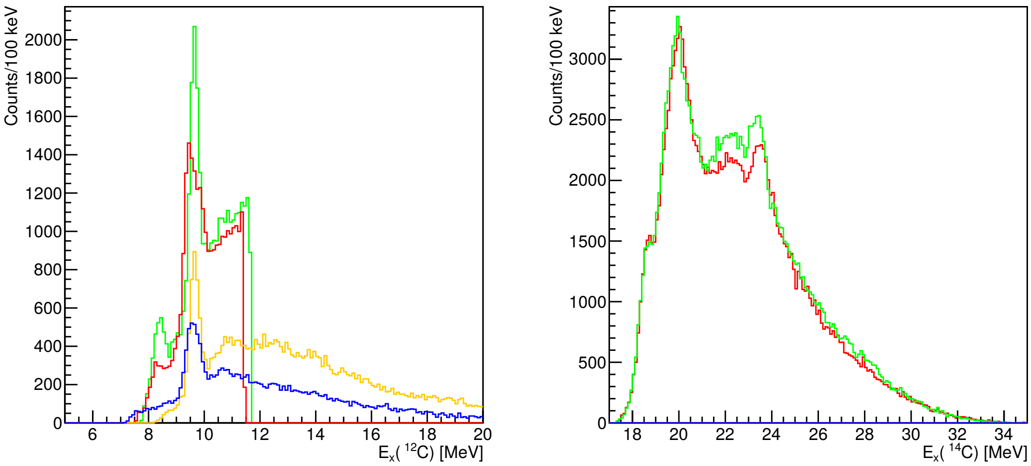

Figure 4.65: The excitation energy spectra of the ^{12}C (left) and the ^{14}C (right) for the ^{10}Be(E_x =3.37 MeV)+^{4}He coincident events. The red line denotes the T1-T2, the green the T2-T1, the orange the T1-T4 and the blue the T2-T3 coincident events. The spectra on the left plot were adjusted to the 9.641 MeV 3^- state of the ^{12}C. The spectra on the right plot were not adjusted.

is much stronger compared to previous plots. The 9.6 MeV peak is less pronounced than for previous reaction channels. The lowest energy-peak doesn't correspond to any known ^{12}C state, while the E_x ≈9.6 MeV peak corresponds to the 9.641 MeV 3^- state, as stated before.

The ^{14}C excitation energy spectrum contains peaks at E_x ≈21.5 MeV, 23 MeV and 24.25 MeV. The position of the lowest peak, at E_x ≈21.5 MeV, is strongly influenced by the steep change in the detection efficiency and therefore it is quite uncertain. The next peak, visible in the previous channel as well, has been observed before by the [88] and [90]. The highest-energy peak at E_x ≈24.25 MeV is most likely to correspond to the 24.0 MeV peak observed by [88].

In conclusion, the ^{10}Be+^{4}He coincident events proved to be a robust tool for study of the ^{12,14}C states populating the ^{10}Be+^{4}He+^{8}Be reaction channels. Three reaction channels were identified: the ground-state channel, the $E_x(^{10}\mathrm{Be}) = 3.37$ MeV channel and the $E_x(^{10}\mathrm{Be}) \approx$ 6.2 MeV channel (any of the four states in the vicinity of the peak may contribute to it). The E_r-E_r plots revealed clear loci, corresponding to the excited states of ^{12,14}C, no locus corresponding to the excited state of the ^{18}O was observed. A simple cut was applied to separate the ^{12}C and the ^{14}C loci before a projection and an excitation energy calculation.

Excitation energy plots for the ^{12}C show a prominent 9.641 MeV 3^- state, decreasing in strength with increasing excitation of the detected ^{10}Be. A low-energy peak, not related to known states of the ^{12}C was observed as well at $E_x \approx 8$ MeV, its position and shape probably a result of steep fall of detection efficiency and a peak laying outside of range.

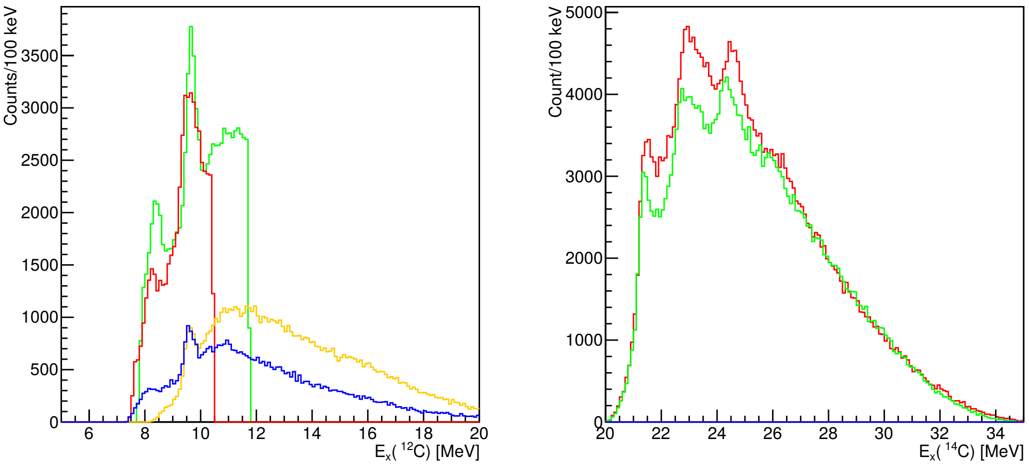

Figure 4.66: The excitation energy spectra of the ^{12}C (left) and the ^{14}C (right) for the ^{10}Be($E_x \approx$6.2 MeV)+^{4}He coincident events. The red line denotes the T1-T2, the green the T2-T1, the orange the T1-T4 and the blue the T2-T3 coincident events. The spectra on the left plot were adjusted to the 9.641 MeV 3^- state of the ^{12}C. The spectra on the right plot were not adjusted.

Multiple states of the ^{14}C were observed, corresponding fairly to the results of previous measurements ([88], [89], [90] and [92]). They are summarized in the Tab. 4.2.

Table 4.2: The ^{14}C states populated in the ^{9}Be(^{13}C,^{10}Be^{4}He)^{8}Be reaction. Columns represent different exit channels, with the ^{10}Be in its ground state, the first excited state and a group of excited states around the $E_x = 6$ MeV. Strongest peaks are designated in bold.

^{10}Be+^{4}He	^{10}Be($E_x = 3.37$ MeV)+^{4}He	^{10}Be($E_x \approx 6.2$ MeV)+^{4}He
15.2 MeV		
16.2 MeV		
19.0 MeV	19.0 MeV	
20.0 MeV	**20.0 MeV**	
		21.5 MeV
	22.3 MeV	
	23.5 MeV	**23 MeV**
		24.25 MeV

Detection of ^{4}He+^{4}He coincidences and ^{8}Be reconstruction

The detection of ^{8}Be nucleus is slightly more complicated than the rest of the nuclei due to the fact that its ground state lays 91.8 keV above the ^{4}He+^{4}He decay threshold. Therefore, it instantly decays to a pair of α-particles.

The process of the reconstruction goes as follows: two detected α-particles have their respective detected energies and angles (polar angle ϑ and azimuthal angle φ). The total energy of the detected α particle consists of the energy deposited in the thin ΔE and thick E detectors as well as the energy lost in the target.

The conservation of momentum applied to the decay gives:

$$\vec{p}_{^8\mathrm{Be}} = \vec{p}_{\alpha_1} + \vec{p}_{\alpha_2}. \tag{4.43}$$

The total momentum of the ^{8}Be nucleus is

$$p_{^8\mathrm{Be}} = \sqrt{(p_{x\alpha_1} + p_{x\alpha_2})^2 + (p_{y\alpha_1} + p_{y\alpha_2})^2 + (p_{z\alpha_1} + p_{z\alpha_2})^2}, \tag{4.44}$$

where x, y, z denotes Cartesian vector components. Once one have a total momentum of the ^{8}Be nucleus, its energy can be obtained:

$$E_{^8\mathrm{Be}} = \frac{p^2_{^8\mathrm{Be}}}{2m_{^8\mathrm{Be}}}. \tag{4.45}$$

The components of the ^{8}Be momentum are a sum of the components of momentum of both α-particles:

$$p_{x^8\mathrm{Be}} = p_{x\alpha_1} + p_{x\alpha_2} \qquad p_{y^8\mathrm{Be}} = p_{y\alpha_1} + p_{y\alpha_2} \qquad p_{z^8\mathrm{Be}} = p_{z\alpha_1} + p_{z\alpha_2}. \tag{4.46}$$

The polar and azimuthal angle of the ^{8}Be can be calculated from components of its momentum:

$$\vartheta_{^8\mathrm{Be}} = \arccos\frac{p_{z^8\mathrm{Be}}}{p_{^8\mathrm{Be}}} \qquad \varphi_{^8\mathrm{Be}} = \arctan\frac{p_{y^8\mathrm{Be}}}{p_{x^8\mathrm{Be}}} \tag{4.47}$$

Now the ^{8}Be decay energy can be calculated:

$$E_{\mathrm{decay}} = E_{\alpha_1} + E_{\alpha_2} - E_{^8\mathrm{Be}} = Q. \tag{4.48}$$

The ground state of the ^{8}Be decaying to a pair of α-particles will show a peak in the E_{decay} located at approx. 100 keV.

In the data analysis a number of conditions have to be met for a series of ADC signals to form a good hit. The generalities of the procedure were discussed in detail in the section on the data analysis and apply here as well. In order to minimize the influence of the pile-up in the forward-angle detector telescopes, several additional requirements were imposed on events:

1. the number of ΔE detector strips above the threshold in a single detector telescope has to be smaller than or equal to 2
2. the multiplicity of good hits in the E detector in which ^{8}Be was detected has to be equal to 2

The aforesaid conditions are robust enough to discard pile-up and inter-strip events. In the case of inter-strip ΔE hits at least one of the α-particles would not lay inside the α-paticle locus of the ΔE-E plot and therefore such pair of hits cannot be reconstructed as ^{8}Be.

The decay energy of reconstructed ^{8}Be nuclei for detector telescopes T1 to T4 are presented in the Fig. 4.67.

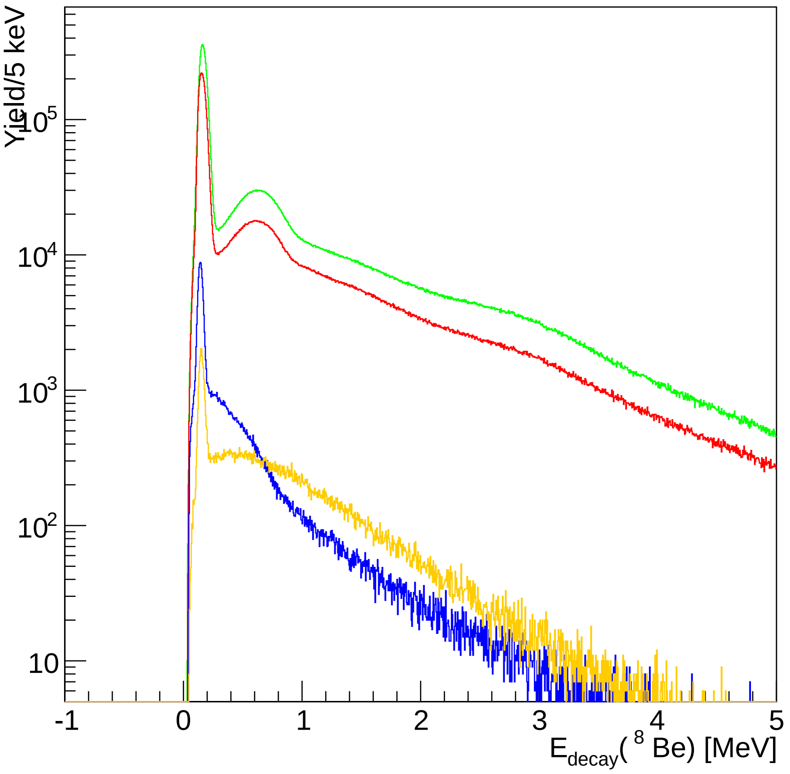

Figure 4.67: Decay energy spectra for the detected α+α coincidences in the first four detector telescopes (T1 spectrum is displayed in red, T2 in green, T3 in blue and T4 in orange).

One can clearly see the peak belonging to the ground state of the ^{8}Be, which is centred at approx. 150 keV in the spectra. The broad bump at approx. 0.7 MeV visible in the forward detector telescopes T1 and T2 is known as a decay of an excited ^{9}Be nucleus in the $^9\mathrm{Be}_{E_x=2.429\,\mathrm{MeV}}$,

$J^{\pi} = \frac{5}{2}^{-}$ state through the tail of the 2^+ ^{8}Be state at $E_x \approx 3$ MeV. Reactions not involving ^{9}Be nucleus in the entrance channel, but involving two alpha particles in the exit channel form this peak due to the rapid increase of the α-α penetrability in that energy region (by five orders of magnitude) that causes a deformation of the high-energy tail of the ^{8}Be ground-state wave function [95].

The ^{8}Be ground-state was selected using the criterion $0 < E_{\text{decay}} < 0.25\,\text{MeV}$.

Finally, the ^{8}Be reconstruction can provide us with the estimate of the resolution and systematic error for the ^{4}He detected in a single detector telescope. For the detector telescopes T1, T2, T3 and T4 the energy of the ground-state peak is 154, 166, 144 and 151 keV, respectively. Therefore, the systematic shift is approx. +60 keV in average. The full width at half-maximum of the peak is 70 keV for the T1, 72 keV for the T2, 51 keV for the T3 and 56 keV for the detector telescope T4.

^{8}Be+^{4}He coincidences

The coincident events studied in this section belong to the three-particle coincidences. After identifying good hits in the E detector and pairing them with hits in one of the corresponding ΔE strips, particle-identification cuts on the ΔE-E plots were used to assign a mass number A, an atomic number Z and a mass m to each of the hits. The following step was the ^{8}Be reconstruction loop, in which all the α-particles in the event were examined, forming all the possible pairs. Only the pairs which gave the ^{8}Be in its ground state were used to form a new ^{8}Be hit, while two α-particle hits were removed from the event. The rest of the analysis is the same as for any other two-particle coincidence event, which was described in the section on the data analysis.

Let us start with the Catania and Q-value plots for various detector combinations. The plots for the ^{8}Be$_{\text{gs}}$ detected in the T1 and ^{4}He in the T2 are displayed in the Fig. 4.68. Four loci are visible. They correspond to the calculated loci for the undetected ^{10}Be nucleus in the ground state and the excited states at 3.37 MeV, group of excited states at ≈ 6.2 MeV and the state at 7.37 MeV. The corresponding Q-values equal to -5.50, -8.87, -11.68 and -12.87 MeV, respectively. In the Q-value plot, the ground state channel and the one corresponding to the first excited state of the ^{10}Be are well defined.

The plots for the opposite combination, in which a ^{8}Be is detected in the T2 detector telescope and ^{4}He in the T1 can be found in the Fig 4.69. One might observe a better statistics than

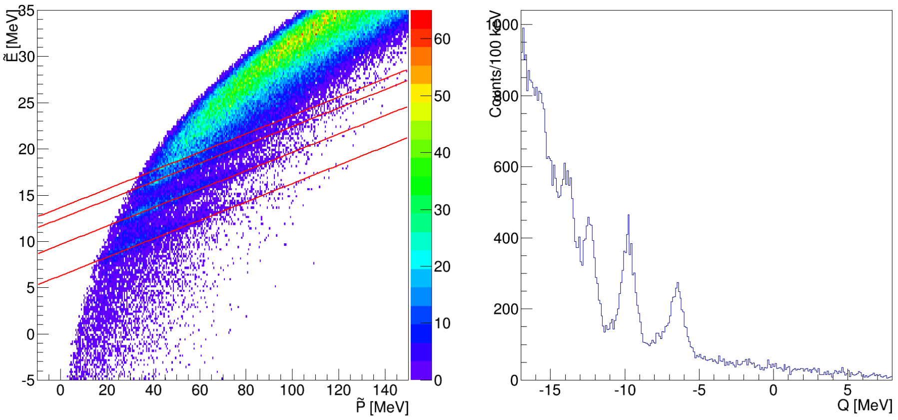

Figure 4.68: Left: The Catania plot for the ^{9}Be(^{13}C,^{8}Be$_{gs}$ ^{4}He) reaction, ^{8}Be$_{gs}$ detected in the T1 and ^{4}He in the T2. The four red lines are denoting the position of reaction loci for undetected ^{10}Be: the lowest for all nuclei in the ground state, while the other three lines for the reaction channels in which the undetected ^{10}Be nucleus excited to the $E_x = 3.37$, ≈ 6.2 and 7.37 MeV. All four lines were shifted by +0.75 MeV to reproduce the data. **Right:** The corresponding Q-value spectrum.

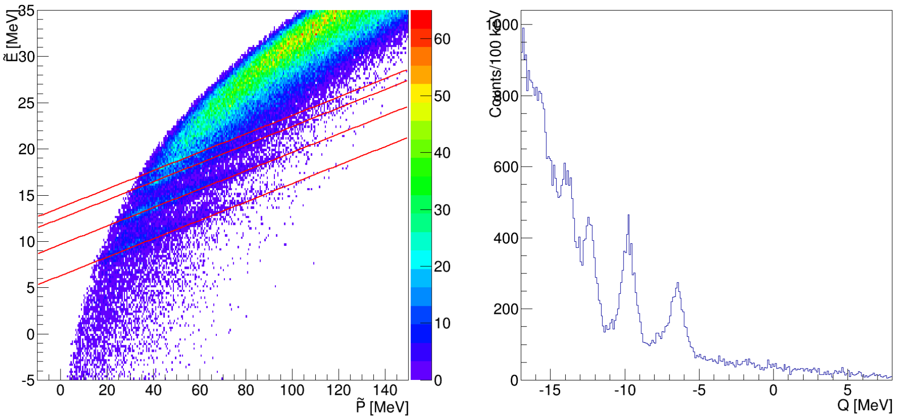

Figure 4.69: Left: The Catania plot for the ^{9}Be(^{13}C,^{8}Be$_{gs}$ ^{4}He) reaction, ^{8}Be$_{gs}$ detected in the T2 and ^{4}He in the T1. The four red lines are denoting the position of reaction loci for undetected ^{10}Be: the lowest for all nuclei in the ground state, while the other three lines for the reaction channels in which the undetected ^{10}Be nucleus excited to the $E_x = 3.37$, ≈ 6.2 and 7.37 MeV. All four lines were shifted by +0.5 MeV to reproduce the data. **Right:** The corresponding Q-value spectrum.

for the previous combination. However, the main features of the plots did not change.

Let us continue with the coincident events between the front-angle detector telescopes (T1 and T2) and the central angle detector telescopes (T3 and T4). The plots of the ^{8}Be$_{gs}$(T1)+^{4}He(T4) are displayed in the Fig. 4.70, while the ^{8}Be$_{gs}$(T2)+^{4}He(T3) coincidences are displayed in the Fig. 4.71. The Catania plots show rather nice loci for the ^{8}Be$_{gs}$(T1)+^{4}He(T4), although the statistics are much lower than for the forward-angle coincidences. The Q-value plots show well defined narrow peaks for the ground state, the first excited state at 3.37 MeV and the group of

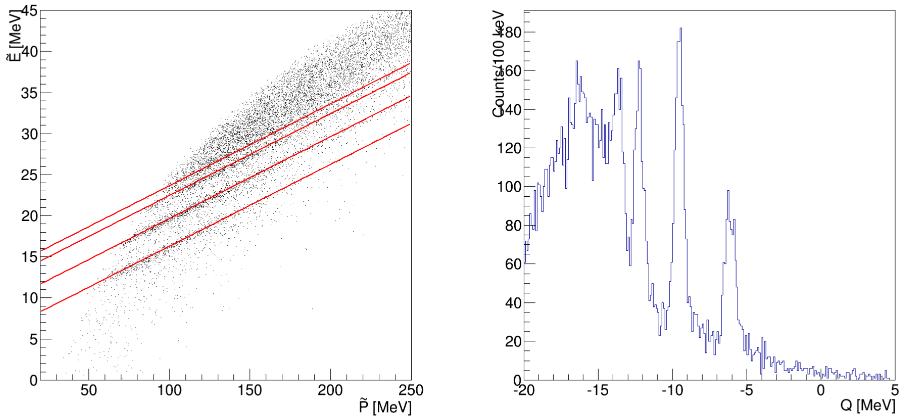

Figure 4.70: Left: The Catania plot for the ^{9}Be(^{13}C,^{8}Be$_{gs}$ ^{4}He) reaction, ^{8}Be$_{gs}$ detected in the T1 and ^{4}He in the T4. The four red lines are denoting the position of reaction loci for undetected ^{10}Be: the lowest for all nuclei in the ground state, while the other three lines for the reaction channels in which the undetected ^{10}Be nucleus excited to the $E_x = 3.37$, ≈ 6.2 and 7.37 MeV. All four lines were shifted by +0.75 MeV to reproduce the data. **Right:** The corresponding Q-value spectrum.

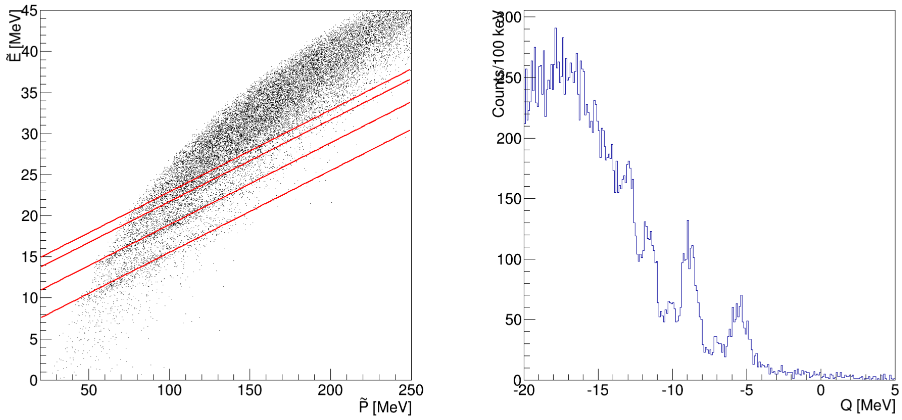

Figure 4.71: Left: The Catania plot for the ^{9}Be(^{13}C,^{8}Be$_{gs}$ ^{4}He) reaction, ^{8}Be$_{gs}$ detected in the T2 and ^{4}He in the T3. The four red lines are denoting the position of reaction loci for undetected ^{10}Be: the lowest for all nuclei in the ground state, while the other three lines for the reaction channels in which the undetected ^{10}Be nucleus excited to the $E_x = 3.37$, ≈ 6.2 and 7.37 MeV. The four lines were not adjusted to reproduce the data. **Right:** The corresponding Q-value spectrum.

the states at $E_x \approx 6.2$ MeV. The quality of the data for the ^{8}Be$_{gs}$(T2)+^{4}He(T3) coincidences is much lower, resulting in broader peaks.

For all the aforementioned detector combinations the detection angle and the detected energy for both detected particles were plotted versus the Q-value (see Appendix D). The Q-value loci on the plots show a general vertical trend with occasional minor discrepancies, mostly for the E_{det}-Q plot. Therefore, the Q-values depend neither on the energy nor on the angle of the detected particle and one can proceed with the further analysis.

Now a channel with all the outgoing particles in the ground state can be selected and relative energies may be plotted for all the detector telescopes combination.

Relative energies were computed using the kinematical formulae from the section on the data analysis. In the Figs. 4.72 and D.5 one can find relative energy plots for the ground-state channel. The detector combination TM TN is the one in which the ^{8}Be nucleus was detected in the M-th detector telescope and the ^{4}He in the N-th detector telescope. The amount of the data for the T1-T4 and the T2-T3 coincidences is very small, consequently no loci can be unambiguously identified (although there are hints of possible loci corresponding to the ^{14}C excited states). For the front-angle coincident events, multiple loci belonging to the excited states of the ^{12}C ($E_{r12} \approx 4$, 7 MeV) and ^{14}C ($E_{r23} \approx 2.5$, 4 MeV) are visible. No loci are visible in the relative energy $E_{\mathrm{r}13}$, which would correspond to the excited states of the ^{18}O.

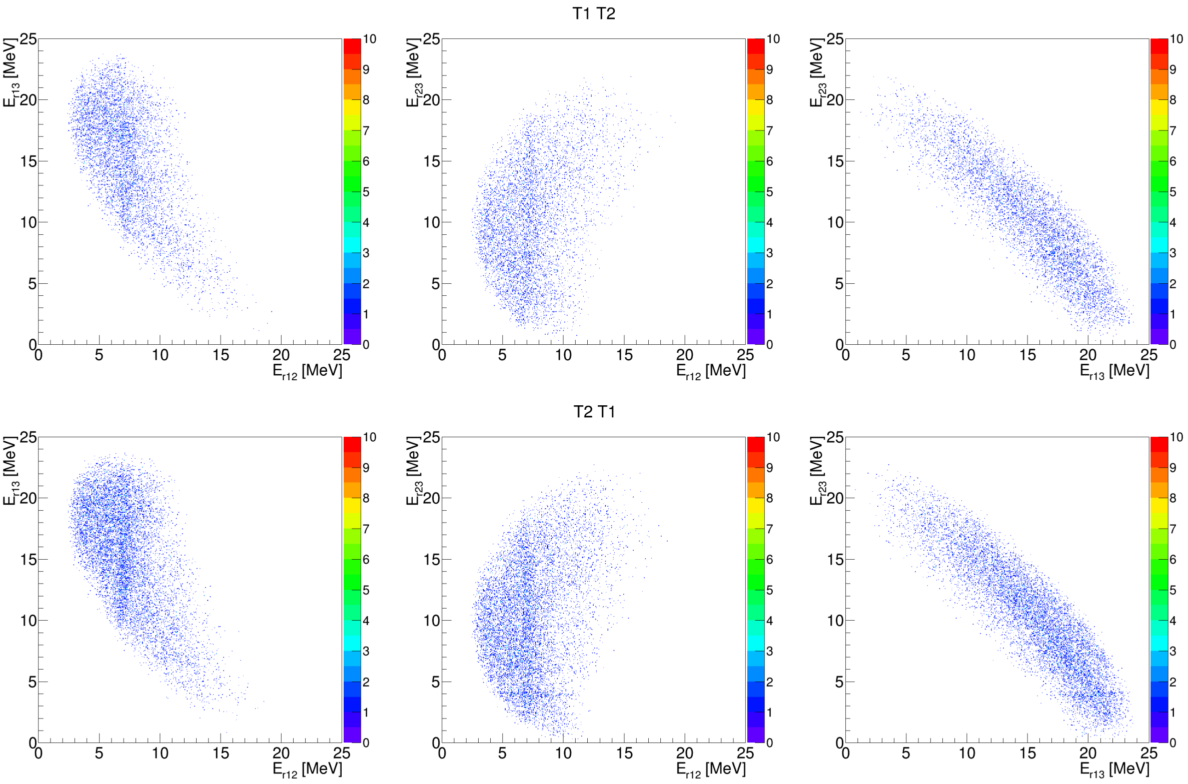

Figure 4.72: Relative-energy plots for the ^{9}Be(^{13}C,^{8}Be$_{\mathrm{gs}}$ ^{4}He)^{10}Be$_{\mathrm{gs}}$ reaction. Different detector combinations are displayed one per row. ^{8}Be$_{\mathrm{gs}}$, ^{4}He and ^{10}Be are designated by numbers 1, 2 and 3, respectively.

Results for the ^{9}Be(^{13}C,^{8}Be$_{\mathrm{gs}}$ ^{4}He)^{10}Be(E_x =3.37 MeV) channel are presented in the Figs. 4.73 and D.6. This reaction channel has a better statistics than the ^{10}Be ground-state channel. Here one may note faint loci in the $E_{\mathrm{r}13}$-$E_{\mathrm{r}12}$ plot at approx. $E_{\mathrm{r}13}$=4 and 7 MeV that might correspond to the excited states in the ^{18}O decaying to the ^{8}Be$_{\mathrm{gs}}$+^{10}Be(3.37 MeV) channel. The

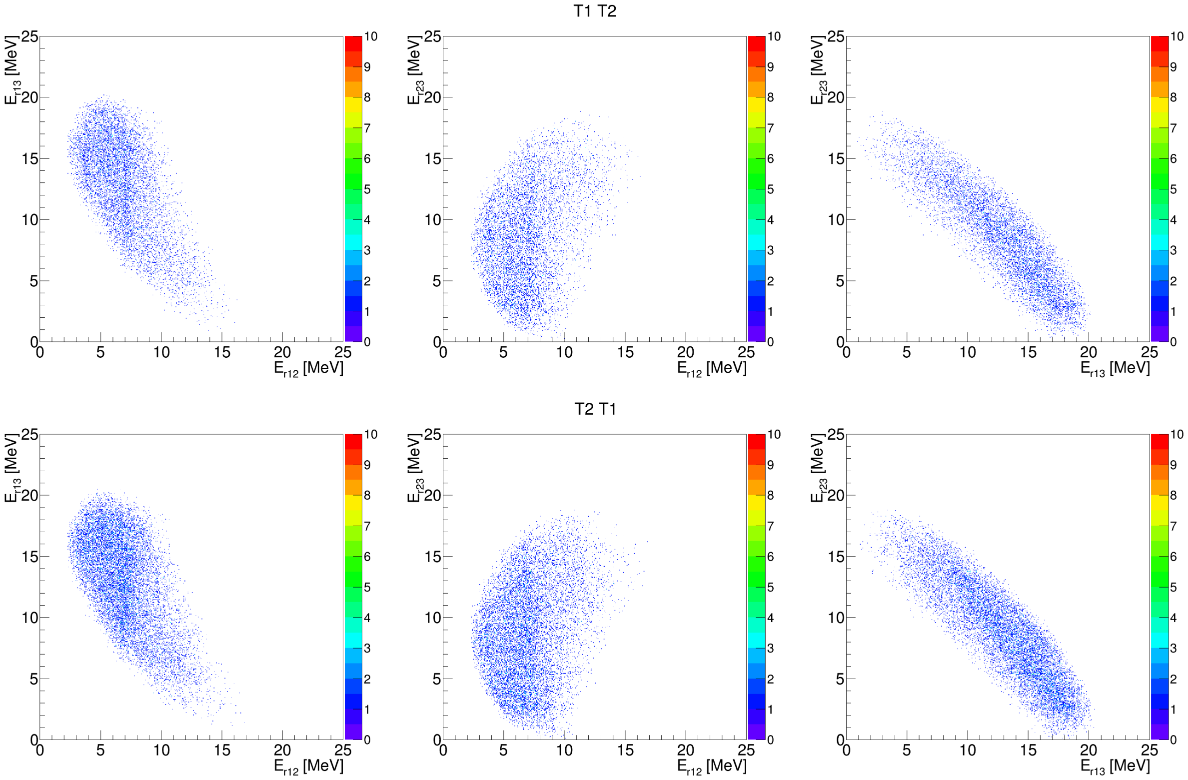
T1 T2

T2 T1

Figure 4.73: Relative-energy plots for the ^{9}Be(^{13}C,^{8}Be$_{gs}$ ^{4}He)^{10}Be(3.37 MeV) reaction. Different detector combinations are displayed one per row. ^{8}Be$_{gs}$, ^{4}He and ^{10}Be are designated by numbers 1, 2 and 3, respectively.

loci belonging to the excited states of the ^{12,14}C are present as well. The ^{12}C states are visible at the $E_{r12} \approx 3.5$ and 7.0 MeV. Two or three ^{14}C loci are visible bellow $E_{r23} = 6$ MeV.

The relative energy spectra for the ^{9}Be(^{13}C,^{8}Be$_{gs}$ ^{4}He)^{10}Be($E_x \approx$6.2 MeV) reaction (Figs. 4.74 and D.7) contain loci of ^{12}C states at approx. $E_{r12} = 4$ and 7 MeV. Faint ^{14}C loci are visible bellow $E_{r23} = 5$ MeV, as in the case of the previous reaction channel.

In all three reaction channels the strongest loci have been the ones associated with the excited states of the ^{12}C. States of the ^{14}C are visible, as well. In order to check for the possible ^{18}O states, strongest ^{12,14}C loci will be excluded using two conditions:

$$E_{r12} > 8.0\,\text{MeV} \tag{4.49}$$

$$E_{r23} > 6.0\,\text{MeV} \tag{4.50}$$

Using this conditions plots for the T1-T2 and T2-T1 detector combinations were plotted for all three channels (ground state, the first excited state and the group of ^{10}Be states at $E_x \approx 6.2$ MeV) and are displayed on Figs. 4.75, 4.76 and 4.77, respectively. The red line denotes the data

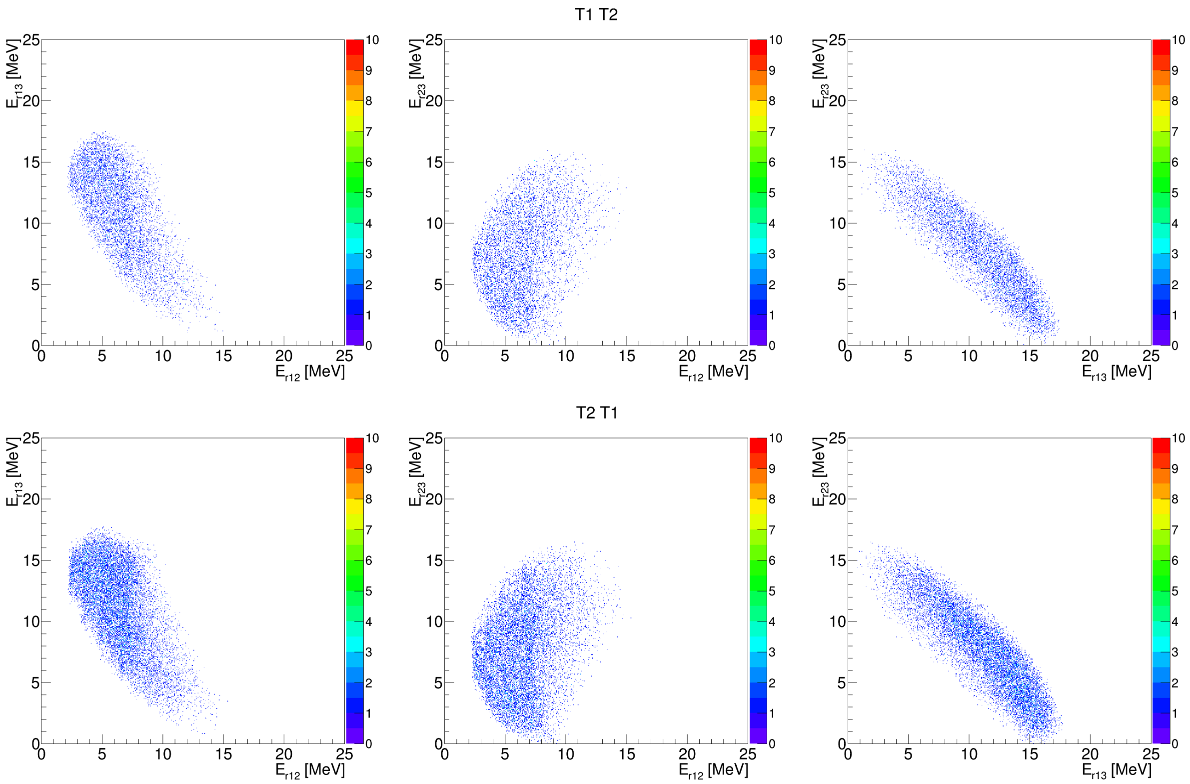

Figure 4.74: Relative-energy plots for the ^{9}Be(^{13}C,^{8}Be$_{gs}$ ^{4}He)^{10}Be(6.2 MeV) reaction. Different detector combinations are displayed one per row. ^{8}Be$_{gs}$, ^{4}He and ^{10}Be are designated by numbers 1, 2 and 3, respectively.

without the relative energy cuts while the green line shows the data with both cuts applied. The relevant decay thresholds are:

$$E^{\text{threshold}}_{^{12}\text{C}\to{}^{8}\text{Be}^{4}\text{He}} = 7.367\ \text{MeV} \tag{4.51}$$

$$E^{\text{threshold}}_{^{14}\text{C}\to{}^{10}\text{Be}^{4}\text{He}} = 12.012\ \text{MeV} \tag{4.52}$$

$$E^{\text{threshold}}_{^{18}\text{O}\to{}^{10}\text{Be}^{8}\text{Be}} = 18.332\ \text{MeV} \tag{4.53}$$

With the cuts applied, the excitation energy spectra should be free of the strongest contributions originating from the excited states of the ^{12}C and the ^{14}C. The two rightmost plots of the Fig. 4.75 (the ground-state reaction channel) display the excitation energy spectrum of the ^{18}O. The red line denotes the original spectrum while the green line denotes the spectrum with the strongest ^{12,14}C states excluded. The peak is located at $E_x(^{18}\text{O}) \approx 25$ MeV and is seen both for the T1-T2 and the T2-T1 coincidences.

The rightmost plots in the Fig. 4.76 (undetected nucleus ^{10}Be in the 3.37 MeV excited state) show excitation energy spectra of the ^{18}O. The two spectra contain a peak at approx. 25 MeV.

In the Fig. 4.77 (the channel with an undetected ^{10}Be in the group of excited states around the E_x ≈6.2 MeV) a possible peak is located at $E_x(^{18}\text{O})$ ≈29.0 MeV (visible for the ^{8}Be(T1)+^{4}He(T2) coincident events but not for the ^{8}Be(T2)+^{4}He(T1)).

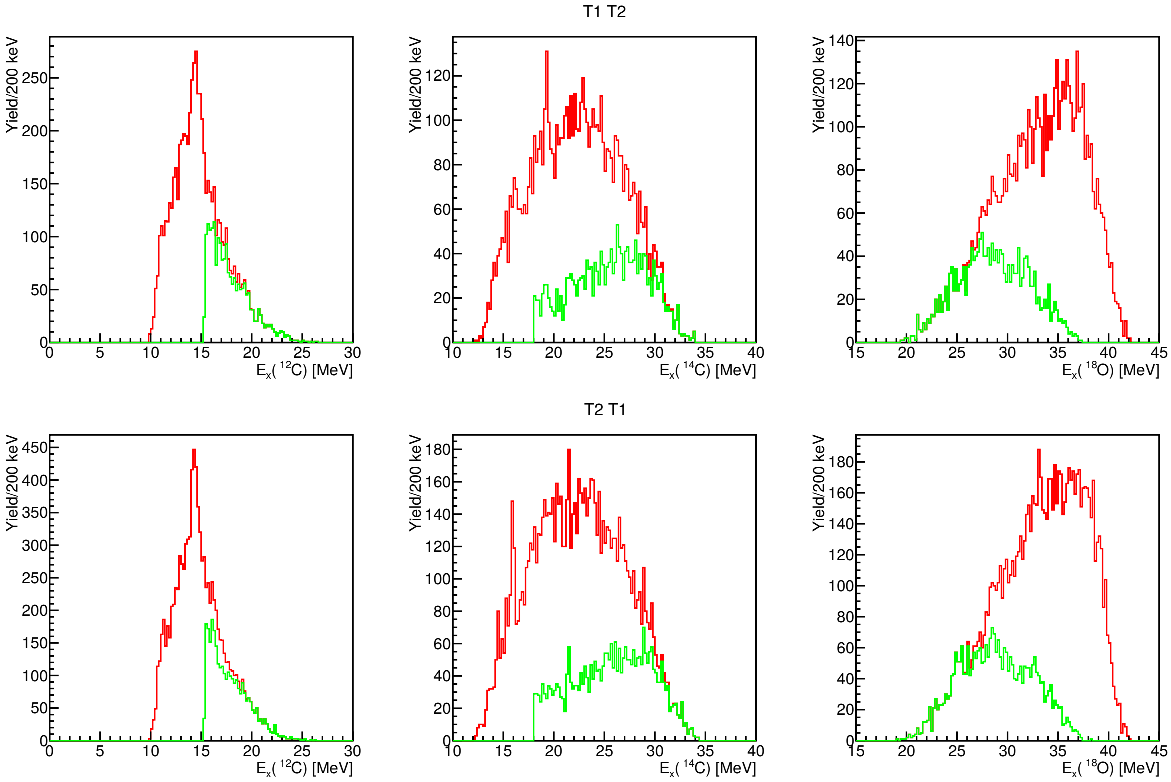

Figure 4.75: Excitation energy plots of the ^{12}C, ^{14}C and ^{18}O calculated from the relative energies of the outgoing particles from the ^{9}Be(^{13}C,^{8}Be$_{\text{gs}}$ ^{4}He)^{10}Be$_{\text{gs}}$ reaction. The red line denotes the data without and the green line with relative-energy cuts excluding the strongest states of the ^{12,14}C.

Finally, let us comment on the excited states of the ^{12,14}C reconstructed by studying the ^{8}Be+^{4}He coincidences. The most prominent ^{12}C state populated in the ground-state reaction channel is located at $E_x \approx$ 14.2 MeV. The other peak is located at $E_x \approx$ 13 MeV. At the lower edge of the spectrum there is a peak at approx. 11 MeV. The strongest peak corresponds to the 14.083 MeV 4^+ excited state, while the 13.0 MeV peak, judging by the offset of the 14.2 MeV peak, may correspond to the 12.710 MeV 1^+ excited state. The peak at the lower end of the spectrum probably corresponds to the 10.844 MeV 1^- state. For the ^{10}Be(E_x =3.37 MeV)+^{8}Be$_{\text{gs}}$+^{4}He reaction channel, the ^{12}C excitation energy spectrum still has a prominent peak at $E_x \approx$ 14.2 MeV. The E_x ≈11 MeV peak is still visible for the T1-T2 coincidences, but is missing for the T2-T1 events. Finally, for the ^{10}Be(E_x ≈6.2 MeV)+^{8}Be$_{\text{gs}}$+^{4}He reaction channel a peak at E_x ≈13 MeV is nearly as high as the $E_x \approx$ 14.2 MeV peak. The E_x ≈11 MeV peak is visible only for the T2-T1 coincident events.

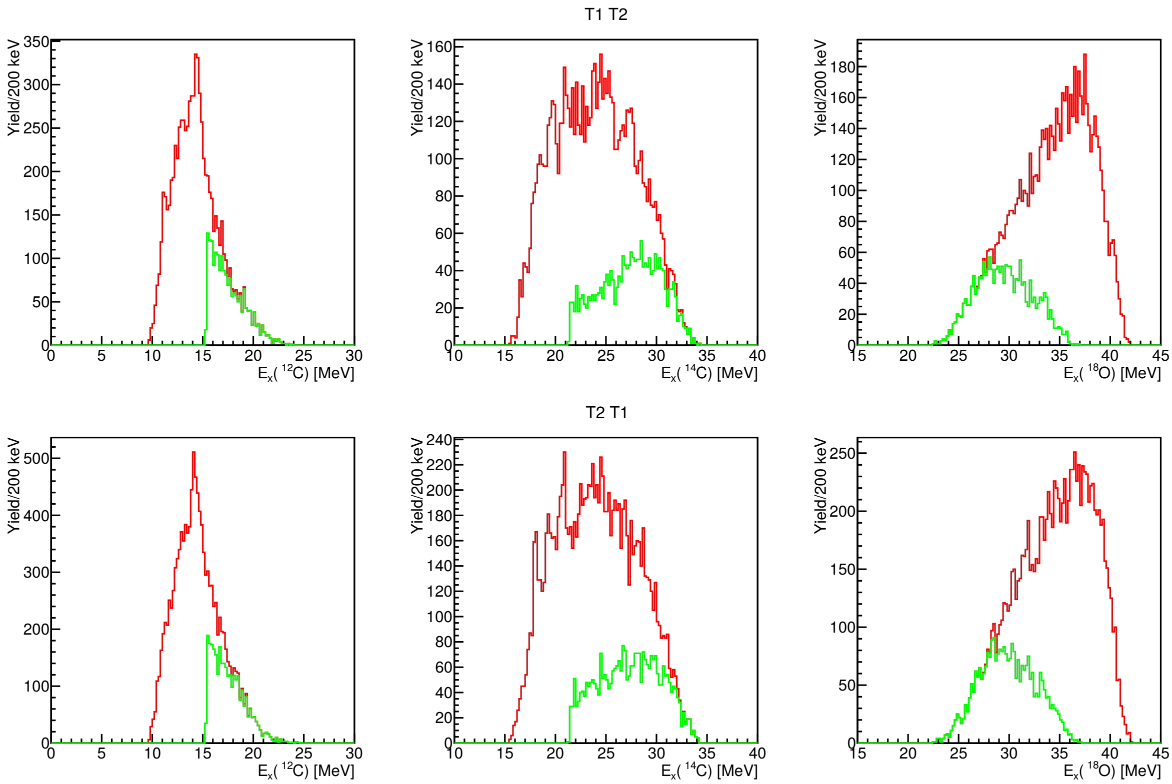

Figure 4.76: Excitation energy plots of the ^{12}C, ^{14}C and ^{18}O calculated from the relative energies of the outgoing particles from the ^{9}Be(^{13}C,^{8}Be$_{gs}$ ^{4}He)^{10}Be(3.37 MeV) reaction. The red line denotes the data without and the green line with relative-energy cuts excluding the strongest states of the ^{12,14}C.

The ^{14}C states decaying to the ground-state reaction channel visible in the spectrum are located at $E_x \approx$16 MeV and 19 MeV. For the ^{10}Be(E_x =3.37 MeV)+^{8}Be$_{gs}$+^{4}He reaction channel peaks are located at $E_x \approx$17, 19.5 and 20.5 MeV. For the last reaction channel peaks are more difficult do identify, but a peak at the $E_x \approx$ 21 MeV could be present. Some of this peaks were observed by studying the ^{10}Be+^{4}He coincidences as well (see Tab. 4.2), therefore it can be concluded that the excited states of the ^{14}C seen in the ^{10}Be+^{4}He and the ^{8}Be$_{gs}$+^{4}He are consistent.

^{8}Be+^{10}Be coincidences

In the previous section the study of the ^{13}C+^{9}Be→ ^{4}He+^{8}Be$_{gs}$+^{10}Be reaction was performed by studying the ^{8}Be$_{gs}$+^{4}He coincidences. Here the ^{8}Be$_{gs}$+^{10}Be coincidences will be studied. The difference between the former and the latter results are:

- ^{8}Be$_{gs}$+^{10}Be coincidences allow for only particle-bound excited states of the ^{10}Be
- both decay products from a possible ^{18}O excited state decaying to the ^{8}Be$_{gs}$+^{10}Be (particle-bound states) are detected

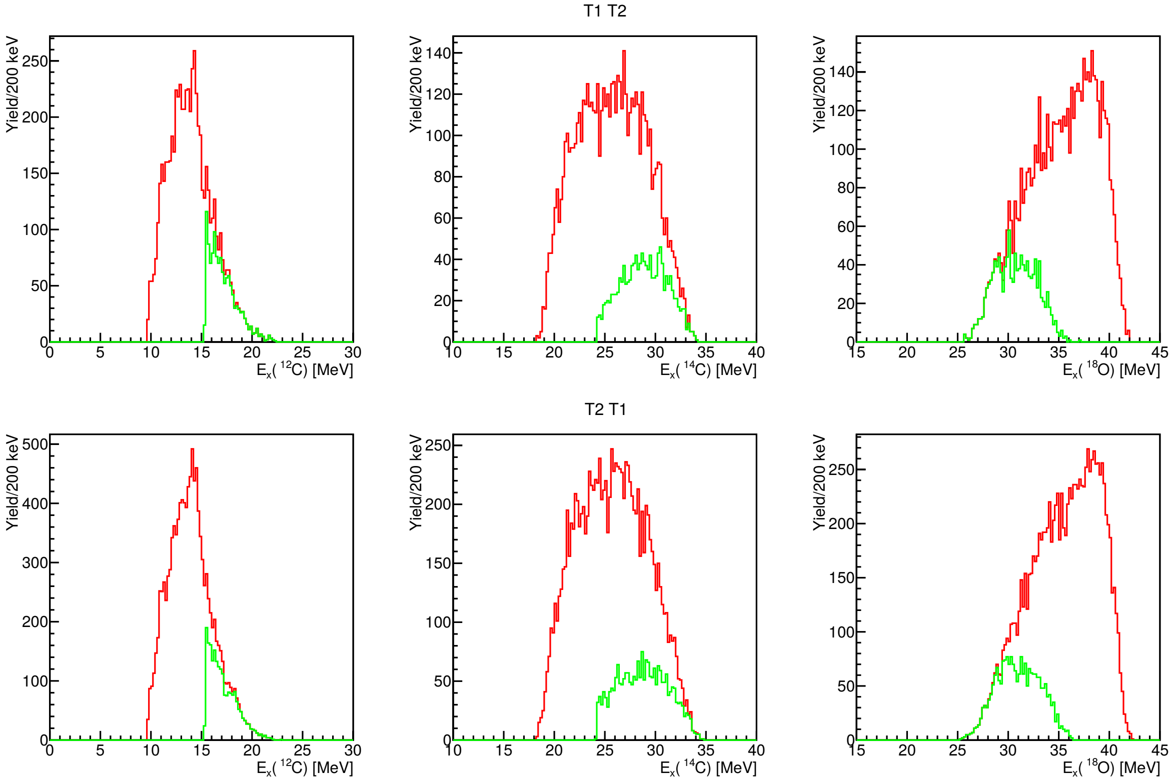

Figure 4.77: Excitation energy plots of the ^{12}C, ^{14}C and ^{18}O calculated from the relative energies of the outgoing particles from the ^{9}Be(^{13}C,^{8}Be$_{gs}$ ^{4}He)^{10}Be(6.2 MeV) reaction. The red line denotes the data without and the green line with relative-energy cuts excluding the strongest states of the ^{12,14}C.

- ^{10}Be nucleus can be identified only in the front detector telescopes T1 and T2

One can start with the Catania plots in order to identify exit channels populated in this reaction. In the Fig. 4.78 plots for the ^{8}Be$_{gs}$(T1) and the ^{10}Be(T2) are displayed. Three prominent loci are visible on the Catania plot, their slope and position corresponding to the ground state, the first excited state and the group of the ^{10}Be states at $E_x \approx$6.2 MeV. The corresponding Q-values equal to -5.50 MeV, -8.87 MeV and -11.68 MeV, respectively. The fourth locus visible in the ^{8}Be+^{4}He exit channel is missing here because it corresponds to the particle-unbound excited state of the ^{10}Be. The three loci form well-separated peaks in the Q-value plots, enabling us to separate the three channels properly.

The opposite combination of the front-angle detector telescopes ^{8}Be$_{gs}$(T2) and the ^{10}Be(T1) (Fig. 4.79) provides a slightly higher number of events than the former one. The three loci are visible, their slope and position fairly matching the predicted ones if shifted by +1.0 MeV. The Q-value spectrum has the same features, although the separation between the peaks pertaining to the channels with ^{10}Be* is not so good as in the former case. However, different reaction-channels can still be separated using the Q-value plot.

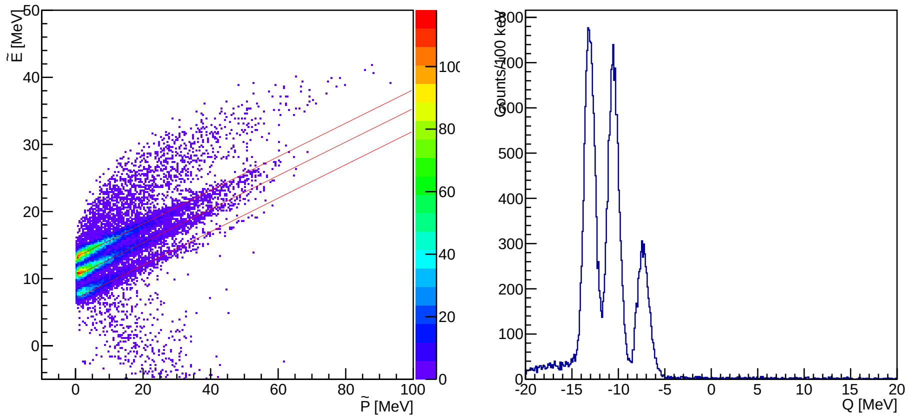

Figure 4.78: Left: The Catania plot for the ^{9}Be(^{13}C,^{8}Be$_{gs}$ ^{10}Be) reaction, ^{8}Be$_{gs}$ detected in the T1 and ^{10}Be in the T2. The three red lines are denoting the position of reaction loci for undetected ^{10}Be: the lowest for all nuclei in the ground state and the other two for the reaction channels in which the undetected ^{10}Be nucleus is in the 3.37 MeV excited state and the group of excited states at $E_x \approx 6.2$ MeV, respectively. All three lines were shifted by +1.5 MeV to reproduce the data. **Right:** The corresponding Q-value spectrum.

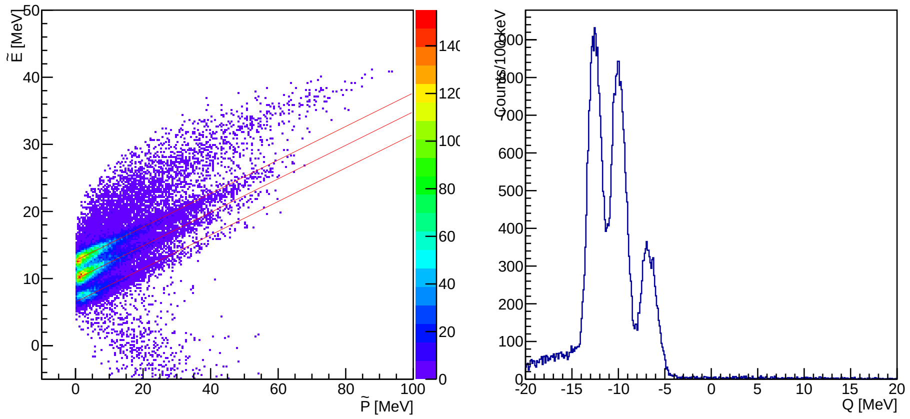

Figure 4.79: Left: The Catania plot for the ^{9}Be(^{13}C,^{8}Be$_{gs}$ ^{10}Be) reaction, ^{8}Be$_{gs}$ detected in the T2 and ^{10}Be in the T1. The three red lines are denoting the position of reaction loci for undetected ^{10}Be: the lowest for all nuclei in the ground state and the other two for the reaction channels in which the undetected ^{10}Be nucleus is in the 3.37 MeV excited state and the group of excited states at $E_x \approx 6.2$ MeV, respectively. All three lines were shifted by +1.0 MeV to reproduce the data. **Right:** The corresponding Q-value spectrum.

The Q-value plotted against the detection angles and detected energies of the particles can be found in the Appendix E. The forward-telescope coincident events, in both the T1-T2 and the T2-T1 combination, do not show strong angular or energy dependence. Consequently, one can proceed to study the relative energy spectra for the three aforementioned reaction exit channels.

Let us start with the Fig. 4.80, displaying the relative energy spectra for the ground-state exit channel. The loci of the E_{r12} correspond to the ^{18}O states, E_{r13} to the ^{12}C states and E_{r23}

to the states of the ^{14}C. The E_{r12} locus can be seen at E_{r12} ≈9 MeV in both the E_{r13}-E_{r12} and the E_{r23}-E_{r12} plots. The loci in the E_{r13} are not strong: in the T1-T2 combination, a locus at E_{r13} ≈2 MeV is present and hints of some other loci, but not strong enough to be unambiguously identified. The two ^{14}C loci are visible at the E_{r23} ≈6 and 8 MeV.

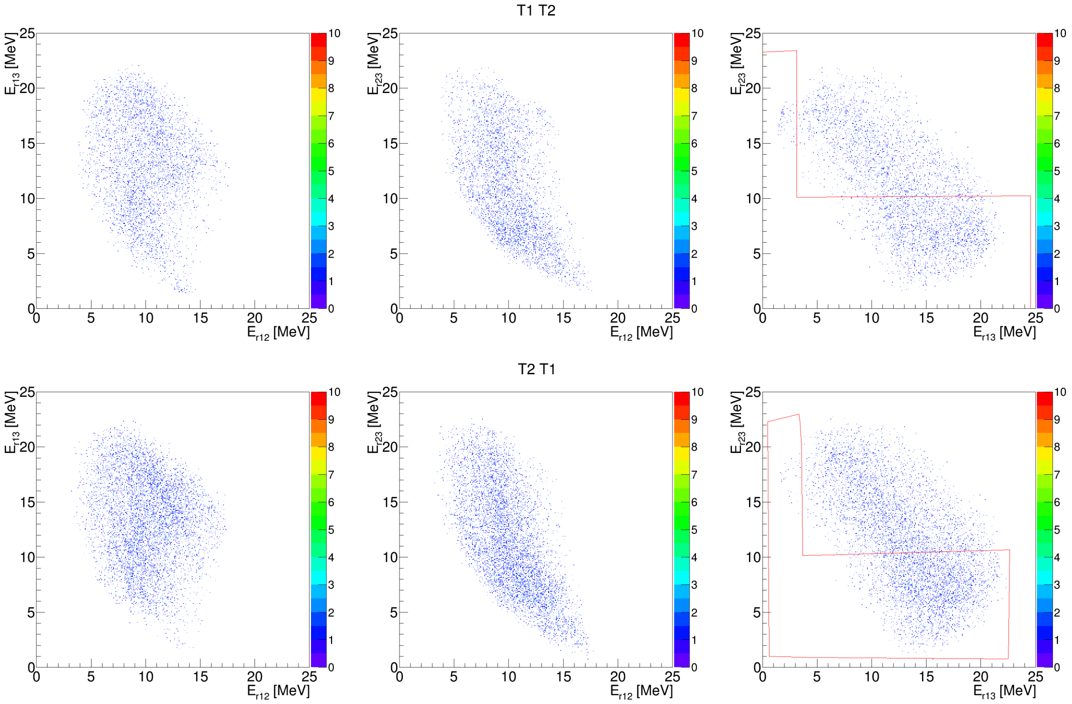

Figure 4.80: E_r-E_r plots for the ^{9}Be(^{13}C,^{8}Be$_{gs}$ ^{10}Be) reaction. Different detector combinations are displayed one per row. The ^{8}Be$_{gs}$, the ^{10}Be and the ^{4}He nuclei are designated by numbers 1, 2 and 3, respectively. The red line denotes the border of the graphical cut used in subsequent analysis (see text for details).

The E_r-E_r plots for the $E_x(^{10}\text{Be}) = 3.37$ MeV exit channel (Fig. 4.81) show multiple loci that are easier to identify than those for the ground-state reaction channel. One may start with the E_{r13} loci corresponding to the excited states of the ^{12}C. Apart from the locus at $E_{r13} \approx$ 2 MeV, seen in the ground state exit channel as well, one more locus may be identified at approx. 6 MeV. The states of the ^{14}C decaying to this reaction channel correspond to the E_{r23} loci, visible at $E_{r23} \approx 4$ and 5 MeV. Finally, ^{18}O excited states are visible as loci of the constant E_{r12}. In these spectra they are visible at E_{r12} ≈8.5 and 11.0 MeV.

Finally, the plots displayed in the Fig. 4.82 are the relative energy spectra for the reaction exit channel with $E_x(^{10}\text{Be}) \approx 6.2$ MeV (a group of states). The ^{12}C excited state decaying through this reaction channel is visible at $E_{r13} \approx 2$ MeV. Loci at higher energies are much weaker and not easy to identify. Possible loci of ^{14}C may be seen at $E_{r23} \approx 3$ and 5 MeV. A possible ^{18}O loci cannot be unambiguously identified.

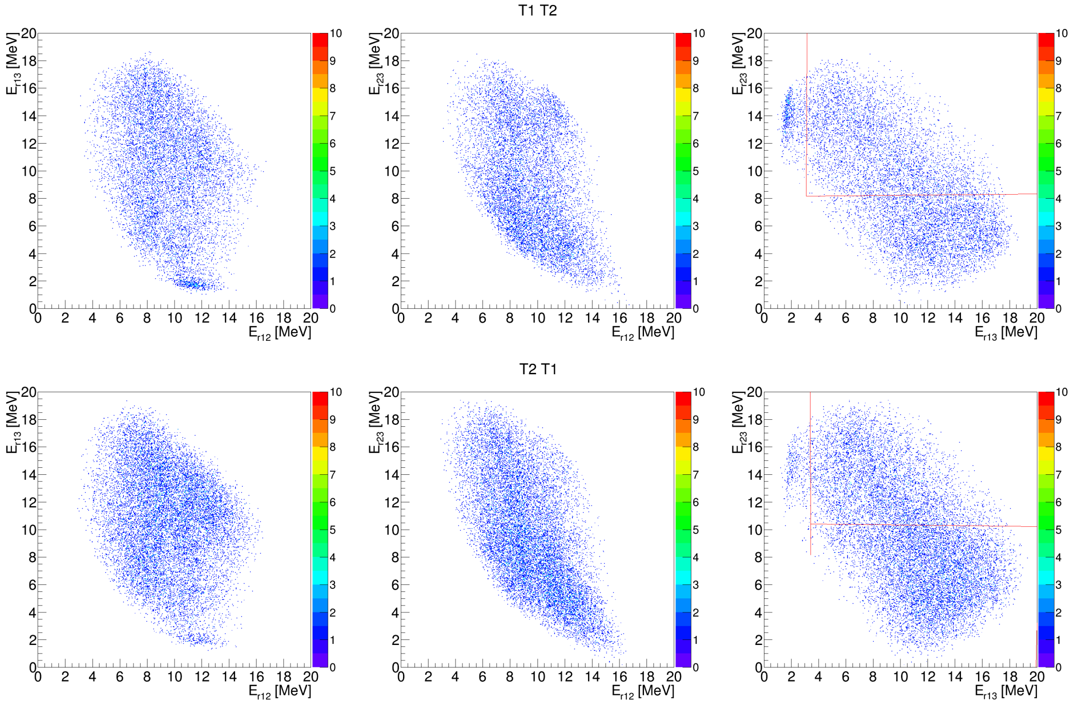

Figure 4.81: E_r-E_r plots for the ^{9}Be(^{13}C,^{8}Be$_{gs}$ ^{10}Be(E_x=3.37 MeV)) reaction. Different detector combinations are displayed one per row. The ^{8}Be$_{gs}$, the ^{10}Be and the ^{4}He nuclei are designated by numbers 1, 2 and 3, respectively. The red line denotes the border of the graphical cut used in subsequent analysis (see text for details).

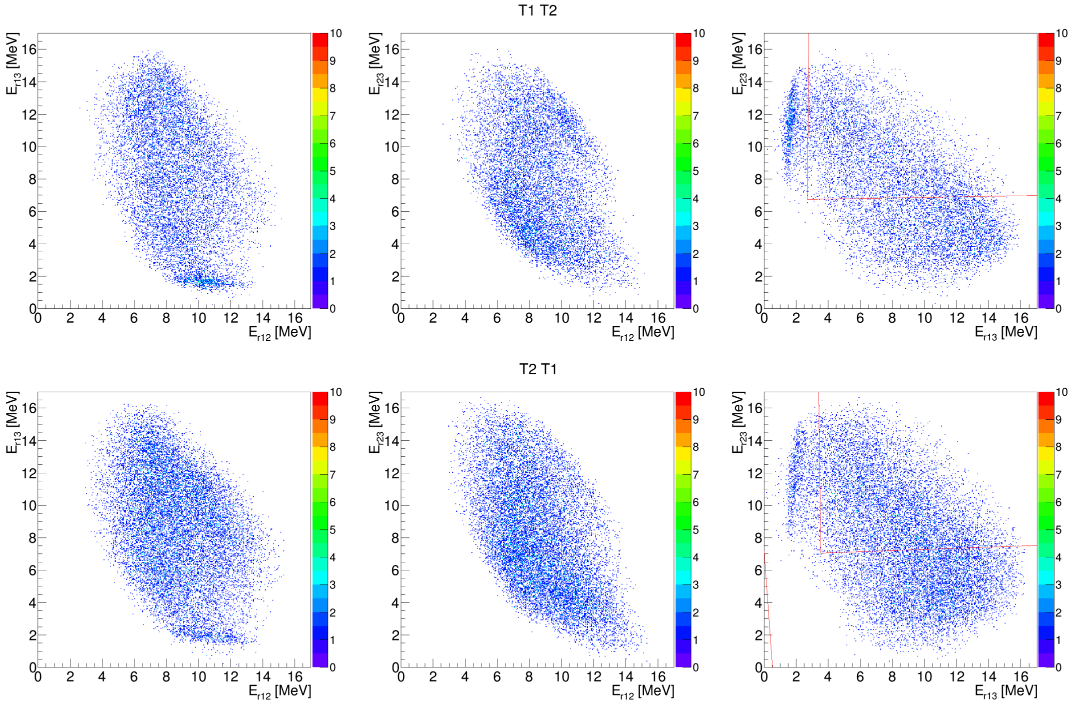

Figure 4.82: E_r-E_r plots for the ^{9}Be(^{13}C,^{8}Be$_{gs}$ ^{10}Be(E_x ≈6.2 MeV)) reaction. Different detector combinations are displayed one per row. The ^{8}Be$_{gs}$, the ^{10}Be and the ^{4}He nuclei are designated by numbers 1, 2 and 3, respectively. The red line denotes the border of the graphical cut used in subsequent analysis (see text for details).

The excitation energy spectra of the ^{12}C, ^{14}C and the ^{18}O for the ground state exit channel are displayed in the Fig. 4.83. The green line depicts the excitation energy with the cut applied (see Fig. 4.80). The ^{12}C states visible are 9.641 MeV $J^{\pi} = 3^{-}$ (T1-T2 coincidences, out of range for the T2-T1 coincidences) and a higher energy peak visible in both cobinations, approx. at 16.5 MeV and may correspond to the 16.57 MeV $J^{\pi} = 2^{-}$. The ^{14}C excitation energy spectrum begins at approx. $E_x = 15$ MeV and contains possible peaks at approx. 16.5 and 18 MeV. The ^{18}O excitation energy spectrum shows a possible peak at 24 MeV, more clear for the T1-T2 coincidences. In both detector combinations there is a peak visible at higher energies (e.g. $E_x \approx$27 MeV peak). At such a high energies no states are documented in Ref. [87].

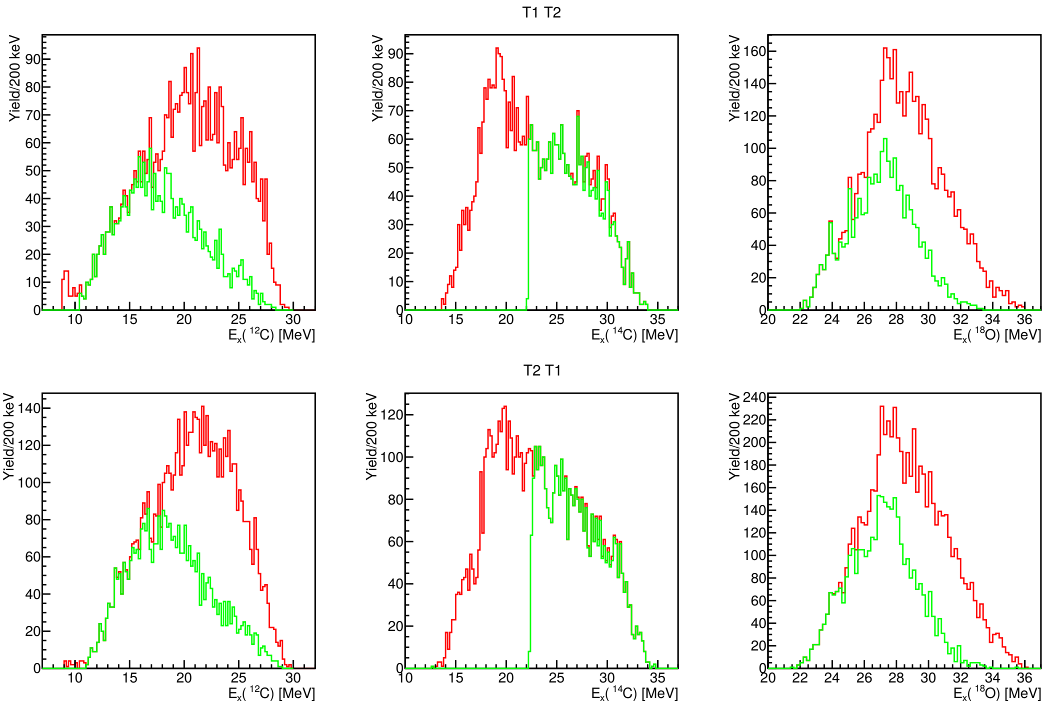

Figure 4.83: Excitation energy spectra of the ^{12,14}C and ^{18}O, calculated from the the ^{8}Be$_{gs}$+^{10}Be coincident events. The red line denotes the spectra calculated without the relative-energy cuts, while the green line labels the data calculated with the graphical cut E_{r23}-E_{r13} (see Fig. 4.80).

The plots for the ^{8}Be+^{10}Be($E_x = 3.37$ MeV) exit channel are displayed in the Fig. 4.84. A peak corresponding to the 9.641 MeV $J^{\pi} = 3^{-}$ state of the ^{12}C is well pronounced, while higher excited states are not visible. The ^{14}C excitation energy spectrum on the same figure doesn't show any narrow peak, although there is a structure consisting of one or two broad peaks. The excitation energy spectrum of the ^{18}O shows a broad structure. Loci that were observed at E_{r12} $\approx$8.5 and 11 MeV in the two-dimensional E_r-E_r plots in the Fig. 4.81 correspond to the structures at $E_x \approx 30$ and 33 MeV.

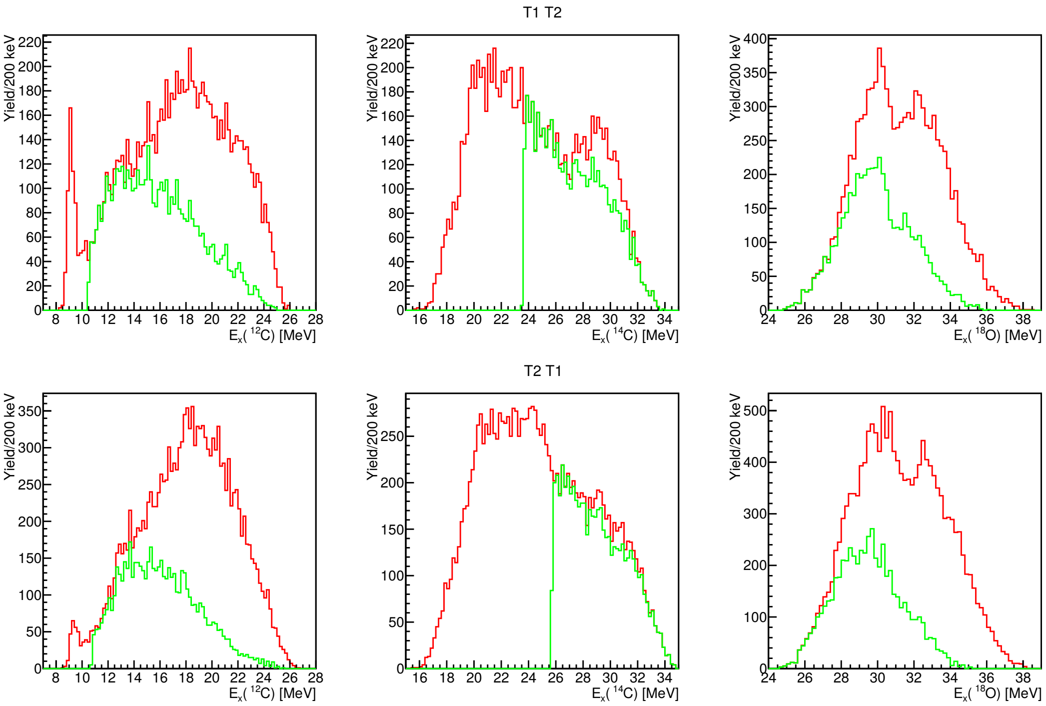

Figure 4.84: Excitation energy spectra of the ^{12,14}C and ^{18}O, calculated from the the ^{8}Be$_{gs}$+^{10}Be(3.37 MeV) coincident events. The red line denotes the spectra calculated without the relative-energy cuts, while the green line labels the data calculated with the graphical cut E_{r23}-E_{r13} (see Fig. 4.81).

Finally, the ^{8}Be$_{gs}$+^{10}Be(E_x ≈6.2 MeV) coincident events provide the excitation energy spectra displayed in the Fig. 4.85. The peak corresponding to the 9.641 MeV $J^{\pi} = 3^{-}$ state of the ^{12}C is very strong. The ^{14}C spectrum shows a weak peak at approx. 23 MeV, while the ^{18}O excitation energy spectrum doesn't have any pronounced features.

In conclusion, the E_r-E_r plots for the ^{8}Be$_{gs}$+^{10}Be coincidences show strong loci only for the ^{12}C states. Several peaks were observed in the ^{14}C excitation energy spectra, possibly linked with a highly excited state at approx. 20 MeV for the ground-state and the ^{10}Be(3.37 MeV) channel and 24 MeV for the ^{10}Be(6.2 MeV) reaction channels. These peaks may correspond to the 20.02 MeV peak observed by [92], which was observed by [90] at 20.3(1) MeV, and the 24.0 MeV peak observed in Ref. [88], respectively. The excitation energy spectra of the ^{18}O (with graphical cuts applied) show a peak at $E_x \approx 24$ MeV for the ground-state reaction channel.

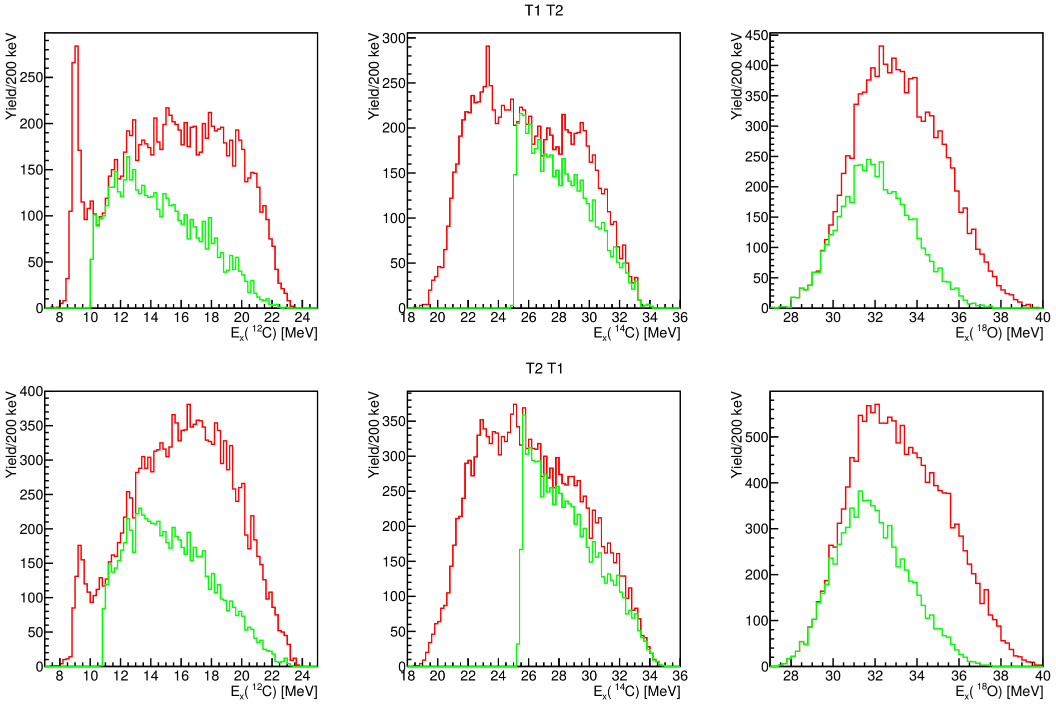

Figure 4.85: Excitation energy spectra of the ^{12,14}C and ^{18}O, calculated from the the ^{8}Be$_{gs}$+^{10}Be(6.2 MeV) coincident events. The red line denotes the spectra calculated without the relative-energy cuts, while the green line labels the data calculated with the graphical cut E_{r23}-E_{r13} (see Fig. 4.82).

Chapter 5

Discussion

In this chapter the data obtained from the two experiments will be compared to results of previous experiments and to known states listed in the compilation [50]. The chapter is divided in two parts: in the first the data on the ^{17}O structure will be discussed and in the second the results for the ^{18}O. The observed states of the nuclei other than oxygen isotopes are discussed in the chapters on their respective experiments.

5.1 Excited states of the ^{17}O nucleus

In this section the excited states of the ^{17}O studied in the ^{13}C+^{4}He resonant elastic scattering experiment and the $^{13}\mathrm{C} + {}^{9}\mathrm{Be} \rightarrow {}^{17}\mathrm{O}^{*} + {}^{5}\mathrm{He} \rightarrow {}^{13}\mathrm{C} + {}^{4}\mathrm{He} + {}^{5}\mathrm{He}$ reaction are presented and compared to previously published results.

5.1.1 States observed in the ^{13}C+^{4}He resonant elastic scattering experiment

The ^{13}C+^{4}He resonant elastic scattering experiment on a thick gas target enabled us to study the ^{17}O excitation function. The ^{17}O excitation function for the ^{13}C+^{4}He resonant elastic scattering was previously known up to $E_x(^{17}\mathrm{O}) = 11.1$ MeV. This measurement extended that range up to $E_x \approx 13.8$ MeV. The published R-matrix parameters from the most recent well-constrained multichannel fit [7] reproduce the low-energy part of the excitation function well, discrepancies getting larger with increasing excitation energy and opening of additional reaction channels. Due to the lack of experimental data on the channels other than elastic scattering for the $E_x >$ 11.1 MeV the R-matrix fit could not be extended to higher energies. A simplified, qualitative approach was used instead to study several quasi-isolated resonances (see section 3.3.4 for details). Using that approach, five resonances were studied, two of which were known. The results are summarized in the Tabs. 3.7 (p. 59) and 3.9 (p. 62). An increased value of the Wigner ratio has been determined for the two known resonances, indicating a possible α-cluster structure. For the three quasi-isolated resonances outside the range of the previous studies at $E_x(^{17}\text{O}) = 12.0$, 12.8 and 13.6 MeV tentative spin and parity as well as a corresponding Wigner ratios were obtained.

The lowest of the three peaks, at 12.0 MeV, is likely to correspond to a high-spin state. If spin and parity equal to $\frac{13}{2}^-$, the resonance may have pronounced α-cluster structure. This state of the ^{17}O has been observed in multiple experiments ([61],[96], [97] and [98]) and listed as a 12.005 MeV state in the compilation [50]. In the ^{13}C+^{9}Be experiment this state has been observed as a part of a broad peak at $E_x \approx 12.25$ MeV.

For the 12.8 MeV peak the simplified fit gave a tentative spin of $\frac{7}{2}^-$. A state at 12.81 MeV has been observed in the ^{13}C(^{4}He,^{4}He) and ^{13}C(^{4}He,n) reactions [99] and is included in the compilation [50]. Lastly, the spin and parity of the resonance corresponding to the 13.6 MeV peak is likely to be $\frac{11}{2}^-$, the corresponding Wigner ratio indicating possible α-cluster structure.

Of the five aforementioned peaks, four are inside the excitation energy range covered by the second experiment, studying the reaction ^{9}Be(^{13}C,^{13}C^{4}He)^{5}He. The three peaks from the resonant elastic scattering experiment at $E_x = 9.2$, 12.0 and 13.6 MeV correspond to the 9.15, 12.25 and 13.6 MeV peaks in Fig. 4.25 left. The reactions that populate these states and the corresponding references are discussed in the next section on the states observed in the ^{13}C+^{9}Be experiment, and summarized in the Tab. 5.1. Here one may note that the most pronounced peaks in the Fig. 4.25 left are the 9.15 MeV and 13.57 MeV peaks, the former being on the border of the excitation energy range covered in the ^{13}C+^{9}He experiment where detection efficiency gets lower.

5.1.2 States observed in the ^{13}C+^{9}Be experiment

In this section the peaks observed in the $^{9}\text{Be}+^{13}\text{C} \rightarrow ^{13}\text{C}+^{4}\text{He}+^{5}\text{He}$ and the $^{9}\text{Be}+^{13}\text{C} \rightarrow ^{13}\text{C}^{*}(E_x = 3.7\text{ MeV})+^{4}\text{He}+^{5}\text{He}$ reactions will be discussed and their correspondence to the excited states of the ^{17}O observed in other experiments.

When interpreting the results, one should keep in mind that due to several difficulties with the experiment set up and during the course of the experiment only limited calibration data was available, which influenced the quality of the calibration. Furthermore, due to less than optimal beam tuning and collimation on the one hand and the limitations of the data acquisition system on the other hand, the dead time of the acquisition system was larger than anticipated and the coincident events data collected contained elastic scattering events too. Therefore, there are systematic shifts of the excitation energy spectra that have to be corrected for.

The ^{13}C and the ^{4}He, or the ^{13}C$^{*}(E_x = 3.7$ MeV$)$ and the ^{4}He nucleus, were detected in coincidence in the front-angle detector telescopes T1 and T2. The resonant particle spectroscopy technique was used to select the events originating from the ^{9}Be+^{13}C $\rightarrow$^{17}O*+^{5}He$\rightarrow$^{13}C+^{4}He+ +^{5}He, or the ^{9}Be+^{13}C $\rightarrow$^{17}O*+^{5}He$\rightarrow$^{13}C$^{*}(E_x = 3.7$ MeV$)$+^{4}He+^{5}He reactions, and the corresponding ^{17}O excitation energy spectrum was obtained (for the ground-state channel see the Fig. 4.25 left on the p. 93 and for the excited-state channel see the Fig. 4.30 left on the p. 95). The discussion presented here has been built upon the discussion from the [6].

The ground-state reaction channel ^{13}C+^{4}He+^{5}He

For the sake of clarity, the states observed in the ground-state exit channel are presented in the Tab. 5.1, together with the data on the states observed in other experiments.

One may start with the strongest peak that is likely to be linked with the 13.58 MeV $(\frac{11}{2},\frac{13}{2})^{-}$ state listed in the [50], reported therein to be observed in the ^{13}C(^{6}Li,d)([4], [5]) and the ^{13}C(^{7}Li,t) [4] reactions, as well as in the ^{17}O(e,e') inelastic scattering [98]. The α-transfer reactions populated the 13.58 MeV state strongly. In the ^{5}He transfer reactions ^{12}C(^{7}Li,d)^{17}O and ^{12}C(^{6}Li,p)^{17}O a number of states were populated [100], among them the 13.58 MeV state. A similarity of the angular distributions of the aforesaid reactions with the ^{12}C(^{6}Li,d) and the ^{12}C(^{7}Li,d) reactions were studied and an absence of this peak in the ^{15}N(α,d) reaction was observed [4]. In the same reference the structure of the 13.58 MeV state was proposed to be a weak coupling configuration of ^{16}O$(6^{+}, 16.29\,\text{MeV}) \otimes p_{1/2}$. The ^{13}C+^{4}He resonant elastic scattering measurement reported in this work indicates that this state is likely to have a pronounced α-cluster structure.

The $E_x \approx 9.15$ MeV peak has been observed in the ^{13}C(^{6}Li,d) and the ^{13}C(^{7}Li,t) reactions [5], the ^{12}C(^{18}O,^{13}C^{4}He) reaction [101] and the ^{17}O(e,e') reaction [98]. In the compilation [50] the state is assigned an excitation energy $E_x = 9.147$ MeV and the spin and parity $\frac{1}{2}^{-}$. Apart from the foregoing reactions, this state was observed in the ^{18}O(d,t)^{17}O reaction [102], ^{13}C(^{4}He,n) and ^{13}C(^{4}He,^{4}He) reactions ([7] and references therein). The R-matrix evaluation suggests the excitation energy $E_x = 9.194$ MeV and the widths $\Gamma_\alpha = 7.33$ keV and $\Gamma_n = 0.23$ keV [7].

The 10.0 MeV peak could correspond to the 9.976 MeV $\frac{5}{2}^-$ state, found to have a large partial α–width $\frac{\Gamma_\alpha}{\Gamma} = 0.78$ [50]. In the recent comprehensive R-matrix fit excitation energy of 9.961 MeV and the spin and parity $\frac{7}{2}^+$ are proposed [7]. The deduced partial widths are $\Gamma_\alpha = 95.4$ keV and $\Gamma_n = 1.81\,\text{keV}$. The pronounced peak at 10.0 MeV is observed in the resonant elastic scattering cross section. This peak is composed of the contributions of multiple resonances, some of which have a large α-width, determined by the comprehensive R-matrix fit in Ref. [7].

The next peak lays at $E_x = 10.75$ MeV, corresponding to the 10.8 MeV peak found in [6]. This is the 10.7 MeV peak observed in the [101], using the ^{12}C(^{18}O,^{13}C^{4}He) reaction. It was also observed in the ^{12}C(^{7}Li,d) and the ^{12}C(^{6}Li,p) reactions [100]. The peak is reported in the [50] as a 10.777 MeV $\frac{1}{2}^+, \frac{7}{2}^-$, having $\frac{\Gamma_\alpha}{\Gamma} = 1.00$. The pronounced peak at 10.75 MeV could be related to the intense peak in the resonant elastic scattering cross section, both from this work and from [7], at $E_x(^{17}\text{O})$ =10.68 MeV. According to Ref. [7], this peak is due to the $E_x = 10.69$ MeV $J^\pi = \frac{9}{2}^+$ state with $\Gamma_\alpha/\Gamma \approx 0.8$ (listed as the state 56 in Tab. 3.4).

The next peak at the $E_x \approx 12.25$ MeV is composed of multiple unresolved states, including the 12.0 and 12.8 MeV peaks observed in the ^{13}C+^{4}He resonant elastic scattering experiment.

The 14.9 MeV peak, apart from being observed in the [6], has been observed in the ^{13}C(^{6}Li,d) and the ^{13}C(^{7}Li,t) reactions [4] at excitation energy of 14.86 MeV. This peak is clearly seen in the ^{12}C(^{7}Li,d) [100]. The [50] lists it at 15.1 ± 0.1 MeV, assigning it tentative $J^\pi = \left(\frac{9}{2}^+, \frac{11}{2}^+\right)$.

Next to the 14.9 MeV peak, there is a small peak at $E_x \approx 15.8$ MeV. It was observed by [100] in the ^{12}C(^{7}Li,d) reaction, as well as in the ^{12}C(^{6}Li,p) reaction [103]. The [50] compilation lists a state at 15.95 MeV, observed in the ^{13}C(^{6}Li,d)^{17}O reaction [4], assigning it the $\left(\frac{9}{2}^+, \frac{11}{2}^+\right)$. It was observed in the corrected data from Ref. [6] as well.

The last peak in the spectra on the Fig. 4.25 is the one at $E_x \approx 19.3$ MeV. This peak was also found in [6], where it was interpreted in terms of the 18.9 MeV peak observed in the ^{13}C(^{13}C,^{9}Be) reaction at $E = 105$ MeV [104] and the strong 19.24 MeV peak populated in the ^{13}C(^{7}Li,t) reaction [3]. Anyhow, none of these is included in the compilation [50].

For excitation energy plot of the ^{9}Be on the right side of the Fig. 4.25, the position of both spectra has to be adjusted by -0.4 MeV to reproduce the known ^{9}Be states. Two prominent peaks are visible at $E_x \approx 2.8$ and 6 MeV. The narrow peak at 2.8 MeV most likely corresponds to the narrow 2.4294 MeV $\frac{5}{2}^-$ state, observed in numerous experiments [82]. The second broad peak could correspond to the 5.59 MeV $\left(\frac{3}{2}^-\right)$ state (both the position of the peak and the width match the values from [82]). However, all excited states of ^{9}Be from $E_x = 4$ to 8 MeV may contribute to it, as well.

The excited-state reaction channel ^{13}C($\mathbf{E_x = 3.7}$ MeV)+^{4}He+^{5}He

The ^{17}O excitation energy spectrum obtained from the ^{13}C($E_x = 3.7$ MeV)+^{4}He coincident events is displayed on the Fig. 4.30 left on the p. 95. For the sake of clarity this and previous results are summarized in the Tab. 5.1.

Six prominent peaks are visible. The lowest-energy peak is located at $E_x \approx 12.9$ MeV. This state was not populated in the previous, ground-state reaction channel. However, in ^{12}C(^{6}Li,p) and ^{12}C(^{7}Li,d) reaction a peak was observed at 13.07 MeV or 13.06, respectively [100]. The compilation [50] lists a state at the $E_x = 12.93$ MeV observed in the ^{13}C(α,n) and the ^{13}C(α,α) reactions.

The next peak in the spectra is located at $E_x \approx 14.8$ MeV and most likely corresponds to the same states as the 14.9 MeV peak for the ground-state reaction channel. This peak is also observed in the ^{13}C*+^{4}He coincident events in the corrected [6] data (see Fig. 4.31).

After the $E_x \approx 14.8$ MeV the 15.7 MeV peak follows. This peak corresponds to the same states as the $E_x \approx 15.8$ MeV peak observed for the ^{13}C+^{4}He coincident events (the ground state reaction channel). The peak is visible in Fig. 4.31 as well [6].

The $E_x \approx 17.3$ MeV peak was not observed in the ground-state reaction channel. It is listed as the $E_x = 17.06$ MeV, $J^\pi = \frac{11}{2}^-$, $T = \frac{1}{2}$ state in the [50]. It was observed in the ^{13}C(^{6}Li,d)^{17}O reaction [3], ^{17}O($\pi^\pm$,$\pi^\pm$)^{17}O scattering at $E_\pi = 164$ MeV [105] and the ^{17}O(e,e') scattering [98]. This peak is the most pronounced in [6] (see Fig. 4.31).

The last two peaks are prominent for the ^{13}C*(T2)–^{4}He(T1) coincident events, but weak for the ^{13}C*(T1)–^{4}He(T2) coincidences, most likely due to the difference in the detection efficiency between the two detector combinations.

The 18.6 MeV peak could correspond to the 18.72 MeV state listed in the [50], observed only in the ^{17}O(e,e') inelastic electron scattering. The 18.5 MeV peak on the Fig. 4.31 was previously observed by [6].

The 19.6 MeV peak that was observed by [3] is likely to correspond to the 19.9 MeV peak observed in the spectrum. The [50] compilation assigns it tentative spin and parity $\left(\frac{13}{2}^+, \frac{15}{2}^+\right)$.

A broad structure at $E_x \approx 19.9$ MeV on the Fig. 4.31 [6] most likely corresponds to the peak observed in this measurement. Due to the large width of the peak, it may be related to the strong peak observed at $E_x = 19.3$ MeV in the ground-state channel.

Observed states systematics

The α-decaying ^{17}O states observed in this work can be plotted in the E-$J(J+1)$ plane to see if they could correspond to some existing rotational band. The Fig. 5.1 is an extension of the Fig. 2.8 (p. 14), containing the positive and negative parity ^{17}O rotational bands proposed in Refs. [6] and [37]. The states at 12.0, 15.8 and 19.6 MeV observed in this work have been added to the plot (blue points). The tentative value of spin for the 12.0 MeV state determined in this work was $\frac{11}{2}^+$ or $\frac{13}{2}^-$, the former value has been selected in this case. The 15.8 MeV peak, listed as the 15.95 MeV $(\frac{9}{2}^+, \frac{11}{2}^+)$ state in Ref. [50], has been assumed to have a spin $\frac{13}{2}^+$. Finally, the 19.6 MeV $(\frac{13}{2}^+, \frac{15}{2}^+)$ state listed in Ref. [50] has been added to the Fig. 5.1 as the $\frac{15}{2}^+$ state. The slope of the three states added here doesn't match the slope of the $K^\pi = \frac{1}{2}^+$ rotational band proposed in [37] and it is clear that more spectroscopic information are needed to clarify the structure of the $K^\pi = \frac{1}{2}^+$ rotational band.

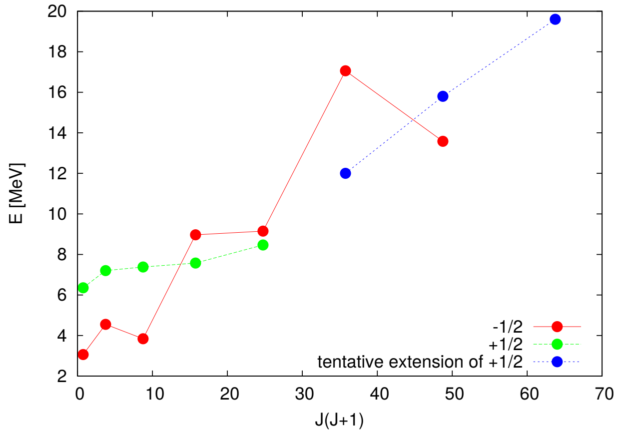

Figure 5.1: A tentative extension of the proposed ^{17}O positive-parity rotational band from [37]. The negative-parity rotational band is proposed in Refs. [6] and [37].

In conclusion, spin and parity of the ^{13}C ground-state is $J^\pi = \frac{1}{2}^-$ and $J^\pi = \frac{3}{2}^-$ for the ^{13}C$^*(E_x = 3.7$ MeV$)$ state. The two states have a similar structure, therefore excited ^{17}O states decaying to one channel should decay to the other as well. The differences observed in the spectra could be due to the detection efficiency, noise, contribution of other possible reaction channels which act as a background in the spectra (e.g. ^{9}Be states) and the problems with the calibration that are influencing ^{13}C*+^{4}He+^{5}He reaction channel more due to lower energy of the outgoing particles.

Table 5.1: The ^{17}O states populated in reactions studied in this work. Peaks observed in the resonant elastic scattering experiment, but not fitted using a simplified method, are labelled with †. The reference [6]* refers to the corrected version of the ^{17}O excitation energy spectrum published in Ref. [6], reconstructed from the ^{13}C*+^{4}He coincident events, displayed in Fig. 4.31.

No.	^{13}C+^{4}He res. el.		^{13}C+^{9}Be reactions		References	Tilley *et. al.* [50]	
	E_x [MeV]	J^π	^{13}C+^{4}He coinc.	^{13}C*+^{4}He coinc.		E_x [MeV]	J^π
1	8.9	$\left(\frac{7}{2}^-\right)$ or $\left(\frac{9}{2}^-\right)$			[7]		
2	9.2	$\left(\frac{7}{2}^-\right)$ or $\left(\frac{9}{2}^-\right)$	9.15		[5], [7], [98], [101], [102]	9.147	$\frac{1}{2}^-$
3	10.0†		10.0		[7]	9.976	$\frac{5}{2}^-$
4	10.75†		10.75		[6], [100], [101]	10.777	$\frac{1}{2}^+, \frac{7}{2}^-$
5	12.0	$\left(\frac{11}{2}^+\right)$ or $\left(\frac{13}{2}^-\right)$	12.25 (wide)		[61], [96], [97], [98]	12.005 ± 15	$> \frac{3}{2}$
6	12.8			12.9	[100]	12.93	
7	13.6	$\left(\frac{11}{2}^-\right)$	**13.57**		[4], [5], [98], [100]	13.58	$(\frac{11}{2}, \frac{13}{2})^-$
8			14.9	14.8	[4], [6], [100]	15.1 ± 0.1	$\left(\frac{9}{2}^+, \frac{11}{2}^+\right)$
9			15.8	**15.7**	[4], [6]*, [100], [103],	15.95	$\left(\frac{9}{2}^+, \frac{11}{2}^+\right)$
10			(weak peak)	**17.3**	[3], [6]*, [98], [105]	17.06	$\frac{11}{2}^-$
11			(weak peak)	18.6	[6]*	18.72	
12			19.3		[6], [4], [104]		
13				19.6	[3], [6]*	19.6	$\left(\frac{13}{2}^+, \frac{15}{2}^+\right)$

5.2 Excited stated of the ^{18}O nucleus

In contrast to the ^{17}O states, which were studied in both experiments, the ^{18}O states are studied using the ^{13}C+^{9}Be reaction data only. In this section the states of the ^{18}O observed in the various reaction exit channels will be discussed and compared to published results. The resonant particle spectroscopy technique was used to study the seven reaction channels which could be populated by the ^{18}O decay: ^{14}C+^{4}He+^{4}He, ^{14}C($E_x \approx 7$ MeV)+^{4}He+^{4}He, ^{12}C+^{6}He+^{4}He, ^{12}C($E_x = 4.4$ MeV)+^{6}He+^{4}He, ^{10}Be+^{8}Be+^{4}He, ^{10}Be($E_x = 3.37$ MeV)+^{8}Be+^{4}He and ^{10}Be($E_x \approx 6.2$ MeV)+ +^{8}Be+^{4}He. Results for each of those channels will be discussed in the subsections which follow. For the sake of clarity the results on the states observed for this experiment are summarized in the Tab. 5.2.

5.2.1 The reaction channel ^{14}C+^{4}He+^{4}He

The excitation energy spectrum obtained for the ^{14}C+^{4}He coincident events is displayed in the Fig. 4.42, p. 103. The lowest peak at 10.30 MeV most likely corresponds to the 10.290 MeV 4^+ state. The total width of the state deduced from the R–matrix fit of the ^{14}C+^{4}He resonant elastic scattering data is $\Gamma_{\mathrm{tot}} = 29\,\mathrm{keV}$ and the partial widths $\Gamma_\alpha = 19\,\mathrm{keV}$ and $\Gamma_n = 10\,\mathrm{keV}$ [14]. The state was previously observed in an older resonant elastic scattering measurement [106], the ^{12}C(^{7}Li,p) reaction at $E_{\mathrm{lab}} = 44\,\mathrm{MeV}$ [13], the ^{14}C(^{6}Li,d)^{18}O reaction at beam energy of 34 MeV [107], the ^{14}C(^{18}O,^{14}C^{4}He)^{14}C reaction at 102 MeV [12], the ^{14}C(^{4}He, ^{4}He)^{14}C reaction [108], the ^{9}Be(^{18}O, ^{14}C^{4}He)^{9}Be reaction [109], inelastic electron scattering [110], ^{13}C(^{6}Li,p)^{18}O reaction at beam energy of 28 MeV [111], ^{16}O(t,p)^{18}O reaction at a beam energy of 15 MeV [112], ^{12}C(^{18}O,^{14}C^{4}He)^{12}C at a beam energy of 140 MeV [113] and ^{16}O(^{4}He,^{2}He)^{18}O reaction [114].

The first of the two most prominent peaks lays at 11.63 MeV and corresponds to the 11.62 MeV 5^- state. In [14] excitation energy of 11.627(4) MeV and the widths $\Gamma_{\mathrm{tot}} = 40\,\mathrm{keV}$, $\Gamma_\alpha = 30\,\mathrm{keV}$ and $\Gamma_n = 10$ keV were obtained using the R-matrix fit to the ^{14}C+^{4}He resonant-elastic scattering data. This state has been observed in the number of experiments: [12], [13], [101], [106], [107], [108], [109], [111] and [113]. The aforesaid state belongs to the negative-parity rotational band with the 8.0378 MeV 1^- state as a band-head.

The second strong peak at 12.51 MeV corresponds to the 12.53 MeV 6^+ state observed in [12], [107], [108], [109] and [111]. The excitation energy of this state was observed to be 12.557 MeV in [106] and [13], and the results from [14] determine $E_x = 12.575(9)$ with $\Gamma_{\text{tot}} = 70\,\text{keV}$, $\Gamma_\alpha = 50\,\text{keV}$ and $\Gamma_n = 20\,\text{keV}$.

The next peak is located at 13.75 or 13.79 MeV (depending on the spectrum, labelled on the figure as 13.75), and is likely to correspond to the 13.8 MeV 1^- state [87] seen in the [111] or to the 13.82 MeV 5^- state observed in [13] and [14]. Due to the selectivity of this reaction, one can expect that the contribution from the 13.82 MeV 5^- state is stronger.

The peak at 15.73 or 15.80 MeV (labelled as 15.75) is likely to correspond to the strong peak at 15.8 MeV observed in the [111], tabulated as the 15.8 MeV 1^- state in the [87].

The E_x =16.82 or 16.95 MeV (labelled as 16.9) peak is most likely to correspond to the 17.0 MeV state observed in [107], for which a $J^\pi = 4^+$ was proposed in the same paper, or to the 16.8 MeV state observed in the [109] that corresponds to the 16.948 MeV $(2,3)^-$ state in the [87] or a combination of these two states.

At the excitation energy of 17.96 or 18.17 MeV another peak is visible, labelled on the plot as 18.0 MeV. At such a high excitation energy the data on the ^{18}O structure was obtained using inelastic electron scattering [115] and a peak, listed in the compilation [87], was observed at 18.049 MeV. In general, the electron scattering should usually excite collective degrees of freedom of nuclei rather than the α-decaying states.

The 18.84 MeV peak is more pronounced for the ^{14}C(T2)+^{4}He(T1) coincident events. It may correspond to the 18.68 MeV 4^- state observed in [115] and [110], listed in the compilation [87].

The next peak is located at 19.65 or 19.87 MeV and labelled 19.8. One cannot assign this peak to known excited states.

The highest energy peak that was observed is located at an excitation energy of 21.3 MeV and may correspond to the 21.42 MeV peak with tentative (4^-) spin and parity assignment from the [110].

At the excitation energy of 25.8 MeV there is a weak peak. The compilation [87] does not contain states that could correspond to the peak. The energy of this peak is beyond the range of the inelastic electron scattering measurement presented in Ref. [110]. Thus this weak peak is observed for the first time.

On the right side of the Fig. 4.42 the excitation energy spectra of the ^{18}O for the ^{14}C(T1)-+^{4}He(T4) and the ^{14}C(T2)+^{4}He(T3) coincident events are displayed in orange and blue, respectively. In this case due to low resolution of the spectra it was not possible to unambiguously identify the peaks, but the position of the spectra was adjusted for them to overlap. The cause of the lower resolution in comparison with the plot on the left side of the Fig. 4.42 is due to the fact that the detected ^{4}He nucleus is the recoil from the first step of reaction. The difference in this case is that the relative energy between the ^{18}O decay products is calculated using only the energy of the recoil ^{4}He nucleus, unlike the previous case where it was calculated from the energies of the two ^{18}O decay products (see Eqs.(4.14) and (4.27)). Therefore, the resolution of the excitation energy is lower for this case.

The low-energy peak at $E_x \approx 8.0$ MeV most likely consists of the contibutions of multiple states in the excitation energy range between 7.5 and 8.5 MeV: among them the 8.04 MeV 1^- and the 8.22 MeV 2^+ states could be prominent (see [12], also observed in [111] and [13]). Apart from the two aforesaid states, the following states may contribute to the peak: 7.6159 MeV 1^-, 7.864 MeV 5^-, 8.125 MeV 5^-, 8.282 MeV 3^-, 8.410 MeV (2^-) and 8.521 MeV (4^-) state, all listed in Ref. [87].

The second peak most likely contains the contributions of a group of states around the $E_x(^{18}\mathrm{O}) \approx 12.0$ MeV, its large width spanning the 10–14 MeV range. The most prominent contributions to this range are most likely those of the 10.290 MeV 4^+, 11.62 MeV 5^-, 12.53 MeV 6^+ and the 13.8 MeV 1^- state, observed as a set of narrow peaks at the left side of the Fig. 4.42. Additionally, the 11.42 4^+ state observed in the [13], [14], [111] and [106], as well as the 11.699(1) MeV 6^+ state seen in [13], [107], [108] and [111] may contribute to the peak. A number of other states in the excitation energy region covered by this peak may contribute as well (see [87]).

The ^{14}C($E_x \approx 7$ MeV)+^{4}He+^{4}He reaction channel

The excitation energy spectrum of the ^{18}O obtained from the ^{14}C($E_x \approx 7$ MeV)+^{4}He coincident events is displayed on the Fig. 4.48, p. 107. In this reaction channel the ^{14}C nucleus can be excited to any of the five states: 6.0938 MeV 1^-, 6.7282 MeV 3^-, 6.9026 MeV 0^-, 7.0120 MeV $2+$ or 7.3414 MeV 2^- state.

The systematic error of the position of the peaks is the same as for the ground-state channel: -300 and -170 KeV for the T1-T2 and the T2-T1 coincident events, respectively.

The lowest peak at $E_x \approx 16.3$ MeV is likely to correspond to the 16.42 MeV peak observed in the [12], decaying to both ^{14}C+^{4}He and ^{14}C*+^{4}He channel. However, that state was not observed in spectra obtained from ^{14}C+^{4}He coincidences. The next peak is located at $E_x \approx$

19.5 MeV. In vicinity of that excitation two peaks were observed by [110], but it is not clear whether they could correspond to it. The 20.7 MeV peak in the spectrum could correspond to the 20.86 MeV peak observed in Ref. [110] in the inelastic electron scattering from the ^{18}O target. In vicinity of the 22.5 MeV peak observed in the spectra [110] found the 22.40 MeV peak. The peak at $E_x(^{18}\mathrm{O}) \approx 23.7$ MeV could correspond to the 23.8 MeV 1^- state listed in the compilation [87], observed in [116] and [110]. The peak at 26.5 MeV may correspond to the 27 MeV 1^- state observed in the [116] and listed in [87].

5.2.2 The ^{12}C+^{6}He+^{4}He reaction channel

The states of the ^{18}O populating this channel could be detected either as ^{12}C+^{6}He, ^{12}C+^{4}He or ^{6}He+^{4}He coincident events. The ^{12}C+^{4}He coincident events did not show clear ^{18}O loci. The ^{6}He+^{4}He coincident events of interest for the ^{18}O structure would require detection of the ^{4}He at backward angles, but in this case those detectors were not usable. That leaves us with the coincident detection of ^{6}He+^{12}C at forward angles. Due to the intense pile-up in the detector telescope T2, the ^{6}He locus could not be well isolated. Therefore, only the ^{6}He(T1)+^{12}C(T2) coincident events were studied. The spectrum of ^{18}O states populated in this channels is displayed in the Fig. 4.52, together with the E_r-E_r plots. It should be noted that the ^{6}He decay of the ^{18}O excited states has not been observed before. A single wide peak was observed at $E_x = 26.5$ MeV. Furthermore, there is the indication of a peak at 29.5 MeV and possible weak peak around 23.5 MeV. The energy and the width of the peak depend on the energy and angular calibration, which has a certain systematic offset (see Fig. 4.50), and the detection efficiency variation throughout the measured region. Judging by the position of the $E_x(^{10}\mathrm{Be})$ peaks obtained from the ^{6}He+^{12}C coincident events, the systematic error of the position of peaks is smaller than 0.5 MeV.

Both the 23.5 MeV and the 26.5 MeV peaks observed in this decay channel coincide in excitation energy with the peaks observed tin the ^{14}C*+^{4}He decay channel.

The ^{12}C$(\mathrm{E_x} = 4.4\ \mathrm{MeV})$+^{6}He+^{4}He reaction channel

No ^{18}O* states decaying to this reaction channel were observed. Unlike the ground-state channel, the final excitation energy plot did not show any pronounced features that would indicate such decay.

5.2.3 The ^{10}Be+^{8}Be$_{gs}$+^{4}He reaction channel

For the ^{10}Be+^{8}Be+^{4}He reaction channel the ^{10}Be+^{4}He, ^{10}Be+^{8}Be$_{gs}$ and ^{10}Be+^{4}He$_{gs}$ coincident events were studied. Note that each of the coincident events where one of the particles is the ^{8}Be$_{gs}$ is a three-particle coincident event, therefore statistics is lower than for the two-particle coincidences. Apart from lower statistics, the limitations of calibration influence the ^{8}Be$_{gs}$ reconstruction and are visible as the bending of the loci in the $E_{^8\mathrm{Be}_{gs}}$-Q plots (see appendices D and E). Therefore, results obtained from the coincident events involving the ^{8}Be$_{gs}$ have to be interpreted with caution.

This reaction exit channel is strongly populated by the ^{12}C* and the ^{14}C* decaying to ^{8}Be$_{gs}$+^{4}He and ^{10}Be+^{4}He, respectively. The ^{12}C and the ^{14}C states observed are discussed in the section 4.3.4 and are in accordance with the published data. Here the three types of coincidences will be discussed one by one. All the three types share a common feature: the E_r-E_r loci for the ^{12}C and the ^{14}C are much stronger than the possible ^{18}O loci.

The E_r-E_r plots of the ^{10}Be+^{4}He contained no loci that could correspond to the ^{18}O states. Instead the excitation energy ^{12}C and ^{14}C were obtained (for details see the section 4.3.4).

The ^{8}Be$_{gs}$+^{4}He coincident events had lower statistics and the loci were harder to identify. The ^{12}C and the ^{14}C loci were observed and strict conditions were set to exclude them, in order to obtain the ^{18}O excitation energy spectrum free from those contributions. In spectra a possible peak is observed at $E_x \approx 25$ MeV (Fig. 4.75).

The ^{10}Be+^{8}Be$_{gs}$ coincident events were treated in the same way as the ^{8}Be$_{gs}$+^{4}He events: after the strongest ^{12}C and ^{14}C states were removed the excitation energy spectrum of the ^{18}O was obtained. The spectra, displayed in Fig. 4.83, show a possible peak at $E_x \approx 24$ MeV. In conclusion, some indications for the peak at 24–25 MeV have been found in the data.

The ^{10}Be($E_x = 3.37$ MeV)+^{8}Be$_{gs}$+^{4}He reaction channel

For the reaction channel with the ^{10}Be in its first excited state (3.37 MeV, 2^{+}) the possible peak at the ^{18}O excitation $E_x \approx 25$ MeV is observed for the ^{8}Be$_{gs}$(T2)-^{4}He(T1) coincident events only (see Fig. 4.76). Indications for possible broad peaks at higher excitations are visible in the spectra.

The excitation energy spectrum obtained from ^{10}Be($E_x = 3.37$ MeV)+^{8}Be$_{gs}$ coincident doesn't contain peaks which could correspond to the excited states of the ^{18}O.

The ^{10}Be($E_x \approx 6.2$ MeV)+^{8}Be$_{gs}$+^{4}He reaction channel

While the excitation energy spectrum obtained from the ^{10}Be$(E_x \approx 6.2\,\text{MeV})$+^{8}Be$_{gs}$ coincident events doesn't show pronounced peaks, the ^{18}O excitation energy plot from the ^{8}Be$_{gs}$+^{4}He coincidences show a possible peak at $E_x \approx 29$ MeV (see Fig 4.77).

Observed states systematics

The ^{18}O rotational band proposed in Ref. [12] is displayed in Fig. 5.2 (red dots), the black line denoting the linear fit to the states of the band from [12]. States observed in this work are added to the plot (blue dots), with the spin adjusted to place them close to the line. The 13.57 MeV state has been added as $J^\pi = 7^-$, 15.75 MeV and 16.9 MeV as $J^\pi = 8^+$, 18.0 and 18.8 MeV as $J^\pi = 9^-$, 19.8 and 21.3 MeV as $J^\pi = 10^+$. It should be noted that these values are much higher than the values listed in Ref. [87], they are available for known states observed at these high excitations. It is very likely that these already known states observed in electron scattering measurements are different states than ones observed here. Their structure should be different because the states observed in this work have large overlap with the ^{14}C$_{gs}$+α structure.

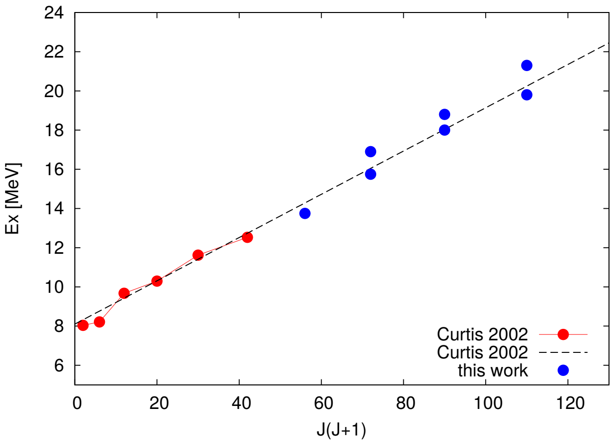

Figure 5.2: A tentative extension of the proposed ^{18}O rotational band from [12].

The structure of the ^{14}C nucleus ground state is compact due to the closure of the proton subshell and neutron shell. Therefore, the ^{18}O states decaying to the ground state of the ^{14}C cannot have molecular structure, because the neutrons are well-bound inside the ^{14}C nucleus. However, for the ^{14}C*$(E_x \approx 7\,\text{MeV})$ group of states the neutrons are not in the closed shell. Therefore, molecular states of the ^{18}O may decay to both ^{14}C*$(E_x \approx 7\,\text{MeV})$+^{4}He and ^{12}C+^{6}He channels. Therefore, the ^{18}O excited states decaying to both of these channels are a good molecular-state candidates (the 23.5 and the 26.5 MeV states in Tab. 5.2). Of course, the molecular-state candidates observed in this work are not the lowest ones. The energy threshold for the ^{6}He decay of ^{18}O equals 18.38 MeV, while the ^{18}O$\rightarrow$ ^{14}C$^{*}(E_x \approx 7$ MeV$) +$ ^{4}He threshold is even lower, at $\approx$ 13.2 MeV. Therefore, in accordance with the Ikeda picture, one can expect the molecular states to appear already at E_x $\approx$14 MeV. It is quite likely that some of the states observed in ^{14}C*+α decay channel below the ^{12}C+^{6}He decay threshold possess the molecular nature and might be the band-heads of possible rotational bands built on ^{12}C+2n+α structure.

Table 5.2: The ^{18}O states populated by the ^{13}C+^{4}He reactions.

No.	$E_x(^{18}\mathrm{O})$ from the ^{13}C+^{9}Be reactions			References	Tilley *et. al.* [87]	
1	^{14}C+^{4}He	^{14}C*+^{4}He	^{12}C+^{6}He		E_x [MeV]	J^{π}
2	10.30 MeV			[12], [13], [14], [106], [107], [108], [109], [110], [111], [112], [113], [114]	10.290 MeV	4^{+}
3	**11.63 MeV**			[12], [13], [14], [101], [106], [107], [108], [109], [111], [113]	11.62 MeV	5^{-}
4	**12.51 MeV**			[12], [13], [14], [106], [107], [108], [109], [111]	12.53 MeV	6^{+}
5	**13.75 MeV**			[111]	13.8	1^{-}
6				[13], [14]	13.82	5^{-}
7	15.75 MeV			[111]	15.8	1^{-}
8		**16.1 MeV**		[12]	16.315	$(3,2)^{-}$
9	16.9 MeV			[107], [109]	16.948	$(2,3)^{-}$
10	18.0 MeV			[115]	18.049	
11	18.8 MeV			[110], [115]	18.68	(4^{-})
12		19.3 MeV				
13	19.8 MeV					
14		**20.5 MeV**		[110]	20.86	
15	21.3 MeV			[110], [117]	21.42	(4^{-})
16		22.3 MeV		[110]	22.4	4^{-}
17		23.5 MeV	23.5 MeV	[110], [116]	23.8	1^{-}
18		26.3 MeV	26.5 MeV	[116]	27	1^{-}
19			29.5 MeV	[116]	30	

Chapter 6

Conclusion

In this work the results of the two experiments are presented: the ^{13}C+^{4}He resonant elastic scattering measurement and the ^{13}C+^{9}Be reaction measurements at $E_{^{13}\mathrm{C}} = 72$ MeV. These two experiments have been chosen due to their selectivity in populating excited states of the ^{17}O and ^{18}O that could have a cluster structure.

The ^{13}C+^{4}He resonant elastic scattering experiment on a thick gas target provided the excitation function of the ^{17}O, measured at $\approx 0^\circ$ in the laboratory frame of reference or $\approx 180^\circ$ in the centre of mass system. Results presented in this work extended the measured range, both in angle and in energy, presenting results for the range 11.1 MeV $< E_x(^{17}\mathrm{O}) <$ 13.8 MeV. The extended part of the spectrum contains two peaks of particular interest: the 13.6 MeV peak, proposed to have a $^{16}\mathrm{O}(6^+, 16.29\ \mathrm{MeV}) \otimes p_{1/2}$ structure [4], and a strong peak at 12.0 MeV. The published parameters from a comprehensive R-matrix fit provided a calculated cross section for a previously known range of this measurement [7]. The calculated cross-section reproduces the data on the low energies rather well, discrepancies starting with opening of the inelastic neutron reaction channels. The magnitude and the trend of the discrepancy are in accordance to general trend of the published fit [7]. Missing data on other reaction channels for the $E_x > 11.1$ MeV did not allow for the R-matrix fit to be extended to the higher energies. Therefore, a simplified fit, that included only a narrow region comprising a single quasi-isolated resonance and the elastic scattering channel, was performed. The results suggest that both resonances have a high spin (the most likely equals $\frac{11}{2}^+$ for the 12.0 MeV peak and $\frac{11}{2}^-$ for the 13.6 MeV peak) and, in this simplified picture, elevated Wigner ratios. In the resonant particle spectroscopy experiment the excited stated of the ^{17}O were populated in the ^{13}C+^{9}Be$\rightarrow$^{13}C+^{4}He+^{5}He reaction and the 13.58 MeV peak is the strongest one. Although the spin and parity of this state have not been determined yet, the evidence suggest a high spin, in accordance with Refs. [4] and [6]. However, further measurements are needed to determine the exact value of spin and parity, with resolution high enough to determine whether this state is a single state or a doublet of states.

The 12.0 MeV peak, corresponding to the 12.005 MeV state in the Ref. [50], is not observed in ^{13}C+^{9}Be reactions as an isolated peak, but is present in the broad peak centred at $E_x \approx$ 12.25 MeV.

Apart from this two resonances, the low-energy part of the excitation function contains two resonances proposed to be a part of the ^{17}O 4-particle–3-hole rotational band [6]: the 8.97 MeV $\frac{7}{2}^-$ and the 9.15 MeV $\frac{9}{2}^-$ states. The comprehensive R-matrix fit [7] included a large set of elastic scattering data, among the other relevant channels. The energies and spins of these two resonances deduced in the fit are: 8.9124 MeV $\frac{9}{2}^-$ and 9.1737 MeV $\frac{7}{2}^-$, both having $\Gamma_\alpha >> \Gamma_n$. The two states are listed in the compilation as 8.9672 MeV $\frac{7}{2}^-$ and the 9.18 MeV $\frac{7}{2}^-$ states, observed in ^{13}C(^{6}Li,d)^{17}O and ^{13}C(^{7}Li,t)^{17}O reactions as well [50]. Therefore, the evidence show the two states have a pronounced α-structure. The spin assignment for this two states varies and yet has to be determined.

The measurement of the ^{13}C+^{9}Be reactions was well suited for the study of the neutron rich oxygen isotopes due to the high probability of the α and ^{5}He pick-up, because of the pronounced α+^{5}He structure of the ^{9}Be ground state (see Ref. [118]). This reaction has been previously used for the study of ^{17}O structure in Ref. [6], however in that experiment not enough data was collected to investigate the ^{18}O structure [67]. Here presented experiment used a highly segmented silicon detector array, comprising six 20 μm ΔE-1000 μm E detector telescopes, four of which were successfully calibrated, enabling high statistics of the data.

The ^{17}O states decaying to the ^{13}C+^{4}He match the pronounced α-cluster states observed in the resonant elastic scattering experiment: the 9.15 MeV and the 13.57 MeV peaks, both having a pronounced α-cluster structure. Multiple ^{13}C*($E_x = 3.7$ MeV)+^{4}He decaying states coincide with the states decaying to the ground-state exit channel, indicating the similarity of their structure. The ^{17}O excited states decaying to both the ground- and excited-states match those published in the [6] (the corrected plot in Fig. 4.31), adding to statistics and extending excitation energy range of the previous measurement.

In conclusion, the results presented in this work indicate that the 8.9 MeV, 9.15 MeV and the 13.58 MeV states of the ^{17}O have a pronounced α-cluster structure and could belong to the rotational band built upon the ^{16}O(6.05 MeV, 0$^+$) cluster state. The 12.0 MeV peak, observed as a strong peak in the resonant elastic scattering, is not very strongly populated in the ^{13}C+^{9}Be reaction, but is present as a part of a broad peak at $E_x \approx 12.25$ MeV. Two states are observed decaying to both the ^{13}C+^{4}He and the ^{13}C*+^{4}He channels (the 15.1 MeV and the 15.95 MeV state). The 17.06 and the 18.72 MeV states are strong in the ^{13}C*+^{4}He decay channel, but very weak in the ^{13}C+^{4}He channel (visible as the two wide bumps in the spectrum). Further measurements are needed to determine the spins and parities of the aforesaid states.

The states of the ^{18}O were studied in the ^{13}C+^{9}Be resonant particle spectroscopy experiment. The states decaying to the known channels, like ^{14}C+^{4}He and ^{14}C*($E_x \approx 7$ MeV)+^{4}He were observed, as well as a novel decay mode ^{12}C+^{6}He.

The states decaying to the ^{14}C+^{4}He channel matched the states observed in Refs. [14] and [13], as well as the previous resonant particle spectroscopy experiments [101] and [119]. The excitation energy range covered in this work extended much higher, therefore the states decaying to the ^{14}C+^{4}He channel were observed for the first time at $E_x(^{18}\mathrm{O}) = 15.75$, 16.9, 18.0, 19.8 and 21.3 MeV.

The states decaying to the ^{14}C*+^{4}He channel do not coincide with the states decaying to the ^{14}C+^{4}He channel, probably due to their different structure. The states are observed at 16.1, 19.3, 20.5, 22.3, 23.5 and 26.3 MeV, the 16.1 and 20.5 MeV being the strongest.

The ^{10}Be+^{8}Be$_{\mathrm{gs}}$ +^{4}He reaction channel has been studied, as well. The low statistics didn't permit to reach conclusions, although the spectra contains some possible peaks. It is important to emphasize that the ^{18}O states decaying to the ^{10}Be+^{8}Be$_{\mathrm{gs}}$, if they exist, are not likely to have neutrons providing an additional binding of the α-particles in molecular orbitals, but rather having them well localized inside the ^{10}Be.

Finally, the ^{12}C+^{6}He decaying state has been observed for the first time, at $E_x(^{18}\mathrm{O}) \approx 26.5$ MeV. A weak possible peaks were observed at $\approx$23.5 and $\approx$29.5 MeV as well. This is an indication of possible exotic cluster structure in the ^{18}O. Further experiments are required to confirm this decay mode and detect α-decay of these states. Such results would provide evidence for the molecular ^{12}C+2n+^{4}He structure in ^{18}O.

While reactions selectively populating excited states via α-transfer or α+n transfer provide valuable data, it is clear that clear spin and parity assignments are crucial for the clarification of the nature of cluster structure in ^{17,18}O, complemented by the measured α- and total widths. Further experiments, extending the excitation energy range of Ref. [14] are needed. The quality and quantity of data collected in the ^{14}C+^{4}He resonant elastic scattering experiment could be dramatically improved over previous works by meticulous preparation, optimizing the setup for the coincident detection of both ^{14}C and ^{4}He in the excitation energy regions of interest employing the dedicated simulation package [84]. The challenges of this experiment would be the inelastic channels, that have to be measured to ensure the proper interpretation of the data using the phenomenological R-matrix method, and finding the accelerator facility able to provide the ^{14}C beam (the natural abundance of the ^{14}C is $\approx 10^{-12}$, therefore it has to be produced either as a radioactive beam or delivered from a dedicated ion-source for radioactive targets). The resonant particle spectroscopy method, used in the ^{13}C+^{9}Be experiment in this work, can provide valuable information as well. Had it not been for various difficulties in this experiment, the back-angle detector telescopes would provide the information on excited states from recoiling α-particle detected at back angles and a decay fragment detected at forward angles. An improved ^{13}C+^{9}Be experiment would include a setup carefully optimised for coincident measurement of overlapping excitation energy ranges for different channels under stable experimental conditions. High quality data could be used to extract information the structure using a DWBA calculation.

To conclude, in this work the existing data on the structure of the ^{17}O and ^{18}O were complemented by extending the excitation energy range covered in the previous measurements. Multiple highly excited states of the ^{17}O decaying to the ^{13}C+^{4}He or visible in the ^{13}C+^{4}He coincident events from the ^{13}C+^{9}Be reactions were identified. The ^{18}O exited states decaying to the ^{14}C+^{4}He and the ^{14}C*+^{4}He channels were populated in the ^{13}C+^{9}Be reaction, many of those not observed before in this decay channel. The ^{12}C+^{6}He decay of the highly excited ^{18}O state has been observed for the first time.

Appendices

Appendix A

^{9}Be(^{13}C,^{13}C^{4}He)^{5}He reaction

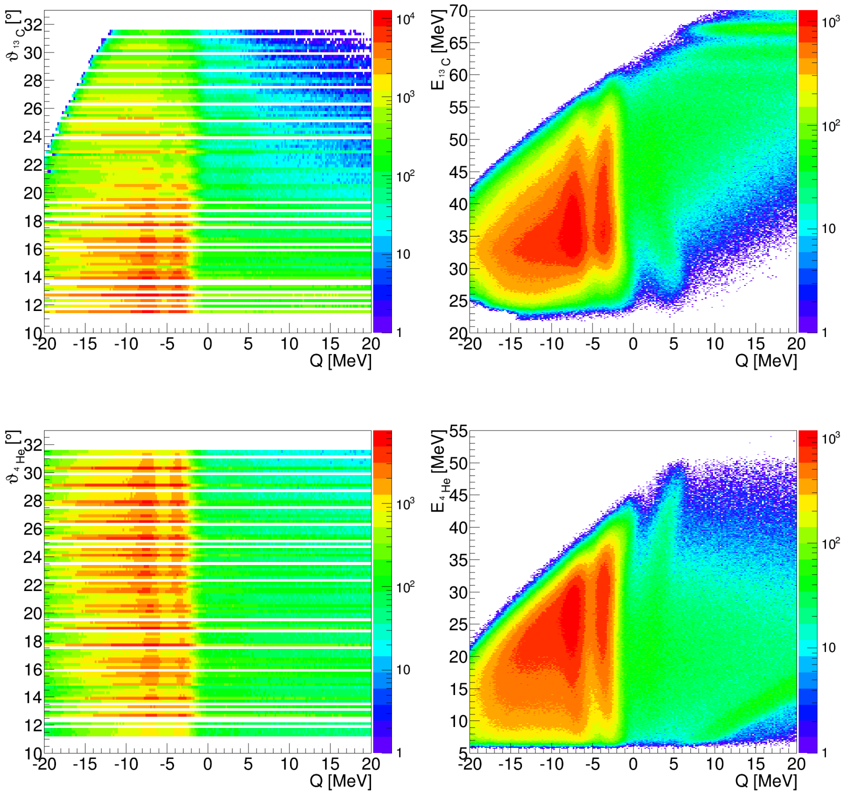

Figure A.1: The ϑ_{det}–Q and the E_{det}–Q spectra for the ^{13}C(T1)–^{4}He(T2) coincident events.

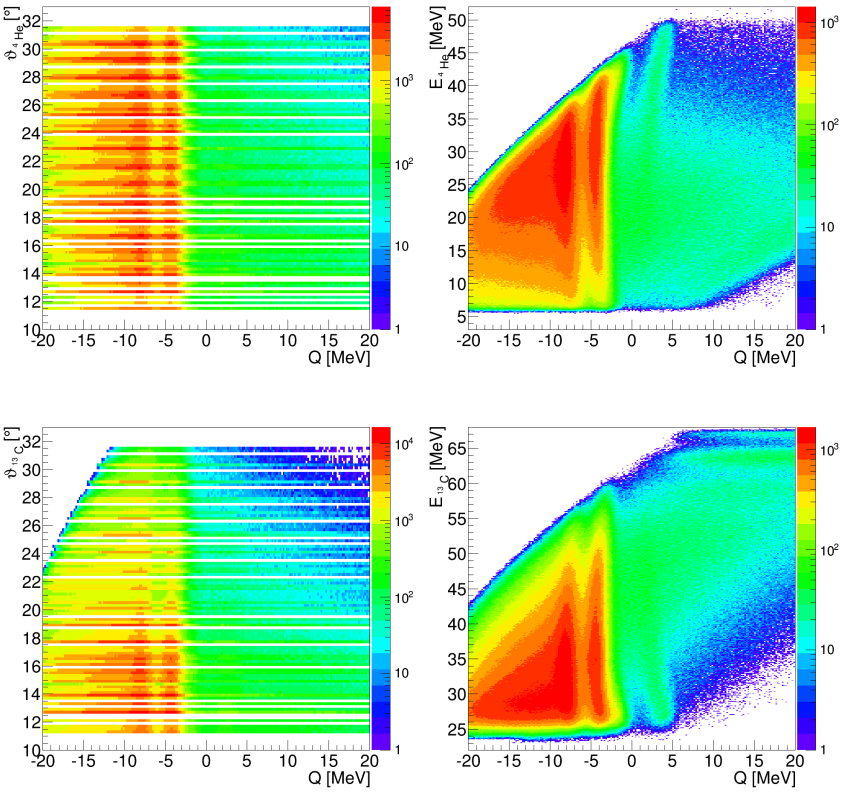

Figure A.2: The ϑ_{det}–Q and the E_{det}–Q spectra for the ^{13}C(T2)–^{4}He(T1) coincident events.

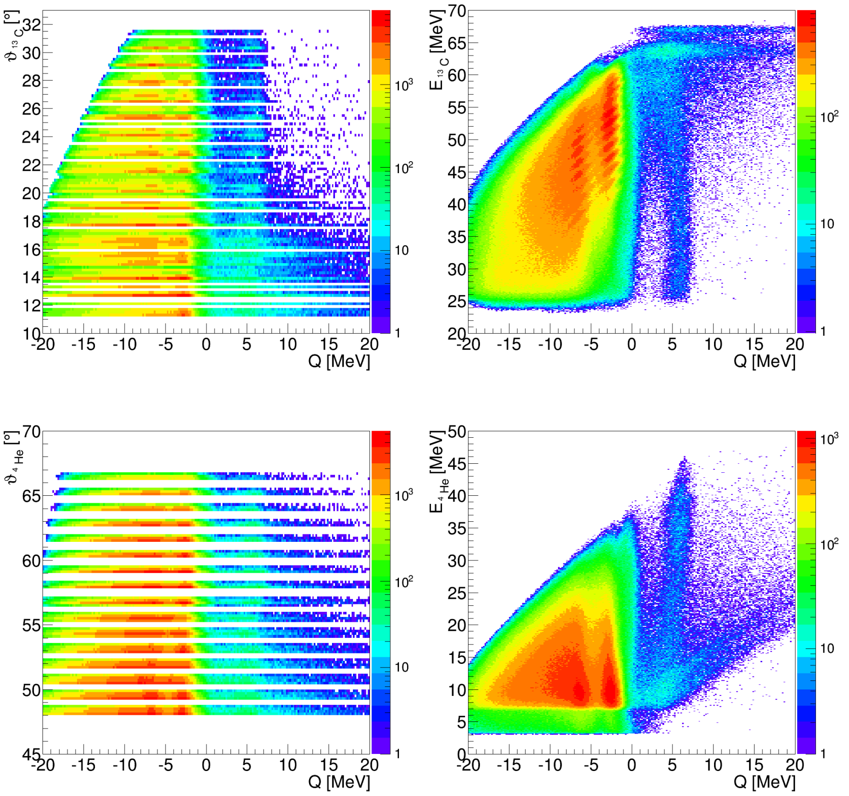

Figure A.3: The ϑ_{det}–Q and the E_{det}–Q spectra for the ^{13}C(T2)–^{4}He(T3) coincident events.

Appendix B

^{9}Be(^{13}C,^{14}C^{4}He)^{4}He reaction

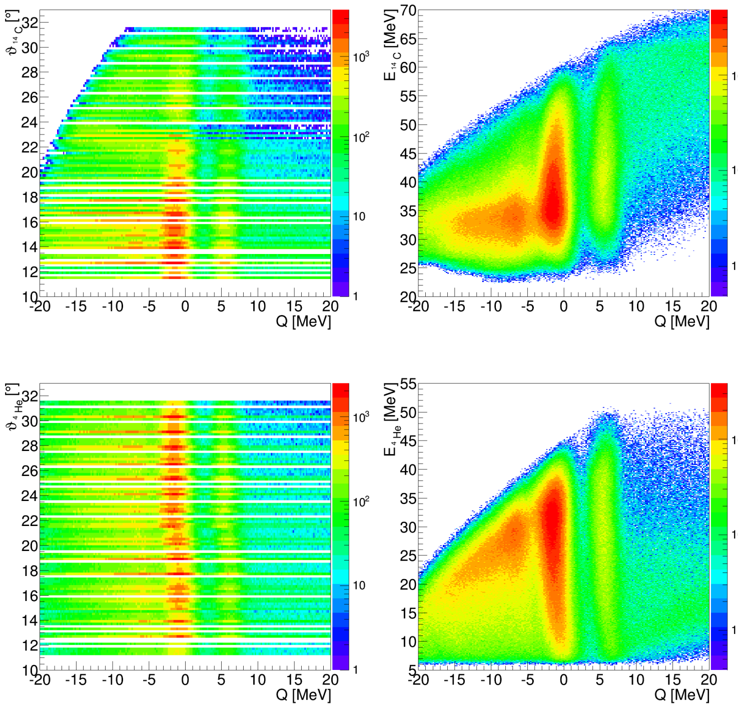

Figure B.1: Q-value dependence on energy and angle of detected particles for the ^{9}Be(^{13}C,^{14}C^{4}He) reaction. ^{14}C and ^{4}He were detected in detector telescopes T1 and T2, respectively.

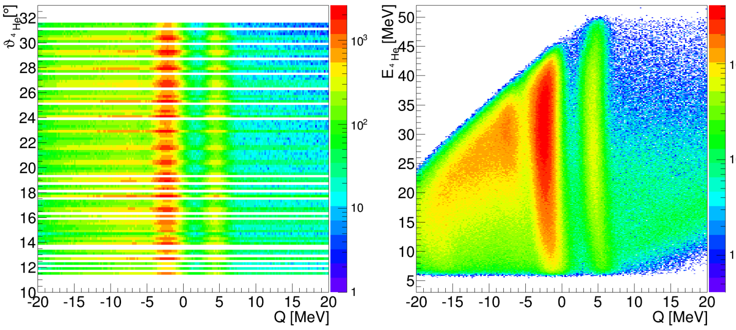
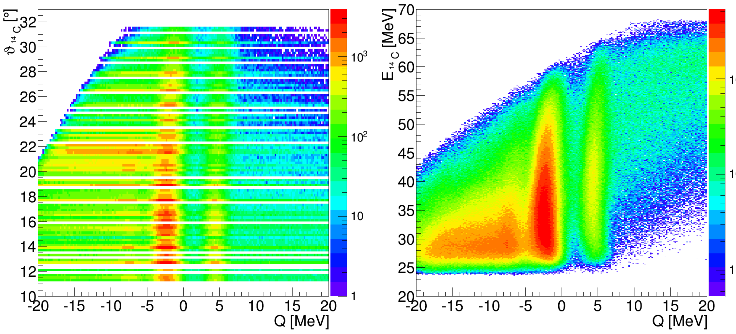

Figure B.2: Q-value dependence on energy and angle of detected particles for the ^{9}Be(^{13}C,^{14}C^{4}He) reaction. ^{14}C and ^{4}He were detected in detector telescopes T2 and T1, respectively.

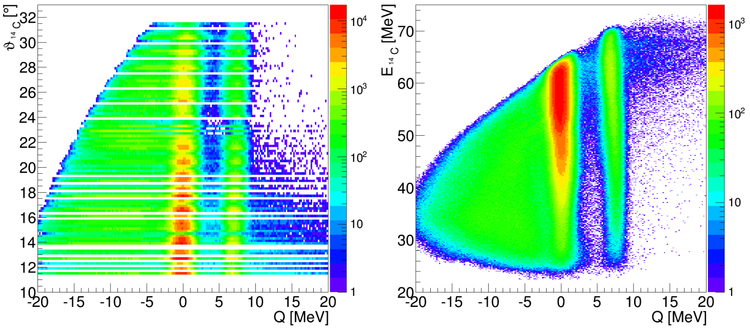
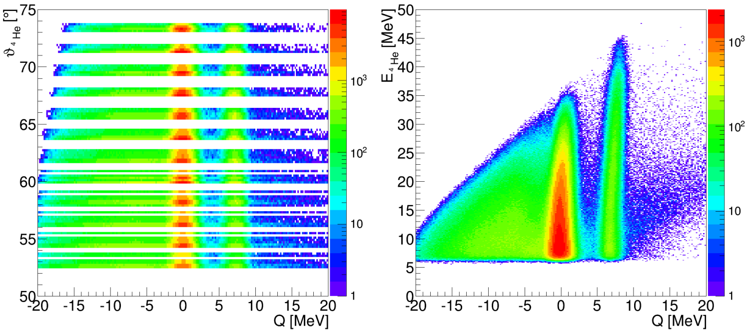

Figure B.3: Q-value dependence on energy and angle of detected particles for the ^{9}Be(^{13}C,^{14}C^{4}He) reaction. ^{14}C and ^{4}He were detected in detector telescopes T1 and T4, respectively.

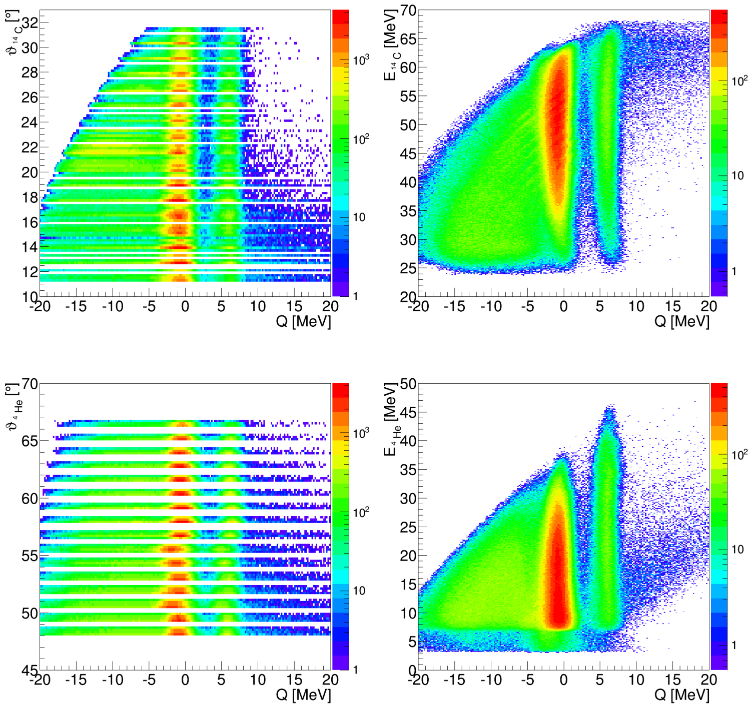

Figure B.4: Q-value dependence on energy and angle of detected particles for the ^{9}Be(^{13}C,^{14}C^{4}He) reaction. ^{14}C and ^{4}He were detected in detector telescopes T2 and T3, respectively.

Appendix C

^{9}Be(^{13}C,^{10}Be^{4}He)^{8}Be reaction

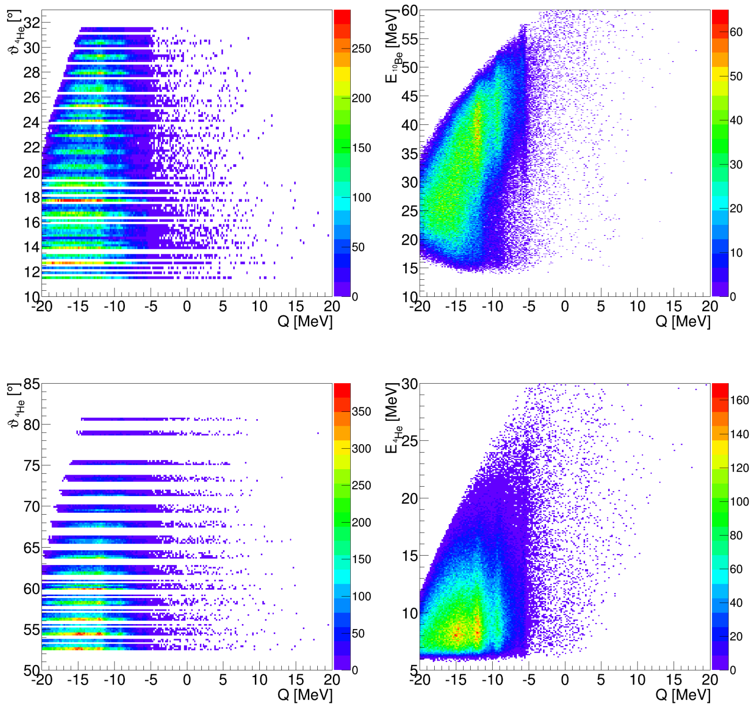

Figure C.1: Q-value dependence on energy and angle of detected particles for the ^{9}Be(^{13}C,^{10}Be^{4}He) reaction. ^{10}Be and ^{4}He were detected in detector telescopes T1 and T2, respectively.

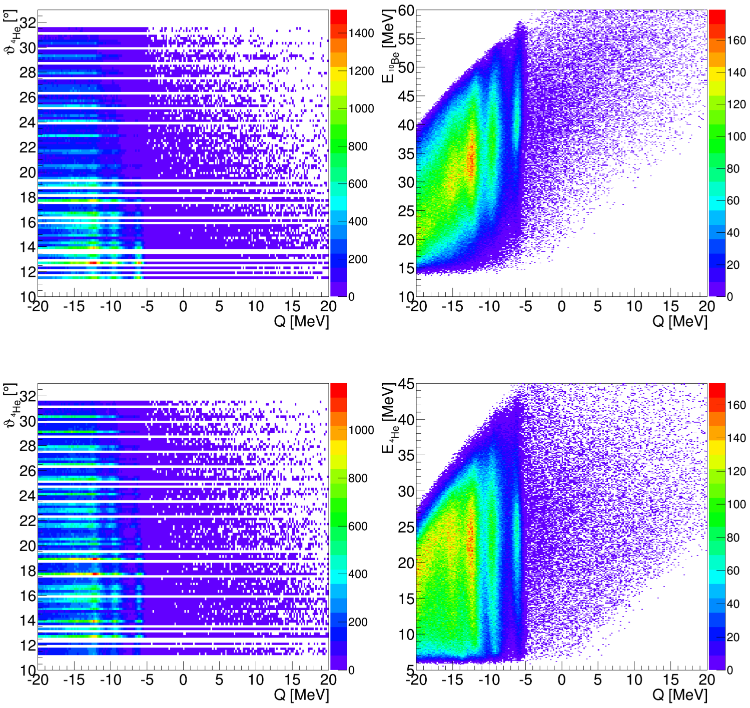

Figure C.2: Q-value dependence on energy and angle of detected particles for the ^{9}Be(^{13}C,^{10}Be^{4}He) reaction. ^{10}Be and ^{4}He were detected in detector telescopes T2 and T1, respectively.

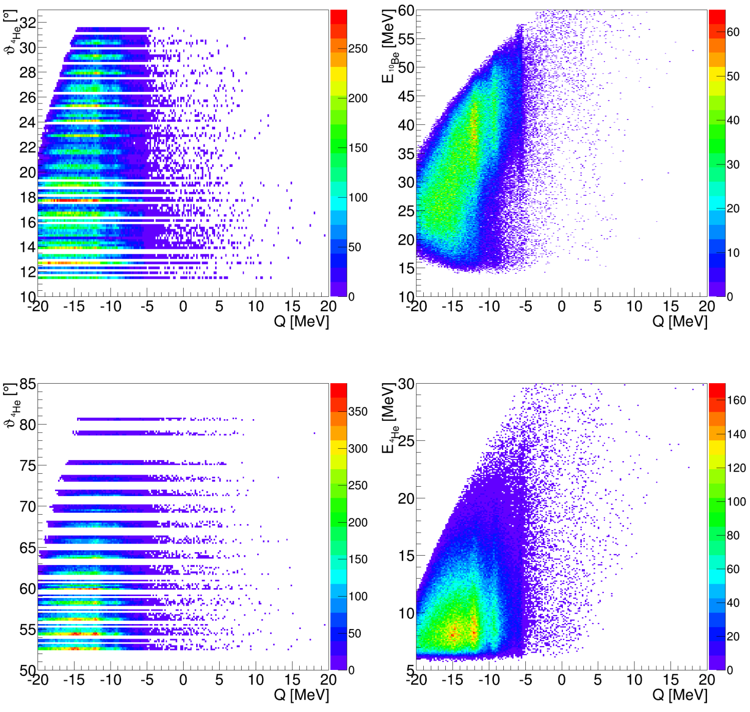

Figure C.3: Q-value dependence on energy and angle of detected particles for the ^{9}Be(^{13}C,^{10}Be^{4}He) reaction. ^{10}Be and ^{4}He were detected in detector telescopes T1 and T4, respectively.

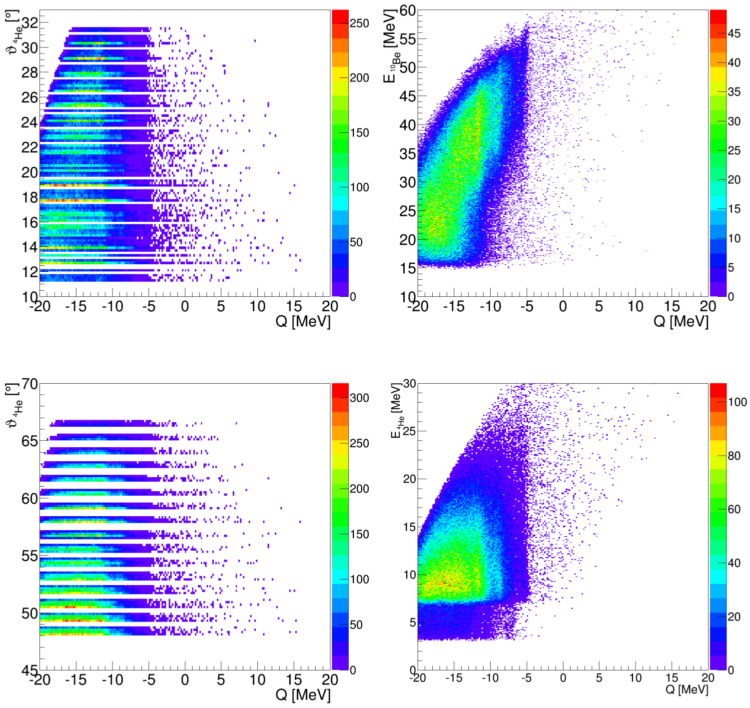

Figure C.4: Q-value dependence on energy and angle of detected particles for the ^{9}Be(^{13}C,^{10}Be^{4}He) reaction. ^{10}Be and ^{4}He were detected in detector telescopes T2 and T3, respectively.

Appendix D

^{9}Be(^{13}C,^{8}Be$_{gs}$ ^{4}He)^{10}Be reaction

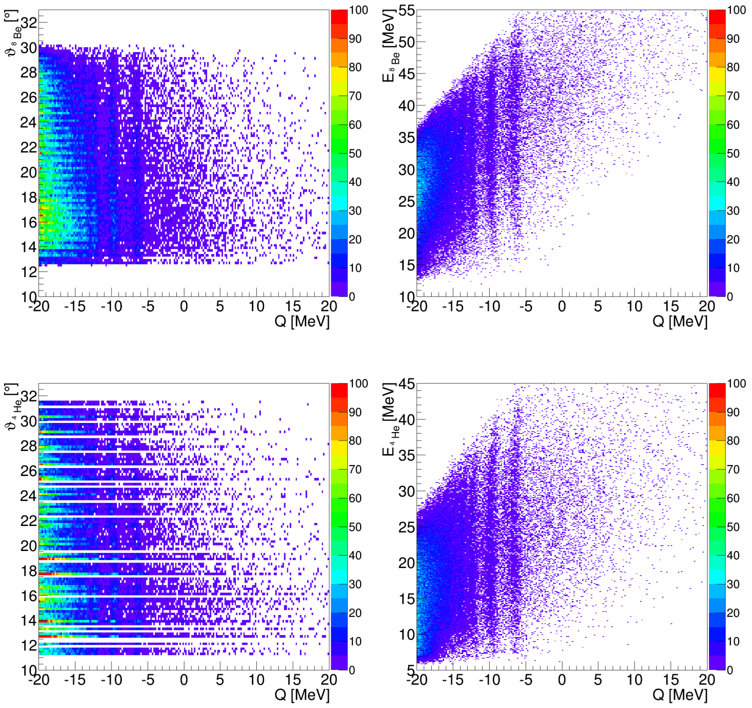

Figure D.1: Q-value dependence on energy and angle of detected particles for the ^{9}Be(^{13}C,^{8}Be$_{gs}$ ^{4}He) reaction. ^{8}Be$_{gs}$ and ^{4}He were detected in detector telescopes T1 and T2, respectively.

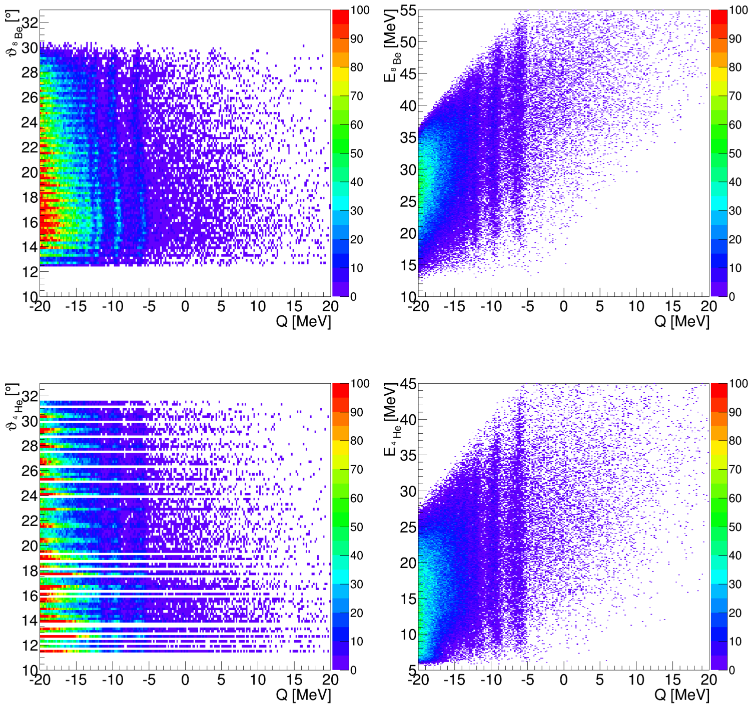

Figure D.2: Q-value dependence on energy and angle of detected particles for the ^{9}Be(^{13}C,^{8}Be$_{gs}$ ^{4}He) reaction. ^{8}Be$_{gs}$ and ^{4}He were detected in detector telescopes T2 and T1, respectively.

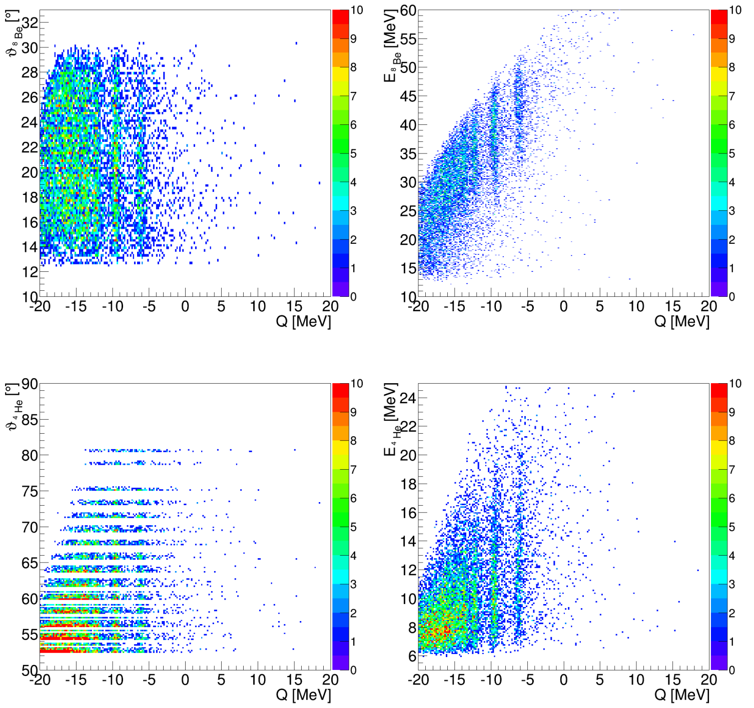

Figure D.3: Q-value dependence on energy and angle of detected particles for the ^{9}Be(^{13}C,^{8}Be$_{gs}$ ^{4}He) reaction. ^{8}Be$_{gs}$ and ^{4}He were detected in detector telescopes T1 and T4, respectively.

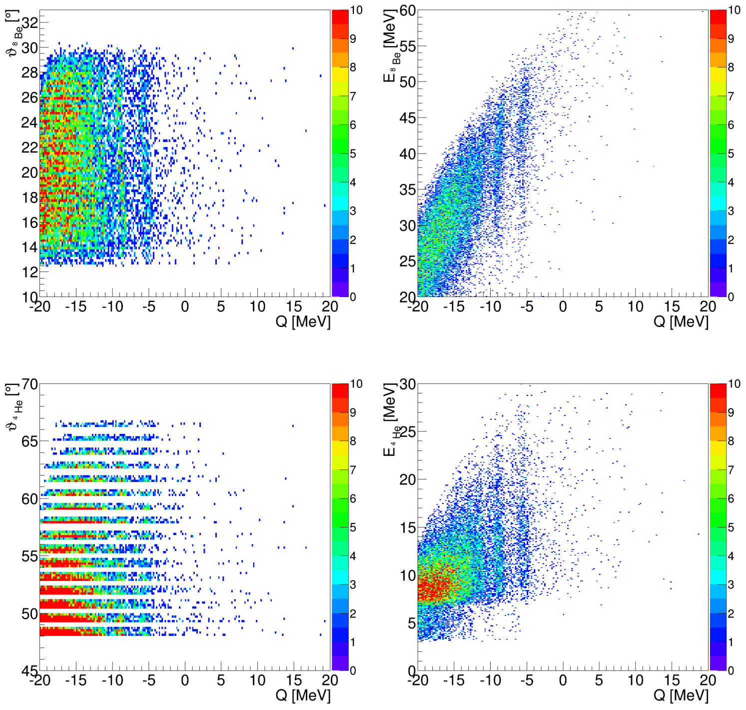

Figure D.4: Q-value dependence on energy and angle of detected particles for the ^{9}Be(^{13}C,^{8}Be$_{gs}$ ^{4}He) reaction. ^{8}Be$_{gs}$ and ^{4}He were detected in detector telescopes T2 and T3, respectively.

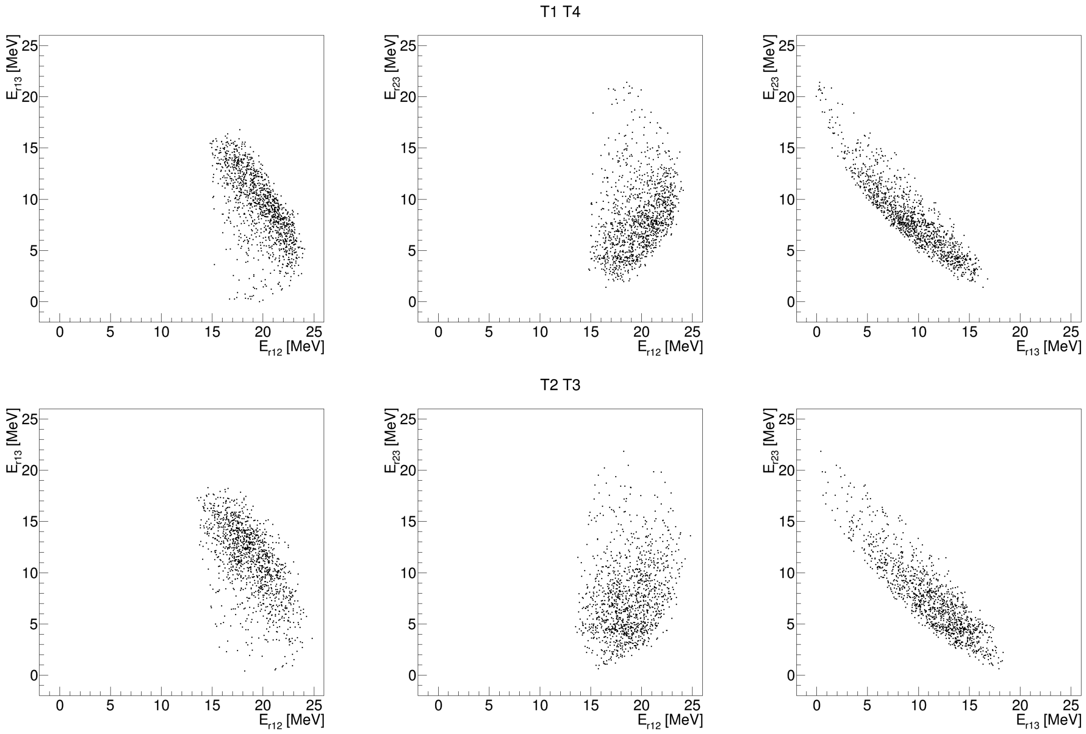

Figure D.5: Relative-energy plots for the ^{9}Be(^{13}C,^{8}Be$_{gs}$ ^{4}He)^{10}Be$_{gs}$ reaction. Different detector combinations are displayed one per row. ^{8}Be$_{gs}$, ^{4}He and ^{10}Be are designated by numbers 1, 2 and 3, respectively.

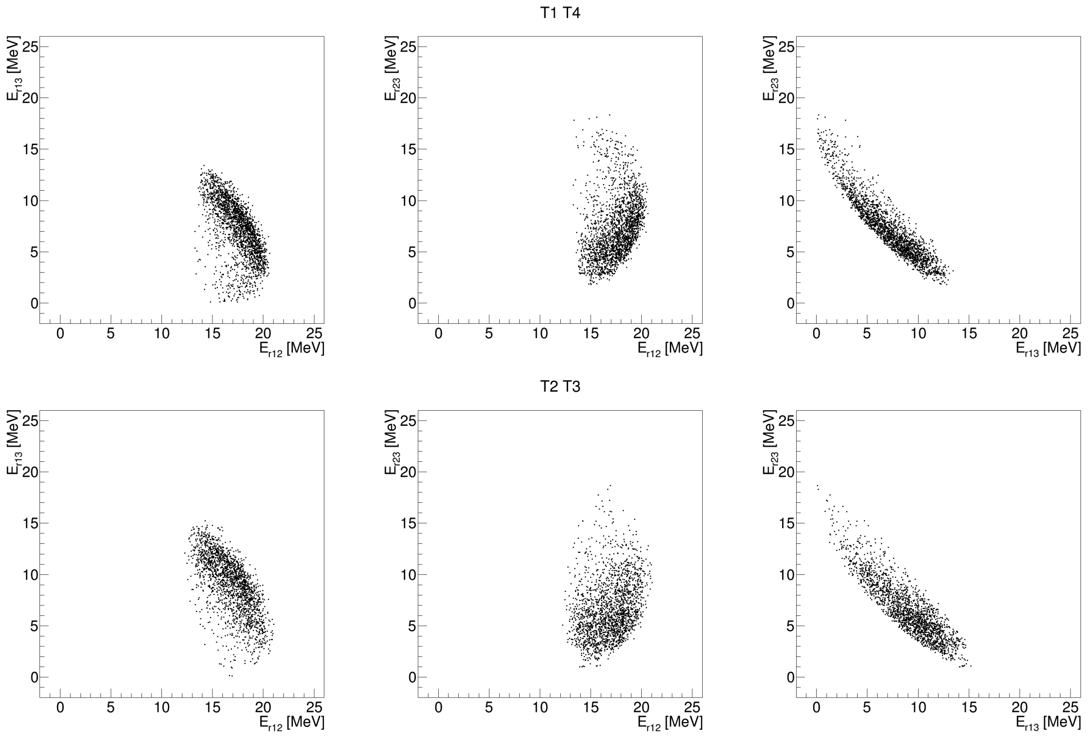

Figure D.6: Relative-energy plots for the ^{9}Be(^{13}C,^{8}Be$_{\mathrm{gs}}$ ^{4}He)^{10}Be(3.37 MeV) reaction. Different detector combinations are displayed one per row. ^{8}Be$_{\mathrm{gs}}$, ^{4}He and ^{10}Be are designated by numbers 1, 2 and 3, respectively.

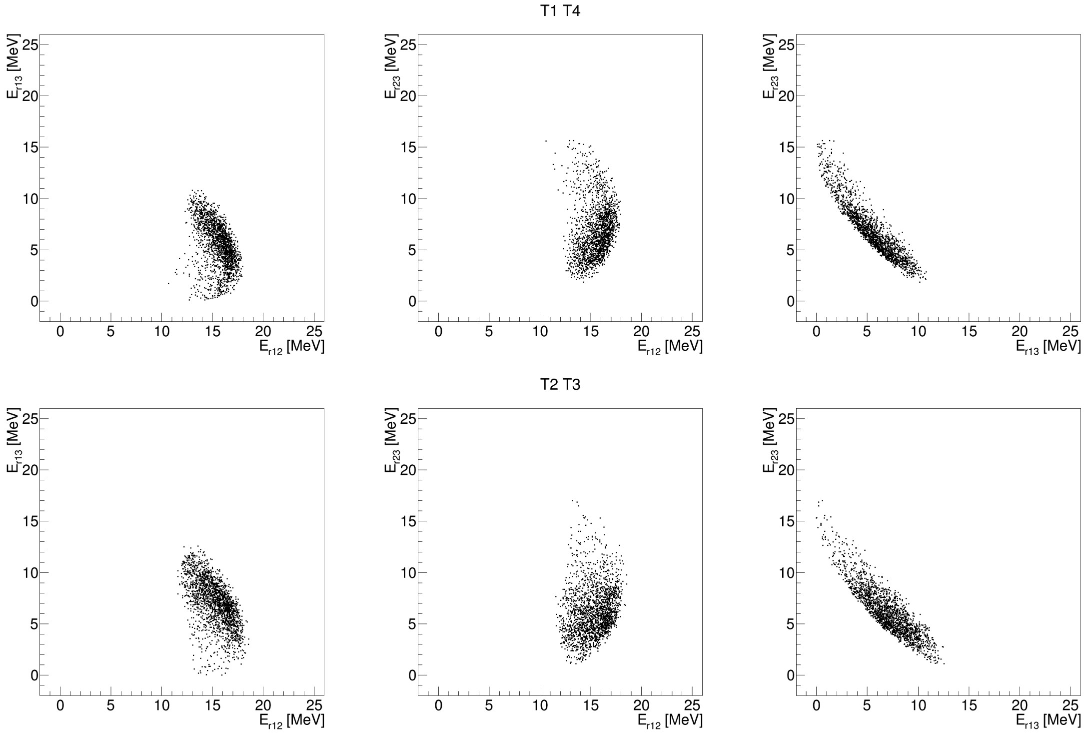

Figure D.7: Relative-energy plots for the ^{9}Be(^{13}C,^{8}Be$_{\mathrm{gs}}$ ^{4}He)^{10}Be(6.18 MeV) reaction. Different detector combinations are displayed one per row. ^{8}Be$_{\mathrm{gs}}$, ^{4}He and ^{10}Be are designated by numbers 1, 2 and 3, respectively.

Appendix E

^{9}Be(^{13}C,^{8}Be$_{gs}$ ^{10}Be)^{4}He reaction

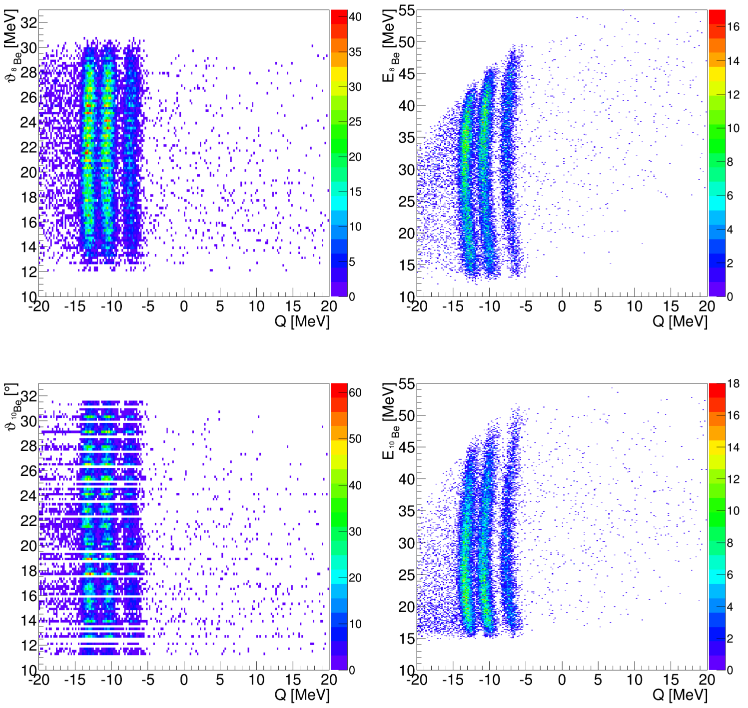

Figure E.1: Q-value dependence on energy and angle of detected particles for the ^{9}Be(^{13}C,^{8}Be$_{gs}$ ^{10}Be) reaction. ^{8}Be$_{gs}$ and ^{10}Be were detected in detector telescopes T1 and T2, respectively.

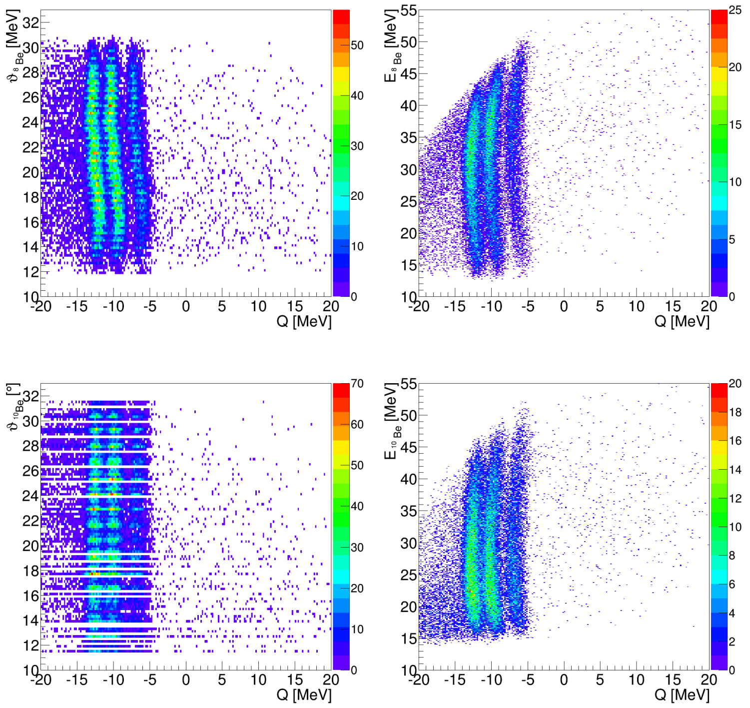

Figure E.2: Q-value dependence on energy and angle of detected particles for the ^{9}Be(^{13}C,^{8}Be$_{gs}$ ^{10}Be) reaction. ^{8}Be$_{gs}$ and ^{10}Be were detected in detector telescopes T2 and T1, respectively.

Bibliography

[1] Wildermuth, K., Tang, Y. C., A Unified Theory of the Nucleus. Vieweg+Teubner Verlag, 1977, [Online]. Available: http://dx.doi.org/10.1007/978-3-322-85255-7

[2] Venikov, N., Glukhov, Y., Manko, V., Novatskii, B., Ogloblin, A., Sakuta, S., Stepanov, D., Unezhev, V., Chuev, V., Chumakov, N., "Nuclear Reactions Induced by Beryllium Ions", Soviet Journal of Nuclear Physics, Vol. 22, 1976, p. 481.

[3] Artemov, K., Goldberg, V., Petrov, I., Rudakov, V., Serikov, I., Timofeev, V., Wolski, R., Szmider, J., "α-Cluster States in ^{17}O Observed in the Reaction ^{13}C(^{6}Li, d)^{17}O(α)^{13}C", Soviet Journal of Nuclear Physics, Vol. 28, 1978, p. 145.

[4] Clark, M. E., Kemper, K. W., Fox, J. D., "Location of high spin 4p-3h strength in ^{17}O", Physical Review C, Vol. 18, No. 3, 1978, pp. 1262–1266, [Online]. Available: http://dx.doi.org/10.1103/PhysRevC.18.1262

[5] Cardella, G., Cunsolo, A., Foti, A., Immè, G., Pappalardo, G., Raciti, G., Rizzo, F., Alamanos, N., Berthier, B., Saunier, N., "Interference effects between ^{17}O states populated in the ^{13}C(^{6}Li,d)^{17}O$^{*}\rightarrow\alpha+^{13}$C reaction", Physical Review C, Vol. 36, No. 6, 1987, pp. 2403–2408, [Online]. Available: http://dx.doi.org/10.1103/PhysRevC.36.2403

[6] Milin, M., Ostashko, V. V., Miljanić, Đ., Bohlen, H. G., Pietro, A. D., Goryunov, O. Y., Kokalova, T., Lattuada, M., Musumarra, A., von Oertzen, W., Pellegriti, M. G., Romano, S., Thummerer, S., Tumino, A., Zadro, M., "States in ^{17}O excited in the ^{13}C+ ^{9}Be $\rightarrow$ $^{13}\mathrm{C}+2\alpha+n$ reaction at 90 MeV", The European Physical Journal A, Vol. 41, No. 3, 2009, pp. 335–339, [Online]. Available: http://dx.doi.org/10.1140/epja/i2009-10827-1

[7] Heil, M., Detwiler, R., Azuma, R. E., Couture, A., Daly, J., Görres, J., Käppeler, F., Reifarth, R., Tischhauser, P., Ugalde, C., Wiescher, M., "The ^{13}C(α,n) reaction and its role as a neutron source for the s process", Physical Review C, Vol. 78, No. 2, 2008, [Online]. Available: http://dx.doi.org/10.1103/PhysRevC.78.025803

[8] Wiescher, M., Käppeler, F., Langanke, K., "Critical reactions in contemporary nuclear astrophysics", Annual Review of Astronomy and Astrophysics, Vol. 50, No. 1, 2012, pp. 165–210, [Online]. Available: http://dx.doi.org/10.1146/annurev-astro-081811-125543

[9] Cognata, M. L., Spitaleri, C., Trippella, O., Kiss, G. G., Rogachev, G. V., Mukhamedzhanov, A. M., Avila, M., Guardo, G. L., Koshchiy, E., Kuchera, A., Lamia, L., Puglia, S. M. R., Romano, S., Santiago, D., Spartà, R., "Measurement of the –3 keV resonance in the reaction ^{13}C(α,n)^{16}O of importance in the s–process", Physical Review Letters, Vol. 109, No. 23, 2012, [Online]. Available: http://dx.doi.org/10.1103/PhysRevLett.109.232701

[10] Fortune, H., Medsker, L., Bishop, J., "Study of the ^{12}C(^{7}Li,p)^{18}O reaction", Nuclear Physics A, Vol. 309, No. 1-2, 1978, pp. 221–232, [Online]. Available: http://dx.doi.org/10.1016/0375-9474(78)90544-4

[11] Gai, M., Ruscev, M., Hayes, A. C., Ennis, J. F., Keddy, R., Schloemer, E. C., Sterbenz, S. M., Bromley, D. A., "Coexistence of single-particle, collective-quadrupole, and α+^{14}C molecular-dipole degrees of freedom in ^{18}O", Physical Review Letters, Vol. 50, No. 4, 1983, pp. 239–242, [Online]. Available: http://dx.doi.org/10.1103/PhysRevLett.50.239

[12] Curtis, N., Caussyn, D. D., Chandler, C., Cooper, M. W., Fletcher, N. R., Laird, R. W., Pavan, J., "Evidence for a molecular rotational band in the $^{14}\mathrm{C}+\alpha$ decay of ^{18}O and the α decay of ^{22}Ne", Physical Review C, Vol. 66, No. 2, 2002, [Online]. Available: http://dx.doi.org/10.1103/PhysRevC.66.024315

[13] von Oertzen, W., Dorsch, T., Bohlen, H. G., Krücken, R., Faestermann, T., Hertenberger, R., Kokalova, T., Mahgoub, M., Milin, M., Wheldon, C., Wirth, H. F., "Molecular and cluster structures in ^{18}O", The European Physical Journal A, Vol. 43, No. 1, 2009, pp. 17–33, [Online]. Available: http://dx.doi.org/10.1140/epja/i2009-10894-2

[14] Avila, M. L., Rogachev, G. V., Goldberg, V. Z., Johnson, E. D., Kemper, K. W., Tchuvil'sky, Y. M., Volya, A. S., "α-cluster structure of ^{18}O", Physical Review C, Vol. 90, No. 2, 2014, [Online]. Available: http://dx.doi.org/10.1103/PhysRevC.90.024327

[15] Johnson, E. D., Rogachev, G. V., Goldberg, V. Z., Brown, S., Robson, D., Crisp, A. M., Cottle, P. D., Fu, C., Giles, J., Green, B. W., Kemper, K. W., Lee, K., Roeder, B. T., Tribble, R. E., "Extreme α-clustering in the ^{18}O nucleus", The European Physical Journal A, Vol. 42, No. 2, 2009, pp. 135–139, [Online]. Available: http://dx.doi.org/10.1140/epja/i2009-10887-1

[16] Rogachev, G., Avila, M., Cherubini, S., Goldberg, V., Gulino, M., Johnson, E., Kuchera, A., Cognata, M. L., Lamia, L., Romano, S., Miller, L., Pizzone, R., Rapisarda, G., Sergi, M., Spitaleri, C., Tribble, R., Trzaska, W., Tumino, A., "Clustering in non-self-conjugate nuclei", Progress of Theoretical Physics Supplement, Vol. 196, 2012, pp. 184–191, [Online]. Available: dx.doi.org/10.1143/PTPS.196.184

[17] Arima, A., Horiuchi, H., Sebe, T., "Weak coupling model of particles and holes in the sd shell nuclei", Physics Letters B, Vol. 24, No. 3, 1967, pp. 129–131, [Online]. Available: http://dx.doi.org/10.1016/0370-2693(67)90499-6

[18] Uroić, M., Milin, M., Pietro, A. D., Figuera, P., Fisichella, M., Lattuada, M., Martel, I., Miljanić, Đ., Pellegriti, M. G., Prepolec, L., Benítez, A. M. S., Scuderi, V., Soić, N., Strano, E., Torresi, D., "Improvements in data analysis obtained by large-area silicon $\Delta E - E$ detector telescopes", European Physical Journal A, Vol. 51, No. 8, 2015, [Online]. Available: http://dx.doi.org/10.1140/epja/i2015-15093-0

[19] Curtis, N., Walshe, J., "RE$_\mathrm{X}$: A Monte Carlo simulation of thick gas target resonant scattering reactions", Nuclear Instruments and Methods in Physics Research Section A: Accelerators, Spectrometers, Detectors and Associated Equipment, Vol. 797, oct 2015, pp. 44–56, [Online]. Available: http://dx.doi.org/10.1016/j.nima.2015.06.027

[20] Horiuchi, H., Ikeda, K., "A Molecule-like Structure in Atomic Nuclei of ^{16}O* and ^{20}Ne", Progress of Theoretical Physics, Vol. 40, No. 2, 1968, pp. 277-287, [Online]. Available: http://dx.doi.org/10.1143/PTP.40.277

[21] Freer, M., “The clustered nucleus—cluster structures in stable and unstable nuclei”, Rep. Prog. Phys., Vol. 70, No. 12, nov 2007, pp. 2149–2210, [Online]. Available: http://dx.doi.org/10.1088/0034-4885/70/12/R03

[22] Bandō, H., “Consequences of the cluster model of light hypernuclei”, Nuclear Physics A, Vol. 450, 1986, pp. 217–236.

[23] Ikeda, K., Takigawa, N., Horiuchi, H., “The systematic structure-change into the molecule-like structures in the self-conjugate 4*n* nuclei”, Prog. Theor. Phys. Suppl., Vol. E68, 1968, pp. 464–475, [Online]. Available: http://dx.doi.org/10.1143/PTPS.E68.464

[24] von Oertzen, W., Freer, M., Kanada-En’Yo, Y., “Nuclear clusters and nuclear molecules”, Physics Reports, Vol. 432, No. 2, sep 2006, pp. 43–113, [Online]. Available: http://dx.doi.org/10.1016/j.physrep.2006.07.001

[25] Wheeler, J. A., “Molecular viewpoints in nuclear structure”, Phys. Rev., Vol. 52, No. 11, dec 1937, pp. 1083–1106, [Online]. Available: http://dx.doi.org/10.1103/PhysRev.52.1083

[26] Griffin, J. J., Wheeler, J. A., “Collective motions in nuclei by the method of generator coordinates”, Phys. Rev., Vol. 108, No. 2, oct 1957, pp. 311–327, [Online]. Available: http://dx.doi.org/10.1103/PhysRev.108.311

[27] Saito, S., “Effect of Pauli principle in scattering of two clusters”, Progress of Theoretical Physics, Vol. 40, No. 4, oct 1968, pp. 893–894, [Online]. Available: http://dx.doi.org/10.1143/PTP.40.893

[28] Ebran, J.-P., Khan, E., Nikšić, T., Vretenar, D., “How atomic nuclei cluster”, Nature, Vol. 487, No. 7407, jul 2012, pp. 341–344, [Online]. Available: http://dx.doi.org/10.1038/nature11246

[29] Kanada-Enyo, Y., Horiuchi, H., “Structure of light unstable nuclei studied with antisymmetrized molecular dynamics”, Prog. Theor. Phys. Suppl., Vol. 142, 2001, pp. 205–263, [Online]. Available: http://dx.doi.org/10.1143/PTPS.142.205

[30] Descouvemont, P., Baye, D., “Multiconfiguration microscopic study of $\alpha+^{14}$C molecular states”, Phys. Rev. C, Vol. 31, No. 6, jun 1985, pp. 2274–2284, [Online]. Available: http://dx.doi.org/10.1103/PhysRevC.31.2274

[31] Abe, Y., Hiura, J., Tanaka, H., “A molecular-orbital model of the atomic nuclei”, Prog. Theor. Phys., Vol. 49, No. 3, mar 1973, pp. 800–824, [Online]. Available: http://dx.doi.org/10.1143/ptp.49.800

[32] Itagaki, N., Okabe, S., “Molecular orbital structures in ^{10}Be”, Phys. Rev. C, Vol. 61, No. 4, mar 2000, [Online]. Available: http://dx.doi.org/10.1103/physrevc.61.044306

[33] Hafstad, L. R., Teller, E., “The alpha-particle model of the nucleus”, Phys. Rev., Vol. 54, No. 9, nov 1938, pp. 681–692, [Online]. Available: http://dx.doi.org/10.1103/PhysRev.54.681

[34] Bauhoff, W., Schultheis, H., Schultheis, R., “Alpha cluster model and the spectrum of ^{16}O”, Phys. Rev. C, Vol. 29, No. 3, mar 1984, pp. 1046–1055, [Online]. Available: http://dx.doi.org/10.1103/PhysRevC.29.1046

[35] Buck, B., Dover, C. B., Vary, J. P., “Simple potential model for cluster states in light nuclei”, Phys. Rev. C, Vol. 11, No. 5, may 1975, pp. 1803–1821, [Online]. Available: http://dx.doi.org/10.1103/PhysRevC.11.1803

[36] Curtis, N., Almaraz-Calderon, S., Aprahamian, A., Ashwood, N. I., Barr, M., Bucher, B., Copp, P., Couder, M., Fang, X., Freer, M., Goldring, G., Jung, F., Lesher, S. R., Lu, W., Malcolm, J. D., Roberts, A., Tan, W. P., Wheldon, C., Ziman, V. A., “Investigation of the 4-α linear chain state in ^{16}O”, Phys. Rev. C, Vol. 88, No. 6, dec 2013, [Online]. Available: http://dx.doi.org/10.1103/PhysRevC.88.064309

[37] Milin, M., Spectroscopy of oxygen istopes (unpublished).

[38] Krane, K., Introductory nuclear physics. New York: Wiley, 1988.

[39] Furutani, H., Kanada, H., Kaneko, T., Nagata, S., Nishioka, H., Okabe, S., Saito, S., Sakuda, T., Seya, M., “Chapter III. study of non-alpha-nuclei based on the viewpoint of cluster correlations”, Prog. Theor. Phys. Suppl., Vol. 68, 1980, pp. 193–302, [Online]. Available: http://dx.doi.org/10.1143/ptps.68.193

[40] Zuker, A. P., “Structure of ^{18}F and ^{18}O”, Phys. Rev. Lett., Vol. 23, No. 17, oct 1969, pp. 983–987, [Online]. Available: http://dx.doi.org/10.1103/physrevlett.23.983

[41] Descouvemont, P., “Microscopic analysis of the ^{13}C(α,n)^{16}O and ^{13}C(α,α)^{13}C reactions”, Phys. Rev. C, Vol. 36, No. 6, dec 1987, pp. 2206–2211, [Online]. Available: http://dx.doi.org/10.1103/physrevc.36.2206

[42] Cunsolo, A., Foti, A., Immè, G., Pappalardo, G., Raciti, G., Saunier, N., “Evidence for 3p-2h rotational bands in ^{17}O”, Physics Letters B, Vol. 124, No. 6, may 1983, pp. 439–442, [Online]. Available: http://dx.doi.org/10.1016/0370-2693(83)91546-0

[43] Volya, A., Tchuvilsky, Y. M., “Cluster properties of nuclear states in the modern shell model approach”, J. Phys.: Conf. Ser., Vol. 569, dec 2014, p. 012054, [Online]. Available: http://dx.doi.org/10.1088/1742-6596/569/1/012054

[44] Furutachi, N., Kimura, M., Dote, A., Kanada-Enyo, Y., Oryu, S., “Cluster structures in oxygen isotopes”, Progress of Theoretical Physics, Vol. 119, No. 3, mar 2008, pp. 403–420, [Online]. Available: http://dx.doi.org/10.1143/ptp.119.403

[45] Lane, A. M., Thomas, R. G., “R-Matrix theory of nuclear reactions”, Reviews of Modern Physics, Vol. 30, No. 2, 1958, pp. 257–353, [Online]. Available: http://dx.doi.org/10.1103/RevModPhys.30.257

[46] Descouvemont, P., Baye, D., “The R-matrix theory”, Rep. Prog. Phys., Vol. 73, No. 3, 2010, p. 036301, [Online]. Available: http://dx.doi.org/10.1088/0034-4885/73/3/036301

[47] Thompson, I. J., Nunes, F. M., Nuclear Reactions for Astrophysics: Principles, Calculation and Applications of Low-Energy Reactions. Cambridge University Press, 2009.

[48] Brune, C. R., “Alternative parametrization of R-matrix theory”, Physical Review C, Vol. 66, No. 4, 2002, [Online]. Available: http://dx.doi.org/10.1103/PhysRevC.66.044611

[49] Azuma, R. E., Uberseder, E., Simpson, E. C., Brune, C. R., Costantini, H., de Boer, R. J., Görres, J., Heil, M., LeBlanc, P. J., Ugalde, C., Wiescher, M., “AZURE: An R-matrix code for nuclear astrophysics”, Physical Review C, Vol. 81, No. 4, 2010, [Online]. Available: http://dx.doi.org/10.1103/PhysRevC.81.045805

[50] Tilley, D., Weller, H., Cheves, C., “Energy levels of light nuclei A = 16–17”, Nuclear Physics A, Vol. 564, No. 1, 1993, pp. 1–183, [Online]. Available: http://dx.doi.org/10.1016/0375-9474(93)90073-7

[51] Artemov, K. P., Belyanin, O. P., Vetoshkin, A. L., Wolskj, R., Golovkov, M. S., Goldberg, V. S., Madeja, M., Pankratov, V. V., Serikov, I. N., Timofee, V. A., Shadrin, V. N., Szmider, J., "Effective method of study of α-cluster states", Soviet Journal of Nuclear Physics, Vol. 408, No. 52, 1990.

[52] Micron Semiconductor Limited, "Design w1 specification sheet", [Online]. Available: http://www.micronsemiconductor.co.uk/pdf/w1.pdf accessed in August 2015.

[53] Knoll, G., Radiation detection and measurement. Hoboken, N.J: John Wiley, 2010.

[54] Grassi, L., Forneris, J., Torresi, D., Acosta, L., Pietro, A. D., Figuera, P., Fisichella, M., Grilj, V., Jakšić, M., Lattuada, M., Mijatović, T., Milin, M., Prepolec, L., Skukan, N., Soić, N., Tokić, V., Uroić, M., "Study of the inter-strip gap effects on the response of double sided silicon strip detectors using proton micro-beams", Nuclear Instruments and Methods in Physics Research Section A: Accelerators, Spectrometers, Detectors and Associated Equipment, Vol. 767, dec 2014, pp. 99–111, [Online]. Available: http://dx.doi.org/10.1016/j.nima.2014.08.009

[55] Bailey, S., Freer, M., Kokalova, T., Cruz, S., Floyd, H., Parker, D. J., "Energy levels of ^{18}F from the $^{14}\mathrm{N}+\alpha$ resonant reaction", Physical Review C, Vol. 90, No. 2, 2014, [Online]. Available: http://dx.doi.org/10.1103/PhysRevC.90.024302

[56] Heil, M., "Neutronenquellen für den s-Prozess un die Rolle der $^{13}\mathrm{C}(\alpha,\mathrm{n})$ Reaktion", Doctoral thesis, Fakultät für Physik und Astronomie, Universität Heidelberg, Heidelberg, Germany, 2002.

[57] Larson, N., Updated users' guide for Sammy: multilevel R-matrix fits to neutron data using Bayes' equations (Rep. ORNL/TM-9179/R8), Oak Ridge National Laboratory, Oak Ridge, TN, USA, 2008.

[58] Schouky, I., Untersuchung der Niveaustruktur von ^{17}O und ^{18}O im Bereich zwichen Neutronbindungsenergie und 12 MeV Anregungsenergie (Rep. KFK-2503), Gesellscaft für Kernforschung M.B.H., Karlsruhe, Germany, 1977.

[59] Lane, R., Langsdorf, A., Monahan, J., Elwyn, A., "The angular distributions of neutrons scattered from various nuclei", Annals of Physics, Vol. 12, No. 2, 1961, pp. 135–171, [Online]. Available: http://dx.doi.org/10.1016/0003-4916(61)90001-X

[60] Sayer, R., Leal, L., Larson, N., Spencer, R., Wright, R., R-matrix evaluation of ^{16}O neutron cross sections up to 6.3 MeV (ORNL/TM-2000/212), Oak Ridge National Laboratory, Oak Ridge, TN, USA, 2000.

[61] Nelson, R., Chadwick, M., Michaudon, A., Young, P., “High-resolution measurements and calculation of photon-production cross sections for ^{16}O(n,xγ) reacions induced by neutrons with energies between 4 and 200 MeV”, Nuclear Science and Engineering, Vol. 138, 2001, pp. 105–144.

[62] Seitz, J., Huber, P., “Wirkungsquerschnitt der ^{16}O(n,α)^{13}C-Reaktion für schnelle Neutronen”, Helvetica Physica Acta, 1955, [Online]. Available: http://dx.doi.org/10.5169/seals-112610

[63] Walton, R. B., Clement, J. D., Boreli, F., “Interaction of Neutrons with Oxygen and a Study of the ^{13}C(α,n)^{16}O Reaction ”, Physical Review, Vol. 107, No. 4, 1957, pp. 1065–1075, [Online]. Available: http://dx.doi.org/10.1103/PhysRev.107.1065

[64] Davis, E., Bonner, T., Worley, D., Bass, R., “Disintegration of ^{16}O and ^{12}C by fast neutrons”, Nuclear Physics, Vol. 48, 1963, pp. 169–175, [Online]. Available: http://dx.doi.org/10.1016/0029-5582(63)90153-6

[65] Drotleff, H. W., Denker, A., Knee, H., Soine, M., Wolf, G., Hammer, J. W., Greife, U., Rolfs, C., Trautvetter, H. P., “Reaction rates of the s-process neutron sources ^{22}Ne(α, n)^{25}Mg and ^{13}C(α, n)^{16}O”, The Astrophysical Journal Letters, Vol. 414, 1993, p. 735, [Online]. Available: http://dx.doi.org/10.1086/173119

[66] Harissopulos, S., Becker, H. W., Hammer, J. W., Lagoyannis, A., Rolfs, C., Strieder, F., “Cross section of the ^{13}C(α,n)^{16}O reaction: A background for the measurement of geo-neutrinos”, Physical Review C, Vol. 72, No. 6, 2005, [Online]. Available: http://dx.doi.org/10.1103/PhysRevC.72.062801

[67] Milin, M., Private communication.

[68] Azaiez, F., Essabaa, S., Ibrahim, F., Verney, D., “The ALTO Facility in Orsay”, Nuclear Physics News, Vol. 23, No. 2, 2013, pp. 5–10, [Online]. Available: http://dx.doi.org/10.1080/10619127.2013.797270

[69] Mesytec GmbH, "MPR-16/L, MPR-32/MPR-64 data sheet V7.0_01", [Online]. Available: http://mesytec.de/datasheets/MPR16.pdf accessed in August 2015.

[70] Caen S.p.A, "N568B & N568LC user manual", [Online]. Available: http://www.caen.it/servlet/checkCaenManualFile?Id=5295 accessed in August 2015.

[71] Silena S.p.A, "Silena 9418/6-V 32 channels spectroscopy grade peak sensing ADC (stand. V430)", [Online]. Available: http://www.geocities.ws/silena_spa/silena/products/camacandvme/94186v.htm accessed in August 2015.

[72] Davinson, T., "Silena 9418 acquisition control module", [Online]. Available: http://npg.dl.ac.uk/MIDAS/VME/sac.html accessed in August 2015.

[73] Motorola Inc., "MVME2400 series VME processor module installation and use", [Online]. Available: http://www-mipp.fnal.gov/TPC/DAQ/v2400ai.pdf accessed in August 2015.

[74] Pucknell, V., Laff, D., "Multi instance data acquisiton system (MIDAS)", [Online]. Available: http://npg.dl.ac.uk/MIDAS/ accessed in August 2015.

[75] Caen S.p.A, "Technical information manual for model v895 16 channel leading edge discriminators", [Online]. Available: http://www.caen.it/servlet/checkCaenManualFile?Id=5369 accessed in August 2015.

[76] Leo, W. R., Techniques for Nuclear and Particle Physics Experiments: A How-to Approach. Springer, 1992.

[77] Dijkstra, E. W., "A note on two problems in connexion with graphs", Numerische Mathematik, Vol. 1, No. 1, 1959, pp. 269–271, [Online]. Available: http://dx.doi.org/10.1007/BF01386390

[78] Milin, M., "Kinematika (unpublished)", 2007.

[79] Goodfellow Cambridge Ltd., "Beryllium sputtering target specification", [Online]. Available: http://www.goodfellow.com accessed in August 2015.

[80] Ohlsen, G., "Kinematic relations in reactions of the form A+B→C+D+E", Nuclear Instruments and Methods, Vol. 37, 1965, pp. 240–248, [Online]. Available: http://dx.doi.org/10.1016/0029-554X(65)90368-X

[81] Costanzo, E., Lattuada, M., Romano, S., Vinciguerra, D., Zadro, M., “A procedure for the analysis of the data of a three body nuclear reaction”, Nuclear Instruments and Methods in Physics Research Section A: Accelerators, Spectrometers, Detectors and Associated Equipment, Vol. 295, No. 3, 1990, pp. 373–376, [Online]. Available: http://dx.doi.org/10.1016/0168-9002(90)90715-I

[82] Tilley, D., Kelley, J., Godwin, J., Millener, D., Purcell, J., Sheu, C., Weller, H., “Energy levels of light nuclei”, Nuclear Physics A, Vol. 745, No. 3-4, dec 2004, pp. 155–362, [Online]. Available: http://dx.doi.org/10.1016/j.nuclphysa.2004.09.059

[83] Freer, M., Casarejos, E., Achouri, L., Angulo, C., Ashwood, N. I., Curtis, N., Demaret, P., Harlin, C., Laurent, B., Milin, M., Orr, N. A., Price, D., Raabe, R., Soić, N., Ziman, V. A., “$\alpha : 2n : \alpha$ molecular band in ^{10}Be”, Physical Review Lettres, Vol. 96, No. 4, 2006, [Online]. Available: http://dx.doi.org/10.1103/PhysRevLett.96.042501

[84] Curtis, N., Ashwood, N. I., Catford, W. N., Clarke, N. M., Freer, M., Mahboub, D., Metelko, C. J., Pain, S. D., Soić, N., Weisser, D. C., “α+Li and H+Be decay of ^{10,11,12}B”, Physical Review C, Vol. 72, No. 4, 2005, [Online]. Available: http://dx.doi.org/10.1103/PhysRevC.72.044320

[85] Milin, M., Aliotta, M., Cherubini, S., Davinson, T., Pietro, A. D., Figuera, P., Galster, W., Miljanić, D., Ninane, A., Ostrowski, A. N., Shotter, A. C., Soić, N., Spitaleri, C., Zadro, M., “The ^{6}He+^{6}Li reactions and exotic states of ^{10}Be”, Europhysics Letters (EPL), Vol. 48, No. 6, 1999, pp. 616–622, [Online]. Available: http://dx.doi.org/10.1209/epl/i1999-00528-3

[86] Soić, N., Blagus, S., Bogovac, M., Fazinić, S., Lattuada, M., Milin, M., Miljanić, D., Rendić, D., Spitaleri, C., Tadić, T., Zadro, M., “^{6}He+α clustering in ^{10}Be”, Europhysics Letters (EPL), Vol. 34, No. 1, 1996, pp. 7–12, [Online]. Available: http://dx.doi.org/10.1209/epl/i1996-00407-y

[87] Tilley, D., Weller, H., Cheves, C., Chasteler, R., “Energy levels of light nuclei A = 18–19”, Nuclear Physics A, Vol. 595, No. 1, 1995, pp. 1–170, [Online]. Available: http://dx.doi.org/10.1016/0375-9474(95)00338-1

[88] Soić, N., Freer, M., Donadille, L., Clarke, N. M., Leask, P. J., Catford, W. N., Jones, K. L., Mahboub, D., Fulton, B. R., Greenhalgh, B. J., Watson, D. L., Weisser, D. C.,

"^{4}He decay of excited states in ^{14}C", Physical Review C, Vol. 68, No. 1, 2003, [Online]. Available: http://dx.doi.org/10.1103/PhysRevC.68.014321

[89] Price, D., Freer, M., Ahmed, S., Ashwood, N., Clarke, N., Curtis, N., McEwan, P., Metelko, C., Novatski, B., Sakuta, S., Soić, N., Stepanov, D., Ziman, V., "Alpha-decay of excited states in ^{13}C and ^{14}C", Nuclear Physics A, Vol. 765, No. 3-4, 2006, pp. 263–276, [Online]. Available: http://dx.doi.org/10.1016/j.nuclphysa.2005.11.004

[90] Price, D. L., Freer, M., Ashwood, N. I., Clarke, N. M., Curtis, N., Giot, L., Lima, V., Ewan, P. M., Novatski, B., Orr, N. A., Sakuta, S., Scarpaci, J. A., Stepanov, D., Ziman, V., "α decay of excited states in ^{14}C", Physical Review C, Vol. 75, No. 1, 2007, [Online]. Available: http://dx.doi.org/10.1103/PhysRevC.75.014305

[91] Haigh, P. J., Ashwood, N. I., Bloxham, T., Curtis, N., Freer, M., McEwan, P., Price, D., Ziman, V., Bohlen, H. G., Kokalova, T., Schulz, C., Torabi, R., von Oertzen, W., Wheldon, C., Catford, W., Harlin, C., Kalpakchieva, R., Massey, T. N., "Measurement of α and neutron decay widths of excited states of C^{14}", Physical Review C, Vol. 78, No. 1, 2008, [Online]. Available: http://dx.doi.org/10.1103/PhysRevC.78.014319

[92] Oertzen, W., Bohlen, H. G., Milin, M., Kokalova, T., Thummerer, S., Tumino, A., Kalpakchieva, R., Massey, T. N., Eisermann, Y., Graw, G., Faestermann, T., Hertenberger, R., Wirth, H.-F., "Search for cluster structure of excited states in ^{14}C", The European Physical Journal A, Vol. 21, No. 2, 2004, pp. 193–215, [Online]. Available: http://dx.doi.org/10.1140/epja/i2003-10188-9

[93] Ajzenberg-Selove, F., "Energy levels of light nuclei A = 13–15", Nuclear Physics A, Vol. 523, No. 1, 1991, pp. 1–196, [Online]. Available: http://dx.doi.org/10.1016/0375-9474(91)90446-D

[94] Soić, N., Freer, M., Donadille, L., Clarke, N., Leask, P., Catford, W., Jones, K., Mahboub, D., Fulton, B., Greenhalgh, B., Watson, D., "α-decaying excited states in carbon and boron isotopes", Nuclear Physics A, Vol. 738, 2004, pp. 347–351, [Online]. Available: http://dx.doi.org/10.1016/j.nuclphysa.2004.04.059

[95] Szczurek, A., Bodek, K., Jarczyk, L., Krug, J., Krug, J., Lübcke, W., Rühl, H., Steinke, M., Stephan, M., Kamke, D., Strzałkowski, A., "Ghost anomaly and first excited state of

^{8}Be in the ^{9}Be(d, tα)^{4}He reaction at 7 MeV", Nuclear Physics A, Vol. 531, No. 1, 1991, pp. 77–92, [Online]. Available: http://dx.doi.org/10.1016/0375-9474(91)90569-R

[96] Hall, H., Bonner, T., "Gamma radiations from inelastic scattering of fast neutrons in ^{12}C, ^{14}N and ^{16}O", Nuclear Physics, Vol. 14, No. 2, dec 1959, pp. 295–313, [Online]. Available: http://dx.doi.org/10.1016/0029-5582(59)90014-8

[97] Etchegoyen, M. C., Etchegoyen, A., Moreno, E. B., "Three-particle transfer on ^{14}N", J. Phys. G: Nucl. Phys., Vol. 10, No. 6, jun 1984, pp. 823–831, [Online]. Available: http://dx.doi.org/10.1088/0305-4616/10/6/015

[98] Manley, D. M., Berman, B. L., Bertozzi, W., Buti, T. N., Finn, J. M., Hersman, F. W., Hyde-Wright, C. E., Hynes, M. V., Kelly, J. J., Kovash, M. A., Kowalski, S., Lourie, R. W., Murdock, B., Norum, B. E., Pugh, B., Sargent, C. P., "High-resolution inelastic electron scattering from ^{17}O", Physical Review C, Vol. 36, No. 5, 1987, pp. 1700–1726, [Online]. Available: http://dx.doi.org/10.1103/PhysRevC.36.1700

[99] Spear, R., Larson, J., Pearson, J., "Excitation function for the reaction ^{13}C(α,nγ)^{16}O", Nuclear Physics, Vol. 41, jan 1963, pp. 353–363, [Online]. Available: http://dx.doi.org/10.1016/0029-5582(63)90514-5

[100] Crisp, A. M., Roeder, B. T., Momotyuk, O. A., Keeley, N., Kemper, K. W., Maréchal, F., Rusek, K., Weintraub, W., Wiedeking, M., "Survey of ^{17}O excited states selectively populated by five-particle transfer reactions", Physical Review C, Vol. 77, No. 4, 2008, [Online]. Available: http://dx.doi.org/10.1103/PhysRevC.77.044315

[101] Rae, W., Bhowmik, R., "Reaction mechanism and spin information in the sequential breakup of ^{18}O at 82 MeV", Nuclear Physics A, Vol. 420, No. 2, 1984, pp. 320–350, [Online]. Available: http://dx.doi.org/10.1016/0375-9474(84)90445-7

[102] Mairle, G., Knöpfle, K., Doll, P., Breuer, H., Wagner, G., "The (d, t) and (d, t) reactions on ^{18}O and the 1p spin-orbit splitting", Nuclear Physics A, Vol. 280, No. 1, apr 1977, pp. 97–108, [Online]. Available: http://dx.doi.org/10.1016/0375-9474(77)90296-2

[103] Meier-Ewert, K., Bethge, K., Pfeiffer, K.-O., "^{6}Li induced reactions on ^{12}C at E_{lab} = 20 MeV", Nuclear Physics A, Vol. 110, No. 1, 1968, pp. 142–160, [Online]. Available: http://dx.doi.org/10.1016/0375-9474(68)90688-X

[104] Bradlow, H., Rae, W., Fisher, P., Godwin, N., Proudfoot, G., Sinclair, D., “Heavy ion induced α-transfer on targets of mass 12 to 15”, Nuclear Physics A, Vol. 314, No. 1, 1979, pp. 207–231, [Online]. Available: http://dx.doi.org/10.1016/0375-9474(79)90562-1

[105] Blilie, C. L., Dehnhard, D., Franey, M. A., Gay, D. H., Holtkamp, D. B., Seestrom-Morris, S. J., Ellis, P. J., Morris, C. L., Millener, D. J., “Isospin structure of transitions in ^{17}O from inelastic pion scattering at 164 MeV”, Physical Review C, Vol. 30, No. 6, 1984, pp. 1989–1998, [Online]. Available: http://dx.doi.org/10.1103/PhysRevC.30.1989

[106] Goldberg, V. Z., Källman, K. M., Lönnroth, T., Manngård, P., Skorodumov, B. B., “Alpha-cluster states in ^{18}O”, Physics of Atomic Nuclei, Vol. 68, No. 7, 2005, pp. 1079–1086, [Online]. Available: http://dx.doi.org/10.1134/1.1992561

[107] Cunsolo, A., Foti, A., Immè, G., Pappalardo, G., Raciti, G., Saunier, N., “^{18}O states via the ^{14}C(^{6}Li,d)^{18}O reaction at 34 MeV incident energy”, Physical Review C, Vol. 24, No. 2, 1981, pp. 476–487, [Online]. Available: http://dx.doi.org/10.1103/PhysRevC.24.476

[108] Morgan, G., Tilley, D., Mitchell, G., Hilko, R., Roberson, N., “Study of ^{18}O through ^{14}C$+\alpha$ reactions”, Nuclear Physics A, Vol. 148, No. 2, 1970, pp. 480–491, [Online]. Available: http://dx.doi.org/10.1016/0375-9474(70)90641-X

[109] Ashwood, N. I., Freer, M., Sakuta, S., Ahmed, S., Clarke, N. M., Curtis, N., McEwan, P., Metelko, C. J., Novatski, B., Soic, N., Stepanov, D., Ziman, V., “Cluster breakup of ^{18}O and ^{22}Ne”, Journal of Physics G: Nuclear and Particle Physics, Vol. 32, No. 4, 2006, pp. 463–474, [Online]. Available: http://dx.doi.org/10.1088/0954-3899/32/4/005

[110] Sellers, R. M., Manley, D. M., Niboh, M. M., Weerasundara, D. S., Lindgren, R. A., Clausen, B. L., Farkhondeh, M., Norum, B. E., Berman, B. L., “Inelastic electron scattering from ^{18}O at backward angles”, Physical Review C, Vol. 51, No. 4, 1995, pp. 1926–1944, [Online]. Available: http://dx.doi.org/10.1103/PhysRevC.51.1926

[111] Smithson, M. J., Watson, D. L., Fortune, H. T., “^{13}C(^{6}Li,p)^{18}O reaction at E(^{6}Li)=28 MeV”, Physical Review C, Vol. 37, No. 3, 1988, pp. 1036–1041, [Online]. Available: http://dx.doi.org/10.1103/PhysRevC.37.1036

[112] Cobern, M. E., Bland, L. C., Fortune, H. T., Moore, G. E., Mordechai, S., Middleton, R., "^{16}O(t,p)^{18}O to low-lying states in ^{18}O", Physical Review C, Vol. 23, No. 6, 1981, pp. 2387–2392, [Online]. Available: http://dx.doi.org/10.1103/PhysRevC.23.2387

[113] Yildiz, S., Freer, M., Soić, N., Ahmed, S., Ashwood, N. I., Clarke, N. M., Curtis, N., Fulton, B. R., Metelko, C. J., Novatski, B., Orr, N. A., Pitkin, R., Sakuta, S., Ziman, V. A., "α-decaying states ^{18}O, ^{20}Ne and ^{22}Ne in ^{18}O beam induced reactions", Physical Review C, Vol. 73, No. 3, 2006, [Online]. Available: http://dx.doi.org/10.1103/PhysRevC.73.034601

[114] Jahn, R., Stahel, D. P., Wozniak, G. J., de Meijer, R. J., Cerny, J., "Survey of the (α, ^{2}He) reaction on 1p- and 2s1d-shell nuclei", Physical Review C, Vol. 18, No. 1, 1978, pp. 9–22, [Online]. Available: http://dx.doi.org/10.1103/PhysRevC.18.9

[115] Bender, D., Richter, A., Spamer, E., Ansaldo, E., Rangacharyulu, C., Knüpfer, W., "High-resolution (e, e) study of isovector M1 and M2 transitions in the oxygen isotopes", Nuclear Physics A, Vol. 406, No. 3, sep 1983, pp. 504–518, [Online]. Available: http://dx.doi.org/10.1016/0375-9474(83)90373-1

[116] Woodworth, J. G., McNeill, K. G., Jury, J. W., Alvarez, R. A., Berman, B. L., Faul, D. D., Meyer, P., "Photonuclear cross sections for ^{18}O", Phys. Rev. C, Vol. 19, No. 5, apr 1979, pp. 1667–1683, [Online]. Available: http://dx.doi.org/10.1103/PhysRevC.19.1667

[117] Manley, D. M., Berman, B. L., Bertozzi, W., Finn, J. M., Hersman, F. W., Hyde-Wright, C. E., Hynes, M. V., Kelly, J. J., Kovash, M. A., Kowalski, S., Lourie, R. W., Murdock, B., Norum, B. E., Pugh, B., Sargent, C. P., "Electroexcitation of M4 transitions in ^{17}O and ^{18}O", Phys. Rev. C, Vol. 34, No. 4, oct 1986, pp. 1214–1222, [Online]. Available: http://dx.doi.org/10.1103/PhysRevC.34.1214

[118] Soić, N., Cali, D., Cherubini, S., Costanzo, E., Lattuada, M., Milin, M., Miljanić, , Romano, S., Spitaleri, C., Zadro, M., "^{7}Li quasi-free scattering off the α-cluster in ^{9}Be nucleus", The European Physical Journal A - Hadrons and Nuclei, Vol. 3, No. 4, dec 1998, pp. 303–305, [Online]. Available: http://dx.doi.org/10.1007/s100500050182

[119] Bhowmik, R., Rae, W., Fulton, B., "Spin measurements and reaction mechanism in the inelastic scattering of ^{18}O on ^{12}C", Physics Letters B, Vol. 136, No. 3, mar 1984, pp. 149–152, [Online]. Available: http://dx.doi.org/10.1016/0370-2693(84)91169-9

List of Figures

List of Tables

Biography

Lovro Prepolec was born in 1984 in Celje, Slovenia. He grew up in Ludbreg, Croatia, attending the elementary school in Ludbreg and secondary school in Varaždin. In 2003 he enrolled in the undergraduate studies of physics at Faculty of Science, University of Zagreb. He graduated in Physics in January 2009 with thesis "Excitation functions of ^{6,7}Li+^{7}Li reactions at low energies" under supervision of Dr. sc. Neven Soić.

Since February 2009 he works at the Ruđer Bošković Institute, in the Laboratory for nuclear physics, Division of experimental phyisics, first as an assistant on the European Comission FP7 project "Clustering phenomena in nuclear physics: strengthening of the Zagreb-Catania-Birmingham partnership" (CLUNA), and since December 2010 as an assistant. He enrolled in the doctoral studies of nuclear physics in late 2009 at Faculty of Science, University of Zagreb.

In 2012 he was awarded the joint Embassy of France-Ruđer Bošković Institute scholarship for a one-month stay at IPN Orsay, France. He participated in more than fifteen experiments at INFN-LNS Catania, INFN-LNL Legnaro, IPN Orsay, GANIL Caen and the local facility at the Ruđer Bošković Institute. The majority of experiments involved nuclear structure measurements using highly segmented silicon detector arrays, but he also participated in several experiments of the PRISMA collaboration. He also worked for three semesters as a teaching assistant for the "Physics 1" and "Physics 2" courses for undergraduate students of chemistry at University of Zagreb. Lovro's main field of research is the study of structure of light nuclei, in particular cluster and molecular structure.

Bibliography of published work

1. Uroić, M.; Milin, M.; Di Pietro, A.; Figuera, P., Fisichella, M.; Lattuada, M.; Martel, I.; Miljanić, Đ.; Pellegriti, M.G.; Prepolec, Lovro; Sanchez Benitez, A.M.; Scuderi, V.;

Soić, N.; Strano, E.; Torresi, D.

Improvements in data analysis obtained by large-area silicon ΔE-E detector telescopes, European physical journal A: hadrons and nuclei 51 (2015), 93

2. Mijatović, T.; Szilner, S.; Corradi, L.; Montanari, D.; Courtin, S.; Fioretto, E.; Gadea, A.; Goasduff, A.; Haas, F.; Jelavić Malenica, D.; Montagnoli, G.; Pollarolo, G.; Prepolec, L.; Scarlassara, F.; Soić, N.; Stefanini, A.M.; Tokić, V.; Ur, C.A.; Valiente-Dobon J.J.

   Pairing Correlation Study in the ^{40}Ar + ^{208}Pb Multinucleon Transfer Reaction, Acta physica Polonica B. 46 (2015), 439–442

3. Grassi, L.; Forneris, J.; Torresi, D.; Acosta, L.; Di Pietro, A.; Figuera, P.; Fisichella, M.; Grilj, V.; Jakšić, M.; Lattuada, M.; Mijatović, T.; Milin, M.; Prepolec, L.; Skukan, N.; Soić, N.; Tokić, V.; Uroić, M.

   Study of the inter-strip gap effects on the response of Double Sided Silicon Strip Detectors using proton micro-beams, Nuclear Instruments and Methods in Physics Research Section A: Accelerators, Spectrometers, Detectors and Associated Equipment 767 (2014), 99–111

4. Walshe, J.; Freer, M.; Wheldon, C.; Achouri, L.N.; Ashwood, N.I.; Catford, W.N.; Celik, I.C.; Curtis, N.; Delaunay, F.; Fernández-Domínguez, B.; Grassi, L.; Kokalova, Tz.; Marqués, M.; Orr, N.A.; Prepolec, L.; Scuderi, V.; Soić, N.; Tokić, V.

   The thick target inverse kinematics technique with a large acceptance silicon detector array, Journal of Physics: Conference Series 569 (2014), 012052

5. Tokić, V.; Soić, N.; Blagus, S.; Fazinic, S.; Jelavić Malenica, D.; Miljanić, Đ.; Prepolec, L.; Skukan, N.; Szilner, S.; Uroic, M.; Milin, M.; Di Pietro, A.; Figuera, P.; Fisichella, M.; Lattuada, M.; Scuderi, V,; Strano, E.; Torresi, D.; Ashwood, N.; Curtis, N.; Freer, M.; Ziman, V.; Martel, I.; Sanchez-Benitez, A. M.; Acosta, L.

   Study of ^{24}Mg Resonances Relevant for Carbon Burning Nucleosynthesis, AIP Conference Proceedings Volume 1595 (2014), 248–250

6. Prepolec, L.; Freer, M.; Ashwood, N.I.; Curtis, N.; Di Pietro, A.; Figuera, P. Fisichella, M.; Grassi, L.; Jelavić Malenica, D.; Kokalova, Tz.; Mijatović, Tea; Milin, M.; Scuderi, V.; Skukan, N.; Soić, N.; Szilner, S.; Tokić, V.; Torresi, D.; Wheldon, C.

   ^{13}C+^{4}He resonant elastic scattering on a thick gas target, Journal of Physics: Conference Series Volume 436 (2013)

7. Freer, M.; Ashwood, N.I.; Curtis, N.; Di Pietro, A.; Figuera, P.; Fisichella, M.; Grassi, L.; Jelavić Malenica, Deša; Kokalova, Tz.; Koncul, Mladen; Mijatović, Tea; Milin, Matko;

Prepolec, Lovro; Scuderi, V.; Skukan, Natko; Soić, Neven; Szilner, Suzana; Tokić, Vedrana; Torresi, D.; Wheldon, C.
Analysis of states in ^{13}C *populated in* ^{9}Be+^{4}He *resonant scattering*, Physical Review C 84 (2011), 034317

8. Uroić, M.; Miljanić, Đ.; Blagus, S.; Bogovac, M.; Skukan, N.; Soić, N.; Majer, M.; Milin, M.; Prepolec, L.; Lattuada, M.; Musumarra, A.; Acosta, L.
$T = 1$ *Isospin Excitation Spectrum in* ^{10}B, International journal of modern physics E 17 (2008), 2345–2348